University of Dublin

Trinity College

School of Physics

Transient Inhomogeneous Ionic Solutions

—

The Influence of the Magnetic Field Gradient

Tim Alexander Butcher

A dissertation submitted for the degree of
Doctor of Philosophy
January 2022

Trinity College Dublin
Coláiste na Tríonóide, Baile Átha Cliath
The University of Dublin

Declaration

I declare that this thesis has not been submitted as an exercise for a degree at this or any other university and it is entirely my own work.

I agree to deposit this thesis in the University's open access institutional repository or allow the library to do so on my behalf, subject to Irish Copyright Legislation and Trinity College Library conditions of use and acknowledgement.

I consent to the examiner retaining a copy of the thesis beyond the examining period, should they so wish (EU GDPR May 2018).

Tim Alexander Butcher
29th September 2021

Submitted: 29th September 2021
Defended: 22nd October 2021

Supervisor: Prof. J. M. D. Coey
Internal Examiner: Prof. Igor Shvets
External Examiner: Prof. Jan Fransaer

Die Natur braucht sich
nicht anzustrengen,
bedeutend zu sein.
Sie ist es.

Robert Walser

Summary

Solutions of paramagnetic ions and their response to magnetic field gradients of permanent magnets were studied. Paramagnetic fluids confined by solid walls only develop internal flows in a magnetic field gradient when a non-uniform concentration of the paramagnetic species is present. The simplest inhomogeneous system comprises two miscible liquids, which start off sharply separated and slowly mix by diffusion.

The method of neutron imaging was adopted to map the concentration evolution of diffusing paramagnetic $Gd(NO_3)_3$ solutions. Magnetic manipulation of the paramagnetic liquid within a miscible non-magnetic liquid such as D_2O is possible by modifying the condition for hydrostatic stability. A magnetic field gradient can capture a concentration of paramagnetic fluid in an ephemeral, purely magnetogravitational phenomenon that is eventually wiped out by diffusion. The addition of non-magnetic $Y(NO_3)_3$ salt to the D_2O can give rise to double-diffusive phenomena such as salt fingering instabilities which significantly hasten the mixing of the liquids by multicomponent convection. It was shown that a magnetic field gradient may serve to prevent and halt such instabilities involving $Gd(NO_3)_3$ solutions by stabilising the paramagnetic fluid.

Concentration gradients in paramagnetic salt solutions can be triggered by electrosorption in porous carbon electrodes. The process of capacitive deionisation was investigated in cells containing paramagnetic Gd^{3+} ions by dynamic neutron imaging. Both carbon aerogels and microporous activated carbon cloths were employed as capacitive deionisation electrodes. The uptake and depletion of Gd^{3+} in the porous electrodes were monitored in situ. A magnetic field gradient was able to modify the concentration distribution in the ensuing inhomogeneous solution after the desalination process.

The possibility of electrochemically separating rare earth ions with the assistance of a magnetic field gradient was explored. The electrolysis of a mixture of $Gd(NO_3)_3$ and $Y(NO_3)_3$ solutions under a magnetic field gradient was analysed. Rare earth hydroxides were precipitated electrochemically and captured by a Nd-Fe-B permanent magnet. Although the deposits on the working electrode followed the magnetic field profile, the method failed to separate the different rare earth hydroxides. No preference of the paramagnetic hydroxide for the regions of highest magnetic field gradient was detected.

Table of Contents

List of Figures

List of Tables

List of Abbreviations

Abbreviation	**Meaning**
ACC	Activated carbon cloth
BET	Brunauer-Emmett-Teller
BJH	Barrett-Joyner-Halenda
CCD	Charge-coupled device
DSC	Differential scanning calorimetry
EDX	Energy dispersive x-ray analysis
Gadox	Gadolinium oxysulfide (Gd_2O_2S)
LLNL	Lawrence Livermore National Laboratory
MHD	Magnetohydrodynamic
QSDFT	Quenched Solid State Density Functional Theory
PIV	Particle image velocimetry
PTFE	Polytetrafluoroethylene
RE	Rare earth
RE^{3+}	Trivalent rare earth ion
sCMOS	scientific Complementary metal-oxide-semiconductor
SEM	Scanning electron microscope
SQUID	Superconducting quantum interference device
TGA	Thermogravimetric analysis

List of Symbols

Symbol	Meaning	Unit
a	Activity	–
b_i	Neutron scattering length	m
c	Concentration	$\mathrm{mol\,m^{-3}}$
e	Elementary charge	$1.6022 \times 10^{-19}\,\mathrm{C}$
g	Gravitational acceleration	$9.81\,\mathrm{m\,s^{-2}}$
$\mathbf{g}$	Gravity vector	$\mathrm{m\,s^{-2}}$
g_J	Landé g-factor	–
$\mathbf{j}$	Current density	$\mathrm{A\,m^{-2}}$
$\mathbf{k}$	Neutron wave vector	$\mathrm{m^{-1}}$
k_B	Boltzmann constant	$1.3807 \times 10^{-23}\,\mathrm{J\,K^{-1}}$
$\mathbf{m}$	Magnetic moment	$\mathrm{J\,T^{-1}}$
n	Amount of substance	mol
$\mathbf{r}$	Position vector	m
r_ion	Ionic radius	m
t	Time	s
$\mathbf{u}$	Flow velocity	$\mathrm{m\,s^{-1}}$
x_i	Mole fraction	–
$\mathbf{B}$	Magnetic flux density	T
C	Curie constant	K
D	Diffusion coefficient	$\mathrm{m^2\,s^{-1}}$
E_th	Thermal energy	J
$\mathbf{F}_{\nabla \mathrm{B}}$	Magnetic field gradient force	$\mathrm{N\,m^{-3}}$
$\mathbf{F}_\mathrm{g}$	Gravitational force density	$\mathrm{N\,m^{-3}}$
$\mathbf{F}_\mathrm{K}$	Kelvin force density	$\mathrm{N\,m^{-3}}$

Symbol	Meaning	Unit
$\mathbf{F}_{\mathrm{H}}$	Korteweg-Helmholtz force density	$\mathrm{N\,m^{-3}}$
E	Energy	J
E	Electric potential	V
E^0	Standard electrode potential	V
F	Faraday constant	$96\,485\,\mathrm{C\,mol^{-1}}$
H^0	Enthalpy of formation	$\mathrm{J\,mol^{-1}}$
$\mathbf{H}$	Magnetic field strength	$\mathrm{A\,m^{-1}}$
I	Current	A
I	Transmitted neutron intensity	–
I_0	Incident neutron intensity	–
I_{dc}	Dark-current intensity	–
I_i	Enthalpy of ionisation	$\mathrm{J\,mol^{-1}}$
J	Total angular momentum quantum number	–
$\mathbf{J}$	Molar flux	$\mathrm{mol\,m^{-2}\,s^{-1}}$
M_i	Molar mass	$\mathrm{kg\,mol^{-1}}$
$\mathbf{M}$	Magnetisation	$\mathrm{A\,m^{-1}}$
N	Particle number	mol
N_A	Avogadro constant	$6.022 \times 10^{23}\,\mathrm{mol^{-1}}$
P	Pressure	$\mathrm{Pa} = \mathrm{N\,m^{-2}}$
Q	Charge	C
R	Universal gas constant	$\mathrm{J\,K^{-1}\,mol^{-1}}$
T	Temperature	K
T	Transmittance	–
V	Volume	$\mathrm{m^3}$

Symbol	**Meaning**	**Unit**
V_{th}	Thermal voltage	V
$\overline{V}_i$	Partial molar volume	$\mathrm{m^3\,mol^{-1}}$
Z	Valence charge of ion	–
γ	Activity coefficient	–
Δc	Concentration change	$\mathrm{mol\,m^{-3}}$
Δz or l	Path length	m
ϵ	Molar neutron attenuation coefficient	$\mathrm{m^2\,mol}$
$\hbar$	Reduced Planck constant	$\frac{h}{2\pi} = 1.055 \times 10^{-34}\,\mathrm{J\,s}$
κ	Ionic conductivity	$\Omega^{-1}\,\mathrm{m^{-1}}$
λ	Wavelength	m
μ	Chemical potential	$\mathrm{J\,mol^{-1}}$
μ_{int}	Internal chemical potential	$\mathrm{J\,mol^{-1}}$
μ_{el}	Electrostatic chemical potential	$\mathrm{J\,mol^{-1}}$
μ_{mech}	Mechanical chemical potential	$\mathrm{J\,mol^{-1}}$
μ_{g}	Gravitational chemical potential	$\mathrm{J\,mol^{-1}}$
μ_{mag}	Magnetostatic chemical potential	$\mathrm{J\,mol^{-1}}$
$\overline{\mu}_{\mathrm{i}}$	Electrochemical potential	$\mathrm{J\,mol^{-1}}$
μ_0	Vacuum permeability	$4\pi \times 10^{-7}\,\mathrm{N\,A^{-2}}$
μ	Magnetic moment	$\mathrm{J\,T^{-1}}$
μ_{eff}	Effective magnetic moment	$\mathrm{J\,T^{-1}}$
μ_B	Bohr magneton	$9.274 \times 10^{-24}\,\mathrm{J\,T^{-1}}$
∇c	Concentration gradient	$\mathrm{mol\,m^{-4}}$
$\nabla \chi$	Volume susceptibility gradient	$\mathrm{m^{-1}}$
$\nabla \mathbf{B}$	Magnetic field gradient	$\mathrm{T\,m^{-1}}$

Symbol	Meaning	Unit
$\nabla\mathbf{H}$	Magnetic field gradient	$\mathrm{A\,m^{-2}}$
$\nabla\mathbf{M}$	Magnetisation gradient	$\mathrm{A\,m^{-2}}$
$\nabla\chi$	Magnetic susceptibility gradient	$\mathrm{m^{-1}}$
$\nabla\Phi$	Electric field	$\mathrm{V\,m^{-1}}$
ρ	Density	$\mathrm{kg\,m^{-3}}$
σ	Neutron cross section	$\mathrm{barn} = 10^{-28}\,\mathrm{m^2}$
σ_a	Neutron absorption cross section	$\mathrm{barn} = 10^{-28}\,\mathrm{m^2}$
σ_c	Coherent neutron scattering cross section	$\mathrm{barn} = 10^{-28}\,\mathrm{m^2}$
σ_{inc}	Inoherent neutron scattering cross section	$\mathrm{barn} = 10^{-28}\,\mathrm{m^2}$
Φ	Electric potential	V
χ	Volume magnetic susceptibility	–
χ_i or χ_m	Molar magnetic susceptibility	$\mathrm{m^3\,mol^{-1}}$
$\chi_{1\mathrm{M}}$	Volume magnetic susceptibility of 1 M solution	–
Ψ	Neutron wave function	$\mathrm{m^{-1/2}}$

1. Introduction

In der chemisch-analytischen Trennung und in der Reindarstellung der 16 seltenen Erden Scandium, Yttrium und Lanthan bis Luthetium liegen Probleme, die bis heute noch keineswegs restlos gelöst sind, ...

Ida Noddack (1896–1978)
and Elisabeth Wicht,
Chem. Techn. **7**, 3 (1955)

A simple way to create a paramagnetic liquid is to dissolve a paramagnetic salt in a solvent. The magnetism of these salts originates in the unpaired electrons of the cations, which bestow a magnetic moment that is preserved after dissolution. Examples of such paramagnetic salts are those containing ions of transition metals with an unfilled d-subshell (Cr, Mn, Fe, Ni and Co) or of rare earths with unpaired 4f electrons (Gd, Tb, Dy, Ho and Er).

The classic hallmark of magnetic materials is their motion upon magnetisation in a magnetic field gradient. Exposing a paramagnetic solution to an inhomogeneous magnetic field gives rise to the Kelvin force density:

$$\mathbf{F}_\mathrm{K} = \mu_0(\mathbf{M}\cdot\nabla)\mathbf{H}. \tag{1.1}$$

This expression relates the force density to the magnetisation of the solution $\mathbf{M}$ (in $\mathrm{A\,m^{-1}}$) and the applied magnetic field $\mathbf{H}$ (in $\mathrm{A\,m^{-1}}$) with the vacuum permeability $\mu_0 = 4\pi \times 10^{-7}\,\mathrm{N\,A^{-2}}$. The Kelvin force is fundamental to ferrohydrodynamics and its exploitation finds application in a variety of areas. Magnetic levitation of objects immersed in paramagnetic liquids has been used for magnetohydrostatic separation since the 1960s [1, 2]. The pioneering work of this technique was carried out in the Soviet Union by Andres and Bunin [1] and was based on the magnetic modification of the effective density of the paramagnetic liquid. Andres persevered with this research after his relocation to Israel and introduced his ideas to the West [3]. Nowadays, magnetic levitation is no longer limited to sink-float separation in mining [4–12]. Furthermore, growing paramagnetic crystals under a magnetic field gradient simulates conditions akin to microgravity [13–17].

Apart from such magnetohydrostatic situations, the Kelvin force can drive convective flow of the paramagnetic fluid as a body force. For such a magnetoconvective flow to materialise, the mere presence of an inhomogeneous magnetic field does not suffice, as gradients of concentration or temperature are necessary to upset the hydrostatic balance [18]. Magnetically induced convective phenomena under a thermal gradient are classed as magnetothermal convection or synonymously as thermomagnetic convection.

Magnetothermal convection modifies the transfer of heat in liquids such as paramagnetic salt solutions [17, 19–23] and regular diamagnetic water [14, 24, 25]. Magnetic fields can also alter mass transport in paramagnetic gases[1,2] [17, 26, 42–46].

Scientific literature is replete with studies of inhomogeneous paramagnetic electrolytic solutions. For instance, it is possible to trap aqueous paramagnetic salt solutions in the stray field of a magnetized iron wire [47]. These paramagnetic liquid tubes are encased by the surrounding water and their collapse due to density difference driven convection is inhibited by the Kelvin force. Magnetically confined liquid tubes offer frictionless flow without the solid wall encountered in regular liquid channels [48]. The idea of utilising magnetic forces in microfluidics has come to prominence in the new millennium [49–53] and this is precisely where liquid tubes may become beneficial.

Paramagnetic salt solutions conduct electricity, bringing ferrohydrodynamics close to the intimately related magnetohydrodynamics under the label of magnetoelectrochemistry. When a current flows, convection can be caused by the Lorentz force [54–56], which lies at the heart of magnetohydrodynamics and is also known as magnetohydrodynamic stirring in magnetoelectrochemistry [57–65]. Aside from this, the Kelvin force becomes pertinent when a concentration gradient of a paramagnetic ionic species is sustained by a chemical reaction at an electrode. Electrodeposition is the prime example of a situation in which the products of the paramagnetic ions can be structured by magnetic field gradients [66–82]. The electrochemical reaction takes place in the electrical double layer on the electrode surface and is accompanied by the formation of a mass transport limited diffusion layer which replenishes the reduced ions. A magnetic field gradient is thus able to cause a magnetoconvective flow of the solution, with profound ramifications for the final morphology of the electrodeposits.

Besides electrolysis, where the driving force is firmly grounded in the gradient of an electric potential, the idea of magnetically separating ions in solution has intrigued the scientific community for nearly a century. This is of particular interest when considering the rare earths, whose separation is complicated due to the chemical similarity originating in their identical valence electrons. The rare earths differ in the number of localised 4f electrons, which are generally unimportant for chemical bonds. In contrast, the filling of the 4f electron subshell along the lanthanide block causes strikingly dissimilar magnetic moments. This variation in the magnetic susceptibility offers a favourable quantity of discriminating between different rare earths, which are currently separated by arduous solvent (liquid-liquid) extraction and ion exchange [83, 84]. The potential benefits of a magnetic separation are self-evident: common Nd-Fe-B permanent

[1] Magnetothermal convection of paramagnetic gaseous oxygen (O_2) was used to measure O_2 levels in high altitude flights during the Second World War [17, 26]. When O_2 is heated by a hot wire, the magnetic susceptibility ($\chi = 0.145 \times 10^{-7}$ at 20°C [27]) decreases according to T^{-2}. This is due to the combined effect of the Curie law ($\chi = \frac{C}{T}$) and the expansion of O_2 ($\rho \propto T^{-1}$). Thus, the warm gas is pushed out of a field gradient and an inhomogeneous magnetic field increases the thermal conductivity by this convective motion.

[2] Polyatomic gases in a homogeneous magnetic field show a decrease in thermal conductivity and viscosity in the order of one percent. The effect in paramagnetic polyatomic gases is known as the Senftleben effect [28–37]. The extension to diamagnetic species is called the Senftleben-Beenakker effect, which also includes electric field [38–41]. The modification of the transport properties relies on the change of the mean free path by the precession of the magnetic moment in the field. The strength of the effect is proportional to $\frac{H}{p}$, with the pressure p.

magnets are readily available, cheap and tailored to a plethora of application with their inhomogeneous stray field [8, 85]. A separation of rare earths will also be essential in any recycling of such permanent magnets [86, 87], although it is clear that such a programme would call for market intervention at the present time [88].

The first recorded attempt of rare earth separation in an inhomogeneous magnetic field dates back to 1929 [89] and is authored by one of the founding fathers of magnetochemistry Pierce W. Selwood (1905–1986) [90] while he was a PhD student of B. Smith Hopkins[3] at the University of Illinois. A sketch of the experimental set up is shown in Fig. 1.1. The pole pieces of an electromagnet provided the desired inhomogeneous magnetic field to a mixed rare earth solution in a glass tube (see Figs. 1.1(a–b)).

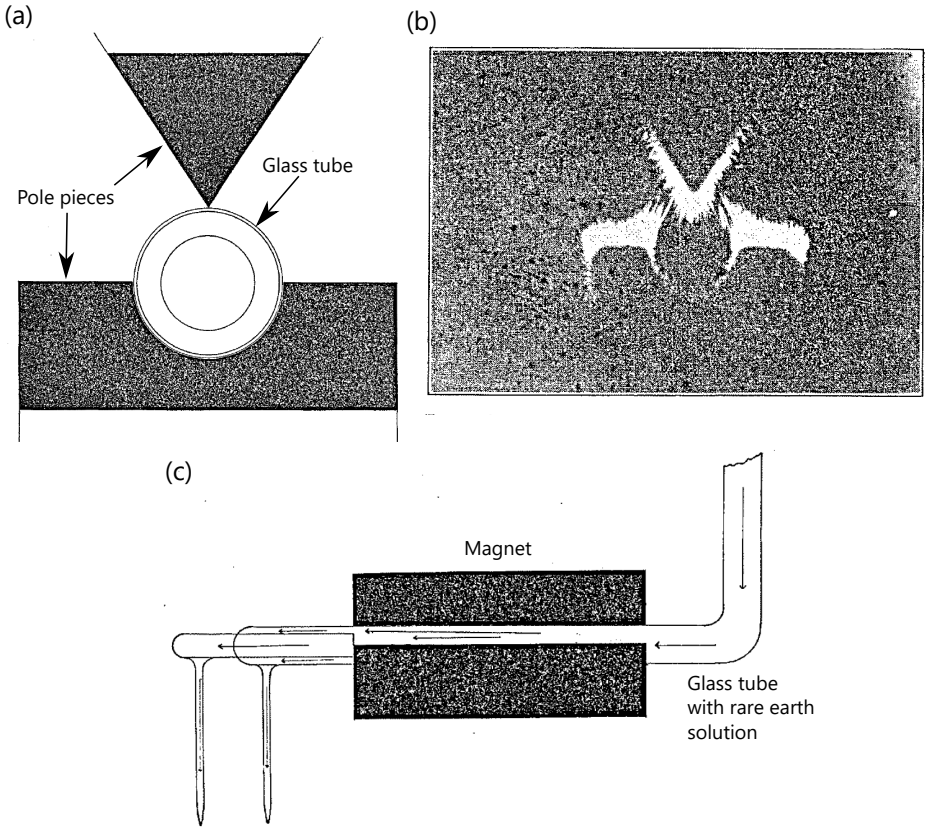

Figure 1.1 – Sketch of flow experiment for magnetic rare earth separation due to Pierce W. Selwood and B. Smith Hopkins [89]. (Adapted from [89] with permission from IOP Publishing. Copyright 1929, The Electrochemical Society. All rights reserved.) (a) A glass tube containing the rare earth solution is nested between the pole piece of an electromagnet. (b) Iron filings indicates the inhomogeneous magnetic field. (c) Side view of the poles pieces and glass tubes. Arrows indicate the flow of the rare earth solution. The magnetic field gradient was supposed to separate the rare earths by their deflections into two different glass tubes, but the method did not yield solutions of differing rare earth concentrations.

[3] In 1926 Hopkins (1873–1952) was one of the ill-fated discoverers of the supposedly missing element with atomic number 61 [91, 92] which was named illinium [93–96] and finds mention in [89]. His claim was later refuted when a combination of other elements showed the same spectral lines [97–100]. The missing element was in fact radioactive promethium (Pm), which was discovered at Oak Ridge laboratory during the Manhatten project around 1944 [101, 102].

The experiment was a liquid analogue of the Stern-Gerlach experiment[4], which was one of the first experiments to employ molecular beams [104–106]. The authors were unable to use gaseous rare earths due to their high boiling point (over 3000 K, except Sm, Eu, Tm and Yb) and resorted to solutions in ethanol which were pumped through a glass tube (see Fig. 1.1(c)). An organic solvent was chosen to avoid any Lorentz force effects on solvated ions. The authors were then faced with what must have been a heart-wrenching task of mixing samarium chloride ($SmCl_3$) and paramagnetic erbium chloride ($ErCl_3$), which had previously been purified by fractional crystallisation [107]. This tedious process took at least one year [108]. The liquid exiting the magnetic field was collected in two smaller tubes (see Fig. 1.1(c)). One in immediate vicinity of the pole piece, where the $ErCl_3$ was expected to be enriched, and one further away. The experiment was not a success, as no effect on the concentration of the rare earth solutions was measurable spectroscopically in either of the collected liquids. Varying the liquid velocity and using aqueous solutions did not improve results and the experimental investigation seems to have been abandoned thereafter[5].

The negative outcome of the experiments comes as no surprise considering two decisive factors. Firstly, there is no temperature or concentration gradient in the system. No magnetoconvection takes place and the Kelvin force is balanced by the pressure in the wall-bounded tube. The second and more pertinent issue is the energy discrepancy between the thermal energy of the ion in the mixed solution $E_{\mathrm{th}} = k_{\mathrm{B}}T = 4.11 \times 10^{-21}\,\mathrm{J}$ (k_{B}: Boltzmann constant with $1.38 \times 10^{-23}\,\mathrm{J\,K^{-1}}$; T: room temperature) and the energy of the magnetic moment in the magnetic field. The magnetic field of the magnet B did not exceeded 1 T, which gives an energy on the order of $E_{\mathrm{mag}} = \mu_{\mathrm{B}}\,B = 9.27 \times 10^{-24}\,\mathrm{J}$ (μ_{B}: Bohr magneton with $9.27 \times 10^{-24}\,\mathrm{J\,T^{-1}}$). There is a factor of nearly 450 between these values, meaning that a single particle will continue its random motion throughout the liquid, blissfully unaware of any magnetic forces. Paramagnetic ions in isothermal solutions do not settle in the magnetic field gradient of a permanent magnet due to their negligible size and mass. Such sedimentation is restricted to some of the more bulky magnetic colloidal particles encountered in ferrofluids with lower diffusion coefficients [117]. It has to be stressed that the Kelvin force is a macroscopic force density and is brought about by the sum of all the microscopic magnetic forces exerted on the solvated paramagnetic ions. Interparticle forces transmit the microscopic forces to the entire medium via collision processes. In solutions these are dipole-dipole interactions such as the van der Waals force or hydrogen bonding, along with entirely electrostatic forces for ions. Considering this, a purely magnetic separation of rare earth ions can be deemed a hopelessly Icarian endeavour.

[4] The same magnet had indeed previously been used in a repeat of the Stern-Gerlach experiment with alkali metal atoms [103].

[5] The publication also details the attempted verification of rare earth separation by differences in their mobilities via ionic migration [89], a method that was previously reported by British chemist James Kendall (1889–1978) at Columbia University [109–111]. This experiment consisted of rare earths embedded in an agar gel which was placed in a 10 m long tube. Electrodes from a 500 V dc generator were then inserted at either end and a current was allowed to flow for several days. The electrophoresis was able to partially separate pairs of Sm/Gd and Er/Y, but the method failed for other combinations and reproducibility was poor. In view of the absence of a substantial difference in the transference numbers of the rare earth ions [112–116], this is unsurprising. The development of solvent extraction and ion exchange in the 1940s discontinued any research in this direction.

Nonetheless, in 1937 Ida[6] and Walter[7] Noddack began their own investigation on the separation of rare earths in an inhomogeneous magnetic field at the University of Freiburg. The research on this topic was interrupted by the Second World War and later continued in the 1950s at their private Geochemical Institute in Bamberg [135–137]. The Noddack experiment also employed a flow of mixed rare earth chloride solution through the inhomogeneous magnetic field of two electromagnet pole pieces ($B = 1.2\,\mathrm{T}$). Their setup was essentially a magnetically modified Clusius-Dickel separation column, which was the first method for isotope separation [138–147]. Sketches of the experimental set up from the last of publication in 1958 [137] are shown in Figs. 1.2(a–b). An explanation of the symbols used for the individual components is given in the caption.

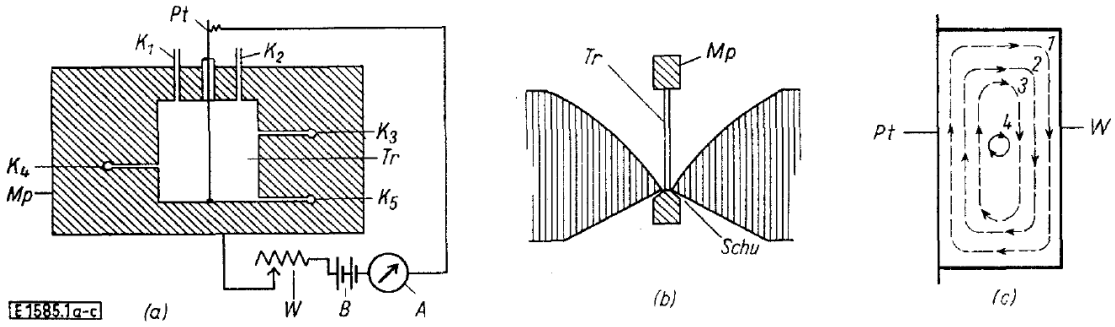

Figure 1.2 – Sketch of magnetically modified Clusius-Dickel column used by Ida and Walter Noddack [137] (Reproduced with permission from [137]. Copyright 1958, Deutsche Bunsen-Gesellschaft). (a) The brass container (M_p) contained a trough (Tr) with two inlets (K_1 and K_2) and three outlets (K_3, K_4 and K_5) for the rare earth solution. An 0.1 mm diameter Pt wire (Pt) was suspended through the centre of the trough and a current was applied externally to heat the solution analogously to a Clusius-Dickel thermodiffusion column [138–147]. The components of the external power supply were a battery (B), an Ampere meter (A) and a variable resistor (W) for controlling the current. (b) The trough with the rare earth solution and the Pt wire was exposed to an inhomogeneous magnetic field by placing it between the pole shoes of an electromagnet ($Schu$). (c) The heating by the Pt wire (Pt) and cooling of the brass trough wall (W) caused circulation of the solution via thermal convection. The stream lines of the flow are shown.

[6] Ida Noddack (1896–1978) (née Tacke) was a German chemist and four time nominee for the Nobel prize in chemistry [118]. Apart from the discovery of rhenium (named after her birthplace the Rhineland) and in all likelihood technetium (named Masurium) [119, 120], Ida Noddack is best known for her astonishingly prescient predictions. She presaged Supernova nucleosynthesis [121, 122] and nuclear fission [123, 124]. In 1934 she critiqued the chemical procedures in the work of Enrico Fermi (1901–1954) [125] and provided the correct interpretation of the results as nuclear fission [123, 124]. Her hypothesis was derided in the scientific community and Fermi was awarded the 1938 Nobel prize in physics under the impression he had discovered new elements after neutron bombardment [126]. Only in 1938 was nuclear fission discovered and she became embroiled in a bitter feud with Otto Hahn (1879–1968) and Lise Meitner (1878–1968) about attribution [127–129]. Hahn grudgingly admitted in a 1966 radio interview: "Die Ida hatte doch Recht" [118, 130]. Allegation exist that suggest the riff was aggravated by the Noddacks' closeness to national socialist ideology at this time [129], but there is no evidence to support this [118, 131]. In 1941 Ida Noddack obtained a professorship in Strasbourg, from where she relocated to Bamberg at the end of the war [131].

[7] Walter Noddack (1893–1960) completed his PhD in Berlin under the supervision of Walter Nernst (1864–1941) and went on to discover the element Rh [130] working at the "Physikalisch-Technische Reichsanstalt". He replaced the later Nobel prize winner George de Hevesy, who was forced to flee to Denmark [132], as professor of physical chemistry in Freiburg [133], where he devoted himself to geochemistry and the study of the rare earths [131]. In 1941 he became a professor in Strasbourg. After the war he set up the Geochemical Institute in Bamberg [134]. He was nominated for the Nobel prize nine times before the Second World War.

The container in which the solution circulated continuously was a brass trough with two inlets and three outlets at different magnetic field strengths. The pole pieces were at the height of the bottom of the trough. A platinum (Pt) wire of 0.1 mm diameter was fixed vertically in the centre of the trough. Heating of the Pt wire was then accomplished by passing a current of up to 2.5 A through it. The outside of the brass trough container was kept at 15°C by a jet of cool air. Thus, the maximum temperature difference between the Pt wire and the inner surface of the brass trough was around 80°C. Thus, in stark contrast to the Illinois experiment, the solution was non-isothermal, triggering a thermoconvective instability. The solution streamed up the heated Pt wire and sank down the cold sides of the trough continuously in a vortex-like motion by thermal convection (see Fig. 1.2(c)). In analogy to the magnetohydrostatic separations, the magnetic field gradient at the bottom of the trough hampers gravity induced buoyancy and the thermogravitational convection turns thermomagnetic. After its circulation in the trough, the rare earth solution was withdrawn through the capillaries at three different heights. The solutions were then converted to oxides and their elemental composition were analysed with spectroscopic methods. The liquid extracted from the bottom of the trough, where the field gradient was applied, showed the highest concentration of rare earths and incidentally exhibited an enrichment of the heavier paramagnetic species. Repetitions of the experiment proved a dependence of the measured separation on magnetic field strength, field inhomogeneity, duration of circulation, concentration of the rare earth solutions, flow velocity of the solution and most critically the temperature of the Pt wire. The thermal gradient points in the direction of a thermodiffusional effect, a fact that is glossed over in the discussion of the results and is crucial for any interpretation of the experiment. Be that as it may, these findings garnered little attention at the time, save a short mention in a 1960 Russian review article on rare earth separation [148]. Walter Noddack himself turned his attention to rare earth separation by ion exchange[8] [150–152].

After a 50 year hiatus, interest in the idea of magnetically separating paramagnetic ions has been revived. The urgency of studies invoking the concept of rare earth separation is compounded by the recent rare-earth crisis [153]. In quick succession, the number of publications claiming an enrichment of paramagnetic ions from homogeneous solutions in the stray field of permanent magnets shot up dramatically [154–159]. The findings would be earth-shattering, as they contradict the basic notions of thermodynamics. But this was a fantasy. Of these reports, the interferometric studies from a group in Dresden are without doubt the most systematic and accurate [154–156]. The authors observed a heightened concentration of paramagnetic ions around the surface of a paramagnetic salt solution when a magnet was placed on top of the cuvette holding the liquid. They did this with the help of a Mach-Zehnder interferometer, which relates concentration changes to variations in the refractive index and is commonly employed to measure diffusion coefficients [160]. An enrichment effect was observed for $MnSO_4$, $GdCl_3$ and $DyCl_3$, but not for the lower susceptibility $CuSO_4$. Upon removing the magnet, the

[8] These results were published posthumously. Interestingly, he supervised a PhD in which the effect of an inhomogeneous magnetic field on rare earth separation via ion exchange membranes was analysed [149]. The findings were inconclusive.

enriched layer of higher density plunged downward via a gravity driven Rayleigh-Taylor instability. In October 2017 two independent publications from the Dresden group [161] and a group at KU Leuven [162] provided the sobering explanation for the observations. In truth, there had been a constant evaporation of water from the surface of the solution and this had caused the concentration gradient of ions. The energy consumption by water evaporation is $40.65\,\mathrm{kJ\,mol^{-1}}$, unquestionably surpassing the necessary threshold for separation set by the chemical potential. Thus, the purported magnetic separation is essentially a distillation process and the region of elevated ion concentration is merely magnetically levitated above the otherwise homogeneous bulk solution. The Leuven group went on to study the manipulation of paramagnetic droplets [163] and thermomagnetic convection [164]. In Dresden the evaporation experiments were continued and backed up by hydrodynamic modelling [165, 166]. The phrase "magnetic separation of rare earth ions" in the title of these two publications is a misnomer. Rare earth ions are neither separated from each other, nor are they magnetically separated from the bulk solution in the first place. For a magnetic field gradient to redistribute the concentration of paramagnetic ions, another form of energy has to be introduced to homogeneous systems for the occurrence of a concentration. Accordingly, any feasible magnetically aided rare earth separation must rely on another driving force to combat the chemical potential which seeks to mix the ions by diffusion.

The purpose of this dissertation is to present a study of transient inhomogeneous systems containing paramagnetic salt solutions on which magnetic field gradients can act. Magnetoconvection will change the specific density distribution of a non-equilibrium paramagnetic liquid until mechanical stability has been attained. On the one hand, reaching thermodynamic equilibrium is a much more protracted process than the comparatively instantaneous imposition of mechanical equilibrium by magnetic forces. On the other hand, in absence of a suitable external energy input, the second law of thermodynamics will rear its head and the system will be homogenised without fail. The main techniques employed to study such systems were standard electrochemical methods as well as dynamic neutron imaging experiments which enabled mapping the concentration evolution of aqueous gadolinium nitrate ($Gd(NO_3)_3$) solutions. The next chapter introduces the main concepts and state of knowledge underpinning the research, covering topics from thermodynamics of electrolytic solutions, mass transport, magnetic forces, capacitive deionisation, aquatic chemistry of the rare earths to neutron absorption. The description of experiments along with their results and discussions are presented in Chapters 3-5. Chapters 6 and 7 summarise the findings and provide a final conclusion, respectively.

2. Background

The essential idea is that in the $N \to \infty$ limit of large systems (on our own macroscopic scale) it is not only convenient but essential to realize that matter will undergo mathematically sharp, singular phase transitions to states in which the microscopic symmetries, and even the microscopic equations of motion, are in a sense violated. The symmetry leaves behind as its expression only certain characteristic behaviors.

P. W. Anderson (1923—2020),
"More is Different",
Science **177**, 393 (1972)

2.1. Equilibrium Thermodynamics of Paramagnetic Electrolyte Solutions

It would be an act of considerable naïvety to embark on an investigation of the dynamics of paramagnetic salt solutions without consulting the thermodynamics of such systems. The word "dynamics" itself has its origin in the ancient Greek word "δύναμις" meaning "power". Many texts describe the thermodynamics of electrolyte solutions [167–170] and the approach sketched here is based on them. The only difference with respect to the treatment of a regular salt solution is the addition of a term accounting for the paramagnetism in the respective thermodynamic equations. Any thermodynamic state is completely described by a thermodynamic potential. In chemistry, the Gibbs free energy G with natural variables temperature T and pressure P is the standard choice[9]. At equilibrium, the Gibbs free energy is minimised and uniform in the entirety of the system. The uniformity and time independence at equilibrium implicitly prohibits fluxes of mass and energy. The change in energy due to transfer of particles is given by the chemical potential μ. It is defined as the derivative of the thermodynamic potentials with respect to the particle number N. It follows that the chemical potential is identical to the molar Gibbs energy in a one component system ($\mu = \frac{G}{N}$) and to the partial molar Gibbs energy in multicomponent systems. Whereas the temperature controls the energy transfer between systems, the chemical potential regulates the particle exchange. In a non-equilibrium system, driving forces appear due to gradients in the total chemical potential. The state variables have both a temporal and spatial dependency due to this (see Section 2.2). The general expression for the total chemical potential of an ion species in an ideal solution is given by the following (unit: $\mathrm{J\,mol^{-1}}$; individual variables are defined in the explanation of the respective terms below):

[9] Confusingly, the Gibbs free energy is often referred to as the free energy in chemistry literature.

$$\mu_{\text{tot}} = \underbrace{\underbrace{\underbrace{\mu_i^0 + RT\ln x_i}_{\text{Internal Chemical Potential}} + \underbrace{Z_i F\Phi}_{\text{Electrostatic}}}_{\overline{\mu}_i\text{: Electrochemical Potential}} + \underbrace{\overline{V}_i\Delta P}_{\text{Mechanical}} + \underbrace{M_i g\Delta z}_{\text{Gravitational}} + \underbrace{\tfrac{1}{2}\mu_0\chi_i H^2}_{\text{Magnetostatic}}}_{\text{External Chemical Potential}} . \tag{2.1}$$

The chemical potential of a species in an ideal system does not depend on the concentration of any other species. The terms in Eq. 2.1 are familiar and they constitute the energy that will bring systems with different values for μ into equilibrium by diffusion. Only differences in the chemical potential of systems have physical meaning. The internal chemical potential is only related to the concentration and temperature[10]. Together with the electrostatic component it forms the electrochemical potential $\overline{\mu}_i$. The other contribution to the chemical potentials are lumped together under the name external chemical potential. Examples for their origin can be mechanical, gravitational or magnetic. In electrolyte solutions, common magnitudes of the electrochemical potential outclass those of the remaining external chemical potential by far. The individual terms of Eq. 2.1 will be discussed below.

Internal Chemical Potential

The internal chemical potential accounts for the energy change due to variations in the particle number of a species. For an ideal system it is given by:

$$\mu_{\text{int}} = \mu_i^0 + RT\ln x_i. \tag{2.2}$$

The first part of Eq. 2.1 is the chemical potential of a species i in a reference state μ_i^0 from which the energy of formation is defined. The second part defines the necessary energy to reach a particular concentration, which is given by the mole fraction $x_i = \frac{n_i}{n_{\text{tot}}}$ with the amounts of the substances n_i ($n_{\text{tot}} = \sum_i n_i$). The prefactor of the natural logarithm is the product of the universal gas constant $R = 8.3145\,\text{J}\,\text{mol}^{-1}\,\text{K}^{-1}$ and the temperature T. When a species is concentrated in solution, the internal chemical potentials in the two states are subtracted and the energy of formation drops out. Any separation process must overcome the energy threshold given by the concentration term to purify a species [172, 173]. At room temperature $RT = 2500\ \text{J}\,\text{mol}^{-1}$ and the minimum energy requirement to enrich 2 M of solvated ions from a 1 M aqueous solution ($n_{\text{H}_2\text{O}} = 55.51\,\text{mol}\,\text{kg}^{-1}$) is:

$$E_{\text{min}} = RT\ln(x_{2\text{M}}) - RT\ln(x_{1\text{M}}) = 1.69\,\text{kJ}\,\text{mol}^{-1}. \tag{2.3}$$

It directly follows from the concentration term that ions in solution must be uniformly distributed at equilibrium without an external energy. A gradient in the concentration is usually equivalent[11] to a gradient of the chemical potential and precipitates mixing by diffusion. Gradi-

[10] Although this is usually done in the literature, one should try to refrain from using the term "chemical potential" without an adjective whenever multiple terms are involved and the meaning becomes unclear [171]. The internal chemical potential is often simply called "chemical potential".

[11] See the short discussion on multicomponent diffusion in Section 2.2.1.

ents in the chemical potential are the driving force of diffusion (see Section 2.2.1). Mixing by diffusion can only be halted when the amount of energy input into the system is sufficient to combat the chemical forces. All this directly follows from the second law of thermodynamics, which states that the entropy of an isolated system never decreases. Temperature enters into the concentration term as thermal energy increases the disorder of the system. Entropy, and thus the temperature, has a strong effect on electrochemical reactions. It is important to note that the dissolution of salt in water is not always accompanied by an increase in entropy, as the formation of a hydration shell around the solvated ions orders the solvent [169, 174]. In aqueous solutions, the solvation of the ion is chiefly an electrostatic effect.

Interactions between the chemical species in solution are neglected in ideal systems and the concept of activity (a_i) has to be introduced for their description [167, 170, 175]. This was first done by Gilbert N. Lewis (1875–1946) in 1907 [176]. The activity coefficient γ_i redresses the mole fraction x_i and converts it to activity a_i:

$$a_i = x_i \gamma_i. \tag{2.4}$$

When γ_i is close to unity, the solution behaves as if it were ideal. The activity simply replaces the mole fraction in any of the thermodynamic equations and represents an effective concentration due to ion-ion and ion-solvent interactions. The internal chemical potential becomes:

$$\mu_{\text{chem}} = \mu_i^0 + RT \ln(a_i). \tag{2.5}$$

The ways in which the constituents can interact include dipolar van der Waals and coulombic interactions. These are distance dependent and therefore vary with concentration. The screened coulombic electrostatic interactions in electrolyte solutions are long-range and already relevant at concentrations in the mM range. The Debye-Hückel theory was developed to calculate the concentration dependence of the activity coefficient of electrolytes by solving the Poisson-Boltzmann equation. It is successful at describing dilute solutions, but fails at high concentrations, for which many extensions to the theory exist [175]. Attractive electrostatic interactions decrease and repulsive interactions increase the activity. Changes in activity due to electrostatic interactions are more pertinent in nonsymmetrical than symmetrical electrolytes. An example of 1-3 electrolytes are solutions of trivalent rare earth ions and they display this behaviour[12].

There are several reasons for the departure from predictions of the Debye-Hückel theory. Firstly, dipolar interactions between ions and molecules become important at higher concentrations. These diminish rapidly with distance ($\sim r^{-6}$) and are irrelevant beyond a distance of 1 nm. They decrease the activity of the ions in solutions over 0.1 M [167, 169]. Secondly, volume exclusion effects, in which the ions come into contact, can occur in highly concentrated solutions in which the ions are increasingly bunched up. An estimate for the concentration c dependence of the distance between ions is $d = 1.2\, c^{-1/3}$ (in nm). The hydrated radii of the rare earths

[12] The activity coefficients of rare earth nitrates were measured by the group of Frank Spedding at Ames laboratory. The tabulated values can be found in a publication by Joseph Rard et al. [177].

are approximately 0.45 nm [178] and the ions touch each other in a 0.6 M solution (keeping in mind the three anions that must be accommodated). An increase in the activity due to volume exclusion is already noticeable in solutions above 0.1 M [169].

Common values for the activity coefficient are between 0.4 and 1.2, meaning that the energy cost for separation is higher than expected in idealisations (such as in Eq. 2.3) by up to a few $\mathrm{kJ\,mol^{-1}}$. The activity is strongly temperature dependent, a fact encapsulated in the van't Hoff equation. Activity coefficients can be experimentally obtained from freezing point measurements, vapor-pressure measurements, isopiestic (osmotic) methods and electromotive force measurements [167, 170].

Electrostatic Potential

Electrochemistry is based on the interplay of the concentration term in the internal chemical potential and the interaction of the charged ions with an electric field. The electrostatic contribution to the chemical potential can readily compete with the internal chemical potential in electrolyte solutions. The Faraday constant $F = 96\,485\,\mathrm{C\,mol^{-1}}$ relates the valence charge of the ion Z_i to the molarity and gives the molar electrostatic energy when multiplied by the electric potential Φ (in V):

$$\mu_{\mathrm{el}} = Z_i F \Phi. \tag{2.6}$$

The value of the Faraday constant gives rise to high energies, a fact that is appreciable when considering the thermal voltage V_{th} necessary for the electrostatic energy of a monovalent ion to compete with the thermal energy E_{th} given by:

$$V_{\mathrm{th}} = \frac{E_{\mathrm{th}}}{e} = \frac{k_{\mathrm{B}}T}{e} = \frac{RT}{F} = 25.7\,\mathrm{mV}. \tag{2.7}$$

A voltage of 25.7 mV is easily attainable. From this, it is also obvious to see why electrostatic effects make up the non-idealities in ionic solutions that enter into the activity coefficient. The mass transport process pertaining to gradients of the electrostatic potential is called migration (see Section 2.2.1). Ions move towards charged surfaces where they form a double layer, which is where the interesting reactions in electrochemistry take place (see Sections 2.3 and 2.3.3). This is also where their immobilisation without a chemical reaction can occur, which is referred to as electrosorption (see Section 2.3.4).

An important point has been ignored up to now. An electric potential can be applied to an electrolyte solution through electrodes. But the electric potential difference between two different media is undefined and cannot be measured experimentally. The transfer of charge in electrochemical cells is a thermodynamic process, not an electrostatic one. It is governed by the gradient of the internal chemical and electrostatic potential. Diffusion and ionic migration are inextricably linked in the mass transport of ions in solution (see Section 2.2.1). The change of the sum of chemical and electric potential is measured by a voltmeter in an electrochemical environment [170, 179–181]. An electrochemical potential $\overline{\mu}_i$ with a real physical meaning is introduced to alleviate the issue:

$$\overline{\mu}_i = \mu_{\text{int}} + \mu_{\text{el}} = \mu_i^0 + RT\ln(a_i) + Z_i F\Delta\Phi. \tag{2.8}$$

Distinguishing between the two components of the electrochemical potential is meaningless. The only reason why $\overline{\mu}_i$ was conceptually decomposed here was to show the orders of magnitudes of the energies relevant for separation.

Mechanical Contribution

The partial derivative of the Gibbs free energy with respect to pressure is the volume. Liquids are mostly incompressible and thus hardly affected by changes in the external pressure. The increase of pressure P with respect to the reference state P_0 on a solute in the liquid changes the chemical potential:

$$\mu_{\text{mech}} = \overline{V}_i(P - P_0). \tag{2.9}$$

In this expression of molar energy, the partial molar volume $\overline{V}_i$ (unit: $\mathrm{m^3\,mol^{-1}}$) of the solute appears. It is defined as:

$$\overline{V}_i = \frac{\partial V}{\partial n_i}. \tag{2.10}$$

Thus, $\overline{V}_i$ reflects the change in total volume V after dissolution of an infinitesimal amount of solute and is often negative due to attractive forces. Partial molar volumes of neutral components can be extracted from density measurements of electrolytic solution (see Appendix of Ref. [182]) and are tabulated in articles such as [183]. Common values for $\overline{V}_i$ are in the order of $10\,\mathrm{cm^3\,mol^{-1}} = 10^{-5}\,\mathrm{m^3\,mol^{-1}}$. For all the trivalent rare earth ions, $\overline{V}_i$ is close to $-40\,\mathrm{cm^3\,mol^{-1}} = -4\times10^{-5}\,\mathrm{m^3\,mol^{-1}}$ [183, 184]. It follows that the doubling of atmospheric pressure to $2\,\mathrm{bar} = 20\,\mathrm{kPa}$ will change the molar free energy by:

$$\overline{V}_i(P - P_0) = 0.1\,\mathrm{J\,mol^{-1}}. \tag{2.11}$$

This is four orders of magnitudes below the energy requirement for enrichment calculated with Eq. 2.3. Evidently, pressures of at least 100 bar must be reached to attain the energetic range of the concentration term for serious effects to occur. However, $\overline{V}_i$ at such high pressures is diminished and the real effect of the pressure is much lower [185]. The effect of pressure on activity coefficients is minute and negligible compared to its temperature dependence[13] [167, 169, 170]. However, gradients of pressure can cause fluid flow (see Section 2.2.1). Significant pressures of over 100 bar can be reached in high-power centrifuges or gravitationally in the deep sea, which will be discussed now.

[13] The pressure dependence of the activity coefficient γ is related to $\frac{\overline{V}_i - \overline{V}_i^0}{RT}$, where $\overline{V}_i^0$ is the value at infinite dilution. As $\overline{V}_i$ hardly depends on concentration, a pressure increase from 1 bar to 100 bar changes γ by 1% [186].

Gravitational Potential

The classical gravitational contribution to the free energy of a body with molar mass M_i (unit: $\mathrm{kg\,mol^{-1}}$) at a height z with respect to a reference height z_0 is given by:

$$\mu_\mathrm{g} = M_i g(z - z_0). \tag{2.12}$$

The gravitational acceleration is $g = 9.81\,\mathrm{m\,s^{-2}}$ and the molar mass of common inorganic salts is around $M_i = 100\,\mathrm{g\,mol^{-1}}$. Lifting a solution of such a salt by 1 m will increase the gravitational chemical potential of the system by $M_i g \Delta z = 1\,\mathrm{J\,mol^{-1}}$. This is a modest value compared to the concentration term and gravity is only relevant in the deep sea [169]. Archimedes principle also applies to ions and the hydrostatic pressure of an aqueous system $P = P_\mathrm{atm} - \rho_w g z$ undergoes changes due to buoyancy. Inserting this pressure into Eq. 2.1 and invoking the condition of uniformity of the molar free energy leads to a version of the barometric formula for aqueous salt solutions:

$$x_i = x_{i_0} \exp\left(-\frac{M_i - \rho_w \overline{V}_i}{RT} g(z - z_0)\right). \tag{2.13}$$

Here, x_{i_0} is the mole fraction of solute at the water surface, which, at height z, changes to x_i due to the gravitational energy. The buoyancy of the solvated ions is accounted for by the product of the density of water $\rho_w = 997\,\mathrm{kg\,m^{-3}}$ and $\overline{V}_i$. The water is considered to be incompressible. The difference between the mass term M_i and the buoyancy pressure defines the ion concentration. This means that ionic species with a negative partial molar volume $\overline{V}_i$ have the tendency to distribute exponentially towards the bottom of a tall water column. An enrichment of 0.035% is obtained 1 m below the surface of a salt solution in which the solute has $M_i = 100\,\mathrm{g\,mol^{-1}}$ and $\overline{V}_i = 10^{-5}\,\mathrm{m^3\,mol^{-1}}$. At a depth of 1 km the concentration changes by 42%. However, at such high pressures (around 100 bar), changes in $\overline{V}_i$ and the solubility equilibrium [169] must be considered. Gravitational effects are minute in laboratory systems (see Section 2.2). They do not play a significant roll in the underlying electrochemistry and can safely be disregarded in chemical reactions. Nevertheless, pressure and density differences can cause mass transport by convection of the bulk solution (see Section 2.2.1). This has consequences for the current distribution in an electrochemical cell.

Magnetostatic Energy

A paramagnetic salt solution subjected to a magnetic field becomes magnetised. The interaction between the external field and the magnetic moments changes the thermodynamic and chemical potentials[14]. The magnetic susceptibility χ relates the applied magnetic field H (unit: $\mathrm{A\,m^{-1}}$) to the induced magnetisation M (unit: $\mathrm{A\,m^{-1}}$). The expression for the dimensionless volume susceptibility of paramagnetic material is:

$$\chi = \frac{\partial M}{\partial H} = \frac{M}{H}. \tag{2.14}$$

[14] Good accounts of thermodynamics in magnetic fields were provided by Edward A. Guggenheim (1901–1970) [187, 188] and Zimmels [189].

The linear susceptibility is only valid for paramagnetic materials and its inverse temperature dependence is given by Curie's law ($\chi = \frac{C}{T}$; C: Curie constant in K). The temperature dependence can be utilised to increase the susceptibility by using an organic solvent with low freezing temperature. A discussion of the magnetic properties of the rare earth ions is presented in Section 2.4.1. Some rare earth salts are soluble in ethanol, which freezes at 159 K. The paramagnetic behaviour of aqueous gadolinium nitrate ($Gd(NO_3)_3$) solutions can be seen in their SQUID magnetisation measurement in Fig. 2.1. The susceptibility χ of the liquid is directly proportional to the concentration of the paramagnetic ion species [190, 191]. There are no magnetic interactions between solvated ions. The formation of complexes or colloids is imperative for the existence of any such interactions in liquids [192].

The constants that enter the paramagnetic chemical potential contribution are the vacuum permeability $\mu_0 = 4\pi \times 10^{-7} \frac{\mathrm{V\,s}}{\mathrm{A\,m}}$ and the molar magnetic susceptibility χ_i (in $\mathrm{m^3\,mol^{-1}}$):

$$\mu_{\mathrm{mag}} = \frac{1}{2}\mu_0 \chi_i H^2. \tag{2.15}$$

The theoretically predicted molar susceptibility of paramagnetic Gd^{3+} is $\chi_i = 330 \times 10^{-9}\,\mathrm{m^3\,mol^{-1}}$ [47]. With this value a magnetic equivalent of the thermal voltage can be calculated. This is the magnetic field necessary to compete with the thermal energy:

$$\mu_0 H_{\mathrm{th}} = B_{\mathrm{th}} = \sqrt{\frac{2RT\mu_0}{\chi_i}} \approx 137.8\,\mathrm{T}. \tag{2.16}$$

A continuous magnetic field of 137.8 T does not exist on planet earth and even pulsed magnets cannot reach such field strengths. With a realistic magnetic field of $B = 1\,\mathrm{T}$, one obtains a magnetic energy of $\mu_{\mathrm{mag}} = 131\,\mathrm{J\,mol^{-1}}$ ($5.2 \times 10^{-5}\,RT$) for Gd^{3+}. It follows that the magnetically induced minute change of Gd^{3+} concentration can be estimated with the Boltzmann factor: $c_{\mathrm{mag}} = c_0 \exp(\frac{\mu_{\mathrm{mag}}}{RT}) = 1.00005\,c_0$. The magnetic energy is far from the values of the internal chemical or electrostatic potential, but similar to the gravitational energy in a laboratory system.

The huge discrepancy between electrostatic and magnetostatic energies is evident from the classical Stern-Gerlach experiment [104, 105, 193–196]. This experiment consisted of a molecular beam [106, 196–198] of gaseous paramagnetic silver atoms that were deflected by a magnetic field gradient. Otto Stern (1888–1969) and Walther Gerlach (1889–1979) chose neutral silver atoms with a magnetic moment due to its unpaired 47th electron. Thus, they avoided any interference due to electrostatic interactions or the Lorentz force. The Stern-Gerlach effect has never been observed with charged particles[15], although proposals for a renewed experimental campaign exist [200, 202–207].

[15] The argument against the observation of such an effect with electrons was first made by Wolfgang Pauli (1900–1958), Niels Bohr (1885–1962) and Neville Mott (1905–1996) [199, 200]. It is based on the uncertainty principle, which dictates that the resulting Lorentz forces tarnish the force on the spin magnetic moment exerted by the field gradient. An idea for an experimental setup for the observation of the spin magnetic moment had been put forward by Leon Brillouin (1889–1969) in 1928 [201].

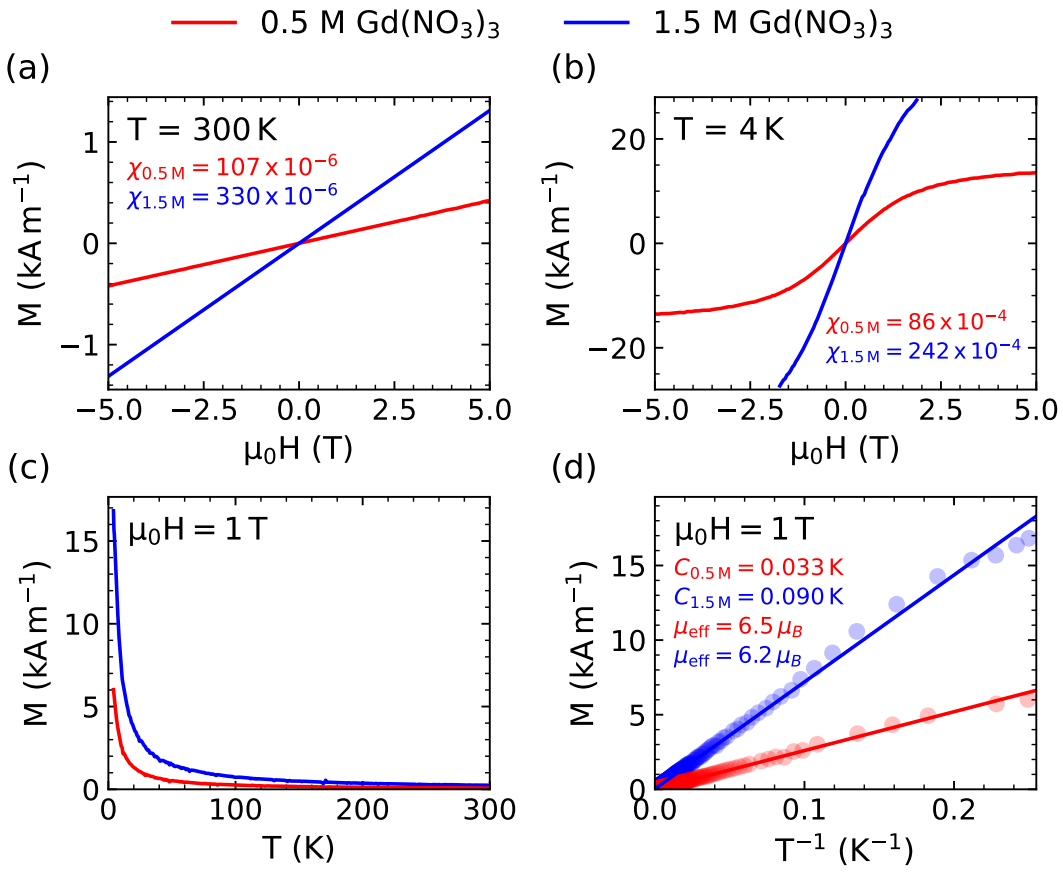

Figure 2.1 – SQUID magnetisation measurements of aqueous 0.5 M (red) and 1.5 M (blue) $Gd(NO_3)_3$ solutions. The solution container was a sealed piece of plastic straw. The diamagnetic contribution of the straw was subtracted[16]. (a) Magnetisation at room temperature; 5 T field sweeps. The susceptibility rises proportionally to the Gd^{3+} concentration. (b) Magnetisation curve at $T = 4$ K; 5 T field sweeps: The magnetisation of the frozen 0.5 M solution saturates at 2.5 T, whereas the 1.5 M solution does not saturate. Saturation indicates that all magnetic moments are aligned with the field. (c) Temperature dependence at $\mu_0 H = 1$ T. (d) Inversely proportional temperature dependence as per Curie's law. The effective magnetic moment was obtained from the Curie constant.

Despite the moderate values of the magnetic energy of a paramagnetic solution, they can give rise to ponderomotive forces in macroscopic media that are neutral on the whole. The bulk electroneutrality condition within electrolytic solutions is the reason why paramagnetic solutions can be manipulated by magnetic field gradients and bulk electric forces largely cancel. The body forces in a magnetic field gradient can cause magnetoconvective phenomena that modify mass transport (see Section 2.2.3). But to reiterate, with such low magnetic susceptibilities no effect on the underlying chemistry of a system is expected [208] and an enrichment of ions relying only on magnetic fields is unfeasible.

[16] The susceptibility values are lower than expected for Gd^{3+} (see Section 2.4.1), which is probably due to the $Gd(NO_3)_3$ salt not being merely hexahydrated. The presence of more H_2O molecules affects the concentration. Errors in the diamagnetic correction and small volume of the liquid sample (40 µL) may also have played a role. The liquid was sealed inside the plastic straw capsule with the flame of a lighter and evaporation is likely to have affected the sample volume.

2.2. Non-Equilibrium Thermodynamics of Paramagnetic Electrolyte Solutions

The discussion in the previous section was built around systems at equilibrium with time-independent thermodynamic states. Technically, these systems lack any dynamical character and can only be applied to reversible processes, in which the system cycles through consecutive equilibrium states adiabatically. In reality, most processes are irreversible and the actual dynamics of the equilibrating system are of interest. This is the realm of non-equilibrium thermodynamics. In its classical form, non-equilibrium thermodynamics aims to use the approach of regular thermodynamics for inhomogeneous and time-dependent systems. For ions in solution, diffusion phenomena are the most common irreversible processes[17] [209, 210]. A general definition of the equilibrium is the state in which entropy is maximised. Chemical, electromagnetic, mechanical and thermal effects synergise to ensure it is reached. At the heart of non-equilibrium thermodynamics lie transport equations such as Fourier's law, Fick's law or Ohm's law. Fluid dynamics and the electromagnetic theory of continua are closely related fields. Mass transport involving ions is clearly a process involving non-equilibrium systems.

The word "ion" means "going" in ancient Greek (ιόν), which already evinces the ionic movement that lies at the heart of electrochemistry. Mass transport in electrolytic solutions is governed by three main mechanisms: diffusion, convection and migration. Before introducing these in Section 2.2.1 below, it is useful to consider the implications for ions in solution when external forces, such as gravity, are applied to the bulk medium. As was previously discussed, these can alter the total chemical potential and the system will react by delicate redistribution of ions. A vertically elongated system exposed to gravity will have a concentration distribution predicted by Eq. 2.13 once it has reached equilibrium. However, this is only eventually established by diffusion. The perusal of historical literature detailing experimental investigations of such non-equilibrium systems will prove to be insightful.

The concept of ions[18] was introduced by Michael Faraday (1791–1867). He explained the ionic current in terms of a tension that the molecules in an aqueous solution were imbued with. James Clerk Maxwell (1831–1879) built on these ideas and proposed a theory that explained electrical currents as the result of electric field induced "electromotive" forces on the underlying particles [213, 214]. It took more than a decade to experimentally prove the existence of these forces on free ions in solution.

This all but forgotten experimental work was conducted by Robert Andreyevich Colley[19] (1845–1891) [215–219]. The Colley experiments relied on the inertia of the ions in solution when the entire aqueous solution is accelerated and the ions lag behind. The anions and cations have different masses and transference numbers[20]. Thus, a tiny voltage can be measured if the liquid containing the ions is accelerated. In experimental work that he performed at the University

[17] The seminal work on irreversible processes in electrolytes was published in 1932 by Lars Onsager (1903–1976) and Raymond Fuoss (1905–1987) [209].

[18] The name was coined by the polymath William Whewell (1794-–1866) [211]. His other neologisms included the words electrode, anode, cathode, electrolyte and scientist [211, 212].

[19] Colley was born into an English merchant family in Czarist Russia. He was active in Moscow and later on as a professor at the Imperial Kazan University.

[20] The experimental proof was provided by Johann Wilhelm Hittorf (1824–1914) [220].

of Berlin[21] and published in 1882, a tube filled with a concentrated cadmium iodide (CdI_2) solution was fitted with electrodes and dropped from the ceiling of the laboratory ($\sim 2\,m$) into sand (see setup in Fig. 2.2(a)). An instantaneous spike in the current was measurable with a galvanometer during the acceleration. The I^- ions experienced a different inertial force than the Cd^{2+} and this caused a current to flow in the cell, providing proof of the electromotive force that MAXWELL had predicted.

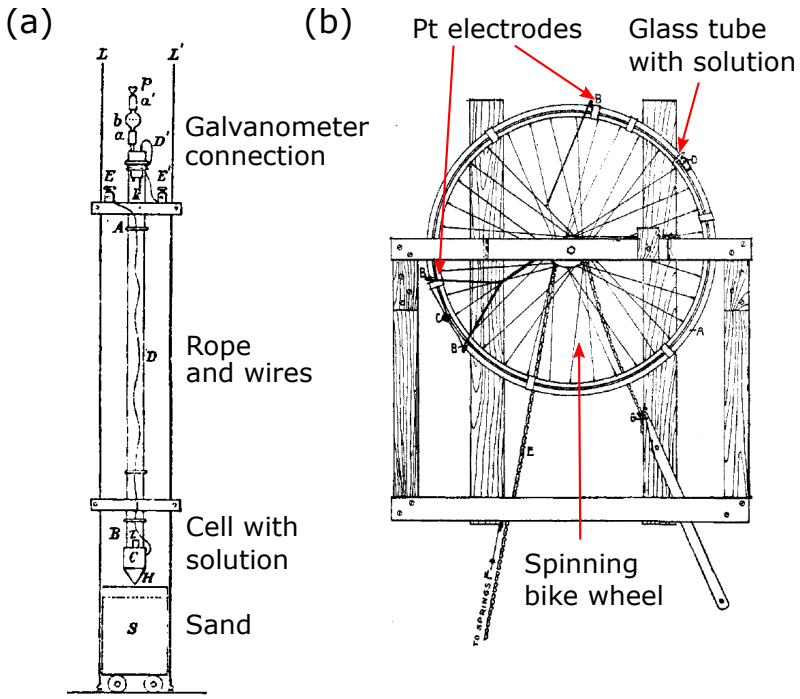

Figure 2.2 – Experiments on ions in solutions exposed to inertial forces: (a) Gravitational drop experiment due to COLLEY (adapted with permission from [219]. Copyright 2006, John Wiley & Sons). A concentrated CdI_2 solution was dropped from 2 m into sand. During deceleration a current due to the difference in ion movement could be measured. (b) TOLMAN experimental setup (Adapted with permission from [221]. Copyright 1914, American Chemical Society). Centrifugal forces spin the sample that is positioned in the middle of a Faraday cage. The inertial forces at play are much higher than in (a).

Prior to these free fall experiments, COLLEY was studying the effect of gravitational acceleration in a simple long vertical tube with the electrodes at the top and bottom [215, 216]. Even in this situation a slight voltage was measurable until the concentration gradient predicted by Eq. 2.13 is established by diffusion. The voltage disappeared as soon as the equilibrium was reached. A rough estimate for the voltage can be calculated thermodynamically from the free energy balance:

$$\Delta\Phi = \frac{-gz(\Delta M_i - \rho_w \Delta \overline{V}_i)}{F}. \tag{2.17}$$

[21] The assistance of director Hermann von HELMHOLTZ, Heinrich HERTZ and Ernst Bessel HAGEN was acknowledged in the publication [219].

This equals around 10 µV. Interestingly, he also mentioned an experiment with paramagnetic iron salt solutions in a magnetic field [216]. He reported unsatisfactory results, but vowed to publish results as soon as he had dealt with the experimental uncertainties. Unfortunately, no further mention of this experiment is made, at least in the German language scientific literature of the time. Is it possible to measure a voltage due to the magnetic migration of Fe^{2+} ions? A thermodynamic inspection yields the following:

$$\Delta\Phi = \frac{\chi_i B^2}{2F\mu_0}, \tag{2.18}$$

with $\chi_{Fe^{2+}} = 153.7 \times 10^{-9}\,\mathrm{m^3\,mol^{-1}}$ and $B = 1\,\mathrm{T}$, one obtains a voltage of 0.63 µV. This is more than one order of magnitude below the estimate for the gravitational voltage, but with a measuring apparatus of high accuracy it is imaginable that an effect could be measured. Diamagnetic susceptibilities of the anions and water ($\chi_{H_2O} = -0.16 \times 10^{-10}\,\mathrm{m^3\,mol^{-1}}$) are of much lower magnitude.

In the 1890s, Theodor DES COUDRES (1862–1926) further developed the gravitational experiment and devised a setup with stronger centrifugal forces [222–224] to increase the measurable voltage. Then, in 1910, Richard C. TOLMAN (1881–1948) [221, 225, 226] performed a more powerful centrifugal experiment with which he could measure the transference numbers of the individual ions of simple salts[22]. A glass tube acted as the liquid sample holder and was placed inside a bike wheel. The acceleration of a motor set the sample spinning and a rapid break caused immense centrifugal forces (see setup in Fig. 2.2(b)). The voltage measurement during this provided estimates for the mass of the charge carriers[23]. Nowadays, ultracentrifuges can reach extremely high pressures up to 500 bar. The pressure gradients created by such centrifugation can cause significant concentration gradients in solutions.

These experiments show that the concentrations of ions can be influenced by comparatively weak body forces on the liquid medium containing them. Of course these effects are only of academic interest, as the effect on the movement of ions on the atomic scale are minuscule and of little relevance to any application. The pressures caused by magnetic fields are in the order of those associated with gravity and cannot be expected to contribute to any significant concentration changes.

The converse situation, in which microscopic forces on the ions in solution cause ponderomotive forces on the bulk medium, gives rise to more pertinent phenomena. An important distinction has to be drawn between these ponderomotive forces and the previously discussed macroscopic external forces. An example of such a magnetic ponderomotive force was demonstrated in a 1950 experiment, which proved that corrosion is an electrochemical reaction [232]. In this experiment a sessile drop of saline water was placed on a magnet pole piece. The ensuing corrosive current,

[22] This was incidentally the topic of the former's concise PhD thesis [227].

[23] In his most well-known experiment he spun copper wires instead of electrolyte solutions and was able to measure that electrons were the charge carriers [228–230]. This was a considerable achievement considering that the electron mass is lower than that of an ion by a factor of 10^5. The experiment later became known as the Stewart-Tolman experiment.

[23] The original experiments of TOLMAN used a 30 horse power de Laval turbine to achieve 5000 revolutions per minute. Due to the fear of explosion the entire apparatus was buried in an underground pit [225, 231].

which flowed from the drop centre to the edge, caused a Lorentz force in combination with the magnetic field. Under the influence of this, the entire drop then began to rotate on the magnet pole piece. The angular velocity could be controlled by the magnitude of the magnetic field. The magnetoconvection of a paramagnetic liquid is another example of such forces. This phenomena will be explained in Sections 2.2.2 and 2.2.3 after the discussion of the mass transport processes below.

2.2.1. Mass Transport

The crucial quantity for the transport of ions in solution is the electrochemical potential $\overline{\mu}_i$. Currents are caused by gradients in $\overline{\mu}_i$. These can be picked up by a voltmeter for measurement [233]. An expression for the flux $\mathbf{J}_i$ (in $\mathrm{mol\,m^{-2}\,s^{-1}}$) of an ion species i is [181]:

$$\mathbf{J}_i = -\frac{c_i D_i}{RT} \nabla \overline{\mu}_i, \tag{2.19}$$

with the concentration c_i and diffusion coefficient D_i (unit: $\mathrm{m^2\,s^{-1}}$). Typical values for the D_i in liquids are around $10^{-9}\,\mathrm{m^2\,s^{-1}}$ (often quoted as $10^{-5}\,\mathrm{cm^2\,s^{-1}}$). Electrochemical equilibrium means $\nabla \overline{\mu}_i = 0$ and $\frac{\partial \overline{\mu}_i}{\partial t}$. The expression in Eq. 2.19 encompasses molecular diffusion due to concentration gradients and ionic migration in electric fields. Bulk motion of the entire fluid will often accompany an ion current flowing through the solution. Such convective motion caused by rotational body forces (see Section 2.2.3) is the third mechanism of mass transport. In reality, these three processes are inexorably linked and occur together. They will be discussed below.

Diffusion

Fick's laws [234, 235] are the archetypal equations that must be solved when the concentration gradient is the driving force for diffusion. The first phenomenological law relates the diffusive flux $\mathbf{J}$ of a species to the diffusion coefficient D and the gradient of concentration ∇c:

$$\mathbf{J} = -D \nabla c. \tag{2.20}$$

This equation dictates that ions flow from areas of high to low concentration. Inserting Eq. 2.20 into the continuity equation ($\frac{\partial c}{\partial t} + \nabla \cdot \mathbf{J} = 0$) leads to Fick's second law:

$$\frac{\partial c}{\partial t} = D \nabla^2 c. \tag{2.21}$$

The evolution of an initially sharp concentration profile is given by the solution of Eq. 2.21, which commonly involves error functions ($\mathrm{erf}\, x = \frac{2}{\sqrt{\pi}} \int_0^x e^{-t^2} dt$). Fick's laws are valid at low concentration. Binary electrolytes in solution are assigned a single diffusion coefficient D, although the diffusion coefficients of the individual components differ. The reason for this is that the movement of the faster ion causes an electric potential gradient with respect to the co-ion

of opposite charge. This accelerates the slow ion while the more mobile ion is reeled in[24]. Thus, charge neutrality is the reason why salt diffuses as a single substance[25].

In real multi-component ion systems, there are a number of situations in which species will move into areas of higher concentrations [173, 237, 238]. At higher concentration and when multiple ionic species are involved, diffusion is correctly described by the gradient of the chemical potential. This general treatment of diffusion is encapsulated in the Maxwell-Stefan law for the driving force on an ion species i in presence of other components j:

$$F_i = \sum_{j \neq i} \xi_{ij} x_j (v_j - v_i). \tag{2.22}$$

Here, ξ_{ij} is the friction coefficient (unit: $\mathrm{N\,s\,mol^{-1}m^{-1}}$) between species i and j, x_j is the mole fraction of species j and v are the diffusive species velocities (unit: $\mathrm{m\,s^{-1}}$). This equation naturally accounts for interparticle effects on diffusion and other forces can be incorporated [173]. This can be useful for the treatment of electrolytes [239]. However, the solution of Eq. 2.22 is computationally cumbersome and the precise determination of the individual ξ_{ij} requires modelling. The practicality of this approach is therefore not as universal as suggested by its proponents and a treatment with Fick's laws at the dilute limit is commonly encountered [240].

Interesting situations can arise when multicomponent systems with differing diffusion rates cause density gradients which can lead to convection [241, 242]. Convection will be discussed after the migration in an electric potential gradient.

Migration

The futility of defining an electrostatic potential between two media was mentioned in Section 2.1. The flow of electricity in an electrolyte solution is of non-equilibrium thermodynamic nature, not electrostatic [179, 187]. Inside the liquid phase, it is possible to define a conceptual electric potential Φ. The movement of ions in a gradient of the electric potential is incorporated in Eq. 2.19 and leads to a migration (or drift) velocity of the ions [243]:

$$\mathbf{v}_{\mathrm{mig}} = -Z_i u_i F \nabla \Phi, \tag{2.23}$$

with the valence charge of the ion Z_i, the mobility u_i (unit: $\mathrm{m^2\,mol\,J^{-1}\,s^{-1}}$) and Faraday constant F. The velocity can be converted to the molar flux $\mathbf{J}_{\mathrm{mig}}$ (unit: $\mathrm{mol\,m^{-2}\,s^{-1}}$) by multiplication with the concentration c_i:

$$\mathbf{J}_{\mathrm{mig}} = -Z_i u_i F c_i \nabla \Phi. \tag{2.24}$$

Ohm's law relates the gradient in electric potential to the current density $\mathbf{j}$ (unit: $\mathrm{A\,m^{-2}}$) and the ions in a homogeneous solution follow it:

[24] Minute imbalances in the acceleration can be measured in experiments such as those performed by Colley and Tolman (see Section 2.2 above).

[25] Diffusion coefficients of the individual ion species can be obtained by measuring the conductivity and the transference numbers of the electrolyte solution [236].

$$\mathbf{j} = -\kappa \nabla \Phi, \tag{2.25}$$

with the ionic conductivity κ (unit: $\Omega^{-1}\,\mathrm{m}^{-1}$). For a binary electrolyte, κ is:

$$\kappa = F^2(z_+^2 u_+ c_+ + z_-^2 u_- c_-). \tag{2.26}$$

The profile of Φ and the electric resistance of the solution can be calculated from Eq. 2.25. When a voltage is applied to an electrolyte solution, surface charge is accumulated on the charged solid and the electrical double layer is modified. This will be discussed in Section 2.3.3. Concentration gradients are bound to form during the transport of ions to the electrode surface. This means the current will be transported by diffusion and migration. The Nernst-Planck equation merges the diffusive current based on Fick's law (Eq. 2.20) and the expression for ionic migration (Eq. 2.24):

$$\mathbf{J_i} = -D_i \nabla c_i - Z_i u_i F c_i \nabla \Phi = -D_i \left(\nabla c_i - \frac{Z_i F}{RT} c_i \nabla \Phi \right). \tag{2.27}$$

The Einstein relation was used to convert the mobility to the diffusion coefficient above. The Nernst-Planck equation is an electrical and dilute case of the Maxwell-Stefan equation (Eq. 2.22).

Convection

The bulk liquid solution may acquire a velocity $\mathbf{u}$ due to convection. The movement of the bulk solution is described by fluid mechanics. There will be a discussion of elementary fluid dynamical concepts in Section 2.2.3. For a detailed introduction to fluid dynamics the reader is referred to introductory text books [244, 245]. A special mention describing the application of fluid dynamics to electrochemistry is the monograph by V. G. Levich (1917–1987) [246].

This velocity of the bulk fluid causes a flux density $\mathbf{J}_{\mathrm{conv}} = c_i \mathbf{u}$, with which the Nernst-Planck equation can be expanded into a form including convection:

$$\mathbf{J_i} = -D_i \left(\nabla c_i - \frac{Z_i F}{RT} c_i \nabla \Phi \right) + c_i \mathbf{u}. \tag{2.28}$$

Convection will not contribute to the net current because of charge neutrality, rather it will modify the flow of the existing current. Bulk movement of fluid is caused by the action of external body forces. It is convenient to subdivide convection into different categories. Natural convection is caused by density differences, which can be due to thermal effects or chemical processes at the electrode. For example, cations can be converted to a solid during electrodeposition. This decreases the concentration of the electrolyte close to the working electrode and a density gradient in the solution evolves [247]. The bulk solution will replenish the depleted ions by diffusion, but the solution in vicinity of the working electrode will become less dense and rise due to buoyancy if the electrode is vertically oriented. Forced convection can originate in mechanical stirring, pressure gradients and a variety of body forces. It is also possible that surface forces drive convective mass transport. An example is Marangoni convection, which is caused by a gradient in surface tension.

From the thermodynamic considerations of electrolyte solutions in Section 2.1, it is clear that the only mass transport mechanism which is in an energy range to be seriously influenced by a magnetic field is convection. Magnetoconvection can be caused by magnetic susceptibility gradients, due to temperature or density of the paramagnetic component. It will be discussed in Section 2.2.3, once the magnetic body forces for a paramagnetic fluid have been introduced in the next section.

2.2.2. Magnetic Force Densities

When a magnetically polarisable material is exposed to a magnetic field gradient, microscopic forces act on the individual magnetic dipoles in the medium. Thus, a magnetic body force arises, which can lead to bulk motion of the magnetised material. High magnetic field gradients are obtained in the stray field of permanent magnets. Their field profile can be calculated analytically with the magnetic charge method (see Appendix A.1) or numerically with finite element methods. However, the ponderomotive force on a magnetically polarisable medium is a non-trivial matter. Derivations and discussions of expressions for the force density are outlined in many texts [117, 248–255]. Some of the discussions are based on dielectric media, but the treatment of paramagnetic matter is largely analogous to this. With the presence of current densities $\mathbf{j}$, a Lorentz force density $\mathbf{F_L} = \mathbf{j} \times \mathbf{B}$ must be added to the magnetic force density to account for the interaction of moving charges with the magnetic field. The Lorentz force density is of much smaller magnitude than the Kelvin force when a considerable concentration of paramagnetic ions are present in the solution [55]. In the following discussion, the absence of currents is assumed.

The microscopic force on a single magnetic moment ($\mathbf{m}$) in a magnetic field gradient is given by:

$$\mathbf{F}_{\mathrm{mag}} = \mu_0(\mathbf{m} \cdot \nabla)\mathbf{H}. \tag{2.29}$$

The effects of this force were measured in the Stern-Gerlach experiment [104, 105]. In a continuum, such as a paramagnetic salt solution, a force density must be introduced to describe the action of the field gradient on the paramagnetic ions. The microscopic forces on the ions are transferred to the bulk fluid via interparticle forces that are mediated by collisions between the individual hydrated ions and water molecules. In order to transform Eq. 2.29 into an expression for the force density, scaling with the number of microscopic magnetic dipoles per unit volume (their number density N) is necessary. The magnetisation $\mathbf{M} = N\mathbf{m}$ is a macroscopic variable that is defined as the number density of magnetic dipole moments multiplied by the microscopic dipole moments. Replacing $\mathbf{m}$ with $\mathbf{M}$ in Eq. 2.29, one immediately obtains the Kelvin force expression for the magnetic force density:

$$\mathbf{F}_{\mathrm{K}} = \mu_0(\mathbf{M} \cdot \nabla)\mathbf{H}. \tag{2.30}$$

Kelvin (1824–1907) arrived at this expression by considering the magnetic moment per unit volume and relating it to the mechanical force in a dipole model [256]. The Kelvin force is often referred to as the magnetic field gradient force in magnetoelectrochemistry. For small magnitudes ($\chi \ll 1$) of magnetic susceptibilities $\mathbf{B} = \mu_0(\mathbf{H} + \mathbf{M}) = \mu_0(\mathbf{H} + \chi\mathbf{H}) \approx \mu_0\mathbf{H}$ and the Kelvin force can be approximated as:

$$\mathbf{F}_{\nabla \mathrm{B}} = \frac{\chi}{\mu_0}(\mathbf{B} \cdot \nabla)\mathbf{B}. \tag{2.31}$$

The form with the magnetic flux density $\mathbf{B}$ is commonly encountered in magnetoelectrochemistry. In magnetohydrodynamics, the expression $\frac{(\mathbf{B}\cdot\nabla)\mathbf{B}}{\mu_0}$ is known as the magnetic tension force. This name is aptly chosen, since the force acts to straightens out magnetic field lines [257].

There is a second expression for the force on an incompressible paramagnetic liquid, which incorporates the gradient of the magnetic susceptibility (or permeability):

$$\mathbf{F}_{\mathrm{H}} = -\frac{\mathbf{H} \cdot \mathbf{H}}{2}\mu_0 \nabla \chi. \tag{2.32}$$

This expression predicts a force density at interfaces at which the susceptibility changes. Here the force acts to pull the medium into the magnetic field. This form of the magnetic force density was developed first by Diederik Korteweg (1848–1941) [258], then by Herman von Helmholtz (1821–1894) [259] within the framework of the thermodynamic principle of minimum energy. It is known as the Korteweg-Helmholtz force [260]. Later work by Gustav Kirchhoff (1824–1887) [261,262] and others followed. In magnetoelectrochemistry, the Korteweg-Helmholtz force is referred to as the concentration gradient force [263,264]:

$$\mathbf{F}_c = -\frac{\mathbf{H} \cdot \mathbf{H}}{2}\mu_0 \chi_m \nabla c \approx -\frac{\mathbf{B} \cdot \mathbf{B}}{2\mu_0}\chi_m \nabla c. \tag{2.33}$$

The implications of the Kelvin and Korteweg-Helmholtz force densities can be demonstrated by applying them to the Quincke tube experiment [265–267]. Georg Quincke (1834–1924) measured the susceptibility of magnetic liquids by analysing the difference of liquid height between the arms of an open glass U-tube, with one of them between the poles pieces of an electromagnet[26] [265,266]. Thus, a magnetic field was applied parallel to the liquid surface and modified hydrostatic equilibrium. On grounds of the Kelvin force, it can be argued that the force density originates in the fringing field of the pole pieces with $\nabla H \neq 0$, which pushes the liquid in the tube upward. Whereas the Korteweg-Helmholtz force acts on the interface between the air and the magnetised liquid ($\nabla\chi \neq 0$) and the level of the magnetised liquid rises. Both the presented argumentations are sound. Nonetheless, there has been controversy over which of the expressions is the correct one since they were first derived. An argument that has not abated to the present day [264,268–270]. Criticism was first levelled at the Korteweg-Helmholtz force by British influenced followers of Lord Kelvin, among others by Joseph Larmor (1857–1942) and G. H. Livens (1886–1950) [256,271,272].

[26] The Quincke tube experimental procedure was also employed for the determination of dielectric constants of liquids in an electric field [267].

On the face of it, the presented situation indeed seems bewildering. The formulae predict force densities in inhomogeneous magnetic fields or at interfaces at which the susceptibility changes, respectively. This apparent paradox can be resolved by re-expressing the Kelvin force density (Eq. 2.30) with the help of vector identities. The first step is to expand the expression with $(\mathbf{H}\cdot\nabla)\mathbf{H} = (\nabla\times\mathbf{H})\times\mathbf{H} + \frac{1}{2}\nabla(\mathbf{H}\cdot\mathbf{H})$ after writing $\mathbf{M} = \chi\mathbf{H}$:

$$\mathbf{F}_\mathrm{K} = \mu_0\,\chi[\underbrace{(\nabla\times\mathbf{H})}_{=0}\times\mathbf{H} + \tfrac{1}{2}\nabla(\mathbf{H}\cdot\mathbf{H})]. \tag{2.34}$$

In the absence of currents $\nabla\times\mathbf{H} = 0$ and the first term disappears. The remaining dot product of $\mathbf{H}$ is already reminiscent of the Korteweg-Helmholtz force (Eq. 2.32) and can be further transformed by employing $\nabla(\chi\mathbf{H}^2) = \chi\nabla\mathbf{H}^2 + \mathbf{H}^2\nabla\chi$:

$$\mathbf{F}_\mathrm{K} = \nabla\underbrace{\left(\frac{\mu_0}{2}\chi\mathbf{H}\cdot\mathbf{H}\right)}_{P_\mathrm{mag}} - \frac{\mu_0}{2}\mathbf{H}\cdot\mathbf{H}\,\nabla\chi. \tag{2.35}$$

The term in the brackets on the left is a magnetic readjustment of the internal pressure in the fluid. This is not present in the Korteweg-Helmholtz version of the force density [117, 273] and instead appears within the definition of the internal pressure[27] itself. The gradient of the magnetically induced pressure is the difference between the two expressions for the magnetic force density on a paramagnetic fluid:

$$\mathbf{F}_\mathrm{K} = \nabla P_\mathrm{mag} + \mathbf{F}_\mathrm{H}. \tag{2.36}$$

What are the implications for the dynamics of a paramagnetic fluid element that is exposed to a magnetic field gradient? The dynamics of such a fluid element are given by Newton's second law. With the Korteweg-Helmholtz expression for the magnetic body force density this becomes:

$$\mathbf{F}_{\mathrm{tot,\,H}} = -\nabla P + \mathbf{F}_\mathrm{H}. \tag{2.37}$$

The expression contains the gradient of the internal pressure ∇P. The Kelvin force version differs by the gradient of the magnetic pressure term, which can be combined with ∇P and written as $\nabla P'$:

$$\mathbf{F}_{\mathrm{tot,\,K}} = \underbrace{-\nabla P + \nabla P_\mathrm{mag}}_{-\nabla P'} + \mathbf{F}_\mathrm{H}. \tag{2.38}$$

Gradients of the internal pressure are unimportant for the prediction of deformation and velocity of a portion of incompressible fluid. As will be discussed in the next section on fluid dynamics, only rotational forces can cause fluid movement which deforms the paramagnetic solution in a closed system. The gradients of internal pressure are by definition irrotational and

[27] An equivalent electric polarisation pressure change was optically measured in a weak dielectric liquid exposed to an electric field with the Schlieren technique [274]. The results were explained with the Korteweg-Helmholtz expression and the authors were critical of the stance of Livens [272].

inconsequential for deformations that leave the volume unchanged. It follows that the Kelvin and Korteweg-Helmholtz expressions for the magnetic force density on a paramagnetic liquid predict the same hydrostatics and hydrodynamics [260, 273, 273, 275, 276], despite the fact that they lead to different distribution of the force density. Deformations of incompressible fluids, such as paramagnetic salt solutions, are equally well described by both expressions. The Kelvin force is conceptually more accommodating. It depends on the situation which expression is more straightforward to interpret, but in the end it does not matter which of them is used.

The futility of the argument about the correct force density was first pointed out in the 1950s [250,273,277], most notably by pioneers of non-equilibrium thermodynamics Peter Mazur (1922–2001) and Sybren de Groot (1916–1994) based at the Lorentz Institute in Leiden [273, 277]. The arguments were later presented again by others [251, 275, 276, 278]. Evidently, these warnings have fallen on deaf ears.

2.2.3. Basics of Magnetohydrodynamics

An elementary understanding of fluid dynamics is necessary to interpret the action of a magnetic field gradient on a paramagnetic liquid. Here a basic account of important concepts will be given. Readers are referred to introductory texts on fluid dynamics [244, 245] and ferrohydrodynamics [117, 253] for further information. The hydrodynamical equations describing the behaviour of a fluid can be derived from statistical mechanics [210, 279, 280].

The Navier-Stokes equation is fundamental for fluid dynamics. This relates the acceleration of the fluid, given by the material derivative of the fluid velocity ($\frac{\mathrm{D}\mathbf{u}}{\mathrm{D}t} = \frac{\partial \mathbf{u}}{\partial t} + \mathbf{u}\cdot\nabla\mathbf{u}$), to force fields and pressure gradients. On the face of it, the problem appears deceptively straight forward, as it follows from Newton's second law with body forces. However, the Navier-Stokes equation is a non-linear partial differential equation due to the material derivative of the velocity and therefore in reality complicated to solve. The Navier-Stokes equation for a paramagnetic liquid can be written:

$$\rho\frac{\mathrm{D}\mathbf{u}}{\mathrm{D}t} = -\nabla P + \eta\nabla^2\mathbf{u} + \rho\mathbf{g} + \mu_0(\mathbf{M}\cdot\nabla)\mathbf{H}, \tag{2.39}$$

with the dynamic viscosity η (unit: $\mathrm{N\,s\,m^{-2}}$) defining the viscous force. The pressure gradient, gravitational and Kelvin force densities are already familiar. Generally, the pressure is unknown and it is impossible to make a direct prediction of fluid motion from Eq. 2.39 without the incompressibility constraint $\nabla\cdot\mathbf{u} = 0$. The issue can be sidestepped by applying the curl operator ($\nabla\times$) to the Navier-Stokes equation, disposing of the bothersome ∇P. This brings into play the vorticity of the flow. Any body force with a non-zero curl is able to change the shape of the fluid and cause it to rotate [281]. If the flow is irrotational, a velocity potential $\mathbf{u} = \nabla\phi$ can be introduced and the situation is known as potential flow. Any irrotational (potential) forces will be balanced by the pressure field in the liquid. These pressure changes are equilibrated by solid walls in a fully filled closed cell and the fluid remains static in the absence of free surfaces. For an incompressible fluid, the pressure serves as an assurance that only deformations in which the volume is conserved are allowed. It follows from the discussion on thermodynamics

in Section 2.1 that no appreciable changes in concentration are to be expected from these small pressure differences. Only rotational body forces contribute to internal flows[28] [54].

In order for paramagnetic solutions to be moved by magnetoconvection, the Kelvin force must be rotational. What is the condition for the non-potentiality of the Kelvin force and the occurrence of magnetoconvection? A strict requirement is that both the magnetised fluid and the magnetic field are inhomogeneous. This means $\nabla H \neq 0$ for the magnetic field and either $\nabla \rho \neq 0$ or $\nabla M \neq 0$ for the paramagnetic fluid in question. These prerequisites can be obtained by deriving the condition for mechanical equilibrium from Eq. 2.39. Any magnetised fluid will undergo convective movement with the aim to establish this mechanical equilibrium. Under zero flow ($\mathbf{u} = 0$) the application of $\nabla\times$ to Eq. 2.39 yields:

$$\nabla \times (\rho \mathbf{g} + \mu_0 (\mathbf{M} \cdot \nabla)\mathbf{H}) = 0. \tag{2.40}$$

With the vector identity $\nabla \times (\psi \mathbf{A}) = \psi \nabla \times \mathbf{A} + \nabla\psi \times \mathbf{A}$ and using the collinearity of $\mathbf{M}$ and $\mathbf{H}$ this becomes:

$$\nabla\rho \times \mathbf{g} + \mu_0 \nabla \times \left(\frac{M}{H} (\mathbf{H} \cdot \nabla)\mathbf{H} \right) = 0. \tag{2.41}$$

The vector identity $(\mathbf{H}\cdot\nabla)\mathbf{H} = \underbrace{(\nabla \times \mathbf{H})}_{=0} \times \mathbf{H} + \frac{1}{2}\nabla H^2$ and the previously used vector identity for the curl lead to the criterium of hydrostatic equilibrium for magnetic liquids:

$$\nabla\rho \times \mathbf{g} + \mu_0 \nabla M \times \nabla H = 0. \tag{2.42}$$

Any departure from this condition will lead to magnetoconvection [18, 283]. Most experiments in which a magnetic modification of mass transport in cells containing paramagnetic salt solutions is observed, can be explained on grounds of this equation. Essentially, the magnetic field gradient modifies density difference driven convection and pulls the magnetic fluid into this external field gradient. The curl of the Kelvin force causes non-potentiality of gravity by introducing density gradients orthogonal to the direction of gravity. This proceeds until Eq. 2.42 is satisfied. Temperature gradients in the magnetic fluid can modify both the magnetisation and the density of the fluid, which is reflected in Eq. 2.42. This would be the case of magnetothermal convection [14, 17, 19–26, 42–46, 253]. In summary, not only is it necessary that gradients of the external magnetic field ∇H and concentration of the paramagnetic species ∇c exist, these must also be non-parallel to each other in order to lead to magnetoconvection.

The condition for hydrostatic equilibrium in Eq. 2.42 is not formulated in terms of the concentration gradient of the paramagnetic species. In magnetoelectrochemistry it is useful to analyse the curl of the magnetic field gradient force (Eq. 2.31) to determine whether convection in a paramagnetic salt solutions takes place. An expression with the molar magnetic susceptibility and the concentration can be obtained:

[28] The situation in magnetohydrodynamics is well demonstrated in a didactic 1965 film by John Arthur Shercliff (1927–1983) [282].

$$\nabla \times \mathbf{F}_{\nabla \mathrm{B}} = \frac{1}{2\mu_0}\chi_m \nabla c \times \nabla B^2, \tag{2.43}$$

which is simply a reformulation of the magnetic part of Eq. 2.42.

An important class of fluid dynamical phenomenon is that of flow separation in which the fluid velocity changes direction with respect to the main fluid velocity. This frequently happens in the vicinity of solid obstacles in the way of the flow, but it can also be triggered by magnetic field gradients in special cases [75]. A necessary requirement for separation to occur is that the vorticity changes sign and is reversed [284]. This change of flow direction cannot be explained within a one-dimensional approximation of the force density [55, 74, 75]. In the case of a solid wall, the fluid passing by in immediate proximity to the obstacle will be spun around and form a counterflow. In the magnetic case, changes in the vorticity can be precipitated by variation in the curl of the Kelvin force (see Section 2.3.2). For magnetoelectrochemistry this is most obvious when considering concentration gradients in the vicinity of negatively charged electrodes and inspecting Eq. 2.43. Magnetoelectrochemistry will be discussed in Section 2.3.2, after a brief discussion on regular electrochemistry in the next section.

2.3. Electrochemistry

2.3.1. Basics of Electrochemistry

Many comprehensive introductions to electrochemistry [170, 285, 286] exist and it is not the aim to provide one here. For this reason only a brief summary of the main concepts will be given.

Electrochemical experiments are generally performed in electrochemical cells, which contain three electrodes: working electrode, counter electrode and reference electrode. A potential difference can be applied between working and counter electrode with a potentiostat. The current flows between them and can be controlled by the potentiostat. The reference electrode is necessary to measure the applied voltage relative to a reference reaction. Ion concentrations build up in the double layer with a huge electric field gradient on counter and working electrodes (see Section 2.3.3) to balance their excess charge. This is where ions from the solution can be immobilised or chemical reactions take place. The application of a voltage to the system can lead to the electrodeposition of a solid substance on the working electrode surface. Reduction and oxidation reactions are balanced:

$$\mathrm{O} + ne^- \rightleftharpoons \mathrm{R}, \tag{2.44}$$

with the oxidising (O), reducing agents (R) and the number of involved electrons n in moles. The equilibrium can be estimated from the applied potential E with the help of the Nernst equation:

$$E = E^{0'} + \frac{RT}{nF}\ln\frac{[\mathrm{O}_*]}{[\mathrm{R}_*]}. \tag{2.45}$$

This includes the concentrations of the oxidiser O_* and reductant R_* ion species on the electrode surface, along with the formal potential $E^{0'}$. The formal potential is dependent on the ratio of the activity coefficients of O_* and R_*. In contrast, the standard electrode potential E^0 is based on concentrations.

Faraday's law relates the mass m of the chemical liberated at the electrode to transferred charge Q:

$$m = \frac{QM}{nF}, \tag{2.46}$$

with the molar mass M. The thickness of an electrodeposited layer can be estimated with this formula. A deposition with a constant current is known as galvanostatic and with a constant voltage as potentiostatic.

Information about the electrochemical kinetics can be inferred from the Butler-Volmer equation [287], which provides a relationship between electrode current density j and electrode potential E. For non-mass-transport limited currents in well stirred cells, it is given by:

$$j = j_0 \left[\exp\left(\frac{\alpha_a nF}{RT}(E - E_{eq}) \right) - \exp\left(-\frac{\alpha_c nF}{RT}(E - E_{eq}) \right) \right], \tag{2.47}$$

with α_a and α_c, the anodic and cathodic charge transfer coefficients respectively. The expression can often be found with the overpotential $\eta = (E - E_{eq})$. The Butler-Volmer equation incorporates the exchange current density j_0, which is defined as the magnitude of both anodic and cathodic current densities precisely at the equilibrium potential of the cell. The expression is valid when there are no large concentration gradients between the electrode surface and the bulk solution.

A versatile electrochemical technique to analyse charge transfer and electrochemical reaction is cyclic voltammetry [285,286,288]. The potential difference between the electrodes is increased or decreased linearly and the current response of the electrochemical cell is recorded. Oxidation and reduction reaction can be identified in these cyclic voltammograms by peaks during the scan, which are caused by the formation of a mass transport limited depletion layer. The replenishment of the reactant in the area close to the electrode due to slow diffusion will cause a drop in the current.

This diffusion limited behaviour is encapsulated by the Cottrell equation, which was derived from Fick's law in order to describe the current response to an applied potential step [289]:

$$i(t) = \frac{nFAc_0\sqrt{D}}{\sqrt{\pi t}}. \tag{2.48}$$

This predicts a $t^{-1/2}$ behaviour of the current at a planar electrode of area A for a bulk electrolyte concentration of c_0 with diffusion coefficient D. The current shortly after the application of the potential step is dominated by the capacitive charging of the double layer, which causes a deviation from the Cottrell equation. Conversely, during lengthy exposures to the potential step, diffusive currents are disturbed by natural convection. This can cause a non-zero contribution

to the current, which keeps it from reaching the predicted zero limit at long times. Vertically placed electrodes with surfaces that are parallel to the gravitational acceleration are particularly susceptible to buoyancy driven convective flows [290]. It is precisely in such situations that a paramagnetic salt solution departs from the magneto-hydrostatic equilibrium and a magnetic field gradient can modify the convective flow in the cell. Scenarios in which magnetoconvection is at large will be discussed in the following section.

2.3.2. Magnetoelectrochemistry

Having internalised the colossal energy discrepancy between the magnetic energy and the electrochemical potential in Section 2.1, the area of magnetoelectrochemistry may strike one as rather quaint. All the same, the transport of the electrolyte to the electrode surface is strongly influenced by bulk movement of the fluid. This is where magnetic body forces can have dramatic effects, not in the underlying electrode kinetics. An overview of the current state of knowledge in magnetoelectrochemistry will be given here.

The first experiments investigating magnetic effects on currents in electrochemical cells can be traced back to the 19th and early 20th century. They were carried out by scientists studying the Lorentz force in liquids [291,292]. The bulk rotation of the salt solution by the Lorentz force density was already identified as the reason for the observed effects by Heilbrunn in 1904 [292]. It was also this Lorentz force induced rotation which proved that corrosion is an electrochemical reaction by rotating a drop of aqueous solution on a magnetic pole piece [232]. In the 1970s and 80s, notable research on the mass transport modification by homogeneous magnetic fields was carried out by Aogaki [293–295], active in Japan, and Fahidy [296–301], working in Canada. This work laid the foundation for what is now known as the magnetohydrodnamic (MHD) effect, namely the stirring of the electrolyte solution by the Lorentz force close to the electrode. A magnetic field parallel to the electrode surface is orthogonal to the current and the electrolytic solution rotates. A direct consequence of this is that the limiting current is increased, as the convective flow helps to replenish the concentration at the electrode. Chronoamperometry of various metal depositions showed this heightened mass transfer due to MHD stirring [61]. The influence of the MHD flow on Ni [57,58] and Cu [302] deposition was also studied around this time. It was also shown that the structure of Cu electrodeposits could be tuned with the Lorentz force [59].

There are reports of particle image velocimetry (PIV) [62] and interferometric measurements of concentration variation [63] which visualise the fluid dynamics governing the MHD stirring. These are backed up by magnetohydrodynamical simulations that model the body forces at play [55]. MHD effects were also studied by electrochemical impedance spectroscopy [303] at the CNRS in Reims. The same group undertook a similar study of a possible magnetic effect on electrochemical kinetics [304]. The conclusion was that no such effect on charge-transfer coefficients exist. All effects were ascribed to modification of convective mass transport by MHD or the magnetic field gradient force [305–309]. This was corroborated by a later study of another group [67].

When strong magnetic field gradients $\nabla B \approx 100\,\mathrm{T\,m^{-1}}$ and paramagnetic species are present in the solution, the Lorentz force tends to pale into insignificance and the Kelvin force becomes dominant as soon as a gradient of paramagnetic ions is established. Systematic electrochemical studies of magnetic field effects, including paramagnetic salt solutions in field gradients, were reported by Hinds et al. [60] and Bund et al. [310]. The classical and much studied example in which paramagnetic ions can be influenced by the Kelvin force is the electrodeposition of Cu [66, 69–71, 74, 76–82]. One of the first reports of structuring copper electrodeposits from $CuSO_4$ solutions with inhomogeneous magnetic fields was reported in 1979 by the group of Fahidy [66]. A steel cathode was employed in these experiments. Since then there has been a huge increase in the obtainable field gradient, with experiments relying on small permanent magnets or the stray field of a magnetised wire to deliver high magnetic field gradients. The electrodeposition in a magnetic field gradient is accompanied by the formation of both gradients in the density and the magnetic susceptibility. This means that an interplay of the gravitational and the Kelvin force densities will kick in to re-establish mechanical equilibrium according to Eq. 2.42 [55]. The observation of this structuring is not limited to paramagnetic Cu^{2+} solutions. In principle, any paramagnetic ion species that undergoes reaction at an electrode will cause a concentration gradient with respect to the bulk solution. This can be effected by magnetic field gradients. An example of an organic compound that can be captured in a magnetic field gradient after electrochemical conversion is nitrobenzene [263, 311–314].

An unexpected phenomenon that was first observed ten years ago is the inverse structuring of electrodeposits in the intense magnetic field gradients of permanent magnets or magnetised Fe wires [72, 73, 76–79]. In these experiments, the electrochemical cell was filled with a solution containing non-magnetic, but electroplatable ion species (such as Bi^{3+} or Zn^{2+}) and a paramagnetic ion species that was non-electroplatable under the employed experimental conditions (such as Mn^{2+} or Dy^{3+}). When an electrodeposition from this mixture was carried out above an array of small Nd-Fe-B permanent magnets, the non-magnetic species exhibited much thicker deposits in the area of low magnetic $(\mathbf{B}\cdot\nabla)\mathbf{B}$. The presence of the paramagnetic species caused the formation of zones into which the transport of electroactive ions from the bulk solution was inhibited. The explanation of this effect was provided by analysing the curl of the magnetic field gradient force [73, 75]. Results from finite element simulations reported in [75] that explain the observed experimental results are shown in Fig. 2.3.

With multiple components of differing magnetic susceptibilities, the curl of the magnetic field gradient force (Eq. 2.43) must be summed over the individual ion species:

$$\nabla \times \mathbf{F}_{\nabla \mathrm{B}} = \frac{1}{2\mu_0} \sum_i \chi_i \nabla c_i \times \nabla B^2. \tag{2.49}$$

The electrochemical conversion of the non-magnetic ions during the deposition causes a concentration gradient in the electrode normal direction $\nabla c_{\chi=0} > 0$. Due to electroneutrality of the solution, the paramagnetic ions will rush into the void left by the deposited non-magnetic ions and cause a small concentration gradient of their own in the opposite direction $\nabla c_{\mathrm{mag}} < 0$. However, the magnetic susceptibility of the paramagnetic ion is usually more than two orders

of magnitudes higher than that of the non-magnetic species. This means that Eq. 2.49 is under total control of the concentration gradient of paramagnetic ions and reverts to the single component case. Hence, the curl changes sign in the region of high $(\mathbf{B} \cdot \nabla)\mathbf{B}$ and forces flow of the electrolyte solution away from the region of the electrode exposed to a high magnetic field gradient (see Fig. 2.3(b)). The flow is the exact opposite of the above-mentioned deposition from purely paramagnetic electrolytic solutions with $\nabla c_{\mathrm{mag}} > 0$ (see Fig. 2.3(a)). It follows that the thicknesses of the copper layers are reversed (see Fig. 2.3(c-d)). These results are backed up by astigmatism particle tracking velocimetry measurements of the solution in which the velocity normal to the electrode was measured [73].

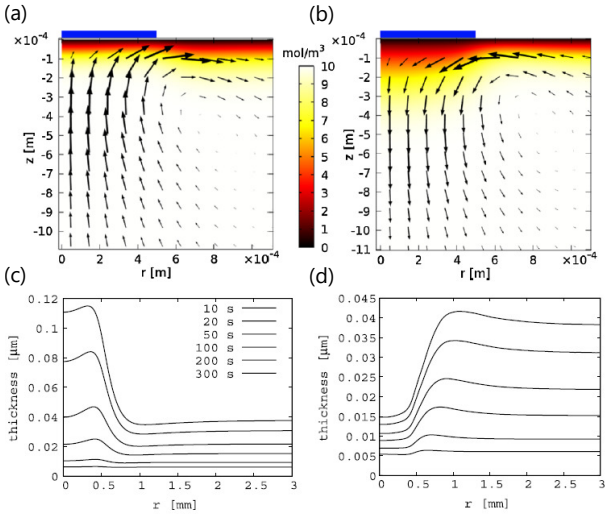

Figure 2.3 – Finite element simulation of magnetoconvection during electrodeposition of Cu on an electrode below a permanent magnet (blue) [75]. (a–b) The top two panels show the Cu^{2+} concentration and normalised velocity. (a) Deposition from pure Cu^{2+} electrolyte solution. The bulk fluid moves towards the part of the electrode backed by the magnet, where the majority of Cu is deposited. The maximum fluid velocity is $0.03\,\mathrm{mm\,s^{-1}}$. (b) Deposition from a mixture of Cu^{2+} and Mn^{2+} electrolyte solution. The bulk fluid moves away from the part of the electrode backed by the magnet, where least Cu is deposited. The maximum fluid velocity is $0.05\,\mathrm{mm\,s^{-1}}$. (c–d) The two panels below show the respective growth of the copper layer in time. The deposition in (d) is reversed with respect to the deposition without Mn^{2+}. Reproduced with permission from [75]. Copyright 2012, American Physical Society.

Evidently, the congested area where the electrode comes into contact with the electrolytic solution is of utmost importance for the dynamics in an electrochemical cell. Interactions at the solid surface are the topic of the next section.

2.3.3. The Electrical Double Layer

A difference in electrode potential brought about by a potentiostat causes the electrodes in solution to become charged due to an imbalance in electrons. This excess charge is compensated by the ions in solution that spread over the charged surface. When the electrodes are charged up, further ions become ordered in the electrical double layer. This means the ionic configuration

entropy decreases and the temperature of the electrolyte slightly rises under adiabatic[29] conditions [315, 316]. The converse is true during discharging. Such small temperature changes have been experimentally verified in porous carbon electrodes [317].

In 1853, the first and simplest model for this electric double layer was proposed by Helmholtz [318]. He assumed a complete charge compensation by the counterions, which are rigidly adsorbed to the electrode surface. If the temperature were so low as to allow the neglect of thermal motion, the Helmholtz theory would perfectly describe the situation at the electrode surface. Such temperatures are not reachable in the liquid state.

In reality, the ions close to the solid surface are not exclusively stuck to the electrode surface and the model must be extended. They are instead slightly delocalised due to thermal motion and form a diffuse layer in the vicinity of the electrode surface. This was first realised by Louis Georges Gouy (1854–1926) [319] and David Chapman (1869–1958) [320] in what became known as the Gouy-Chapman model. This theory relies on a Poisson-Boltzmann equation to predict the extent of the diffusive Gouy-Chapman layer in which the ions are distributed close to the surface. The Gouy-Chapman theory allows an imbalance of cations or anions to compensate the electrode charge and this concentration falls off exponentially with distance from the surface. An estimate for the distribution of counterions around the electrode surface is given by the Debye length λ_D, which is in the order of a few nm to several hundred nm [321].

When high potential differences between the electrodes hold sway, the Gouy-Chapman model has to be extended to account for a certain number of ions that are in fact adsorbed to the surface as suggested by the Helmholtz model. The thermal voltage $V_{\mathrm{th}} = \frac{k_{\mathrm{B}}T}{e} = \frac{RT}{F} = 25.7\,\mathrm{mV}$ is a measure of how much the spatial distribution of ions is affected by a boundary held at a fixed voltage. High double layer voltages are above the thermal voltage at room temperature and can immobilise the ions in an inner layer. This compact layer lies between the electrode surface and the diffuse layer. It goes by the name of Helmholtz or Stern layer after its discoverer Otto Stern [322]. The Stern layer is dielectric, because the ions that compensate the charge of the electrode surface are themselves immediately sandwiched between the solid and a layer of counterions. A sketch of the double layer according to the Gouy-Chapman-Stern theory is shown in Fig. 2.4 (a).

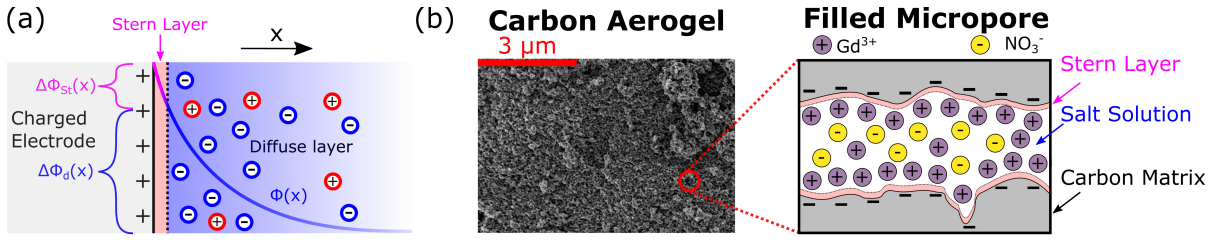

Figure 2.4 – Electrosorption of ions in the electric double layer. (a) The double layer close to a positively charged electrode according to the Gouy-Chapman-Stern model (after [321]). The electric potential ϕ is proportional to the concentration of the electrosorbed ion species c. It decreases exponentially with the distance from the surface. (b) Electrosorption with carbon aerogels from $Gd(NO_3)_3$ solution. Left: SEM image of a porous carbon aerogel monolith. Right: Electrosorption of Gd^{3+} in the double layer in a micropore.

[29] The entropy change is zero in an adiabatic process.

The high electric potential gradient in the double layers provides the forces necessary to concentrate ions. They can then be converted in electrochemical reactions at the working electrode. In addition, ions may be electrosorbed onto electrodes with large surfaces (see Fig. 2.4 (b)). The application of high surface electrodes to the removal of salt from water will be the topic of the next section.

2.3.4. Capacitive Deionisation

In order to remove a concentration of solvated ions from water, the concentration term in the internal chemical potential has to be overcome (see Section 2.1). The most primitive way to separate salt from water is by evaporation, which removes all of the H_2O molecules via a thermally induced phase change and is energy-intensive at a cost of $40.65\,\mathrm{kJ\,mol^{-1}}$. Beginning in the 1950s, the method of reverse osmosis has revolutionised water purification with great success [323]. However, this method also has its limitations among which geographical limitations and a non-negligible energy consumption stand out [324]. Electric fields provide a more efficient way to capture ions from saline water [325,326]. One method that uses the electrical double layer to immobilise a large concentration of ions is capacitive deionisation. It is based on porous carbon electrodes that combine high electrical conductivity and enormous surface areas [321,326]. Pores are classified according to their size: pores over 50 nm are called macropores, between 2–50 nm mesopores and below 2 nm micropores [327]. An electrical double layer in these pores is formed upon charging and the ions are pulled from the solution (see Fig. 2.4). This double layer covers a wide area and the mass transport of the ions from bulk solution into the pores is by no means instantaneous, relying heavily on diffusion.

A sketch of the basic capacitive deionisation process is shown in Fig. 2.5. The capacitive deionisation cell consists of two porous carbon electrodes that are attached to metallic current collectors and connected to a power source. Saline water is let into the cell, wetting the electrodes and filling the pores with liquid. Then a voltage is applied to the porous carbon electrodes and the ions are separated by travelling into the double layer that form in the porous structure. The desalinated water can be withdrawn from the cell and stored. Once the charging current has decayed and the electrode surface is completely covered by ions, the discharge process starts. The voltage is switched off or lowered and the ions are released back into the solution. This water of high salinity is then removed and the process is repeated until a satisfactory purification has been achieved. The arrangement of the porous carbon electrodes resembles a supercapacitor, which means that a portion of the electric energy input during the charging process is reclaimed during the discharge process.

The process is rarely performed statically. Instead, the water flows either along the electrode surface or through the porous electrodes themselves for maximum contact with the charge surface. Capacitive deionisation also works with wire-like electrodes that are alternately dipped into the vessel containing the water to be purified during the charging phase and that containing the brine during the discharge phase [328].

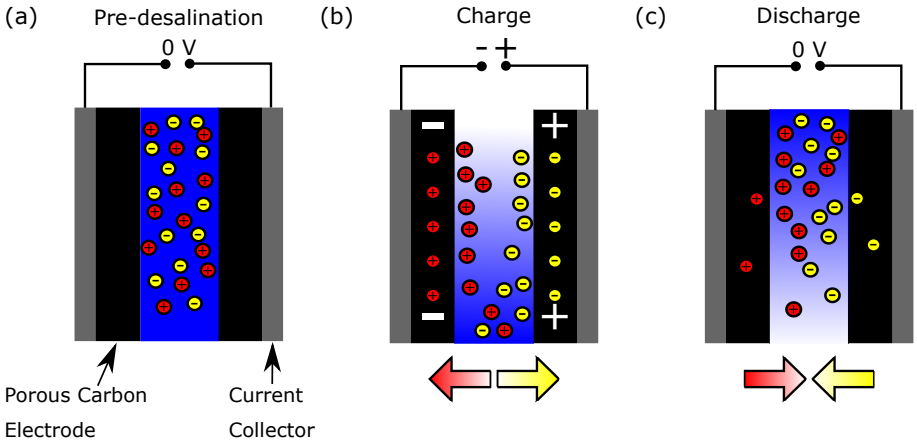

Figure 2.5 – Scheme of a capacitive deionisation process. The porous carbon electrode for the electrosorption are connected to a power source via a current collector. (a) The capacitive deionisation cell is filled with water containing ions. (b) A voltage between the electrodes is applied and the ions are electrosorbed by the porous carbon matrix (see Fig. 2.4). The lower salinity water is then withdrawn from the cell. (c) After the maximum capacity for ions in the pores is reached, the voltage is switched off. The ions are released into the solution from the double layer of the porous carbon. This high salinity solution can then be siphoned off and the cycle begins anew.

For capacitive deionisation, carbon materials with mesoporous and microporous structures are ideally suited. The progress in the field of conductive high porosity materials for applications as electrodes in supercapacitors has ignited great interest in their possible application as desalinating electrodes [324]. Examples for useful carbon materials are activated carbon cloths (microporous), ordered mesoporous carbons, carbide-derived carbon (microporous), carbon nanotubes, carbon black and carbon aerogels (see Fig. 2.4 (b)) [321, 329]. They have high porosity and surface areas up to $3000\,\mathrm{m^2\,g^{-1}}$. Only a few grams of these materials have the surface area of a football field. However, there is no direct relationship between the pore size distribution/surface area and the capacitive deionisation ability. Micropores provide a very high surface area, but they also lead to overlapping of the electric double layer due to their small size. The associated electrostatic repulsion will reduce the actual desalination effect.

When desalinating highly concentrated salt water, a commonly faced issue is the entering of ions with higher mobility into the pores of the electrode containing the opposite charge. Here they combine in an electrostatically favourable manner and block the pores. In some cases, the formation of these pairs is avoidable by applying a potential step of opposing sign during the discharge step and rapidly expelling most of the ions from the carbon matrix. The potential step of the charging phase can also simply be lowered during the discharge phase, avoiding the absence of the applied voltage. However, in most cases there is a significant drop of desalination efficiency after only a relatively small number of cycles in all but the most low concentrated brine solutions. Completely regenerating these electrodes is near to impossible.

In order to avoid the debilitating co-ion adsorption in the porous matrix of the electrodes, ion exchange membranes can be introduced [321, 330]. Cation and anion membranes are placed in front of the respective porous electrodes before exposure to the aqueous solution. These block co-ions from entering the porous structure to neutralise the adsorbed counterions. Thus,

the lifetime of the porous carbon electrodes is increased. Another limiting factor for the speed at which capacitive deionisation can take place is that the electrolysis of water dominates at voltages above 1.2 V with a virulent evolution of gas bubbles. A new development has seen the employment of Faradaic electrodes in capacitive deionisation cells that avoid the issues encountered with the electrosorption in the double layer of porous carbon [324, 331–336].

Many models for the electrosorption of ions during capacitive deionisation have been developed [321,337,338] and the precise ion dynamics during the process is still under ongoing investigation. Parasitic Faradaic reactions in the porous electrodes also take place under applied voltages [321, 339, 340].

An interesting development in the area of capacitive deionisation is the observation of salt shocks during flow in microchannels [341–343]. This shock desalination has also been demonstrated in shock electrodialysis [344].

Capacitive deionisation cells can be tuned to favour the removal of a specific ion species [345–349]. The mechanism by which this can be achieved is still under active investigation. It is becoming clear that the charge, ionic radii, hydration ratios and mobilities of the ions have a profound effect on their behaviour inside porous electrodes.

2.4. Aquatic Chemistry of the Rare Earths

The rare earth elements comprise the lanthanides in the f-block of the periodic table, as well as yttrium (Y) and scandium[30] (Sc) which are chemically similar. Perplexingly, their name does not refer to their abundance, but their near to indistinguishable chemical properties, which pose great challenges in their purification. A rule of thumb is that the rare earths only differ markedly in properties which concern their 4f electrons, such as their magnetic moments.

As the rare earths occur together in ores, their separation is an arduous and lengthy process. The main commercially mined rare earth bearing minerals is bastnäsite [351]. Monazite, laterite clays and loparite are more seldomly mined. There are plans to start mining xenotime [352]. A breakdown of the rare earth contents of exemplary bastnäsite, monazite and xenotime are listed in Table 1. The compositions of these ores are dominated by La, Ce and Y. In addition, monazite has a high Nd content. Bastnäsite and monazite are rich in light rare earths. Xenotime has a higher concentration of heavy rare earths and Y, with its similar ionic radius. The same is true for laterite clays, but their composition is more variable. At present, the bulk of commercially available rare earths emanates from mines in China, although there have been significant efforts to diversify the supply chain [153].

An overview of the electronic structure, ionic radii and other information is given in Table 2. The aqueous chemistry of the individual rare earth ions is almost indistinguishable. In aqueous solutions, the rare earth ions are trivalent under normal conditions. The only rare earth ions to have a stable divalent state are Sm, Eu and Yb. Of these, only Eu^{2+} is stable in aqueous solution [353, 354]. The separation of these by a chemical or electrochemical reduction to their

[30] Scandium has similar properties and is at times also referred to as a rare earth element. Unlike Y, the ionic radius of Sc is smaller $r_{\text{ion}} = 89\,\text{pm}$ [350] and lies outside of the range of the rare earths. Its geochemistry is different.

divalent state is comparatively uncomplicated. A tetravalent state is only viable for Ce, which can rid itself of its final 4f electron, emptying the f-orbital. For the remaining rare earth elements, the situation is more tricky.

Ore	Y	La	Ce	Pr	Nd	Sm	Eu	Gd	Tb	Dy	Ho	Er	Tm	Yb	Lu
Bastnäsite	0.1	32.2	49.2	4.3	12	0.8	0.1	0.16	0.02	0.03	0.005	0.004	0.0009	0.0006	0.0001
Monazite	2	23	46.5	5.1	18.4	2.3	0.07	1.7	0.16	0.52	0.09	0.13	0.013	0.061	0.006
Xenotime	64.9	1.3	3.2	0.5	1.6	1.2	0.01	3.5	0.9	8.4	2.0	6.5	1.1	6.9	1.0

Table 1 – Rare earth oxide content of main rare earth containing ores (wt%). Bastnäsite and monazite are commercially mined. Origins of the tabulated ores are: bastnäsite (Mountain Pass, USA), monazite (Mount Weld, Australia) and xenotime (Malaysia). From [351, 355].

The reason for the identical properties of the trivalent ions can be found by studying the ionisation and formation enthalpies of the rare earths. Their enthalpies of atomisation and ionisation are plotted in Fig. 2.6. It is necessary to consult the valence electrons in Table 2 to interpret the ionisation enthalpies. The lanthanides shed their 6s electrons first, which leads to a slight increase of enthalpy with atomic number due to changing attractive forces from the nucleus. A different picture is presented when the third electron is ionised off. This is a 4f electron for all rare earths except Y, La and Gd. Strong exchange effects come into play with the electrons in the f-shell and the ionisation energy for trivalent ions I_3 increases until Gd, which has a half filled 4f subshell and instead loses a 5d electron. This is known as the gadolinium break[31] and makes Gd stand out among the rest of the rare earths in a delicate fashion [372]. Beyond Gd, the rise of I_3 is non-uniform due to spin-orbit coupling [373]. The enthalpy of atomisation ΔH^0_{at} also behaves irregularly across the series.

Sums of the atomisation and ionisation enthalpies define the enthalpies of formation of the rare earth ions $\Delta H^0_f(RE^{n+}) = \Delta H^0_{at} + \sum_i^n I_i$ (see Fig. 2.7). Monovalent RE^+ and divalent RE^{2+} rare earth ion formation enthalpies follow the irregular trend of the enthalpy of atomisation. In contrast, the trivalent rare earth ions have an almost constant enthalpy of formation. The variations in the enthalpy of atomisation ΔH^0_{at} and ionisation I_3 happen to exactly cancel when they are summed. This is the reason why rare earth ions are hard to distinguish based on their electrode potentials $E^0 = -2.3 \pm 0.1\,V$ (see Table 2) [372]. The divalent rare earth ions Sm^{2+}, Eu^{2+} and Yb^{2+} can also be identified by inspection of Fig. 2.7. They owe their existence to the fact that they lie in the dips of $\Delta H^0_f(RE^{2+})$ before the cusps of Gd^{2+} and Lu^{2+}.

[31] The Gd break is a controversial subject. It was first proposed by Frank Spedding after observing an increase of partial molar volume [184], heat capacity [360], molar entropy [360] and viscosity [361] for Sm, Eu and Gd. The values of these properties decreased with the ionic radius throughout the lanthanide series except for these three elements. The interpretation of these data was an abrupt lowering of the coordination number of hydrated RE^{3+} from 9 to 8 in the middle of the series with Gd. Initially, this found wide acceptance in the community [362, 363]. Cracks appeared in the Gd break hypothesis after x-ray diffraction measurements of concentrated lanthanide chloride solutions by Anton Habenschuss (1944–2015) and Spedding at Ames laboratory suggested a gradual lowering of the $RE^{3+}-H_2O$ distances around Gd^{3+} [364–366]. In the new millennium, x-ray absorption spectroscopy measurements with synchrotron radiation cast further doubt on the existence of the Gd break in the coordination numbers by showing that the $RE^{3+}-H_2O$ distances decrease smoothly along the series [367–371].

Electron Configuration			Radius (pm)		Colour	E^0 (V)	Applications	Origin of name
RE	RE	RE^{3+}	RE	RE^{3+}	RE^{3+}	RE^{3+}/RE		
Y	$5s^2 4d^1$	$5s^0 4d^0$	180	104	-	−2.37	Capacitors, metal alloys, lasers, sensors, superconductors	Ytterby, Sweden
La	$6s^2 5d^1$	$6s^0 5d^0$	183	117	-	−2.38	Ceramics, batteries, car catalysts, phosphors, pigments, X-ray	Greek lanthanein: to escape notice
Ce	$6s^2 5d^0 4f^2$	$6s^0 5d^0 4f^1$	182	115	-	−2.34	Catalysts, polishing, metal alloys, UV filters	Asteroid Ceres discovered in 1801
Pr	$6s^2 5d^0 4f^3$	$6s^0 5d^0 4f^2$	182	113	Green	−2.35	Pigments, lightning, lenses, glasses	Greek praseos + didymos: green twin
Nd	$6s^2 5d^0 4f^4$	$6s^0 5d^0 4f^3$	181	112	Lilac	−2.32	Permanent magnets, lasers, catalysts, infrared filters	Greek neos+didymos: new twin
Pm	$6s^2 5d^0 4f^5$	$6s^0 5d^0 4f^4$	181	111	Pink	−2.29	☢Beta radiation source, fluid-fracking catalysts, phosphors	Prometheus stole fire from heaven
Sm	$6s^2 5d^0 4f^6$	$6s^0 5d^0 4f^5$	180	110	Yellow	−2.30	High-temperature magnets; nuclear reactor control rods	Mineral samarskite
Eu	$6s^2 5d^0 4f^7$	$6s^0 5d^0 4f^6$	208	109	Pale Pink	−1.99	Liquid crystal displays, fluorescent lighting, glass additives, phosphors	Europe
Gd	$6s^2 5d^1 4f^7$	$6s^0 5d^0 4f^7$	180	108	-	−2.28	Magnetic resonance imaging contrast agent, glass additives	Chemist Gadolin
Tb	$6s^2 5d^0 4f^9$	$6s^0 5d^0 4f^8$	177	106	Pale Pink	−2.31	Phosphors, electronic	Ytterby, Sweden
Dy	$6s^2 5d^0 4f^{10}$	$6s^0 5d^0 4f^9$	178	105	Yellow	−2.29	High-power magnets, lasers, guidance systems	Greek dysprositos: hard to get
Ho	$6s^2 5d^0 4f^{11}$	$6s^0 5d^0 4f^{10}$	176	104	Yellow	−2.33	High-power magnets, nuclear industry	Latin Stockholm: Holmia
Er	$6s^2 5d^0 4f^{12}$	$6s^0 5d^0 4f^{11}$	176	103	Rose	−2.32	Lasers, glass colourant, optical fibers, ceramics	Ytterby, Sweden
Tm	$6s^2 5d^0 4f^{13}$	$6s^0 5d^0 4f^{12}$	176	102	Green	−2.32	High-power magnets	Latin Thule: northern land
Yb	$6s^2 5d^0 4f^{14}$	$6s^0 5d^0 4f^{13}$	193	101	-	−2.22	Fiber-optic technology, solar panels, alloys, lasers, source in portable X-ray units	Ytterby, Sweden
Lu	$6s^2 5d^1 4f^{14}$	$6s^0 5d^0 4f^{14}$	174	100	-	−2.30	X-ray phosphors, single crystal scintillators	Latin Lutetia: Paris

Table 2 – Properties of the rare earth ions. Adapted from [350,356–359]. Gd retains one 5d electron to keep its 4f subshell half filled.

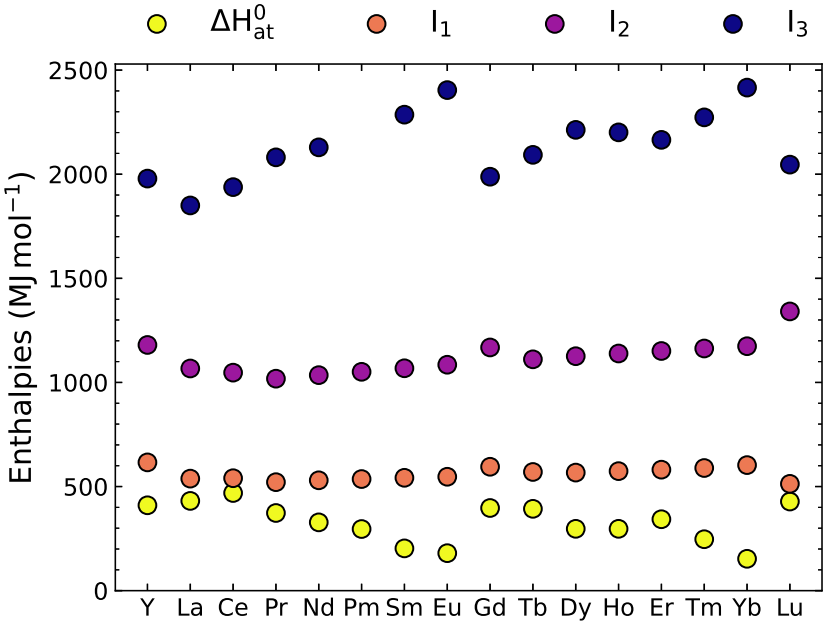

Figure 2.6 – **Enthalpies of atomisation ΔH^0_{at} and ionisation I_n for rare earths.** The data stem from an ionic crystal model and the Born-Haber cycle [373, 374]. The Gd break causes the collapse of the rising I_3 values [372, 375].

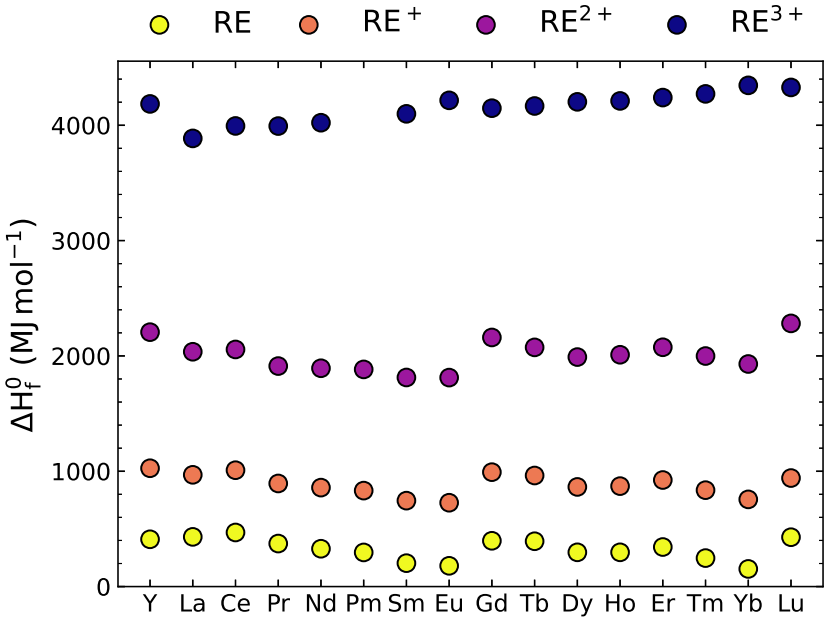

Figure 2.7 – **Enthalpies of formation of gaseous rare earth atoms and ions $\Delta H^0_f(RE^{n+})$.** The data are calculated from Fig. 2.6 with $\Delta H^0_f(RE^{n+}) = \Delta H^0_{at} + \sum_i^n I_i$. The near constant value of $\Delta H^0_f(RE^{3+})$ is due to the oppositely changing values of ΔH^0_{at} and I_3 (see Fig. 2.6).

Another feature of the rare earth ions is the lanthanide contraction of the ionic radii (see Table 2 and Fig. 2.8). The ionic radii of the lanthanides decrease during the successive filling of the f-orbits due to imperfect shielding of the valence electrons from the nuclear charge [356]. The

evolution of their ionic radii is shown in Fig. 2.8 for a coordination number of eight. Despite the lanthanide contraction, the ionic radii are within 17 pm of each other and the resulting differences are only faintly noticeable. Nonetheless, these are critical for the chemical behaviour of the rare earths [376].

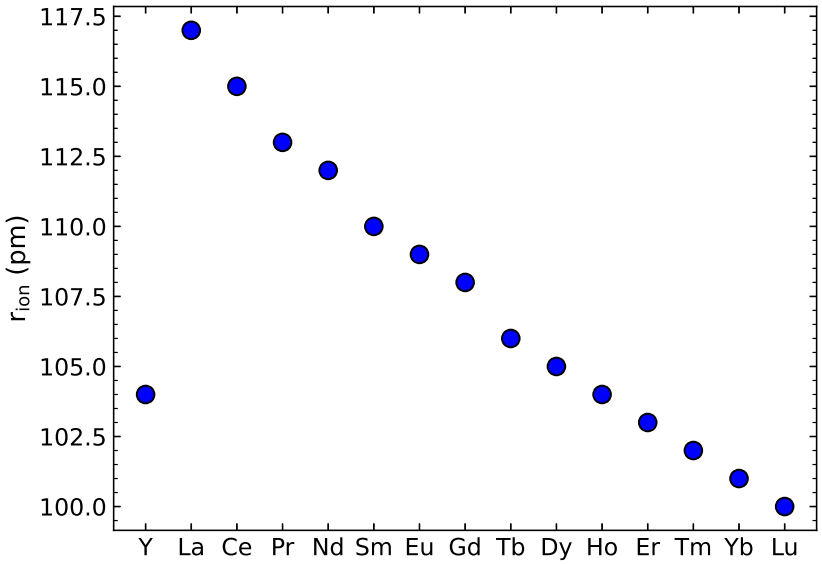

Figure 2.8 – Ionic radii r_{ion} of trivalent rare earth ions with coordination number eight [350]. Lanthanide contraction reduces r_{ion} by 17 pm along the series. This is the reason why Y^{3+} has the same r_{ion} as Ho^{3+}. The gadolinium break is also noticeable as a higher r_{ion} value.

The most accessible information of the aqueous chemistry of ions is contained in Pourbaix diagrams, which are also known as E-pH diagrams [350, 377]. An exemplary Pourbaix diagram of Gd is shown in Fig. 2.9 and an overview diagram of all the rare earths (except radioactive Pm) is shown in Fig. 2.10. The horizontal axis shows the pH value of the solution containing the rare earths. On the vertical axis, the potential value of reduction half-reactions are shown with respect to the standard hydrogen electrode. The Pourbaix diagram of Gd (see Fig. 2.9) is indicative of the behaviour of the trivalent rare earth ions and bears resemblance to an inverted letter T. The rare earth elements are reactive and their sesquioxides are their most stable form[32] [356]. At normal conditions, all the rare earths transform into trivalent cations RE^{3+}. Solid Gd is only stable at applied voltages below -2 V, with the boundary given by the bottom horizontal lines. The low reduction potentials of the rare earths are tabulated in Table 2 and was first reported by Walter Noddack in 1937[33] [379]. The similarities of the rare earth reduction potentials, as can be seen in the lines above $RE_{(s)}$ in Fig. 2.10, are striking and due to the aforementioned subtle balancing of the enthalpies. The electrochemistry of the rare earths

[32] Except Ce, which forms CeO_2 in its tetravalent form.
[33] The first electrolysis of rare earth chloride solution was reported by Gerhart Krüss (1859–1895) as early as 1893 [378].

is largely the same, with the exception of those with divalent (Sm, Eu and Yb) and tetravalent (Ce) states. These are shown with broken lines in Fig. 2.10 and evidently differ from the inverted T-like diagram of the other rare earths.

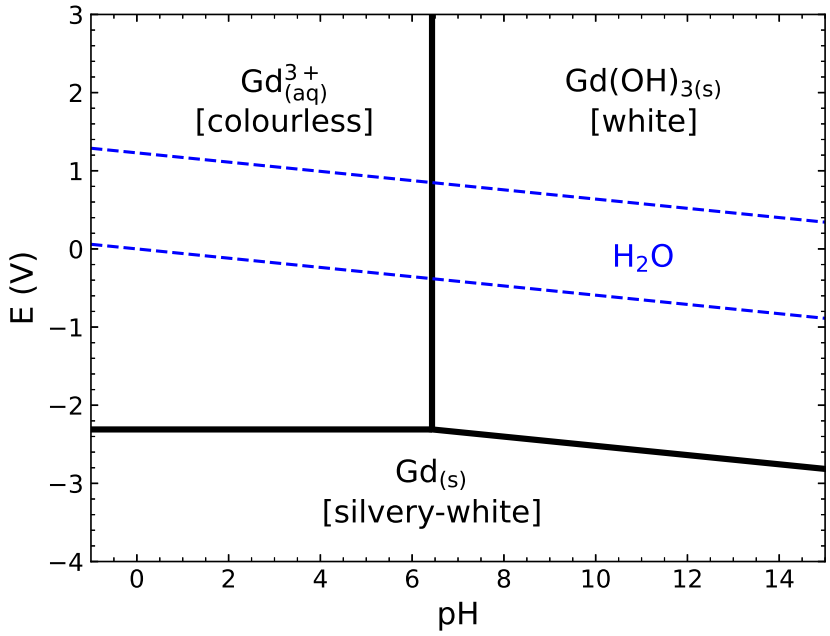

Figure 2.9 – Pourbaix diagram of Gd at c = 0.1 M [350]. The broken blue lines frame the stability region of water. In aqueous solution, Gd is present as Gd^{3+} under acidic and insoluble $Gd(OH)_3$ under basic conditions.

In basic solutions, the rare earths precipitate as hydroxides $RE(OH)_3$, which are insoluble in water. This can be seen on the right hand side of the Gd Pourbaix diagram Fig. 2.9 and in the overview Fig. 2.10. The hydroxides dissolve in slightly acidic solutions. The boundary between $RE(OH)_3$ dissolution and precipitation is seen as a vertical line. These lines lie in the range of approximately 5.5–7.5 for the pH values. The boundary is sensitive to changes in the basicity of the RE^{3+}, which are in turn proportional to their ionic radii [380–382]. Basicity is the tendency to lose electrons or avoid attracting them in the cationic state. The lanthanide contraction rears its head in a noticeable way here. This is particularly obvious when considering Y^{3+}, which fits into the series next to Ho^{3+} with the same r_{ion}.

The change in basicity is pivotal for rare earth separation techniques. The separation by hydroxide precipitation based on differing basicity was explored in the the early 20th century prior to the development of separation based on ion exchange [383–399]. Recently, interest in the hydrometallurgical separation relying on selective hydroxide precipitation by variation in the pH has been revived [400]. But the dominant rare earth separation techniques in use these days are ion exchange and solvent (also known as liquid-liquid) extraction [84, 350].

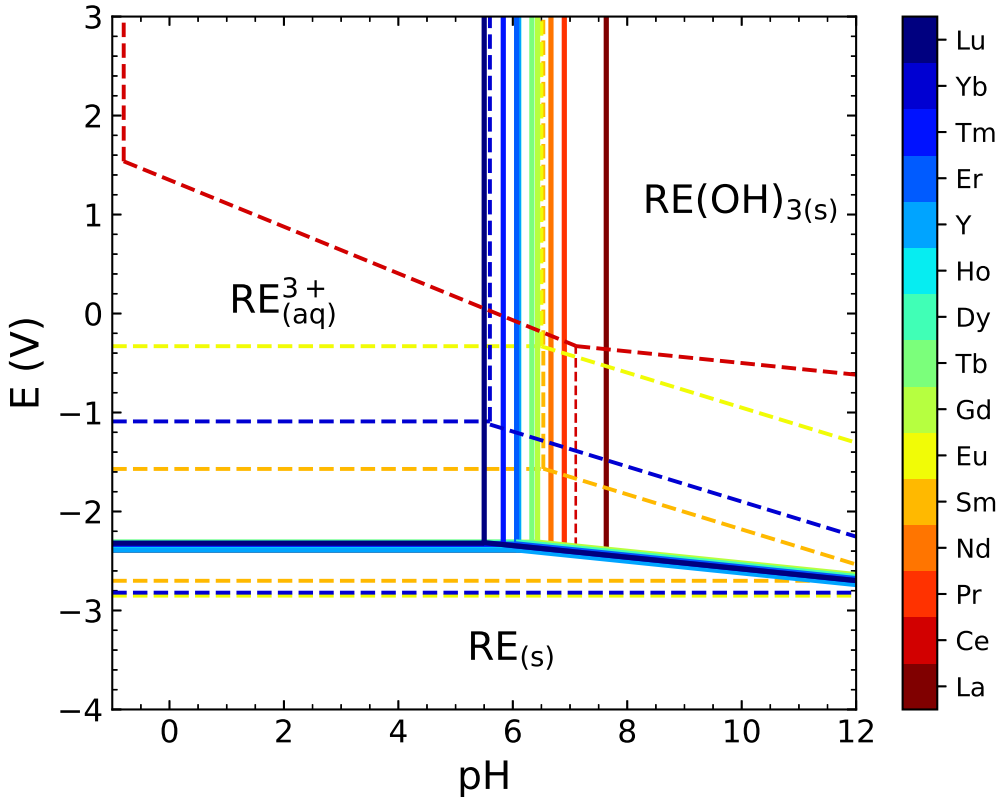

Figure 2.10 – Pourbaix diagram of the rare earths at c = 0.1 M [350]. The broken lines show the RE with divalent (Sm, Eu and Yb) and tetravalent (Ce) states. The basicity of the RE decreases along the series with the ionic radius (see Fig. 2.8). Radioactive Pm has been omitted.

The refinement and separation process from the mined rare earth ores are shown in Fig. 2.11. The separation by ion exchange was developed during the Manhattan project at Ames Laboratory in Iowa under the direction of Frank Spedding (1902–1984) to purify lanthanides for experimental work on nuclear physics [401–408]. In the ion exchange process, the RE^{3+} solution are pressed through an ion exchanger resin, which consists of a column of small spheres (0.1 mm). Here three protons are set free and the cation is retained by the resin. The affinity of the RE^{3+} for the resin depends on the ionic radius and those with smaller radii cling to it the strongest. The ionic radius varies too little between the individual RE^{3+} and a complexing agent is necessary to form RE^{3+} complexes with varying ease. These are then removed from the resin at staggered times. Although this is a time consuming process, the purity of the resulting rare earth solution is practically unrivalled at above 99.99999%.

The separation by solvent extraction was perfected in the 1950s [409] and is the workhorse of all rare earth refinement plants. It is based on different activity coefficients of the rare earths in two immiscible liquids [172]. One of the liquids is usually aqueous, while the other is an organic solvent. The aqueous solution contains rare earths. Both liquids are mixed and a portion of the rare earths are transferred to the organic liquid via diffusion and mainly convection. Differences in the solubilities in the two phases lead to the separation of the rare earths. The extract is

then siphoned off with the organic phase and the aqueous phase is enriched in other rare earths. This cycle is repeated often and counter current operation optimises the available concentration gradient driving the diffusive process between the two phases. Purities of 95–99.5% can be achieved, for higher purity rare earths the ion exchange method is called for.

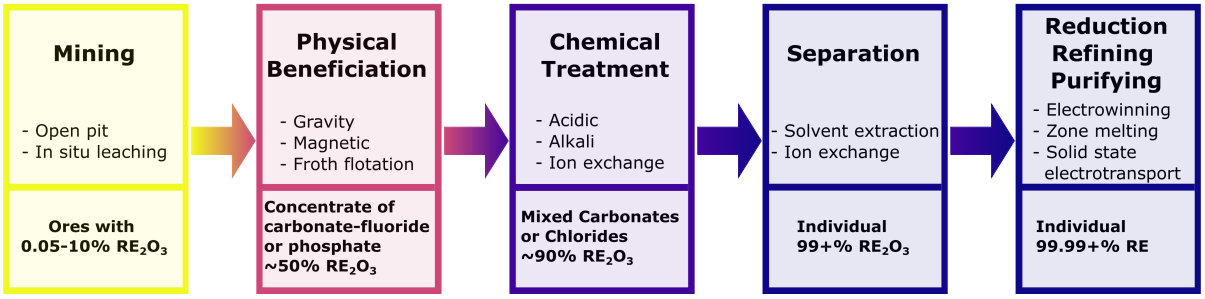

Figure 2.11 – Rare earths: From mined ore to purified element (adapted from [83]).

2.4.1. Magnetic Properties

The current rare earth separation techniques rely on slight changes in properties influenced by the ionic radii, which are changed by the successive filling of the f-orbital. Indisputably, there will be distinct differences between features that are influenced by the number of 4f electrons. The prime example for such a property is the magnetic moment of the rare earth ions, which is directly related to the 4f electrons. Their magnetic moment endows a number of rare earth ions with paramagnetic susceptibilities, which are listed in Table 3. The relationship between electronic structure, magnetic moment and susceptibility is explained in many introductory texts [410,411]. A good estimate of the magnetic moments of the rare earth ions can be obtained empirically from the electronic configuration predicted by Hund's rules [412]. Exact theoretical determination require calculations with Van Vleck's formalism for paramagnetism [413, 414]. Molar Curie law susceptibilities are calculable with this formula:

$$\chi_m = \frac{\mu_0 N_A g_J^2 \mu_B^2 J(J+1)}{3 k_\mathrm{B} T}. \tag{2.50}$$

The constants are the Landé g-factor g_J (dimensionless) [415], the total angular momentum quantum number J and the Avogadro constant $N_A = 6.022 \times 10^{23}\,\mathrm{mol}^{-1}$. An effective magnetic moment $\mu_\mathrm{eff} = g\mu_B\sqrt{J(J+1)}$, also known as paramagnetic moment, can be introduced to shorten the expression:

$$\chi_m = \frac{1.571 \times 10^{-6} \mu_\mathrm{eff}}{T}. \tag{2.51}$$

The molar susceptibilities of the rare earth ions are listed in Table 3 and depicted in Fig. 2.12. In Fig. 2.12, the molar susceptibility χ_m has two peaks: one among the light rare earths around Pr-Nd and one among the heavy rare earths close to Dy-Ho. The magnetic moments of the heavy rare earths, starting with Gd and its half filled f-orbital, is higher than that of the light rare earths. All the rare earth ions without 4f electrons (Y^{3+}, La^{3+} and Lu^{3+}) have no

unpaired electrons in their orbitals (see Table 2). They are diamagnetic, but the magnitude of their magnetic susceptibility is negligible compared to that of water (see Table 3). The fact that nearly all paramagnetic salts are coloured, whereas diamagnetic salts are colourless, is an indicator of the central role played by unpaired electrons [416, 417].

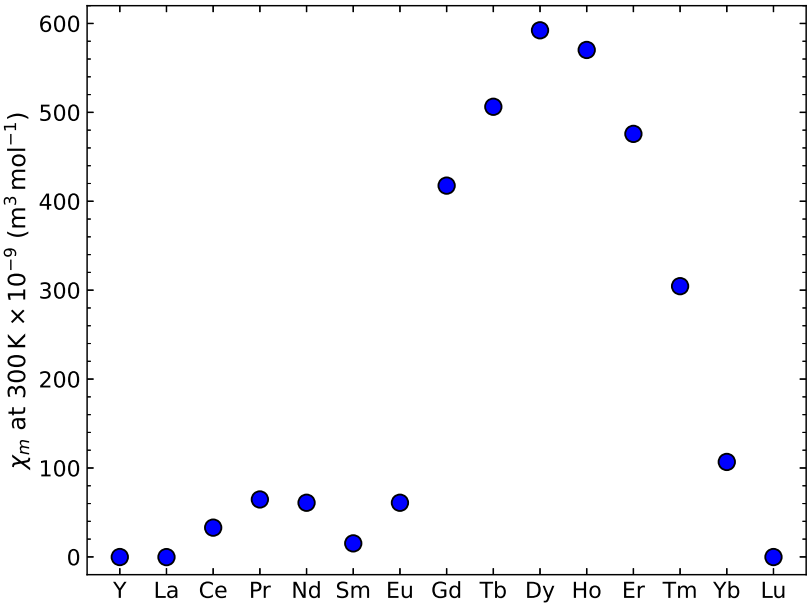

Figure 2.12 – Molar magnetic susceptibilities of the trivalent rare earth ions at 300 K [418]. The respective values are listed in Table 3. Only Y^{3+}, La^{3+} and Lu^{3+} are diamagnetic.

When a rare earth salt is dissolved in water, the susceptibility becomes a sum of multiple components [191, 419, 420]. The magnetic susceptibility of the salt solution is given by the sum of the diamagnetic volume susceptibility of liquid water $\chi_{H_2O} = -9\times10^{-6}$ ($-1.62\times10^{-10}\,m^3\,mol^{-1}$) [421, 422] and the molar susceptibility χ_m of the ion species of concentration c (in $mol\,m^{-3}$):

$$\chi = \chi_{H_2O} + \chi_m c. \tag{2.52}$$

The diamagnetic ions hardly contribute to the total susceptibility of the solution. Susceptibilities of 1 M solutions containing rare earth ions are also listed in Table 3. The magnetisation data of aqueous $Gd(NO_3)_3$ solutions shown in Section 2.1 (see Fig. 2.1) behaves according to the Curie law. Highly concentrated paramagnetic rare earth solutions can show volume susceptibilities up to $\chi = 10^{-3}$. These are moderate values compared to regular ferrofluids with $\chi \approx 1$, but enough for the Kelvin force to compete with gravity (see Section 2.2.2).

The first measurement of the magnetic susceptibility in aqueous rare earth ionic solutions was reported in 1926 by Decker [423]. Later measurements of the magnetic properties of rare earth salts both in solution [424] and in crystalline form [425–427] were carried out by Selwood[34]. The magnetic susceptibility of the solutions was measured with a modification

[34] Review articles from these times by Pearse and Selwood [357, 428] make for didactic reading and provide insight into early rare earth research.

of Quincke's capillary rise method [429]. These magnetic characterisation were accompanied by measurements of the absorption spectra which also differs with varying occupation of the f-orbitals [430–432] and were used to identify different rare earths. This motivated Selwood and Hopkins to explore a magnetic separation of the rare earths [89].

Ion	g_J	μ (μ_B)	$\mu_{\text{eff}}^{\text{exp}}$ (μ_B)	$\chi_m^{\text{exp}} \times 10^{-9}$ ($\text{m}^3\,\text{mol}^{-1}$)	$\chi_{1\text{M}}^{\text{exp}} \times 10^{-6}$
Y^{3+}	0	0	0	-0.16	-9.16
La^{3+}	0	0	0	-0.25	-9.25
Ce^{3+}	6/2	2.14	2.54	32.9	23.6
Pr^{3+}	4/5	3.2	3.58	64.6	55.5
Nd^{3+}	8/11	3.27	3.52	60.9	51.9
Sm^{3+}	2/7	0.71	0.85	15.2	6.2
Eu^{3+}	0	0	0	60.9	51.9
Gd^{3+}	2	7	7.94	417.6	408.5
Tb^{3+}	3/2	9	9.72	506.3	497.3
Dy^{3+}	4/3	10	10.65	592.3	583.3
Ho^{3+}	5/4	10	10.61	570.2	561.1
Er^{3+}	6/5	9	9.58	475.8	466.7
Tm^{3+}	7/6	7	7.56	304.5	295.4
Yb^{3+}	8/7	4	4.53	106.8	97.7
Lu^{3+}	0	0	0	-0.18	-9.18

Table 3 – Magnetic properties of the rare earth ions. Adapted from [410,418]. The Landé g-factor g_J, magnetic moment $\mu = g_J \mu_B J$, the effective paramagnetic moment $\mu_{\text{eff}} = g_J \mu_B \sqrt{J(J+1)}$ and the molar susceptibilities χ_m^{exp} are listed, J being the total angular momentum quantum number. The volume susceptibilities of 1 M solutions $\chi_{1\text{M}}^{\text{exp}}$ are also shown.

As was mentioned in the introduction to this thesis (Section 1), the idea of using the great variations in the magnetic moments to separate the rare earths is not new. Magnetic field gradients already find application in the physical benefication of the rare earth minerals due to modification of buoyancy forces (see Fig. 2.11). However, an actual separation of the individual rare earths with the help of magnetic fields would be of great interest. The rare earth ores are predominately made up of non- or only weakly magnetic La, Ce and Y (see Table 1). An addition of a magnetic field gradient in the separation step in the elemental extraction from the purified ores may be beneficial for the efficiency of the process. Due to the growing importance of xenotime ore, a more efficient separation of Y is of particular interest.

A purely magnetic separation of rare earth ions is illusory, as previously discussed. Many experimental works underpin this [89,161,162,164–166,433]. There are in effect only two reports of a genuine separation of rare earth ions with the involvement of a magnetic field gradient.

One is the flow-through approach of Ida and Walter Noddack in the 1950s [135–137] (see Section 1). Here, rare earth solution streamed into and out of a magnetic field gradient. In

their earliest publication, this showed a moderate effect even without an external energy input [135]. From theoretical considerations (see Sections 2.2.2 and 2.2.3) it is difficult to see how a separation by simply flowing a multicomponent salt solution through magnetic field gradients can function. Recent experiment on paramagnetic ion enrichment in a channel with laminar flow and a magnetic field gradient are inconclusive. One study reported the magnetic concentration of Fe^{2+} ions [159] and another reported negative results for Ho^{3+} [433]. The later publications by the Noddacks report a more sophisticated setup in which a thermal convection induced counter flow was employed [136, 137]. Higher separation factors were achieved with this new approach. The heating with a Pt wire in the centre of the container holding the liquid (description in Section 1) is analogous to a Clusius-Dickel[35] setup for separation [138–147]. Thermodiffusion will undoubtedly play the central role in such a situation, in what is known as the Soret effect [435, 436]. This is known to separate individual ions in seawater [437]. The Clusius-Dickel method is also known as thermogravitational separation[36]. As was discussed in Section 2.2.3, magnetoconvection can augment liquid flows when there are inhomogeneities and this is how the magnetic field gradient will have acted. It is conceivable that the rare earth ions have palpable differences in their thermal diffusivities to allow such a separation. Another point for discussion is that there are little details about the composition and pH of the analysed solutions in these publications. This can have a strong effect on the aquatic chemistry (see Fig. 2.10). A PhD student of Walter Noddack studied the effect of the magnetic field gradient on the ion exchange process [149], discovering only tentative effects that were never published.

The other report on magnetically aided rare earth separation is a recent experimental study by Higgins et al. [438] titled "Magnetic Field Directed Rare-Earth Separations". The authors studied the effect of the stray field of a small Nd-Fe-B cube on the thermal gradient crystallisation from a solution of ligated rare earth complexes. They report a separation of heavy paramagnetic rare earths from the light rare earths due to solubility differences. Although a separation already took place without the magnetic field, a magnetic field reportedly led to a higher separation factor. The best results were achieved for mixtures of paramagnetic Dy^{3+} and diamagnetic La^{3+}. Previous experiments on the crystallisation process in magnetic field gradients may be useful for the interpretation of these results [13–16].

The atomic nuclei of rare earths have vastly different interactions with neutrons. Neutron activation analysis is a routinely performed technique for study of rare earth compounds [439]. Interactions of neutrons with the nuclei can be exploited in the method of neutron imaging, which will be discussed below.

[35] Klaus Clusius (1903–1963) and Gerhard Dickel (1913–2017) reported the separation of gaseous chlorine isotopes with their method in 1939 [139]. Shortly afterwards, the technique was applied to heavy water separation [434] and more critically isotope separation of uranium hexafluoride. This research was carried out under the German nuclear research programme during the second world war, which became known as the "Uranprojekt". Ultimately, large scale uranium isotope separation was never achieved with this project.

[36] The Clusius-Dickel method was used in the early days of the Manhattan project for uranium isotope separation. The ^{235}U content of natural uranium hexafluoride was enriched from 0.715% to 0.86%. The low efficiency and high heating cost of the 2100 separation columns led to its replacement by gaseous diffusion [145]. Research in the method was largely restricted to the Eastern Bloc before 1989 [146].

2.5. Neutron Imaging

Neutron imaging relies on the neutron attenuation properties of the sample to provide contrast of an image. A basic sketch of a neutron imaging setup is shown in Fig. 2.13. A beam of neutrons exits a beam guide and hits a sample. The transmitted neutrons hit a scintillator screen and are converted to light. They pass behind the scintillator onto a mirror from which they are reflected into a camera which records the images. With these the changes in contrast can be used to map the attenuation properties and gain information about the composition of the sample. It is a non-destructive technique as the neutrons only interact with the nuclei of the sample, although care must be taken due to the possibility of induced radioactivity. These interactions with the nuclei give the method different sensitivities compared to other attenuation methods such as those relying on x-rays, which interact with the electrons of the atom. The interactions of the nuclei of all elements is tabulated in the form of absorption and scattering cross sections [440]. A downside of the method is that the high neutron fluxes necessary to obtain useful images restrict the use of the method to a limited number of high-flux neutron sources [441].

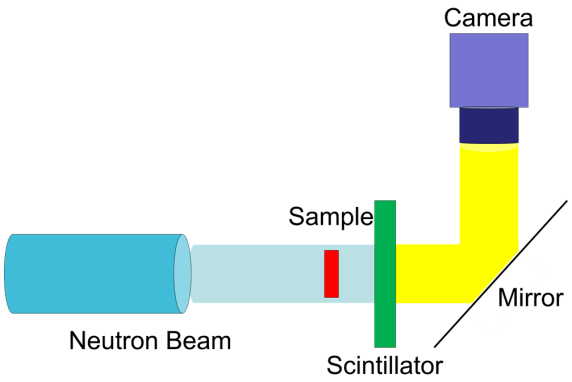

Figure 2.13 – Basic sketch of a neutron imaging setup.

To discover the roots of neutron imaging, one must hark back to 1930s Germany [442]. Neutron imaging was developed in 1930s Berlin[37], only a few years after the discovery of the neutron by Chadwick in 1932 [447]. From the 1950s, neutron sources at nuclear reactors made neutron imaging a viable method for quantitatively analysing sample compositions. Time sequenced neutron images were first obtained with improved counting rate in the 1970s and made the capturing of dynamic processes possible in what became known as dynamic neutron imaging[38].

Nowadays, the boom in the field of electronic imaging has proved to be fruitful for the neutron imaging community. The availability of CCD cameras to capture the scintillator light with ever smaller and denser pixels has enabled both higher resolutions and shorter exposure times. The development of new scintillator materials has also further pushed these boundaries. Current

[37] A patent that was granted in 1940 [443] and the first scientific publication dates back to 1946 [444]. One of the patent holders was Hartmut Kallmann (1896–1978), who authored the first calculations of the deflection of polar molecules by inhomogeneous fields [197]. This laid the groundwork for the Stern-Gerlach experiment [104,105]. Kallmann supervised the PhD of Lieselott Herforth (1916–2010). They announced the discovery of the first organic scintillator together with Immanuel Broser (1924–2013) after the war [445,446].

[38] This was originally dubbed "neutron television" [448].

conventional neutron imaging setups can reach resolutions down to 5 µm with exposure times of minutes [449, 450]. The high resolution is accompanied by a smaller field of view in the order of 1 cm^2. High-speed imaging with exposure times of 1 s down to 1 ms is achievable, but this is to the detriment of the spatial resolution which can sink to 0.5 mm. Wavelength selective, dark-field [451–454] and polarized neutron imaging [449, 455–458] are some recent new additions to the neutron imaging catalogue, which provide higher elemental, phase and magnetic sensitivity respectively.

The scattering of neutrons by the sample will change the measured absorption profile and many methods have been developed to correct for this. Some of these are of computational nature [459], while some involve the deployment of black-body grids [460, 461]. In the following, a derivation of the expression for the neutron attenuation by the nuclei will be presented.

2.5.1. Non-Magnetic Neutron-Matter Interaction

Wave-particle duality accounts for the behaviours of both photons and neutrons. Hence, the interaction of neutrons with matter is best understood by drawing an analogy to optics. A short summary of the main concept is presented in which the approach in [462] is followed. The wave function Ψ of the neutron travelling through matter can be obtained by solving the stationary Schrödinger equation:

$$\left[-\frac{\hbar^2}{2m}\nabla^2 + V(\mathbf{r})\right]\Psi(\mathbf{k},\mathbf{r}) = E\Psi(\mathbf{k},\mathbf{r}). \tag{2.53}$$

The neutrons interact with matter in two ways: with the nuclei via the strong force and electromagnetically with a magnetic field, which can be either internal or external. In the conducted imaging experiments with paramagnetic liquids, the former strongly outweighs the latter. The potential of the nuclei V_{nuc} can be approximated by a sum of Fermi pseudopotentials:

$$V_{\mathrm{nuc}}(\mathbf{r}) = \frac{2\pi\hbar^2}{m}\sum_{i=0}^{N} b_i\delta(\mathbf{r}-\mathbf{r_i}). \tag{2.54}$$

This is a sum of Delta distributions centred on the nuclei $\mathbf{r_i}$ along with their corresponding scattering lengths b_i. The neutron scattering cross sections σ_i and b_i are related by:

$$\sigma_i = 4\pi b_i^2. \tag{2.55}$$

The interaction with a certain material can be obtained by averaging the Fermi pseudopotentials over a macroscopic ensemble of nuclei with density N:

$$\overline{V}_{\mathrm{nuc}} = \frac{2\pi\hbar^2}{m}\bar{b}N. \tag{2.56}$$

Plane waves are the solution of this Schrödinger equation:

$$\Psi(\mathbf{k},\mathbf{r}) = \exp(-\mathrm{i}\mathbf{k}\cdot\mathbf{r}) \quad ; \quad k(\mathbf{r}) = \sqrt{\frac{2m[E-V(\mathbf{r})]}{\hbar^2}}. \tag{2.57}$$

The alteration of the wave vector $k(\mathbf{r})$ by the interaction potential also occurs in optics, where it defines the refractive index:

$$n(\mathbf{r}) = \frac{k(\mathbf{r})}{k_0} = \sqrt{1 - \frac{V(\mathbf{r})}{E}}. \tag{2.58}$$

This contains all information about the neutron-matter interaction. Absorption is accounted for by an imaginary part of the interaction potential and the scattering length $\overline{b}$ is a complex number. It follows that the refractive index is also a complex number. It can be approximated by a Taylor expansion and decomposition of the complex interaction potential (using Equations 2.55 and 2.56):

$$n \approx 1 - \frac{1}{2}\frac{V}{E} = 1 - \delta_{\mathrm{nuc}} + \mathrm{i}\beta = 1 - \frac{b_c N \lambda^2}{2\pi} + \mathrm{i}\frac{(\sigma_a + \sigma_{\mathrm{inc}})N\lambda}{4\pi}, \tag{2.59}$$

with the real δ_{nuc} and the imaginary part β. Refraction is accounted for by the real part. The imaginary contribution describes absorption and stems from the fact that the scattering length b_i is complex. Further decomposition of the expression into coherent scattering length b_c, neutron wavelength λ, absorption σ_a and incoherent scattering cross sections σ_{inc} is possible. It follows that an inbound wave function Ψ_0 exits a material of thickness l as:

$$\Psi = \exp(-\mathrm{i}k\delta_{\mathrm{nuc}}\, l)\exp(-k\beta l)\Psi_0. \tag{2.60}$$

It is now straightforward to find an expression for the transmittance of a neutron beam by dividing the absolute squared values of the outbound and inbound wave functions:

$$T = \frac{I}{I_0} = \left|\frac{\Psi}{\Psi_0}\right|^2 = \exp[-(\sigma_a + \sigma_{\mathrm{inc}})Nl]. \tag{2.61}$$

This is none other than the Beer-Lambert law. It allows the quantification of absorbing species by measuring transmission profile of a neutron beam through a sample.

3. Neutron Imaging of Diffusing Paramagnetic Salt Solutions

Then God said, "Let there be a firmament in the midst of the waters, and let it divide the waters from the waters."

Genesis 1:6–8, King James Version

3.1. Introduction

The study of paramagnetic ions in solution relies on techniques with which concentration evolutions can be imaged. Previous studies employed interferometry [154, 155, 161, 162, 164–166] or ultraviolet/visible (UV-Vis) spectroscopy [158, 433, 463] that rely on delicate shifts in the phase or intensity of light by the solvated ions. These changes are caused by interactions between the light and the electrons of the ions. In contrast, neutron imaging of ionic solutions depends on the nuclear interactions to generate a real space image. This direct method consists of measuring the attenuation of a white neutron beam on passing through a liquid sample. Neutrons interact with the nuclei, which makes the measurement element-specific, allowing the direct study of liquids that are both miscible and visually indistinguishable under normal conditions. Recent advances in detector systems have provided the means for neutron imaging with both high spatial and temporal resolutions [442, 464, 465]. This makes dynamical neutron imaging a viable experimental technique for visualisation of general mass transport phenomena and not only classical diffusion phenomena, as it was in the past.

Of the above mentioned optical measurements, only the experiments analysed with a Mach-Zehnder interferometer captured the dynamics of the paramagnetic fluid with a camera [154, 155, 161, 162, 164–166]. In these time-resolved measurements only solutions of a single salt were analysed, although their motivation was an eventual application in a magnetically supported rare earth separation. For an understanding of this, an analysis of liquid systems containing multiple rare earth ions is indispensable. More specifically, a binary system consisting of a paramagnetic and non-magnetic rare earth salt is a suitable model to study magnetically modified mass transport effects due to convection and diffusion.

In this chapter, the focus will lie on diffusing paramagnetic gadolinium nitrate ($Gd(NO_3)_3$) solutions. Neutron imaging was used to track the concentration distribution of aqueous paramagnetic $Gd(NO_3)_3$ solutions in a liquid-liquid system with a miscible non-magnetic counterpart. There are two reasons why a solution of trivalent Gd^{3+} ions is the perfect candidate for this experiment.

First, Gd has the highest neutron absorption cross section of any element. Table 4 lists the neutron absorption cross sections of the stable and naturally occurring Gd isotopes. It can be seen that the absorption cross section is exclusively due to the odd-numbered isotopes ^{155}Gd ($\sigma_a = 62\,200$ barn) and ^{157}Gd ($\sigma_a = 249\,800$ barn), with remeasured values for thermal neutrons published in 2019 [466]. The two corresponding neutron capture reactions are:

$$^{155}\mathrm{Gd} + {}^{1}\mathrm{n} \longrightarrow {}^{156}\mathrm{Gd} + \gamma + \text{conversion electrons (7.9 MeV)}, \tag{3.1}$$

$$^{157}\mathrm{Gd} + {}^{1}\mathrm{n} \longrightarrow {}^{158}\mathrm{Gd} + \gamma + \text{conversion electrons (8.5 MeV)}. \tag{3.2}$$

Each of these isotopes account for around 15% of naturally occurring Gd [440]. Accordingly, the thermal neutron absorption cross section of elemental Gd is $\sigma_a = 46\,700$ barn. No other element in the periodic table has a nuclear composition that engenders a neutron absorption cross section in this order of magnitude. The contrast of Gd solutions in neutron imaging is unrivalled, but the low magnetic moment lanthanides Sm ($\sigma_a = 5922$ barn) and Eu ($\sigma_a = 4530$ barn) immediately below Gd in the periodic table come close [440].

Gd isotope	Abundance (%)	σ_a (barn)	Contribution to elemental σ_a (barn)
152	0.2	735	1.5
154	2.18	85	1.9
155	14.8	62 200	9 205.6
156	20.47	1.5	0.3
157	15.65	239 800	37 528.7
158	24.84	2.2	0.5
160	21.86	0.77	0.2
Elemental			$\sigma_a \approx 46\,700$

Table 4 – Neutron absorption cross sections σ_a of naturally occurring Gd isotopes (from [440, 466]). The high neutron absorption is dominated by the odd-numbered isotopes ^{155}Gd and ^{157}Gd.

The choice of counterion for the Gd^{3+} is also pertinent. Any salt must be both highly soluble in aqueous environment and not liable to undergo neutron activation, which makes handling of the sample hazardous. Gadolinium nitrate $Gd(NO_3)_3$ combines both of these properties[39].

In addition to the favourable nuclear interaction, Gd^{3+} possesses a large magnetic moment of $7\,\mu_B$ by virtue of unpaired 4f electrons (see Table 3). Consequently, solutions of $Gd(NO_3)_3$ are ideal candidates for neutron imaging of paramagnetic solutions, enabling the direct observation of their response to magnetic fields. The interplay of convection, Kelvin force and diffusion were monitored by variations in the neutron transmission profile. The results were published in January 2020 [467].

[39] $Gd(NO_3)_3$ solution is a common neutron poison with which the reactor core can be flooded in an emergency shutdown (SCRAM). In the reactor ruin of Chernobyl, such a solution has been intermittently sprinkled on any neutron producing remnants beginning in 1990 until the present day.

3.2. Methods and Materials

3.2.1. Neutron Imaging Instrumentation

The neutron imaging experiments were among the last to be carried out at the IMAGINE station [468], which was located in the neutron guide hall of the Orphée reactor at the Laboratoire Léon Brillouin just before its final shutdown in November 2019. A sketch of a classic neutron imaging setup with a generic sample is shown in Fig. 2.13 of the previous chapter.

The spectrum of the white neutron beam contained cold neutrons ($\lambda = 2$–$20\,\text{Å}$) from a liquid hydrogen moderator at 20 K. These emerged from a pinhole and travelled 4 m to the detector where the neutron flux was $2 \times 10^7\,\text{cm}^{-2}\,\text{s}^{-1}$. The detection system consisted of a 50 µm thick ^{6}LiF/ZnS scintillator, with a pixel size of 18 µm. The neutron capture reaction of ^{6}Li causes the emission of tritium ^{3}H and an alpha particle:

$$^6\text{Li} + {}^1\text{n} \longrightarrow {}^3\text{H} + {}^4\text{He} + 4.79\,\text{MeV}, \tag{3.3}$$

with cross section of 941 barn for thermal neutrons. Fine particles of zinc sulfide ZnS detect the reaction products by emission of photons in the blue part of the visible spectrum.

The converted light was reflected by a mirror into a Neo sCMOS (ANDOR) camera, which was kept at −30°C for noise reduction. Recorded images of 2560×2160 pixels correspond to a field of view of 46 mm × 39 mm. The acquisition time of one image was usually 1 min and the spatial resolution was in the order of 50 µm. An acquisition time of 60 s was used for the majority of the measurements. The dead time of the detection system was in the order of 2 s. Occasional fluctuations in the neutron flux of the reactor were corrected by normalising the detected intensity in a part of the image without the sample.

3.2.2. Experimental Procedure

A sketch of the experimental setup viewed from above is shown in Fig. 3.1(a). The liquid solutions were syringed (0.8 mm needle diameter) into quartz cuvettes (Hellma® Suprasil®) with path lengths of 1 mm and placed 5 mm in front of the detector. The outside dimensions of the cuvettes were 40 mm × 23.6 mm × 3.5 mm (height × width × depth).

Incoherent scattering by water molecules ($\sigma_{\text{inc}} = 160.5$ barn) was minimized by dissolving the rare earth nitrate salts in heavy water D_2O ($\sigma_{\text{inc}} = 4.1$ barn). Furthermore, an attempt was made to remove excess water of hydration from the $Gd(NO_3)_3$ hexahydrate crystals by heating the salt in an oven at 65°C under inert atmosphere. For maximum contrast, the analysed paramagnetic salt solutions were restricted to colourless and transparent $Gd(NO_3)_3$ solutions. Densities were measured by placing 2 mL of solution on a weighing balance.

The neutron absorption cross section of Gd dwarfs the scattering cross section of D_2O ($\sigma_s = 19.5$ barn). Thus, effects of parasitic scattering on the final signal were expected to be weak. For the study of magnetic effects, a cube-shaped Nd-Fe-B permanent magnet of side length 20 mm was placed adjacent to the cuvettes (2 mm from the solution within). The horizontal magnetic field was $B = 0.45$ T at the surface of the magnet and $B = 0.13$ T at a distance

of 5 mm. A neutron blocking boron carbide (B_4C) sheet in front of the magnet acted as a shield to avoid neutron activation. The prompt activation of Dy is the most troublesome of any elements in the Nd-Fe-B magnets[40].

The magnetic susceptibility of a 1 M $Gd(NO_3)_3$ heavy water solution ($\chi_{1M} = 322 \times 10^{-6}$) is the sum of the diamagnetic D_2O contribution ($\chi_{D_2O} = -8 \times 10^{-6}$ [469]) and the paramagnetic Curie law contribution of the Gd^{3+} ions [47] (see Section 2.4.1). This value and the magnetic field distribution of the Nd-Fe-B magnet allow the computation of the magnetic field gradient force in the vicinity of the magnet (see Fig. 3.1(b)). The magnetic field was calculated by approximating the magnet as two uniform sheets of magnetic charge (see Appendix A.1) [470].

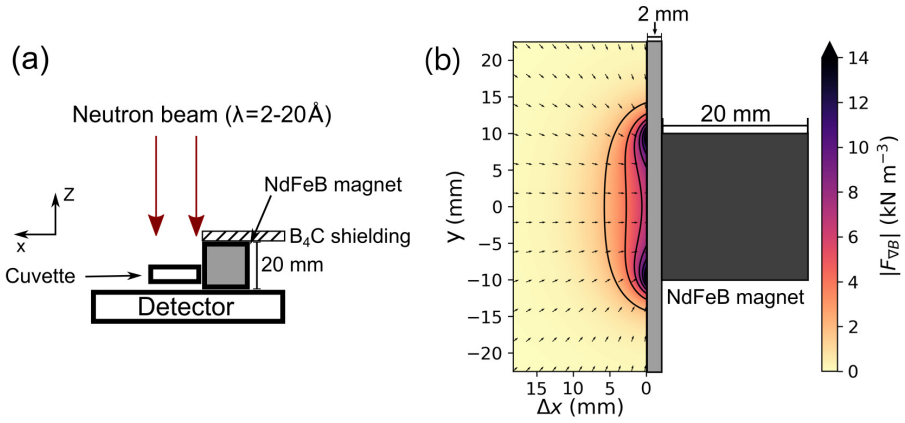

Figure 3.1 – (a) Sketch of the experimental setup (top view). (b) Calculated Kelvin force distribution in the cuvette for a 1 M aqueous $Gd(NO_3)_3$ solution in the field of a uniformly magnetised 20 mm Nd-Fe-B cube.

3.2.3. Image Processing

All images were processed in the open source image processing package Fiji [471], which is based on ImageJ [472,473]. An empty beam was recorded during each measurement session. This was necessary for normalisation to the intensity of the white beam I_0. Furthermore, the electronic noise from the dark-current I_{dc} was subtracted from the image to obtain the transmittance:

$$T = \frac{I - I_{dc}}{I_0 - I_{dc}}. \tag{3.4}$$

The final step of the image processing was the removal of noisy pixels by using an outlier filter. Binning groups of averaged pixels and application of a median filter served to further reduce noise. A raw neutron image, the open beam and the transmittance image after division are shown in Fig. 3.2.

The Beer-Lambert law describes the attenuation of the neutron beam by the Gd^{3+} ions in D_2O:

$$I = I_0\, e^{-\epsilon c \Delta z}, \tag{3.5}$$

[40]The neutron activation of samples can be estimated with tables such as https://www.ill.eu/users/scientific-groups/spectroscopy/useful-links/activation-table-of-elements.

with the molar neutron attenuation coefficient ϵ (unit: $m^2\,mol$), the Gd^{3+} concentration c (unit: $mol\,m^3$) and the sample thickness Δz. Strictly speaking, ϵ depends on the neutron energy and the assumption of a single value for a polychromatic neutron beam is a simplification. This approximation is not a concern, considering the fact that the neutron wavelengths constituting the beam (2–20 Å) lie within one order of magnitude of each other and the bandwidth is smaller than the absorption spectrum.

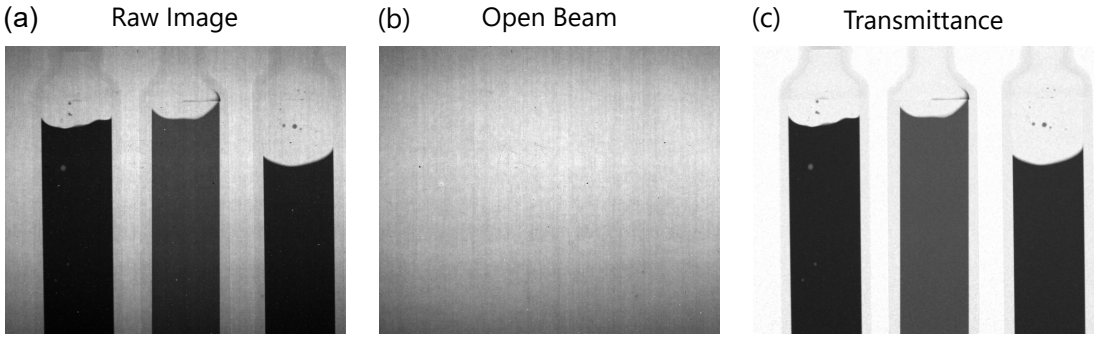

Figure 3.2 – **Neutron image Processing** (a) Raw neutron image. (b) Open beam. (c) The neutron image divided by the open beam with outlier pixels are removed.

A calibration of the transmitted intensity to the Gd^{3+} concentration was performed by recording images of solutions in 1 mm path length cuvettes (see Fig. 3.3). The attenuation follows the Beer-Lambert law up to a concentration of about 0.4 M, when the beam is almost completely absorbed and the transmitted intensity originates predominately from incoherent scattering. An offset exponential fit with an extra variable ($b = 0.07$) captures the behaviour, but quantitative statements cannot be readily made at concentrations higher than 0.5 M.

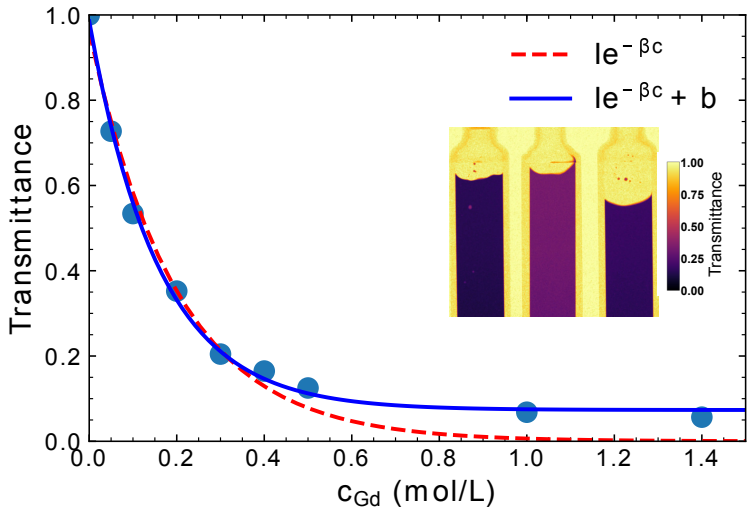

Figure 3.3 – **Gd^{3+} concentration calibration curve in 1 mm path length quartz cuvettes.** Transmittance values were normalised to that of a D_2O filled cuvette and follow the Beer-Lambert law (broken line) up to 0.4 M. An offset $b = 0.07$ (solid line) is needed at higher concentration.

The accessible Gd^{3+} concentration was restricted by the high absorption cross section of cold neutrons. In general, the cross section of neutrons decreases with velocity. Thus, σ_a will be even higher than the value of 46 700 barn for thermal neutrons. It is possible to extract an estimate value of σ_a for cold neutrons from the calibration Fig. 3.3 by expressing the Beer-Lambert law as:

$$I = I_0 \exp\left(-\sum_i \sigma_i N_A c_i \Delta z\right), \tag{3.6}$$

with the Avogadro constant $N_A = 6.022 \times 10^{23}\,\mathrm{mol}^{-1}$, the concentration c_i, the neutron cross sections σ_i and the path length Δz. The argument of the exponential function is summed over all elements in the path of the beam. In the calibration, the only element that contributes to the change in attenuation is Gd and the summation is superfluous. A value of $\sigma_{\mathrm{Gd}} = 80\,700$ barn was calculated from the regular Beer-Lambert fit in the calibration curve (Fig. 3.3). This is a reasonable value at twice the σ_a of thermal neutrons. For the present chapter, this was assumed to be the cold neutron absorption cross section of Gd.

To better visualise the changes of Gd^{3+} concentration (Δc_{Gd}), the time-sequenced neutron images can be normalised by the first image of the series. The Beer-Lambert law (Eq. 3.6) without the sum in the exponent can be inverted to find the Gd concentration change between the images taken at times t_1 and t_2:

$$\Delta c_{\mathrm{Gd}} = -\ln\left(\frac{I(t_2)/I(t_1)}{\sigma_{\mathrm{Gd}} N_A \Delta z}\right). \tag{3.7}$$

3.3. Analysis of Miscible Liquid-Liquid Systems

3.3.1. Regular Diffusive Systems

The preliminary experiment consisted of a $Gd(NO_3)_3$ solution in D_2O that diffused into pure D_2O. In the case of an inhomogeneous solution comprising a paramagnetic and non-magnetic component, a magnetic field gradient non-parallel to the concentration gradient alters the state of mechanical equilibrium [74,283]. The $Gd(NO_3)_3$ solution climbed up the side of the cuvette until the balance between buoyancy ($F_g = \Delta\rho g$) and magnetic field gradient forces was re-established. This can be seen in Fig. 3.4. Here, 100 µL of 0.4 M $Gd(NO_3)_3$ solution ($\rho = 1180\,\mathrm{kg\,m^{-3}}$) at the bottom of a 1 mm path length cuvette was covered with 400 µL D_2O ($\rho = 1110\,\mathrm{kg\,m^{-3}}$). A magnet was placed at the side and the diffusion of the $Gd(NO_3)_3$ was monitored for 3 h. The magnetic field gradient drew the $Gd(NO_3)_3$ solution towards the magnet by magnetoconvection until the skewed profile fulfils the magnetically altered state of mechanical equilibrium.

The chemical potential gradient, which in this simple one component diffusion process becomes the concentration gradient, drives the homogenisation of the $Gd(NO_3)_3$ in the system by diffusion. From the assessment of the driving forces of mass transport in Section 2.2.1, it is clear that neither the magnetic field gradient nor gravity has any effect on molecular diffusion in a small scale system of this kind. Mixing of the liquids by diffusion continues in the presence of the magnetic field gradient, only the profile is warped.

An estimate for the diffusion coefficient D of 0.4 M $Gd(NO_3)_3$ in D_2O can be obtained from the vertical concentration profile by a fit with the solution of the one-dimensional diffusion equation (Fick's second law: Eq. 2.21):

$$c(y,t) = \frac{c_0}{2}\,\mathrm{erfc}\left(\frac{y-y_0}{\sqrt{4Dt}}\right), \tag{3.8}$$

with the Gd^{3+} starting concentration c_0. Fits of the complementary error functions (erfc) to extracted concentration profiles are shown in Fig. 3.4(c). The value of $D = 1.2 \times 10^{-9}\,\mathrm{m^2\,s^{-1}}$ obtained for the non-magnetised region after 3 h is reasonable for concentrated rare earth ions in water [474]. However, this value should be treated with caution, as the initial interface was smeared by introducing the liquids into the cuvette before the onset of diffusion. The diffusion coefficient from the fit for the magnetised region is higher at $D = 1.5 \times 10^{-9}\,\mathrm{m^2\,s^{-1}}$. A factor in this is the inability of the one-dimensional expression to account for horizontal component of diffusion from the warped concentration profile.

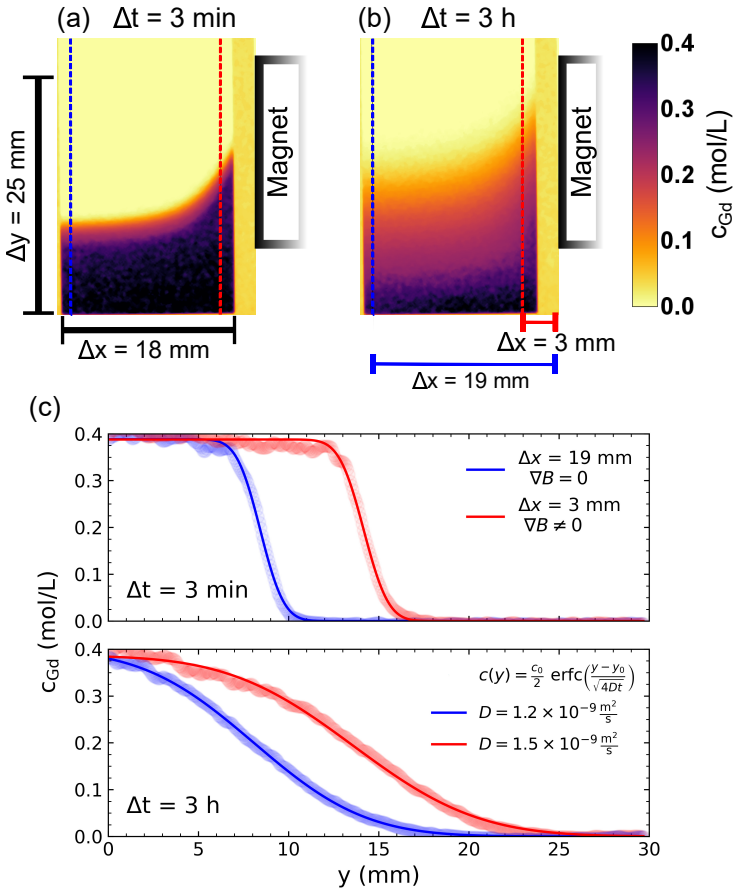

Figure 3.4 – Neutron image of a 1 mm path length quartz cuvette with 100 µL 0.4 M $Gd(NO_3)_3$ solution overlain with 400 µL of D_2O. A 20 mm magnet cube to the right skews the Gd^{3+} concentration profile. (a) After 3 min (b) after 3 h. (c) Fits of Eq. (4) to the vertical cross sections (broken lines in neutron images) of the concentration profiles 3 mm ($\nabla B \neq 0$) and 19 mm ($\nabla B = 0$) away from the magnet show good agreement and the diffusion coefficient D can be obtained.

The data are described rather well by the complementary error function. But the detected c_{Gd} at short times, below the $Gd(NO_3)_3 - D_2O$ interface, lie under the $Gd(NO_3)_3$ concentration plateau predicted by the theory (Fig. 3.4(c)). The effect of this discrepancy was analysed by calculating the concentration change with respect to the first image of the diffusion process (Fig. 3.4(a)). This was extracted with Eq. 3.7 and is shown in Fig. 3.5. The vertical changes in concentration along one line close to the magnet and one further away, are plotted in Fig. 3.5(b). In this, an asymmetry between the vertical minimum and maximum Δc_{Gd} values can be seen in Δc_{Gd} for both x-positions. The magnitude of Δc_{Gd} in the D_2O which gains Gd^{3+} is higher than in the $Gd(NO_3)_3$ solution, which loses Gd^{3+}, by approximately 30 mM. This is unphysical, because the overall concentration should remain constant. An uncertainty of around 5% is expected in the extracted c_{Gd} values for 0.4 M solution, if such a sharp interface between areas of high and low transmittance is present.

The most probable explanation for the measured $Gd(NO_3)_3$ deficiency below the interface is the detection of scattered neutrons from above the interface. These hit the detector in this area and create a higher transmittance than expected based on the absorption. This is most noticeable in the region around 0.4 M, which is most sensitive to slight changes in intensity (see Fig. 3.3). Such edge effects in areas of the neutron image in which the transmittance undergoes abrupt changes are common. It was refrained from showing images converted to Δc_{Gd} for this reason. Correction algorithms for the intensity due to vagabonding scattered neutrons exist [459], but these were not employed at the IMAGINE station. This should be kept in mind for quantitative statements, but for qualitative conclusions this is of no concern.

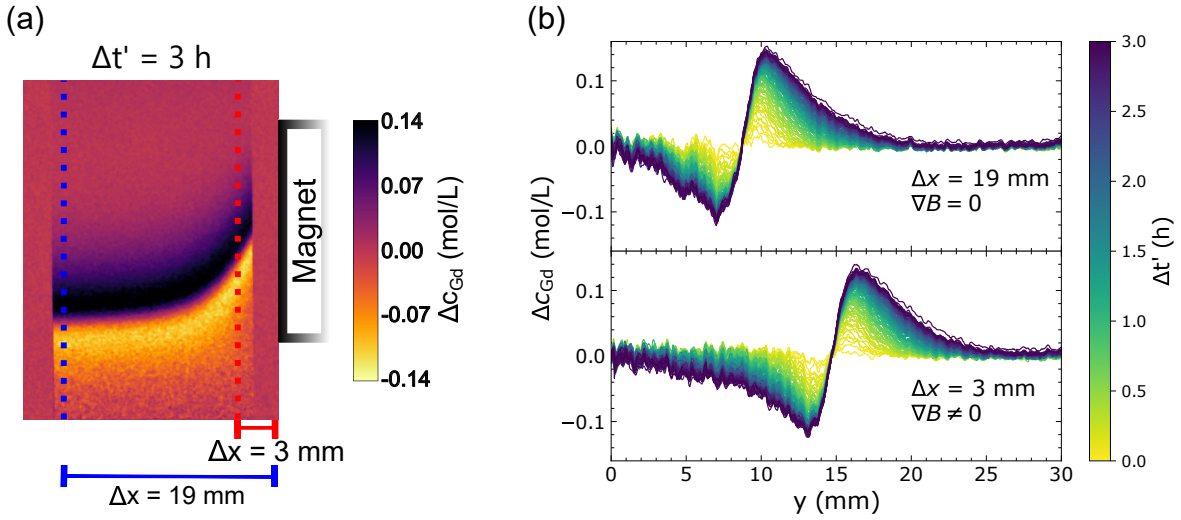

Figure 3.5 – Concentration change due to $Gd(NO_3)_3$ diffusion in D_2O. (a) Neutron image converted to Δc_{Gd} with respect to the first image in the time series. The image shown was obtained by applying Eq. 3.7 for the neutron images shown in Fig. 3.4(a–b). (b) Plot of the temporal evolution of Δc_{Gd} along the vertical lines shown in (a).

Back to the physical interpretation of the results: The diffusion of the $Gd(NO_3)_3$ continuously augmented the density profile of the solution. This in turn meant that the condition of mechanical equilibrium dictated by gravity and the magnetic field gradient ($\nabla\rho \times \mathbf{g} + \mu_0 \nabla M \times \nabla H \stackrel{!}{=} 0$)

underwent permanent changes. Slow diffusion and a succinct convective flow occur together to impose thermodynamic equilibrium on the one hand and mechanical stability on the other. The time which it takes to impose the thermodynamic equilibrium is unchanged by the magnetic field gradient.

The expected concentration evolution due to pure diffusion from 0.4 M $Gd(NO_3)_3$ can be calculated with Eq. 3.8. For $D = 1.2 \times 10^{-9}\,\mathrm{m^2\,s^{-1}}$ and an initial 10 mm column, the evolution is depicted in Fig. 3.6. Mixing by diffusion is a slow process. It will take several days for the $Gd(NO_3)_3$ to uniformly distribute throughout the cuvette. Gradients of the chemical potential, which in this case is equivalent to the concentration, are only acute for an initial step-like profile and quickly tail off.

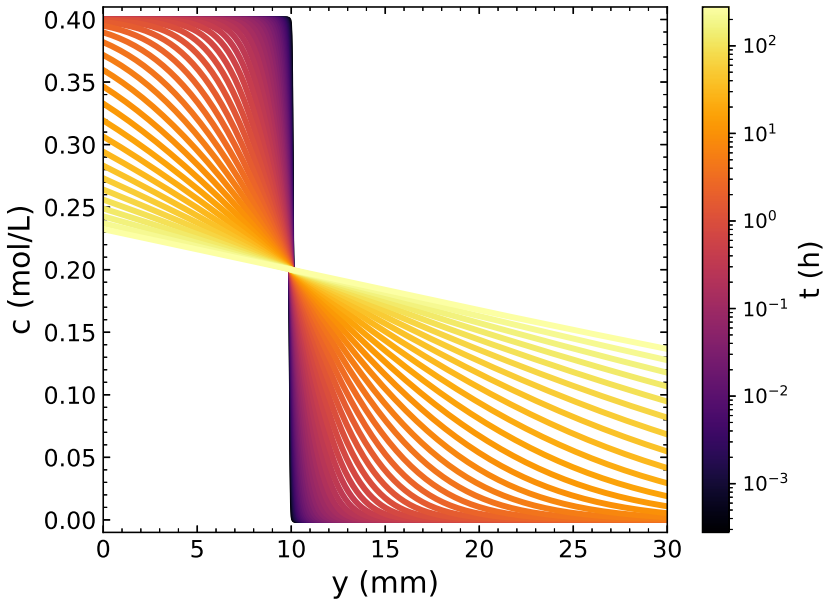

Figure 3.6 – Theoretical evolution of $Gd(NO_3)_3$ concentration by pure diffusion from a 10 mm high column of 0.4 M solution. The lines show the function from Eq. 3.8 with $D = 1.2 \times 10^{-9}\,\mathrm{m^2\,s^{-1}}$. The smearing out of the interface takes place within 1 h, but substantial mixing by diffusion takes several days.

3.3.2. Double-Diffusive Systems

The results with a single diffusing paramagnetic species in the previous section were unsurprising. However, the addition of a non-magnetic solute to the D_2O changes the situation profoundly. A binary system of $Gd(NO_3)_3$ and yttrium(III) nitrate ($Y(NO_3)_3$) solutions was chosen as a model system for rare earth ion diffusion with a paramagnetic and non-magnetic component.

The first thought is that the density difference between the $Gd(NO_3)_3$ solution and the non-magnetic heavy water can be adjusted by dissolution of $Y(NO_3)_3$ in the D_2O, which is transparent to neutrons ($\sigma_a = 7.0$ barn [440]). Decreasing the density difference leads to more vigorous magnetically induced migration and facilitates magnetic confinement. This can be understood by inspecting the condition of mechanical equilibrium in a magnetic field gradient $\nabla\rho \times \mathbf{g} + \mu_0 \nabla M \times \nabla H \overset{!}{=} 0$ (Eq. 2.42 in Section 2.2.3). For small values of $\nabla\rho$, this equation is

only possible to satisfy if ∇M and ∇H are close to parallel. The $Gd(NO_3)_3$ solution will follow the profile of the magnetic field gradient force shown in Fig. 3.1, a process dubbed magnetic confinement [47].

If the density of the Gd solution is higher than that of the Y solution, the removal of the magnet before homogenisation has taken place prompts a buoyancy-driven Rayleigh-Taylor instability and the Gd solution plunges to the bottom of the cuvette in a matter of seconds. This entails mixing of the salt solutions by advection of the solutes. Magnetic levitation of paramagnetic salt solutions has been used in the past, to create perfect starting conditions for the study of such Rayleigh-Taylor instabilities [475, 476].

A different situation arises when the density difference is inverted and the Gd solution floats above the Y solution. This situation was studied here. Such a system was created by injecting 75µL 0.4 M $Gd(NO_3)_3$ solution on top of 300 µL 1.3 M $Y(NO_3)_3$ solution ($\rho = 1320\,\mathrm{kg\,m^{-3}}$) in a 1 mm path length cuvette (see Fig. 3.7). Shortly before this 100 µL 0.5 M $Gd(NO_3)_3$ had been injected into the same solution in another cuvette. The two cuvettes containing these binary salt systems can be seen in Fig. 3.7.

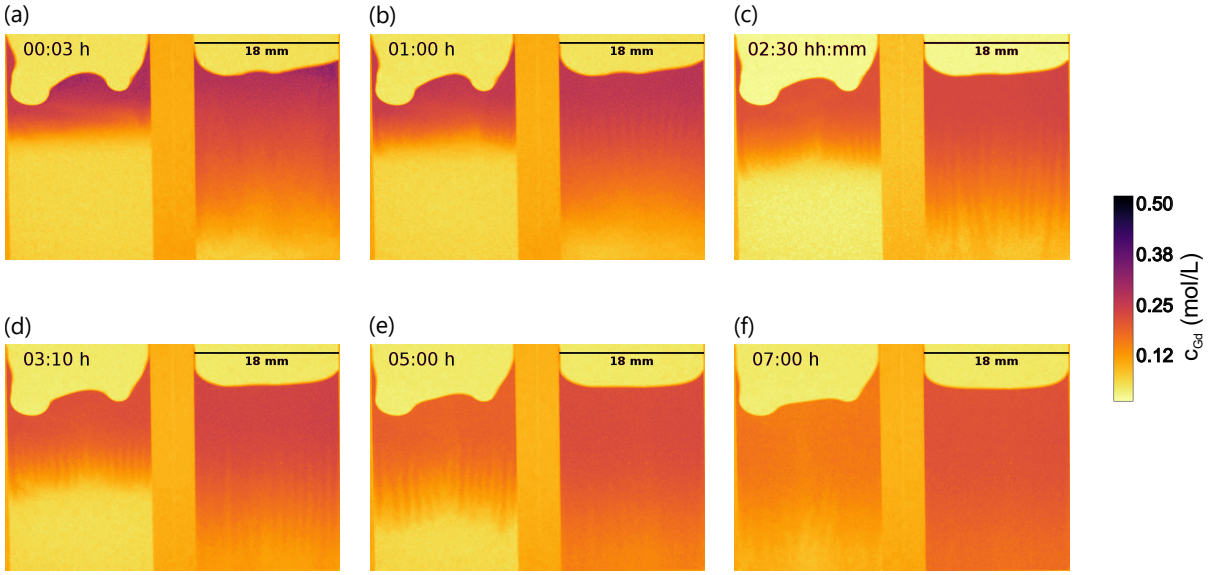

Figure 3.7 – Two 1 mm path length quartz cuvettes with 75 µL 0.4 M $Gd(NO_3)_3$ (left) and 100 µL 0.5 M $Gd(NO_3)_3$ (right) above 300 µL of 1.3 M $Y(NO_3)_3$ ($\rho = 1320\,\mathrm{kg\,m^{-3}}$). $Gd(NO_3)_3$ solutions were injected above the $Y(NO_3)_3$ solution surface in the left cuvette and below it in the right cuvette. Salt fingers form in both systems and mix the solutions within 7 h. Left cuvette: The surface profile is caused by capillary forces. The salt fingers begin to form at the side of the cuvette and propagate inwards.

From a diffusion point of view, these systems are expected to be mechanically stable. Protracted mixing by diffusion should eventually homogenise the ion concentration. In reality, the experiments showed that the system was dynamically unstable and the interface between the salt solutions was destroyed much faster than the smearing by diffusion. This can be seen in Fig. 3.7. A collective instability of cascading finger-like structures forms on the interface between the salt solutions within minutes of the creation of the system. At first, this is difficult to see

due to the limited resolution of the neutron imaging setup. It becomes apparent for the right cuvette after 1 h (Fig. 3.7(b)) and also for the left cuvette after approximately 2.5 h (Fig. 3.7(c)). This phenomenon is known as a salt fingering instability [241, 244, 477–488]. The salt fingers substantially mix the solutions within 7 h. This is much faster than pure diffusion, which would take days (see Fig. 3.6).

Salt fingering instabilities are encountered at the interface of solutions that diffuse into each other at unequal rates[41]. A pictorial explanation of the formation of salt fingers in the $Gd(NO_3)_3$ /$Y(NO_3)_3$ system is presented in Fig. 3.8. The left image shows the initial situation with the lower concentrated 0.4 M $Gd(NO_3)_3$ solution overlaying the 1.3 M $Y(NO_3)_3$ solution. Both solutions are separated by a sharp horizontal interface and the system is mechanically stable. The crux is that the diffusivity of Y^{3+} in the 1.3 M solution exceeds that of the Gd^{3+} in the 0.4 M solution. It follows that $Y(NO_3)_3$ will diffuse laterally into small portions of $Gd(NO_3)_3$ solution that cross the interface. This is illustrated in the zoomed in area of the interface in the middle of Fig. 3.8. The increase in density of this small parcel of $Gd(NO_3)_3$ due to the gained $Y(NO_3)_3$ makes the $Gd(NO_3)_3$ solution plummet in form of organised fingers, which continue to leech $Y(NO_3)_3$ from their surroundings during their descent. These transport the $Gd(NO_3)_3$ advectively, two orders of magnitude faster than regular diffusion and trigger a stratification with neighbouring fingers that rise thanks to the buoyancy acquired by the loss of $Y(NO_3)_3$. This vertical stratification is shown in the right panel of Fig. 3.8. It is quite resilient to disturbances and only disappears once it has been washed out by horizontal diffusion or the fingers dissipate, upon hitting a solid obstacle such as the bottom of the cuvette.

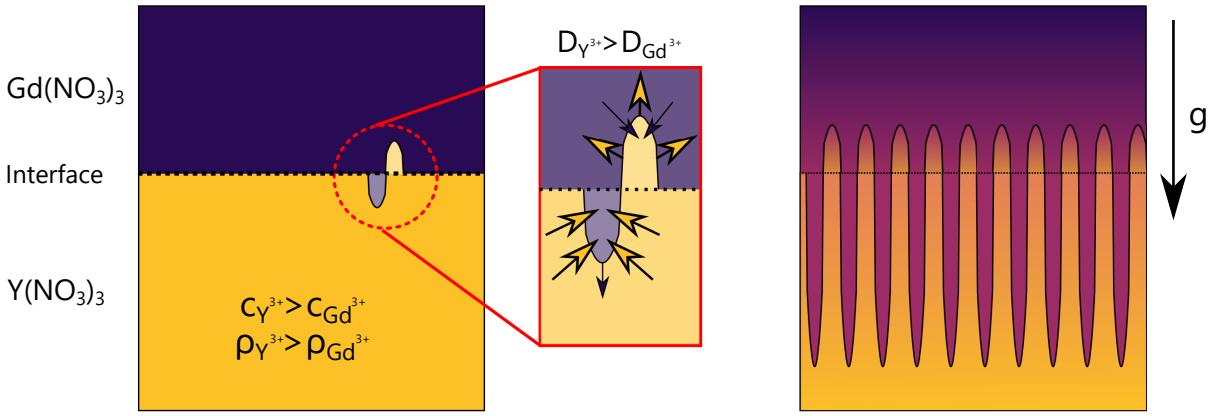

Figure 3.8 – Explanation of salt finger formation. Left: 0.4 M $Gd(NO_3)_3$ is placed above 1.3 $Y(NO_3)_3$ solution. The system is destabilised by faster diffusing Y^{3+} that diffuses into any portion of $Gd(NO_3)_3$ solution, which crosses the interfaces (see the magnified interface). This forms a salt finger of higher density, which is pulled down by gravity. Adjacent fingers of lower density rise. Right: The salt fingering field, which is caused by the double-diffusive convection. Vertical salt fingers protrude far into the $Y(NO_3)_3$ solution.

[41] Salt fingering instabilities had their genesis in oceanography. Double-diffusive convection is particularly important in thermohaline convection (thermo-: temperature; -haline:salinity) [479,489]. It successfully explains both temperatures and ion concentrations in the oceans [490]. The explanation of these thermohaline instabilities is that the thermal diffusivities of salt solutions are around 100 times higher than the mass diffusivities. The consequences were first observed in an experiment called the "salt fountain" by Stommel in 1956 [491]. The explanation of the observations was later given by Stern [492]. Further modification by horizontal shearing was then reported [478].

Hence, diffusion can destabilise a mechanically stable system in which the density decreases upwards and mix the solutions on a faster timescale by convection. The irony is that gravity pulls the denser parcel of fluid downwards in the gravitational potential to re-establish mechanical equilibrium. In doing so, it is enabling increased diffusion by maximising the interfacial area between the salt solutions and the density will increase even more. Thus, a salt fingering instability can be understood as a self-amplifying process.

Herbert HUPPERT derived a general criterion for the appearance of salt fingering instabilities [481,493]. It is necessary for the ratios (τ_*) of the salt diffusion coefficients to fulfil this inequality:

$$\tau_*^{3/2} = \left(\frac{D_\mathrm{Y}}{D_\mathrm{Gd}}\right)^{3/2} > R_\rho = \frac{\Delta\rho_\mathrm{Y}}{\Delta\rho_\mathrm{Gd}}, \tag{3.9}$$

with the right side of the expression defined by the ratio of initial density excesses due to the rare earth nitrates $\Delta\rho_\mathrm{Y}/\Delta\rho_\mathrm{Gd}$. The observations of the instability in Fig. 3.7 indicate that the system of 0.4 M $Gd(NO_3)_3$ − 1.3 M $Y(NO_3)_3$ − D_2O fulfilled the condition.

At infinite dilution in H_2O, the diffusion coefficients of the lanthanides decrease from 0.62×10^{-9} to $0.55 \times 10^{-9}\,\mathrm{m^2\,s^{-1}}$ [494, 495]. The decrease in D along the lanthanide series seems to follow the lanthanide contraction and Y^{3+} diffuses as a heavy rare earth with $0.55 \times 10^{-9}\,\mathrm{m^2\,s^{-1}}$. All in all, these diffusion coefficients are similar. In contrast, the nitrate ion NO_3^- is more mobile with $D = 1.9 \times 10^{-9}\,\mathrm{m^2\,s^{-1}}$ at infinite dilution [474]. Hence, the diffusion coefficients of the rare earth nitrates are dominated by the heavy trivalent cations. Evidently, the inequality given by Eq. 3.9 is fulfilled and D_Y at $c = 1.3$ M must rise above D_Gd at $c = 0.4$ M. A lower boundary for D_Y of 1.3 M $Y(NO_3)_3$ solution in D_2O can be estimated from the density changes due to the salts $\Delta\rho$ (in $\mathrm{kg\,m^{-3}}$) and the diffusion coefficient D_Gd of 0.4 M $Gd(NO_3)_3$: $D_\mathrm{Y} \geq (\frac{\Delta\rho_\mathrm{Y}}{\Delta\rho_\mathrm{Gd}})^{2/3} D_\mathrm{Gd} = (\frac{220}{80})^{2/3} \times 1.2 \times 10^{-9}\,\mathrm{m^2\,s^{-1}} \approx 2.4 \times 10^{-9}\,\mathrm{m^2\,s^{-1}}$. Ostensibly, 1.3 M $Y(NO_3)_3$ has to diffuse at least twice as fast as 0.4 M $Gd(NO_3)_3$. Precise values are difficult to obtain, because accurate specific gravities of the rare earth nitrates in D_2O solutions are unknown[42].

An important point is that the original nitrate salts were not anhydrous. There will have been H_2O molecules in the solutions from the hexahydrated ions. In reality, the system was tertiary $Gd(NO_3)_3$ −$Y(NO_3)_3$ −D_2O−H_2O. The density changes due to diffusion of H_2O (M= $18\,\mathrm{g\,mol^{-1}}$) are less severe than Y^{3+} (M= $88.9\,\mathrm{g\,mol^{-1}}$) and Gd^{3+} (M= $157.29\,\mathrm{g\,mol^{-1}}$). However, there will have been effects on the diffusion coefficients of the ions, which are slightly higher in H_2O due to lower viscosity. Diffusion of Y^{3+} into the $Gd(NO_3)_3$ layer may have been accelerated by an imbalance of H_2O. An exchange of D_2O−H_2O molecules between the 1 mm thick meniscus and ambient moisture will also have taken place over time [499].

[42] The specific gravities measured with the weighing balance were compared with literature values from pycnometric measurements in regular aqueous solutions [496–498]. The densities measured here agree rather well with the literature values.

Effect of Magnetic Field Gradient on Paramagnetic Salt Fingering

Next, the effect of a magnetic field gradient on the Gd^{3+}/Y^{3+} salt fingering was analysed. To investigate this, 100µL 0.4 M $Gd(NO_3)_3$ solution was injected on top of 300 µL 1.3 M $Y(NO_3)_3$ solution ($\rho = 1320\,\mathrm{kg\,m^{-3}}$) (see Fig. 3.9(a)). After 1 h the system was beset by the salt-fingering instability again (see Fig. 3.9(b–c)). Left to its own devices, the vertical stratification persists for over 8 h as before (see Figs. 3.9(c)). The fingers are approximately 1.2 mm wide (see cross sections in Fig. 3.9(g)). Viscous friction between the liquid and the cuvette walls plays a role in the horizontal scale of the individual fingers, which is inversely proportional to the cell gap width [500]. Thus, a horizontal expansion of the fingers beyond the gap width is achievable in thin cuvettes.

A magnet next to the cuvette erases the stratification and re-establishes a dynamically stable system by capturing the paramagnetic solution (see Figs. 3.9(d) and 3.10). This does not reverse the mixing that has occurred and the Gd^{3+} ions can be seen to continuously diffuse into the $Y(NO_3)_3$ solution. The magnetic field gradient merely prevents the collapse of the liquid-liquid interface. Nonetheless, the system undergoes an immediate change upon its withdrawal (see Fig. 3.9(e)). Bereft of the confining magnetic field gradient force, the boundary between the solutions is once again disrupted. The ensuing release of the paramagnetic liquid is accompanied by convective mixing of the solutions amidst which the salt fingering instability can be witnessed anew. After two hours the system equilibrates as homogenisation sets in (see Fig. 3.9(f)).

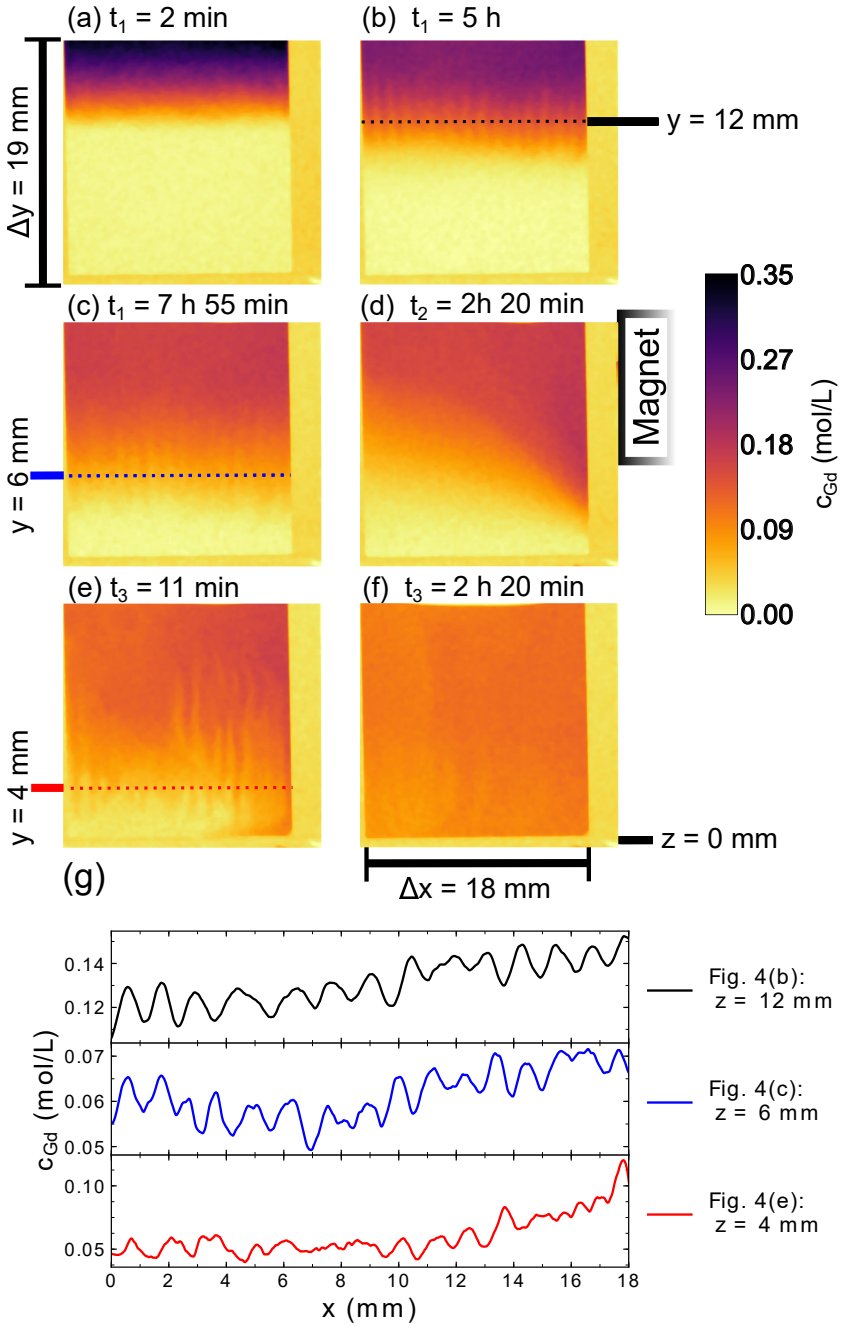

Figure 3.9 – (a–f) Neutron images of 100 µL 0.4 M $Gd(NO_3)_3$ above 300 µL 1.3 M $Y(NO_3)_3$ solution ($\Delta\rho = 140\,\mathrm{kg\,m^{-3}}$) in a 1 mm path length quartz cuvette. The view is restricted to the area below the surface in the vicinity of the liquid-liquid interface. (a) 2 min after the $Gd(NO_3)_3$ solution is suspended above the $Y(NO_3)_3$ surface. (b–c) Double-diffusion imposes Gd salt fingers which protrude into the $Y(NO_3)_3$ solution after 90 min and begin to sink due to the loss of buoyancy. The fingers have a diameter of 1.2 mm and persist for over 8 h. (d) A cubic 20 mm magnet at the side of the cuvette halts the instability growth and destroys the stratification instantly (t_2: time since magnetisation). (e–f) Once the magnet is removed, the control over the $Gd(NO_3)_3$ is relinquished and it fans out. The system snaps back into the stratified state in less than 10 min and the cascading salt fingers homogenise the mixture after 2 h (t_3: time since removal of magnet). (g) Horizontal cross sections (broken lines in the neutron images) of the salt fingers in (b), (c), and (e) show a width of ≈1.2 mm and a periodic variation of the Gd^{3+} concentration by ≈0.02 mol/L.

The magnetic field gradient was able to interrupt salt fingering instabilities, which suggests that it will also prevent them from happening in the first place. To prove this, 50 µL 0.5 M $Gd(NO_3)_3$ solution ($\rho = 1200\,\mathrm{kg\,m^{-3}}$) was placed above 800 µL 1.3 M $Y(NO_3)_3$ solution ($\rho = 1320\,\mathrm{kg\,m^{-3}}$) in a 2 mm path length cuvette with the 20 mm magnet cube adjacent from the onset. The situation is shown in Fig. 3.10 with a montage of the entire process in Fig. 3.11. The concentration calibration performed for the 1 mm cuvette (Fig. 3.3) is no longer valid for higher path lengths. Instead of c_{Gd}, the images show the negative logarithm of the transmittance $-\log(T)$, which is proportional to the Gd^{3+} concentration.

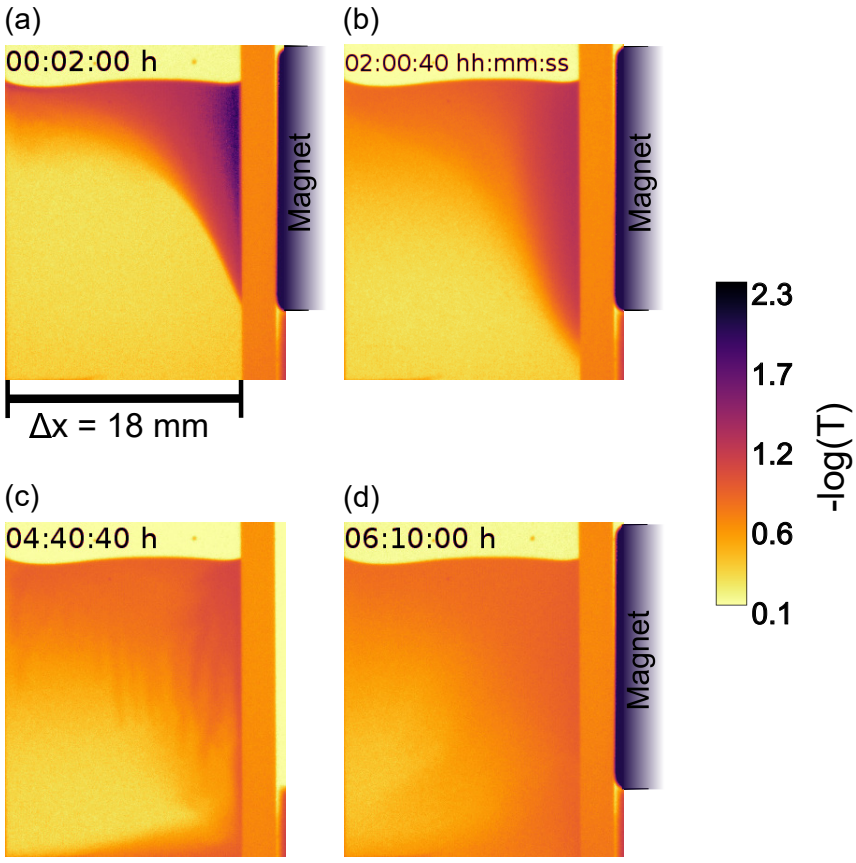

Figure 3.10 – 50 µL 0.5 M $Gd(NO_3)_3$ solution ($\rho = 1200\,\mathrm{kg\,m^{-3}}$) above 800 µL 1.3 M $Y(NO_3)_3$ solution ($\rho = 1320\,\mathrm{kg\,m^{-3}}$) in a 2 mm path length quartz cuvette. The acquisition time was 80 s for this measurement. The calibration from Fig 3.3 is not valid for path lengths above 1 mm. Therefore, the negative of the logarithm of the transmittance is shown. (a) The $Gd(NO_3)_3$ drop migrates to the cubic 20 mm magnet at the side of the cuvette within 2 min. (b) The trapped drop in the magnetic field gradient (see Fig. 1(b)) gradually diffuses into the $Y(NO_3)_3$ solution over the course of 4.5 h. (c) Salt fingers appear immediately after removal of the magnet at $t = 4\,\mathrm{h}\,30\,\mathrm{min}$. (d) At $t = 6\,\mathrm{h}\,10\,\mathrm{min}$, the stratification disappears after placing the magnet next to the cuvette again.

Magnetoconvection pulls the $Gd(NO_3)_3$ solution into the magnetic field gradient during the first hour of recording and the $Gd(NO_3)_3$ forms the contour of the field gradient (Fig. 3.3(a–b)). Diffusion from this interface continues throughout the convective flow. This gradual washing out of the interface is much slower than the fingering instability without the magnetic stabilisation. Once the magnet is removed after 4.5 h, the system jumps directly to a mechanically unstable

state (Fig. 3.9(c)). The lower density $Gd(NO_3)_3$ solution tries to spread over the higher density $Y(NO_3)_3$ solution. It is only partially successful in doing this, as it is pulled apart by a vertical stratification of salt fingers. It can be seen that the longest salt fingers close to the wall, where the magnet had trapped the $Gd(NO_3)_3$, have disintegrated upon hitting the bottom of the cuvette, spilling their advectively transported $Gd(NO_3)_3$. After approximately 90 min of salt fingering, the magnet was returned to its original position and the instability was destroyed. The $Gd(NO_3)_3$ solution organises itself more towards the right hand side of the cuvette with the magnetic field gradient, but no enrichment of $Gd(NO_3)_3$ is possible and regular diffusion continues.

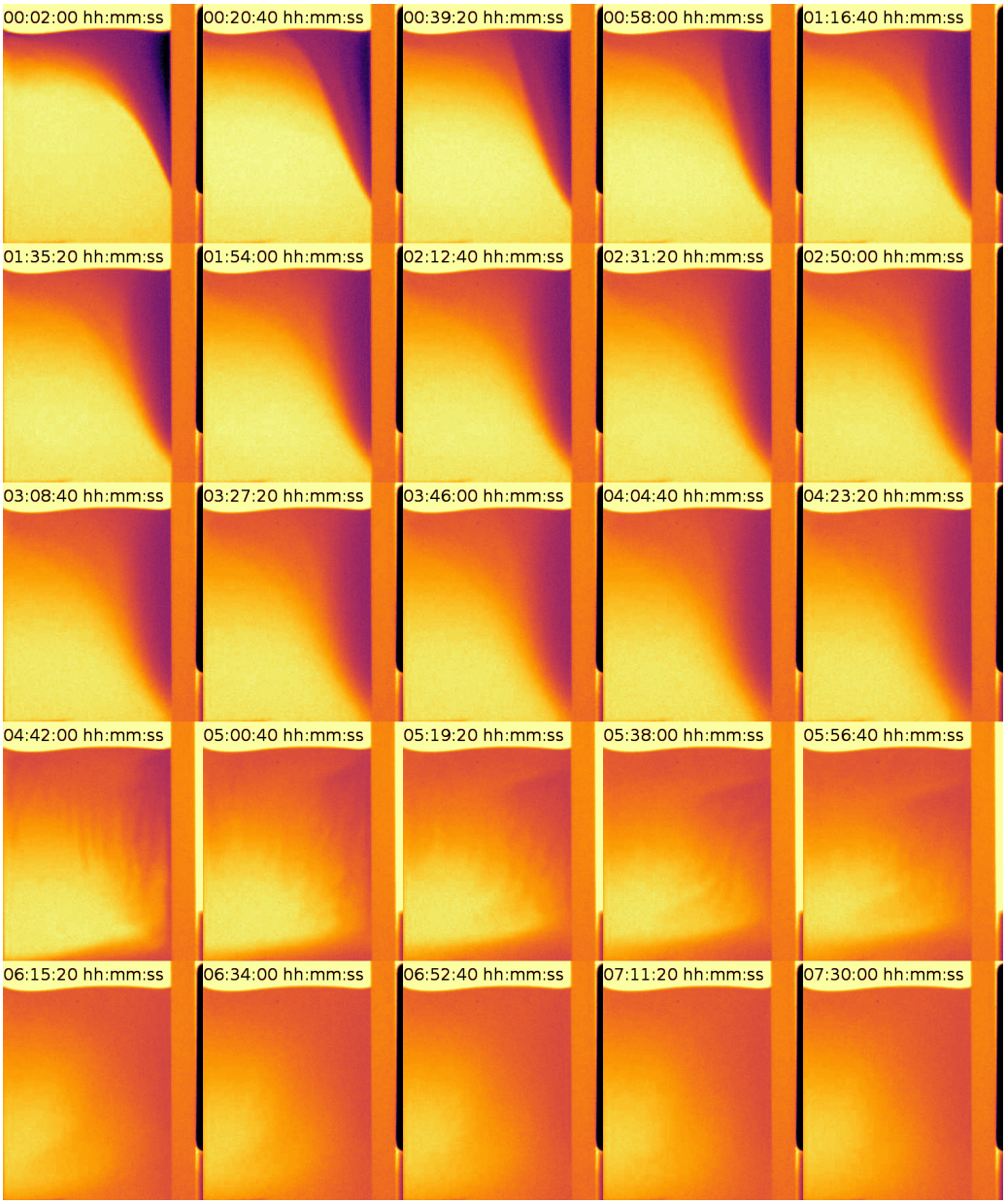

Figure 3.11 – Montage of the 0.5 M Gd^{3+}/1.3 M Y^{3+} system shown in Fig. 3.10.

The effect of the magnetic field gradient in curtailing the salt fingering instability can be understood by inspecting the condition for its appearance (Eq. 3.9). The magnetic field gradient augments the excess density $\Delta\rho_{\mathrm{Gd}}$ caused by the dissolved $Gd(NO_3)_3$ in the D_2O. In a magnetic field gradient, the apparent density of the paramagnetic fluid will be lower, which allows the combatting of density difference convection. For intense field gradients, $\Delta\rho_{\mathrm{Gd}}$ can even become negative and the $Gd(NO_3)_3$ is levitated above the pure solvent. It is clear that for small or negative values, Eq. 3.9 can never be satisfied. Consequently, the interface will not collapse and only regular diffusive mixing without the fast convective motion is possible.

Up to now, the $Gd(NO_3)_3$ /$Y(NO_3)_3$ systems were all created with initial step-like density profiles. These cause a sharp transition in the buoyancy that the salt fingers experience once they cross the diffuse interface. A further experiment was carried out with a smoother density gradient. The liquid sample holder was a 1 mm path length quartz cuvette with a width of 9 mm (see Fig. 3.12). There are many ways to create constant density gradients [501–503]. The method of choice is known as the "double bucket" technique[43] and was invented by Gerald Oster[44] [483, 484, 501–503].

Filling a 350 µL cuvette with a path length of 1 mm by this method is challenging and the reliance on D_2O further complicates matters. A compromise was reached by injecting regular water H_2O ($\rho = 997\,\mathrm{kg\,m^{-3}}$) before the $Gd(NO_3)_3$ solution. A density gradient can form during the rising of H_2O to the surface by buoyancy. A 20 mm Nd-Fe-B magnet cube was placed to the right of the cuvette to capture the $Gd(NO_3)_3$ solution in its stray field and further submerge it. By adding regular water, the role of H_2O in the tertiary $Gd(NO_3)_3$ – $Y(NO_3)_3$ – D_2O–H_2O system is amplified. The presence of another diffusing species in form of the H_2O complicates the interpretation and the discussion of the results will be qualitative.

First, 100 µL of 1.7 M $Y(NO_3)_3$ solution was inserted into the cuvette. Then, 100 µL of H_2O was layered on top. Finally, 150 µL of 0.5 M $Gd(NO_3)_3$ solution was injected on top of the water to fill the cell to the brim. It was pulled under the H_2O by gravity and the magnetic field gradient. Diffusion then created a density gradient in the top part of the cuvette. The regions of different density gradient are shown as two arrows on the right side of the cuvette in Fig. 3.12(d). The system was equilibrated for 30 min to establish a smoother vertical density gradient and ensure sufficient magnetoconvection into the field gradient. The H_2O gravitated towards the top, while the $Y(NO_3)_3$ solution circumfused the trapped $Gd(NO_3)_3$ solution. Then the magnet was removed.

Neutron images in light of the elimination of the magnetic field gradient are shown in Fig. 3.12. The images were acquired every 5 s with a dead time of 1 s, which lowered the resolution. Coupled with the strong incoherent scattering due to H_2O, this meant that a reliable conversion to Gd^{3+}

[43] The technique consists of two buckets connected in series. Both contain miscible liquids: one with a high density and one with lower density. For the creation of the smooth density gradient, liquid is withdrawn from the high density bucket, which is constantly refilled by the low density liquid.

[44] Gerald Oster (1918–1993) was an American physicist who held professorships in polymer science and biophysics. Apart from his scientific accomplishments Oster was renowned for his activities as an artist with a penchant for psychedelic art. Galleries in the mid 1960s would frequently exhibit his works that were inspired by his experiments in photopolymerisation as op art. In the 1980s he retired to Haiti, where he lived for 10 years until he succumbed to wounds sustained during a robbery.

concentration could not be performed. The negative logarithm of the transmittance, which is proportional to c_{Gd} is shown instead. The original location of the magnet prior to its removal is shown in Fig. 3.12(a).

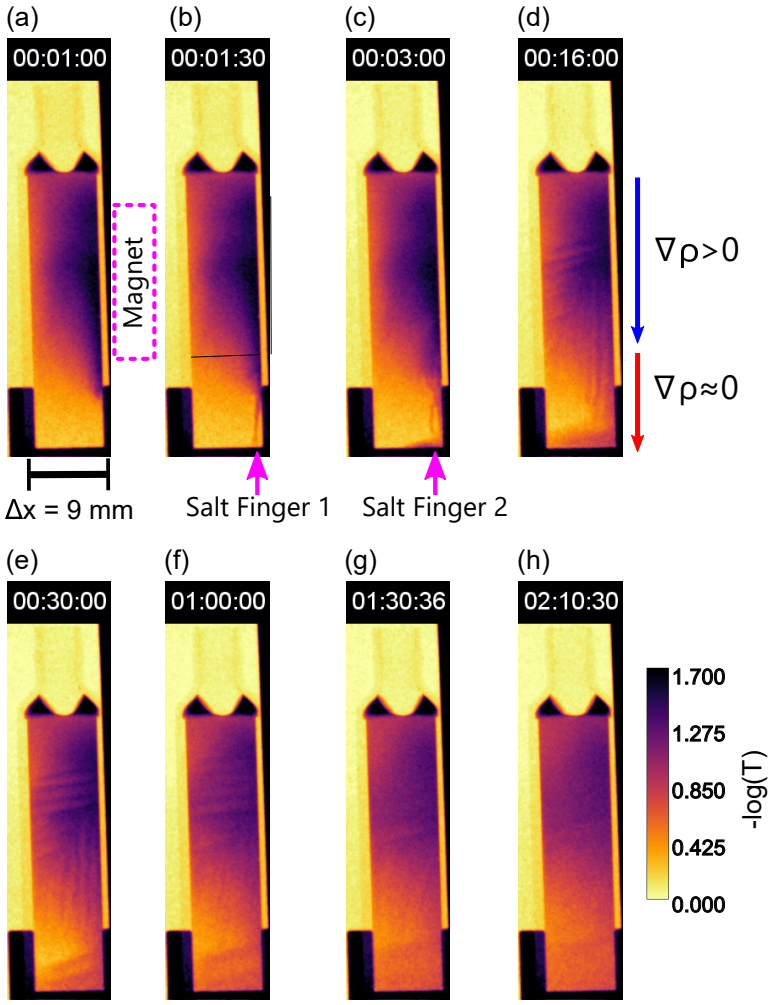

Figure 3.12 – Formation of horizontal salt fingers in a system of 1.7 M $Y(NO_3)_3$, 0.5 M $Gd(NO_3)_3$ and H_2O. The H_2O served to create a smooth vertical density profile. The images show $-\log(T) \propto c_{\mathrm{Gd}}$, after the removal of the 20 mm magnet. (a) Situation 1 min after the withdrawal of the magnet. Its original location right of the cuvette is shown. (b–c) The first two $Gd(NO_3)_3$ salt fingers treacle down into the $Y(NO_3)_3$ solution. (d–f) The interface of the $Gd(NO_3)_3$ solution is ripped up by horizontal salt fingers that remain static in the density gradient. (g–h) The horizontal salt fingers are washed out by diffusion and the stratification disappears.

The images show a system that is near static in the first minute after the magnet removal (Fig. 3.12(a)). This is in contrast to the case shown in Fig. 3.10, where the $Gd(NO_3)_3$ spread horizontally over the $Y(NO_3)_3$ solution after the loss of the stabilising magnetic field gradient. Here, the $Gd(NO_3)_3$ solutions remains practically stuck to the right side of the cuvette at first. But the apparent stability in Fig. 3.12(a) is ephemeral and the first two vertical salt finger appear below the $Gd(NO_3)_3$ solution after 1 min (see (b–c)). The Y^{3+} ions latch onto these fingers and

they drop to the bottom of the cuvette within a matter of seconds, pouring $Gd(NO_3)_3$ onto the cuvette floor.

A more remarkable observation is the formation of horizontal salt fingers in the top part of the cuvette with the smooth density gradient. These are difficult to discern in (c), 3 min after the magnet removal. After 16 min they become prominent in (d) and are visible for an hour afterwards. The Gd^{3+} concentration resembles the left half of a Christmas tree before it is washed out by diffusion.

The results show that buoyancy is critical in dictating the direction of the salt fingers. At the horizontal interface between the $Gd(NO_3)_3$ and the $Y(NO_3)_3$ towards the bottom of the cuvette, vertical salt fingers still formed as before. On the vertical interface of the $Gd(NO_3)_3$ drop, which was near the middle vertical line of the cuvette, the situation was different. The $Gd(NO_3)_3$ solution was initially in a mechanically stable position and resisted departure from its convex shape. Mechanical stability is ensured by the H_2O, which has created a smooth vertical density gradient together with both $Gd(NO_3)_3$ and $Y(NO_3)_3$. If there is such a density gradient, the salt fingers will not be able to minimise their potential energy in the gravitational field by dropping downwards. Instead the $Y(NO_3)_3$ will eat into the $Gd(NO_3)_3$ solution horizontally and the fingering instability will be driven purely by diffusion. This is still self-amplifying, as the area exposed to the $Y(NO_3)_3$ nitrate solution keeps increasing as the finger grows.

The stratification reached its greatest extent after 30 min and was washed out by diffusion after approximately two hours. The transmittance in the top part of the cuvette was still lower than in the $Y(NO_3)_3$ solution below after 2 h. This was in part due to incoherent scattering from water, but the vertical density gradient clearly delayed the mixing by gravity.

Horizontal salt fingers and the formation of a Christmas tree pattern have been previously observed. For example, when a stratified salt solution with a vertical salinity/density gradient is heated by a point source from below, horizontal salt fingers will also grow [484]. They emanate from the rising sharp plume of hot and salty solution that contracts while rapidly cooling off.

3.4. Conclusion

The experiments showed that a pre-existing concentration of paramagnetic fluid in some region can be redistributed within a miscible liquid by a magnetic field gradient. It is well known that the stray field of a permanent magnet can upset mechanical equilibrium and cause magneto-convection to deform the paramagnetic solution in the field gradient. In systems of miscible solutions, a concentration gradient will drive mixing by diffusion. This was shown for Gd^{3+} ions that diffused from a magnetically skewed profile of $Gd(NO_3)_3$ solution into D_2O. Slow magnetoconvection occurs to balance any changes to the mechanical equilibrium by the diffusing $Gd(NO_3)_3$ concentration profile.

The situation for multi-component diffusion is more complex. A tertiary system of 0.4 M $Gd(NO_3)_3$ – 1.3 M $Y(NO_3)_3$ – D_2O–H_2O was shown to be dynamically unstable, prone to the formation of salt fingers at the interface between the rare earth nitrate solutions. Double-diffusive convection causes this stratification and the homogenisation is driven by the descent of

the fingers in the gravitational field. As the diffusion coefficient is inversely proportional to the viscosity, which is 25% higher for D_2O than H_2O, solutions with regular water are also expected to be unstable. Instabilities between aqueous solutions and those with organic solvents, such as ethanol or glycerol, are likely to form.

It was shown that the magnetic field gradient precludes double-diffusive convection by stabilising the interface between the paramagnetic and non-magnetic solution. This is accomplished by shifting the condition for mechanical equilibrium in such a way that it is energetically unfavourable for the fingers to form. For a horizontal boundary, the fingering instability will grow in the direction of gravity and be accompanied by a loss in potential energy [504]. Any magnetic field gradient of sufficient strength, which is non-parallel to gravity, will prohibit the salt fingering instability. An anti-parallel magnetic field gradient, as is the case when the magnet is places on top of the cell, will also prevent the fingering instability.

The implication of the increased stability against salt fingering instabilities is relevant to research on magnetic separation of rare earth ions. Even minor differences in diffusivity can precipitate salt fingering instabilities. The diffusion coefficient of the rare earth ions are similar at infinite dilution, but substantial changes are encountered when their concentrations vary or solutions with different solvents come into contact. If left unchecked, double-diffusive convection can mix separated solutions of rare earths.

This is particularly pertinent when natural convection is invoked via heating. The thermal diffusivity ($k = 10^{-7}\,\mathrm{m^2\,s^{-1}}$) of a salt solution is roughly 100 times higher than its mass diffusivity ($D = 10^{-9}\,\mathrm{m^2\,s^{-1}}$). Hence, salt fingering instabilities can form by rapid cooling of hot and salty layers above cold and fresh ones. Input of thermal energy created density gradients in the original magnetically aided thermodiffusive separation reported by Ida and Walter Noddack. Magnetoconvective flow was able to alter the thermodiffusive processes in these experiments.

More recently, thermal energy has also been used to evaporate water from the surface of paramagnetic rare earth solutions [154,155,161,162,164–166]. A magnet above the surface is then able to levitate the enriched layer above the bulk solution. The potential role of thermohaline double-diffusive convection to these experiments can be understood from the 2020 paper by the Eckert group titled “Stability criterion for the magnetic separation of rare-earth ions”. In this publication, Lei et al. report a maximum enrichment of 30 mM in the evaporation layer from 0.5 M bulk solution of $DyCl_3$. However, this layer begins to leak Dy^{3+} ions vertically after around 30 s from a hydrodynamic instability at the apex of the convex magnetically enriched contour (see Fig. 3.13). Further evaporation refreshes the concentration in the enrichment layer, but the instability sets a natural boundary to the extent of the enrichment layer.

The authors explained the observed instability in their following publication [166] as a Rayleigh-Taylor instability of the enrichment layer brought about by magnetoconvection vortices into the magnetic field gradient. This downward flow of the $DyCl_3$ solution can pick up enough kinetic energy to escape the magnetic field gradient and sink with gravity. This effect may be amplified by a heated top layer and thermal contraction thereof. Thermal diffusion will cool down the warm enriched solution on the top within seconds, which increases the density. This is accompanied by decreased buoyancy and a salt finger is formed. The Dy^{3+} ions are

unable to escape the salt finger on such short timescales because this is governed by slow mass diffusivity. The threat of instability due to thermohaline salt fingering instabilities can be expected to remain in the presence of a magnetic field gradient.

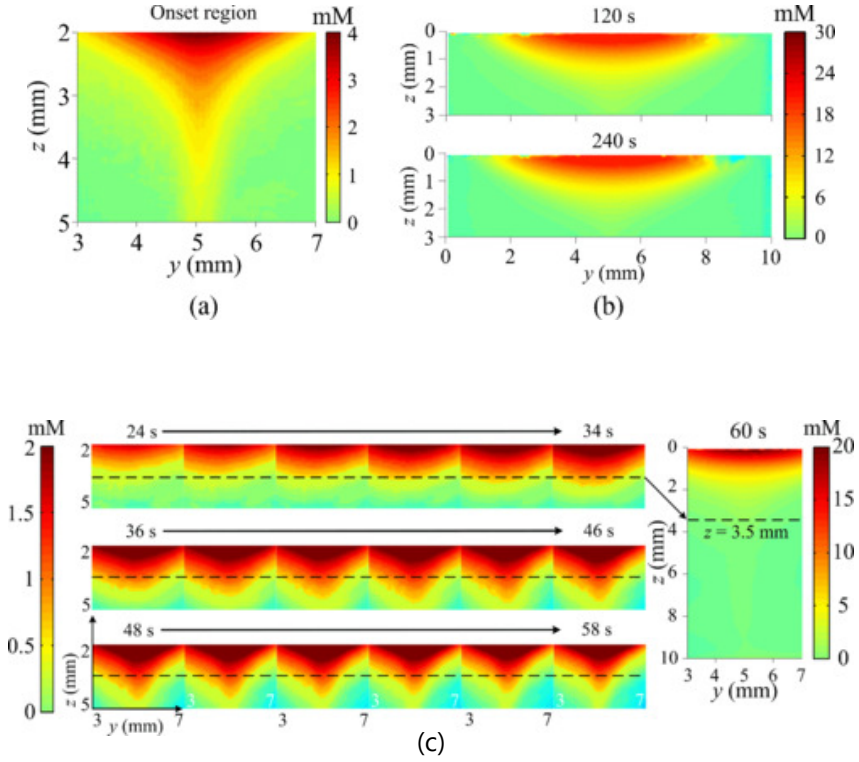

Figure 3.13 – Observed hydrodynamic instability in magnetically levitated evaporation layer of $HoCl_3$ (From [165]). The bulk solution has a concentration of 0.5 M and a 10 mm cube magnet is above the surface. (a) A strand of 2 mM solution breaks free of the magnetic confinement and drops to the cell, 30 s after the enrichment layer is established. (b) The entire enriched layer from which the instability forms is shown with a different concentration range. (c) Formation of the instability. Reproduced with permission from [165]. Copyright 2020, American Physical Society.

Besides the relevance for magnetic rare earth separation, salt fingering instabilities with a paramagnetic component are of general interest in ferrohydrodynamics. Magnetically driven diffusion instabilities of ferrofluids were discovered in the early 1980s in Latvia [505, 506] and are still under active investigation [507–510]. The experiments are performed in Hele-Shaw cells, which have a thin gap. It was shown that a magnetic field can profoundly influence the growth of these double-diffusive instabilities [507–510]. Images of magnetically driven micro-convection in a Hele-Shaw cell reported by Ērglis et al. in 2013 [507] are shown in Fig. 3.14. The rivalry between gravity, diffusion and magnetic forces lies at the heart of further investigations for ferrofluids. Such micro-convective flows are interesting for any envisaged microfluidic application.

For ferrofluids with $\chi \approx 1$, modest homogeneous magnetic fields of 1 mT are enough to accelerate or even drive these instabilities (see Fig. 3.14) [507, 511]. In the case of paramagnetic salt solution $\chi \approx 10^{-3}$ stronger fields are necessary to influence the interface. The modification of the free surfaces of paramagnetic liquids by normal Maxwell stress contributions has recently

been demonstrated in sessile drops [512,513] and as oscillatory magnetic deformations [514]. In addition, the diffusion coefficients of ions are two order of magnitude higher than those of the colloids in ferrofluid. Different ionic diffusion coefficients could also be obtained by employing organic solvents for the solutions. Whether a magnetic effect could be measured for paramagnetic salt fingering instabilities is an open question and could be a topic of a concerted study of rare earth solutions.

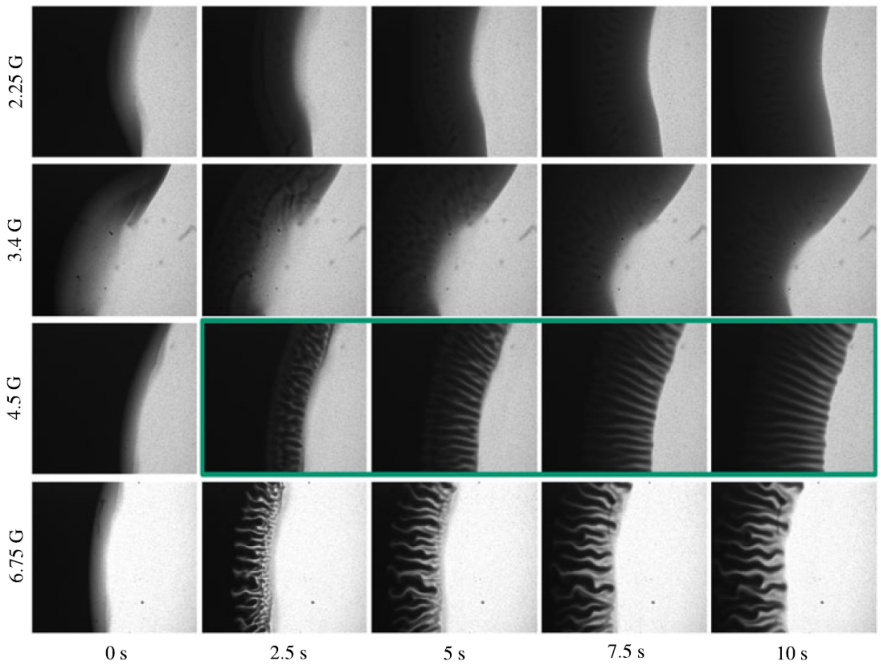

Figure 3.14 – Magnetically created fingering instability between a magnetic ferrofluid and miscible non-magnetic water-glycerine mixture in a Hele-Shaw cell [507]. The magnetic field is shown in Gauss ($1\,\mathrm{G} = 10^{-4}\,\mathrm{T}$). It points out of the image plane and the images with the threshold value for the magnetic instability (4.5 G) are framed in green. Reproduced with permission from [507]. Copyright 2013, Cambridge University Press.

Such a study would only make use of neutron imaging in the unlikely event that there were to be an interest in solutions of D_2O. Although it was shown that neutron imaging is a viable method for capturing quasi two-dimensional convective and diffusive processes in solutions containing Gd^{3+} ions, this is not the experimental technique of choice. Comparatively low temporal resolution and spatial resolution in the order of 50 µm stand in the way of obtaining high quality time-resolved images. Furthermore, the presence of neutron scattering hampers the quantitativeness of the obtained data. Most importantly, it is an expensive method and limited to only around 50 stations at neutron sources worldwide [441]. A significant number of these have low flux and are unsuited for dynamic imaging.

Interferometric techniques are clearly much more suitable to study solutions of a single component. In multicomponent system with two rare ions, interferometric analysis becomes more difficult because the phase shifts are often similar. Usually, real space image with a high resolution camera can be employed instead of interferometers. For this to work, one of the rare earth

solutions must have a colour. If both solutions are colourless, as was the case for $Gd(NO_3)_3$ and $Y(NO_3)_3$, a slowly diffusing dye can be added. Alternatively, illumination with ultraviolet light can be employed. The classic choice would be to use either shadowgraph or Schlieren techniques.

If neutrons are chosen to image Gd^{3+} concentration, radiographic imaging with cold neutrons is discouraged due to the restrictively low concentration and path length ranges. This is caused by the absorption cross section, which is twice that for thermal neutrons. Thus, imaging Gd with thermal neutrons is preferable in most situations. Ideally, Gd^{3+} concentration would be imaged in porous media, which are inaccessible to optical techniques. The penetrative properties and great sensitivity of the neutrons to Gd shine in such a study. This is the topic of the next chapter.

4. Neutron Imaging Capacitive Deionisation of Paramagnetic Solutions

Nichts ist drinnen, nichts ist draußen;
denn was innen, das ist außen.

JOHANN WOLFGANG VON GOETHE
(1749–1832), Epirrhema

4.1. Introduction

The previous section dealt with binary systems containing paramagnetic $Gd(NO_3)_3$ solutions. These were created artificially and the system reimposed thermodynamic equilibrium by diffusion, which was assisted by convection in multicomponent diffusive systems. Magnetoconvection of a paramagnetic solution in magnetic field gradients only occurs when a concentration gradient of the paramagnetic ion species is present. To create this, the concentration term in the chemical potential $RT\ln(a_i)$ (with $RT = 2.5\,\mathrm{kJ\,mol^{-1}}$ and the activity a_i, see Section 2.1) must be overcome by introducing energy into the system [172, 515–518]. This is in the order of $\mathrm{kJ\,mol^{-1}}$ for concentrated solutions, whereas the magnetic energy for a $Gd(NO_3)_3$ solution in a magnetic field of 1 T is $E_{\mathrm{mag}} = \frac{\chi}{2\mu_0}B^2 \approx 130\,\mathrm{mJ\,mol^{-1}}$ (with $\chi = 330 \times 10^{-9}\,\mathrm{m^3\,mol^{-1}}$ [47]). Magnetic forces can deform the bulk paramagnetic fluid or move it in a gravitational potential. An example for the Kelvin force distribution for Gd^{3+} ions in the stray field of a permanent Nd-Fe-B magnet is shown in Fig. 4.1(a). The Kelvin force can reach $1\,\mathrm{N\,mol^{-1}}$ for paramagnetic solution in common field gradients.

In comparison, ions in electrostatic potentials $\Phi \approx 10\,\mathrm{mV}$ have sufficient energy to overwhelm the concentration term. For trivalent ions (valence charge $Z = 3$), the energy at $\Phi = 10\,\mathrm{mV}$ is $E_{\mathrm{el}} = ZF\Phi = 2.9\,\mathrm{kJ\,mol^{-1}}$, with the Faraday constant $F = 96\,485\,\mathrm{C\,mol^{-1}}$. The driving force on ions is generated by gradients of the electric potential $\nabla\Phi$ and the subsequent movement is known as migration (see Section 2.2.1). The corresponding expression for the force is $F_{el} = -FZ\nabla\Phi$. An electric double layer forms at the interface between a charged electrode and an electrolytic solution. This region is of the order of 3 nm with a potential gradient of $\nabla\Phi = 10^7\,\mathrm{V\,m^{-1}}$ [173]. Hence, the resulting forces[45], $\sim 10^{12}\,\mathrm{N\,mol^{-1}}$, are sufficiently gigantic for charge separation, and a mass transport-limited diffusion layer is formed through which the ions travel. Thus, a current with a diffusion and migration component flows. The current distribution in a cell with two cylindrical electrodes is shown in Fig. 4.1(b).

An energy-efficient approach for the continuous removal of ions from water is capacitive deionisation [321, 326], which was introduced in Section 2.3.4. This relies on the immobilisation of ions in the electric double layer of porous electrodes with enormous surface areas. Once the pores of the electrodes are filled, the fully charged electrodes can be discharged and the ions are released into the surrounding liquid. Then, the cycle begins anew. This cyclic process, in

[45] These values are for illustrative purposes. In general, the potential between differing media is thermodynamically defined, not electrostatically [168, 179]. The definition of an artificial electrostatic force does not hold.

which the ions are not transformed into a solid, makes the procedure more attractive for hard to plate ions, such as trivalent rare earths. What is more, capacitive deionisation is far more energy efficient than a desalination based on evaporation.

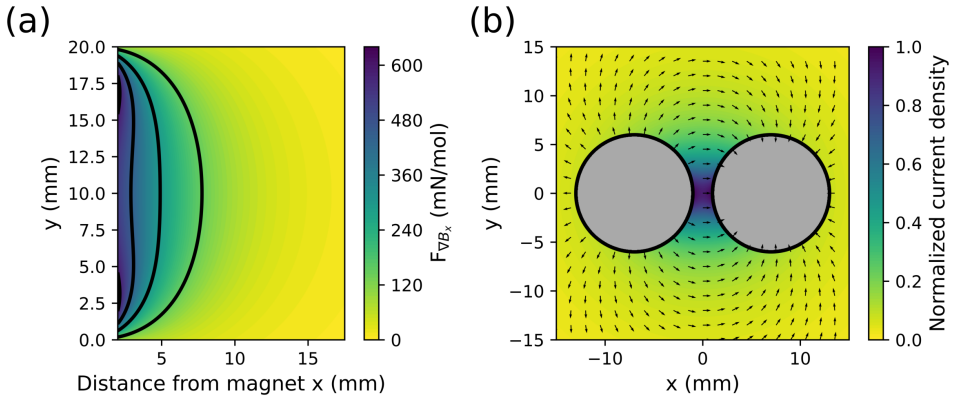

Figure 4.1 – (a) Kelvin force distribution for Gd^{3+} ions in the field of a uniformly magnetised 20 mm Nd-Fe-B cube. The magnetic charge model was used [470] (see Appendix A.1). (b) Normalised current distribution between two cylindrical electrodes of 12 mm diameter in a liquid with uniform conductivity [519]. The separation between the electrodes is 2 mm.

Although magnetic forces pale in comparison with those of electric nature, previous studies have shown that electrodeposits from solutions containing paramagnetic ions can be structured on electrodes with magnetic field gradients [66, 69–82]. In these depositions, the paramagnetic ions in solution are converted at the working electrode, causing a concentration gradient and convective flow, which the magnetic field gradient drastically alters. In comparison, the influence of a magnetic field gradient on an electrochemical cell with desalinating porous electrodes remains uncharted territory. There are two reasons why such an investigation is of particular interest. Firstly, magnetic field enhanced magnetic storage devices such as batteries and supercapacitors have been recently reported [520]. Secondly, the separation of rare earth ions in functionalised mesoporous hybrid structures has become a new method under investigation [521, 522] (and references within).

This chapter focuses on dynamic neutron imaging studies of the capacitive deionisation of paramagnetic $Gd(NO_3)_3$ solutions. The reasons behind the choice of $Gd(NO_3)_3$ salts for the solutions were listed in the previous chapter. Unlike methods such as small-angle neutron scattering that provide information on ion adsorption by pores in reciprocal space [523, 524], neutron imaging yields a direct transmission profile in real space[46]. The technique has previously found use in the study of lithium batteries [526, 527] and capacitive deionisation with ordered mesoporous carbon electrodes of ∼10 nm pore size [528–530]. The first of these capacitive deionisation studies was restricted to a relatively dilute $Gd(NO_3)_3$ solution of 8.74 mM in a flow-through cell and neutron images were obtained every 5 min [528]. Later studies of lithium (Li) ion dynamics were performed with ^{6}LiCl solution at higher concentrations [529, 530]. These experiments used cold neutrons, which amplify the absorption cross sections. In contrast to

[46] Desalination of $GdCl_3$ in a reverse osmosis system has also been quantified by monitoring the absorption in small-angle neutron scattering signals [525].

the previous chapter, the neutron imaging experiments at the heart of the present chapter were performed with thermal neutrons with $\sigma_a = 46\,600$ barn.

This chapter is split between capacitive deionisation experiments with carbon aerogels (Section 4.3) and microporous activated carbon cloths (Section 4.4). Both of these porous carbon samples were characterised prior to the neutron imaging experiments and an introduction to their respective properties is given before the neutron imaging experiments are described.

4.2. Methods and Materials

The porous carbon materials were characterised prior to the neutron imaging experiments. First, their surface morphology was recorded with SEM. Then, the porous properties were quantified with mercury porosimetry and nitrogen adsorption measurements (BET surface analysis). Mercury porosimetry is a technique with which pore diameters and total pore volume can be measured by monitoring the intrusion of pressurised non-wetting mercury into the material. For micropores (< 2 nm) and mesopores (< 50 nm), nitrogen gas adsorption must be employed to give an in depth overview of the pore size distribution and surface area. This is based on the physisorption of inert nitrogen gas on the solid carbon walls, which is recorded as adsorption/desorption isotherms [531]. The instruments and techniques will be introduced in the corresponding characterisation sections 4.3.1 and 4.4.1. Although a succinct description of the individual methods will be given, readers are referred to review articles on pore size determination for further information [531–533]. Differential scanning calorimetry/thermogravimetric analysis and x-ray diffraction were used to ensure the purity of the carbon sample content. The neutron imaging instrumentation that was used for all capacitive deionisation experiments will be described below.

4.2.1. Neutron Imaging Instrumentation

Neutron imaging experiments were performed at the measuring position 2 of the NEUTRA station [534] in the Paul Scherrer Institute. This station operates with thermal neutrons from a 25 meV Maxwellian spectrum. The neutron flux at the sample position was approximately $1.3 \times 10^7\,\mathrm{cm^{-2}\,s^{-1}}$. The thermal neutrons made probing higher path lengths of $Gd(NO_3)_3$ solution possible in comparison to the experiments with cold neutrons at the IMAGINE station at Laboratoire Léon Brillouin (see previous chapter).

The detection system consisted of a 30 µm thick terbium doped Gadox (Gd_2O_2S:Tb - terbium-doped gadolinium oxysulfide) scintillator, fitted in the MIDI camera box and coupled with a CCD camera (Andor, iKon-L). Gadox scintillators detect neutrons by the same neutron capture processes that are used in absorption studies of Gd^{3+} solutions. These were already introduced in Eqs. 3.1 and 3.2 of the chapter, but will be repeated here:

$$^{155}\mathrm{Gd} + {}^{1}\mathrm{n} \longrightarrow {}^{156}\mathrm{Gd} + \gamma + \text{conversion electrons (7.9 MeV)}. \tag{4.1}$$

$$^{157}\mathrm{Gd} + {}^{1}\mathrm{n} \longrightarrow {}^{158}\mathrm{Gd} + \gamma + \text{conversion electrons (8.5 MeV)}. \tag{4.2}$$

The conversion electrons in these reactions stimulate the scintillation of the Gadox[47]. Effective cross section of the ^{155}Gd/^{157}Gd nuclear reactions are significantly larger than for ^{6}Li in ^{6}LiF/ZnS scintillators (see Eq. 3.3 in previous chapter) [537, 538]. This means that Gadox scintillator layers are thinner and detect neutrons more efficiently [537–540]. What is more, the free mean path of the conversion electrons ($R_{ce} = 12\,\mu m$) in Gadox is one magnitude below that of the emitted ^{3}He nuclei in ^{6}LiF/ZnS scintillators [538]. Disadvantages of Gadox scintillators in neutron imaging are mainly the high sensitivity to x-rays and lower light output by the scintillation due to the conversion electrons.

Recorded images of 2048×2048 pixels corresponded to a field of view of 67.67 mm × 67.67 mm with a pixel size of 33.04 µm. The pixel size was measured with a Siemens star (see Fig. 4.2(a)) [541]. Series of neutron images were acquired with an exposure time of 10 s and read out time of approximately 3 s. Occasional interruptions of the imaging sequence were caused by fluctuations of the neutron beam intensity. Such occurrences were more frequent at NEUTRA than at the IMAGINE station in the Laboratoire Léon Brillouin, because the neutrons originated from a spallation source (Swiss Spallation Source: SINQ) and not from a reactor with smoother output.

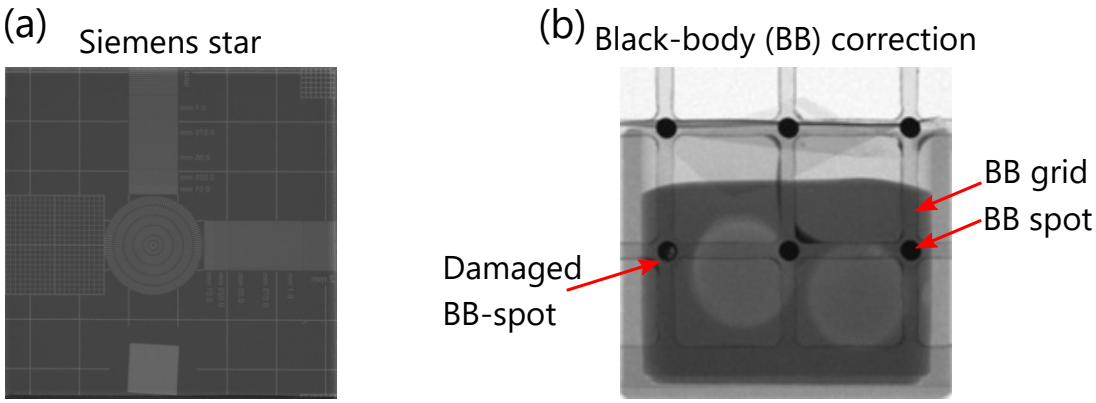

Figure 4.2 – (a) Siemens star for the determination of the pixel size [541]. (b) Neutron image with the black-body grid in place. The silhouette of the Al grid can be discerned in front of the cuvette. Black spots consisting of a Gd based material block the neutrons from transmitting to the detector behind them. Any detected intensity is due to scattered neutrons and can be removed via interpolation. However, here this was not possible due to the damaged black spot in the left of the image.

Unlike the neutron imaging experiments at the IMAGINE station, the neutron imaging group at the Paul Scherrer Institute routinely correct for sample and background neutron scattering in their imaging experiments. Since 2018, a black-body grid has been used to quantify the scattering contribution [460, 461]. The black-body grid is made of Gd containing circular spots, which completely absorb the incoming neutrons. Any detected intensity on the detector behind these spots can be assumed to stem only from scattering. An interpolation can be performed to remove this contribution.

[47] The radiative neutron capture of Gd salts is also used in particle physics. For example, the performance of the SuperKamiokande neutrino detector was significantly improved by dissolving 100 t of $GdCl_3$ in the gargantuan tank of 50 000 kt ultrapure water surrounded by the Cherenkov detectors. The reaction of the electron antineutrinos with protons is $\overline{\nu}_e + p \rightarrow e^+ + n$ and the Gd^{3+} helps the detection of the neutrons [535, 536].

For dynamic neutron imaging this correction is less common, as the transmission profile is continuously modified. One way to still use the black-body correction is to only take images with the grid in place when the system is quasi-static and no longer changing. A neutron image with the black-body grid in place is shown in Fig. 4.2(b). Unfortunately, these attempts were not met with success. The main reason for this was that a black-body grid with a damaged Gd spot was used, which can be seen in Fig. 4.2(b). This made an interpolation impossible. Furthermore, the grid was not dense enough for the samples used here and placed too low. For this reason, no scattering correction of the data could be performed and the analysis followed that in the previous section.

A more severe repercussion of the failed black-body correction was that certain parts of the time-sequenced dynamics were lost, because either the grid was in front of the experiment or was being removed from the chamber. The grid was made of aluminium, which becomes activated by neutrons, albeit with a short decay time. In general, approximately 10 min worth of time-sequenced images were lost before and after every measurement due to this.

The first of the experiments performed at the NEUTRA station was the neutron imaging of the capacitive deionisation with carbon aerogels (Section 4.3). The motivation behind this will be discussed at the beginning of Section 4.3 below. After this, the characterisation of the aerogels and the results of the neutron imaging experiments will be described in Sections 4.3.1 and 4.3.2, respectively.

4.3. Capacitive Deionisation with Carbon Aerogels

Aerogels are materials with extremely low density and high porosity. They are formed from gels in which the liquid component has been substituted by gas, while the gel structure stayed intact. Aerogels behave like solid foams in many ways, although they are generally much more brittle and shatter like glass when exposed to pressure. Samuel Stephens Kistler discovered silica aerogels in 1931 [542] and these are used as thermal insulators due to their negligible heat conductivity. In 1989 Pekala reported a new class of organic aerogels derived from the polycondensation of resorcinol with formaldehyde [543], while working at the Lawrence Livermore National Laboratory (LLNL). These transparent resorcinol–formaldehyde aerogels are composed of approximately 10 nm large nanoparticles and have a dark red tinge [543–545]. Shortly after their discovery, it was recognised that resorcinol–formaldehyde aerogels could be be pyrolysed under inert atmosphere in order to form vitreous carbon aerogels [544]. These are the aerogels that will be investigated in this section.

Carbon aerogels combine many properties that are beneficial to their use as porous carbon electrode. The main highlights are their monolithic mesoporous structure, huge surface area and good electrical conductivity. This was directly realised by the researchers at the LLNL in a 1993 publication [546], in which they presented an “aerocapacitor”, which was essentially a supercapacitor. An application with a more long-lived impact was the use of carbon aerogels as capacitive deionisation electrodes, first reported by Farmer in 1996 [515, 547, 548]. A curious fact is that the term “capacitive deionisation” was coined in these publication [326], which kick-

started research in this area that continues to the present day. Prior to this, only activated carbons had been used. Although the commercialisation attempt of capacitive deionisation with carbon aerogels by the group at the LLNL eventually ran into a brick wall, mainly due to low efficiency of the salt adsorption, the technique has not ceased to attract the attention of researchers [345,549–554]. Noteworthy are models that explain the adsorption in electric double layer, reported first by Yang et al. [550] and then further developed by Ying et al. [549].

The neutron imaging experiments described here concerned the electrosorption of paramagnetic Gd^{3+} by carbon aerogel monoliths. The results have been published [555]. First, the characterisation of the samples is described.

4.3.1. Carbon Aerogel Characterisation

Resorcinol-formaldehyde polymer [543,545] derived carbon aerogel monolith disks of approximately 12 mm diameter were purchased from Aerogel Technologies. The disks were concave with 3 mm thickness on the sides and 2 mm in the centre. Their cross section is shown in Fig. 4.9 (b), which can be found in Section 4.3.2 below. The bulk density was approximately $0.25\,\mathrm{g\,cm^{-3}}$. The samples underwent characterisation, which will be the subject of the present section.

Scanning Electron Microscopy

A shard of the carbon aerogel was analysed by SEM at various magnifications (see Fig. 4.3). The sample had a smooth visual appearance with some cracks on the millimetre scale (see Fig. 4.3(a)). These cracks, or fracture surfaces, exposed the arrangement of carbon nanoparticles. The interparticle spacing between the carbon nanoparticles gives rise to porosity, which appears as darker regions in the image. These mesopores are clearly visible as voids between the carbon nanoparticles in the higher magnification micrographs in Fig. 4.3 (e-f). Separately, clumping and agglomeration of microscopic carbon result in macroporosity. An example of this is a porous opening in the order of 1 µm, visible in the top right hand corner of Fig. 4.3(c).

In order to estimate the pore size distribution from a scanning electron micrograph, pores were identified in a selected SEM image (see Fig. 4.4). These labelled pores are shown in Fig. 4.4(a). The diameter of the pores was then extracted as the Feret diameter, which was binned to count pore diameter frequencies. A histogram of binning with 10 bins is shown in Fig. 4.4(b). The resultant pore size distribution has a maximum at 100 nm and is asymmetric. The average of the extracted pore diameters was calculated around 94 nm.

Although these values are a useful guide to the mesopore distribution in the carbon aerogel, they do not provide a reliable quantitative result. Pores below 25 nm are beyond the resolution of the SEM. Furthermore, the SEM is surface sensitive and struggles to detect pores hidden deeper in the sample. Identifying the pore networks responsible for the interparticle mesoporosity is not possible from two-dimensional images. However, mercury porosimetry, which is based on the intrusion of a non-wetting liquid into the material, combined with gas adsorption analysis, are suitable techniques to quantify the porous properties of bulk materials.

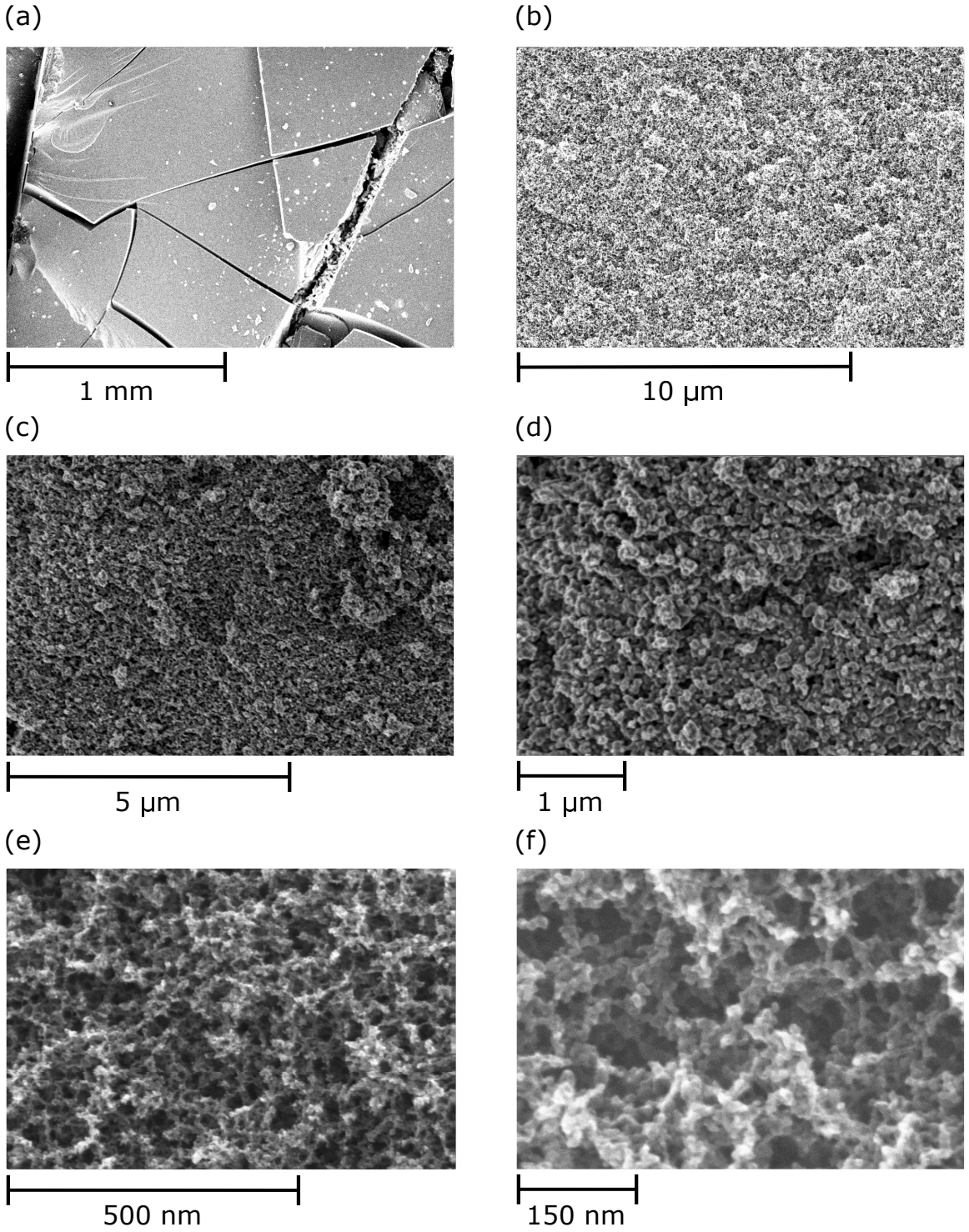

Figure 4.3 – **SEM images of carbon aerogel.** (a) The carbon aerogel shard at low magnification. (b-d) A network of 100 nm globules becomes visible at higher magnification. This morphology is responsible for the macroporosity. (e-f) Mesopores are indicated by dark voids at the highest magnification. A large portion of the mesopores is far below the resolution of the SEM.

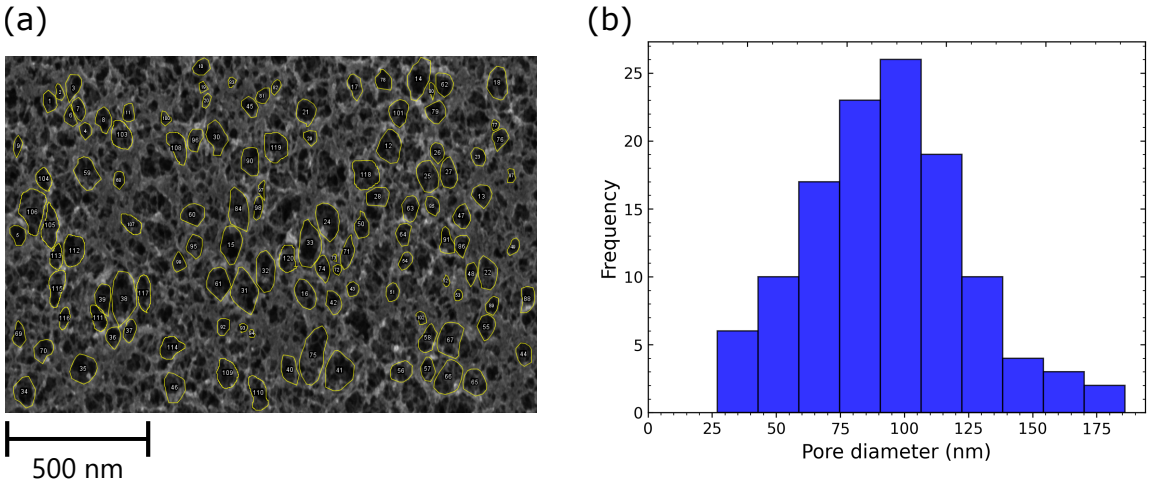

Figure 4.4 – Pore size distribution from SEM image. (a) SEM image of the skeletal carbon particle network of the aerogel with identified pores. (b) A histogram of the extracted pore diameter after binning the Feret diameters of the pores.

Mercury Porosimetry and BET Surface Area Analysis

A quantitative determination of the pore size distribution was accomplished with mercury (Hg) porosimetry and Brunauer-Emmett-Teller (BET) surface area analysis (see Fig. 4.5). The instruments used were an Autoscan-33 Porosimeter (Quantachrome, UK) and a Nova 2400e Surface Area Analyser (Quantachrome, UK) with nitrogen gas adsorbate. Mercury porosimetry was performed up to a maximum pressure of 33 000 psi with a default contact angle of 140° between mercury and carbon. Prior to analysis, the carbon aerogel particulates were de-gassed for 1 h at 200°C under vacuum.

Mercury porosimetry revealed pores in the approximate range 7 nm-10 µm (see Fig. 4.5(a)). The dashed curve in Fig. 4.5(a) shows the intrusion of mercury into the aerogel as a function of pressure. This behaviour is encapsulated by the Washburn equation [556], which relates the pressure of the liquid Hg (P_{Hg}) to the pore diameter of cylindrical pores (D_P):

$$P_{\mathrm{Hg}} - P_G = -\frac{4\sigma\cos\theta}{D_\rho}. \tag{4.3}$$

The variables P_G, σ and θ are the gas pressure, Hg surface tension and Hg contact angle respectively. Mercury porosimetry is performed under vacuum and P_G drops out. The surface tension σ of Hg at 20°C under vacuum is 480 mN m^{-1}. With this value and $\theta = 140°$, Eq. 4.3 becomes:

$$D_P = \frac{1470\,\mathrm{kPa}}{P_{\mathrm{Hg}}}\ [\mu\mathrm{m}], \tag{4.4}$$

with pore diameter inversely proportional to the pressure. During mercury intrusion, large pores fill first, followed by increasingly smaller ones.

Little activity was observed in the initial low pressure range. An increase of pressure caused the gradual filling, first of large pores of 2 µm to 150 nm diameter. This filling continued until a significant intrusion of mercury occured for pores <150 nm diameter. The intrusion proceeded

to approximately 20 nm, with the total pore volume up to this point equalling 2.5 $cm^3\,g^{-1}$. Then a further pronounced intrusion of mercury occured in the mesopore range, beyond which the curve plateaus out as all pores are fully filled.

The solid curve in Fig. 4.5(a) shows the pore size distribution, plotted as the derivative of volume with respect to pressure. Large changes in volume over small pressure ranges yield sharp peaks, and vice versa. A large broad peak with a maximum at 115 nm was found in the range 20 nm-10 µm. These pores account for 2.5 $cm^3\,g^{-1}$ of the 3.62 $cm^3\,g^{-1}$ total pore volume, which corresponds to 69%, on a volume basis. The broad peak is flanked by a sharper peak representing a high concentration of mesopores between 10 and 20 nm. These account for 1.12 $cm^3\,g^{-1}$, or 31% of the sample, on a volume basis. This sharp peak indicates a high concentration of mesopores, constricted to a tight size range. These are of utmost importance to ion storage and particularly capacitive deionisation, because overlapping of the electrical double layers formed on these are avoided.

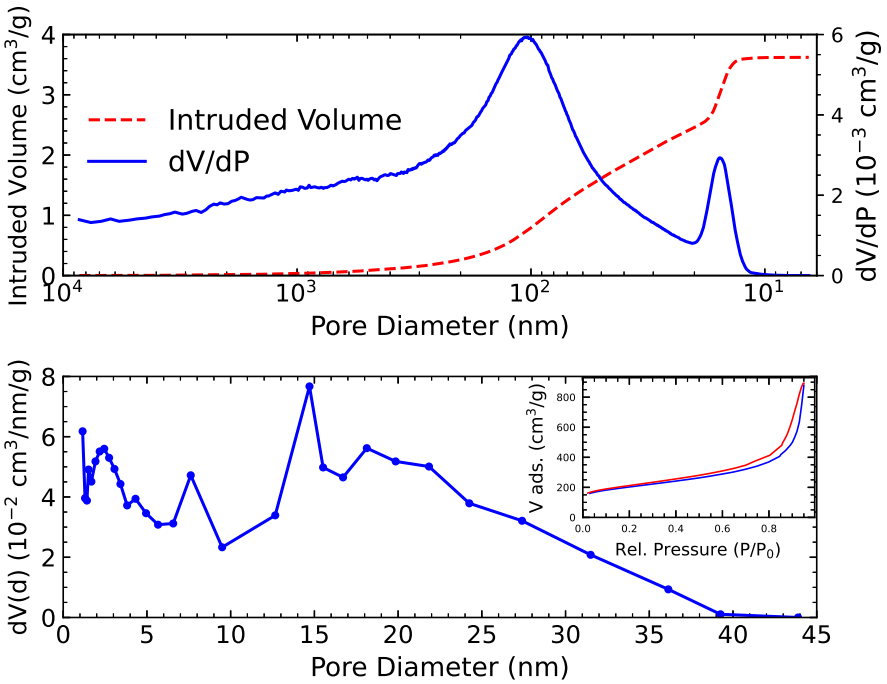

Figure 4.5 – Pore size distribution of carbon aerogel sample. (a) Hg porosimetry with two pronounced regions of pores with maxima at 115 nm and 16 nm. (b) BJH pore size distribution of the mesopores; inset: Type-IV nitrogen adsorption isotherm (blue: adsorption, red: desorption). The measured BET surface area is 720 $m^2\,g^{-1}$.

In order to better understand the mesoporosity, which provides the high surface area for capacitive deionisation, BET surface area analysis [557] was carried out. A surface area of 720 $m^2\,g^{-1}$ was measured by five-point BET analysis. The isotherm was Type-IV [558], with hysteresis for P/P_0 values above approximately 0.6 (see inset of Fig. 4.5(b)). The Barrett-Joyner-Halenda (BJH) method [559] was used to calculate the pore size diameter and pore volume, from the desorption branch of the isotherm (see Fig. 4.5(b)). This yielded pores in the range of 1-40 nm and a total adsorbed volume of 1.28 $cm^3\,g^{-1}$. Sub-10 nm pores account for

approximately 0.4 $cm^3\,g^{-1}$ of this. Within this size range lie two peaks: a broad peak at 2.5 nm and a sharper peak at 7.5 nm. This porosity could not be detected by porosimetry as it falls outside the measurement range of the instrument. In addition, the BJH method is not valid for micropores and other models would have to be used for their characterisation [560, 561].

The remaining mesoporosity is above 10 nm and accounts for 0.88 $cm^3\,g^{-1}$. The main feature within this size range is the presence of a peak at 14.7 nm, with further significant porosity occurring up to 40 nm. The sharp peak at 16.4 nm in the Hg porosimetry (Fig. 4.5(a)) is consistent with the maximum at 14.7 nm observed in the BJH analysis.

The porous properties agree well with the corresponding morphology uncovered by SEM (see Fig. 4.3). The detected macropores are clearly visible in the SEM images. Spacings between the carbon agglomerates give rise to the primary porosity of circa 100 nm. This loosely-packed morphology has a high pore volume (2.5 $cm^3\,g^{-1}$), consistent with a low bulk density material having an open, interconnected pore network and 89.1% porosity. However, most of the mesopores below 25 nm could not be observed by SEM analysis.

Surface areas of aerogels are usually between 400-1100 $m^2\,g^{-1}$ [321, 549, 550, 562–564] and the measured value of 720 $m^2\,g^{-1}$ lies in the middle of this range. Bimodal pore size distributions in carbon aerogels have previously been reported, although the locations of the two peak maxima tend to vary slightly [549, 550].

Differential Scanning Calorimetry and Thermogravimetric Analysis

Differential scanning calorimetry (DSC) and Thermogravimetric analysis (TGA) were performed in order to confirm the pure carbon composition of the carbon aerogel monolith, free from any organic residues. DSC/TGA measurements of small fragments (∼1 mm) of the carbon aerogel disks with a scan rate of 5 K per minute are shown in Fig. 4.6. Two different conditions were used: air and flowing inert nitrogen. The carbon aerogel combusts above 500 °C in air (Fig. 4.6 (a)). The sample weight plummets and the DSC shows an exothermic peak.

The carbon aerogels absorb moisture from their surroundings and this manifests as a slight weight loss before the combustion in the TGA. In the absence of oxygen, no combustion occurs. Weight changes under nitrogen atmosphere are therefore predominately due to water loss (Fig. 4.6 (b)). Carbon does not react with nitrogen under temperatures of around 2000 °C. In all likelihood, the slight weight loss above 200 °C is caused by a baseline drift of the TGA. The results show that the resorcinol-formaldehyde polymers were completely pyrolysed with no organic residues present within the carbon matrix.

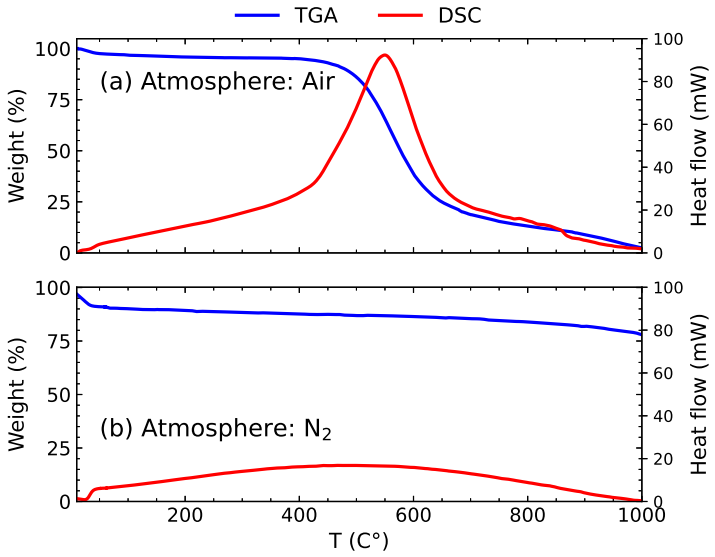

Figure 4.6 – **DSC/TGA measurement of carbon aerogel.** (a) In air: TGA (blue) and DSC (red) show the exothermic combustion of carbon at temperatures above 500 °C. (b) Carbon does not react below 2000 °C under nitrogen atmosphere. Weight loss is due to water in the porous structure.

X-Ray Diffraction

An x-ray diffraction pattern of the carbon aerogel monolith was obtained with a PANalytical Philips X'Pert Pro XRD System (Cu K_α radiation) and is shown in Fig. 4.22. All broad peaks are due to microscopic pieces of graphite, which are randomly distributed in the aerogel. The low angle (002) graphite peak is visible on top of the background at 22°. Peaks for (101) and (110) are located at 44° and 79° respectively [565, 566]. The dominant peak around 44° is due to (101), but it may be masked by (100) at 42°. There are no other contributions to the x-ray diffraction pattern as expected.

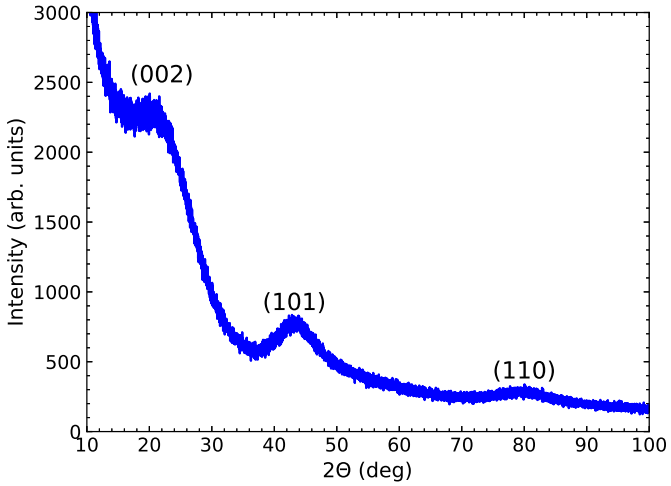

Figure 4.7 – **X-ray diffraction pattern of carbon aerogel monolith.** The broad peaks are all due to microscopic graphite particles.

4.3.2. Neutron Imaging of Capacitive Deionisation with Carbon Aerogels

Experimental Setup and Analysis Method

Fibre reinforced PTFE cells with outside dimensions of 34 mm × 28 mm × 10 mm (height × width × depth) and a path length of 6 mm were placed 12 mm from the detector (see sketch and neutron image in Fig. 4.9). PTFE is transparent to neutrons and easy to machine in comparison to quartz glass. The empty PTFE cell transmitted around 80% of the thermal neutron beam. The cutting tool with which the PTFE was hollowed out for the liquid cavity left a rounded edge on the sides of the cuvette and the path lengths here were in fact lower than 6 mm. But due to neutron scattering also changing the intensity at the sample edges, the transmittance could not be easily corrected because both effects overlap. This effect is restricted to a 0.5 mm zone and unimportant for the discussion.

Once again, the $Gd(NO_3)_3$ solutions were prepared in D_2O to avoid incoherent scattering from hydrogen nuclei. The transmitted neutron intensity I by the sample is given by the Beer-Lambert law:

$$I = I_0 \exp\left(-\sum_i \sigma_i N_A c_i \Delta z\right), \tag{4.5}$$

with the Avogadro constant $N_A = 6.022 \times 10^{23}\,\mathrm{mol}^{-1}$, the concentration c_i (in $\mathrm{mol\,m}^{-3}$), the neutron cross sections σ_i and the path length Δz. The argument of the exponential function is summed over all elements in the path of the beam. Neutron absorption by Gd is the dominant factor in the Beer-Lambert law. At high attenuation ($I/I_0 < 0.2$), the Beer-Lambert law loses its validity due to scattering events and a linear offset must be introduced as it was done in Section 3.2.3 of the previous chapter.

From the Beer-Lambert law, molarities between 50 and 100 mM Gd^{3+} solution were estimated as providing the best compromise between concentration and transmittance. To check this, calibrations with 20, 50, 70 and 200 mM $Gd(NO_3)_3$ solutions were performed to identify the most suitable concentration. The results are shown in Fig. 4.8. The broken blue line is a fit with the offset Beer-Lambert law (see Section 3.2.3) and the red line is the prediction based on the thermal neutron absorption cross section of Gd $\sigma_a = 46\,700$ barn (Eq. 3.6). Both curves coincide below 70 mM and it is possible to use the regular expression of the Beer-Lambert law. Thus, a molarity of 70 mM provided the best balance between contrast and concentration with a path length of 6 mm. This was low enough to avoid the high absorption limit, which is dominated by incoherent scattering, while retaining the Gd^{3+} concentration for the paramagnetic susceptibility [467].

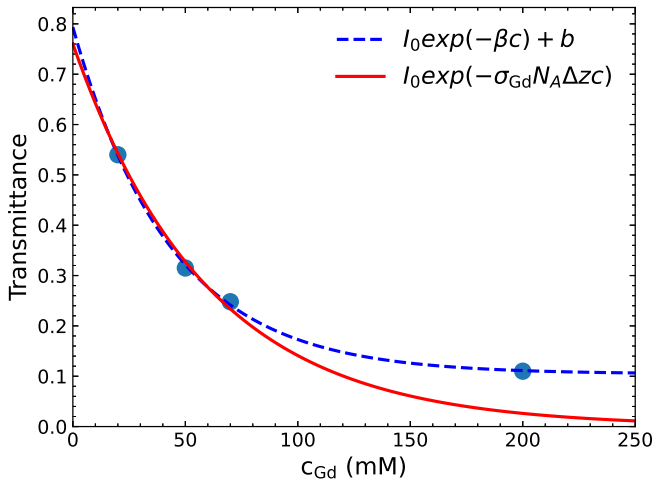

Figure 4.8 – Thermal neutron transmittance ($T = I/I_0$) calibration in PTFE cell with 6 mm liquid path length and 2 mm wall thickness. The concentration dependence of the transmittance follows the Beer-lambert law (red line) up to $Gd(NO_3)_3$ concentrations of 70 mM. Above these concentrations, an offset must be used (broken blue line).

Prior to the experiment, the carbon aerogel monoliths were soaked in D_2O to fill the pores. The D_2O percolated the aerogel and removed air bubbles from the porous network. This avoided the formation of air bubbles later on during the neutron imaging. An electrical connection to a potentiostat (Biologic SP-300) was maintained by 100 µm diameter silver wires that were contacted to the aerogels by silver paint and hook clipped to the power leads. The aerogel electrodes were placed inside the cell, which was then filled with 3 mL of 70 mM $Gd(NO_3)_3$ solution (see Fig. 4.9). The aerogels were stabilised in the liquid by buoyancy and their wire connection to the potentiostat. Their concave form can be seen in the cross section in Fig. 4.9(b). The cell was covered with parafilm to minimise evaporation and exchange with H_2O [499]. A DC voltage was applied to the cell, while changes in the transmission profile were monitored. A dark-current corrected neutron image during the first charging process, which was normalised by the open beam, is shown in Fig. 4.9(c).

A 20 mm Nd-Fe-B permanent magnet cube was placed next to the cell when the magnetic field gradient force was investigated. The surface of the magnet with a horizontal magnetic field of $B = 0.45$ T was separated from the solution by the 2 mm thick cell walls. The resulting force distribution was shown in Fig. 4.1(a). Boron carbide (B_4C) shielding protected the magnet from neutron activation by the beam.

Variations in the transmitted neutron intensity due to concentration changes range from a few percent in the aerogels down to per mille in the solution. To better visualise these fine changes of Gd^{3+} concentration (Δc_{Gd}), the time-sequenced neutron images were normalised by the first image of the series. Then, the Beer-Lambert law was inverted under the assumption that any alteration of the transmitted intensity stemmed exclusively from a movement of Gd^{3+} [528]:

$$\Delta c_{Gd} = -\ln\left(\frac{I(t_2)/I(t_1)}{\sigma_{Gd} N_A \Delta z}\right). \tag{4.6}$$

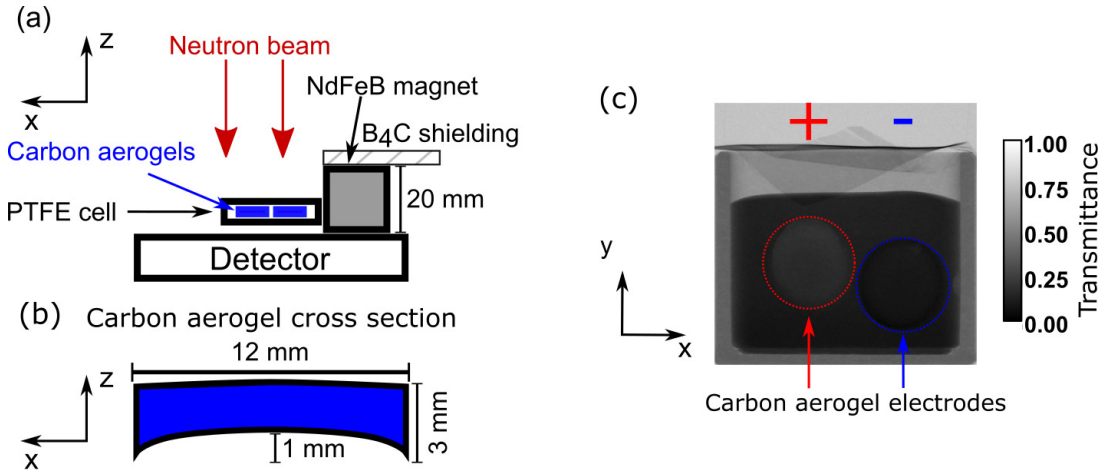

Figure 4.9 – (a) Sketch of the experimental setup (top view). The PTFE cell contained the carbon aerogels and $Gd(NO_3)_3$ solution. The aerogels were connected to a potentiostat. (b) Cross section of the concave carbon aerogel disks. (c) Dark-current corrected neutron image (normalised by open beam: $T = \frac{I-I_{dc}}{I_0-I_{dc}}$) of the 6 mm path length PTFE sample holder with 70 mM $Gd(NO_3)_3$ solution: 10 min into first charge at 1.0 V. Right aerogel: negative charge (Gd^{3+}); Left aerogel: positive charge (NO_3^-). Accumulation of Gd^{3+} ions in the right aerogel manifests itself in lower neutron transmission, whereas the reduced Gd^{3+} concentration leads to a transmittance increase.

This assumption is reasonable, considering that the neutron cross section of all other constituents in the path of the beam are overshadowed by the absorption cross section of Gd. These are mainly the cross sections of D_2O, carbon ($\sigma_C = 5.5$ barn) and silver ($\sigma_{Ag} = 68.3$ barn). This treatment removes any absorption contribution of the immobile components of the sample and scattering is taken into account implicitly by the division of the transmission profiles. All the results presented in this chapter will be shown as Δc_{Gd} with respect to the initial neutron image.

Results and Discussion

Immediately upon coming into contact with the aerogel, the 70 mM $Gd(NO_3)_3$ solution began to fill the macropores. This process took place in the first 10 min, but was not captured due to the black-body grid in the path of the beam (see Fig. 4.2(b) in Section 4.2.1). Approximate values for the Gd^{3+} transport into the macropores can be extracted with the grid in place and are shown in Fig. 4.10. These evince the creation of a concentration gradient in the cell, but an exact quantification is not possible. An estimated depletion of c_{Gd} can be expected in the liquid above the aerogels. The presence of the initial concentration profile is dealt with by only analysing changes of the c_{Gd} with respect to this starting condition. Only differences induced by the capacitive deionisation process will be shown from here on.

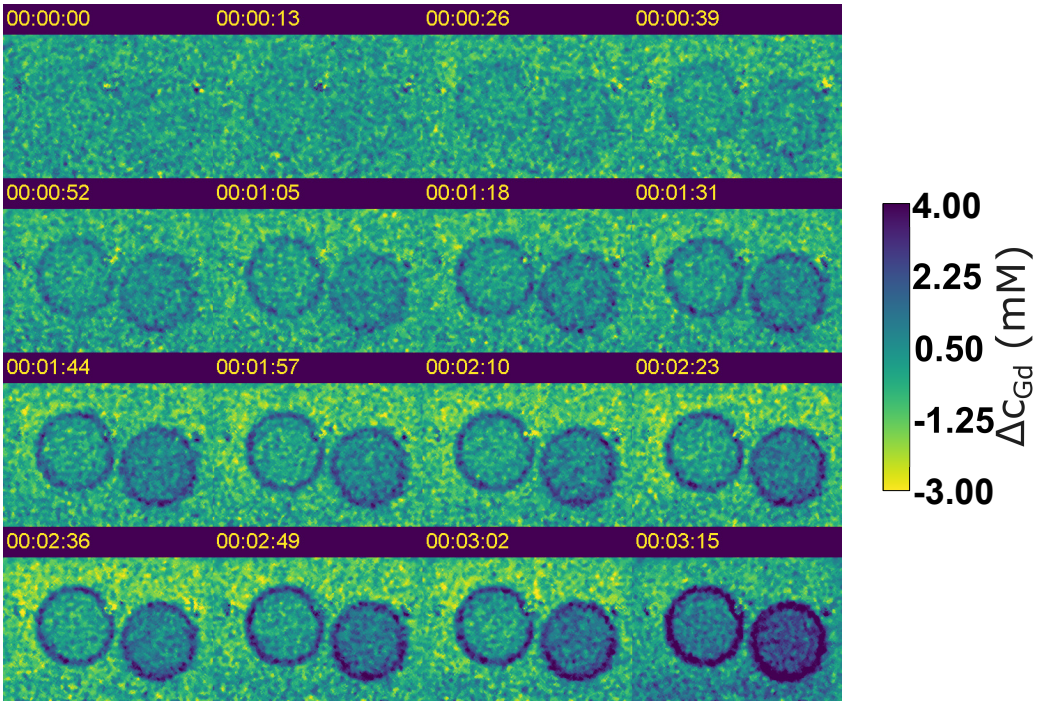

Figure 4.10 – Filling of carbon aerogel macropores with 70 mM $Gd(NO_3)_3$. The blackbody grid was in front of the cell. The values for Δc_{Gd} are unreliable due to the grid blocking the sample from the neutron beam.

Unlike the macropores, the mesopores remain inaccessible to the ions on the timescale of minutes and require an electric field to force ionic migration into them. One full capacitive deionisation cycle was recorded with neutron imaging and is displayed in Fig. 4.11. All neutron images were converted to mean values of Δc_{Gd} along the path length of the cell interior. For the solution, this is the true Δc_{Gd}. But the path length of the aerogels is lower and the concentration change here is actually larger than indicated in Figs. 4.11(a–f). The mean concentration change in the aerogels themselves is displayed in Fig. 4.11(g), below the neutron images of the corresponding stages of the process. These values were calculated under the premise that Δc^{ae}_{Gd} was entirely due to adsorption in the aerogel within the area defined by their contour. This is an approximation, because there is bulk solution of roughly 3.5 mm thickness behind the aerogels, which loses Gd^{3+} during the charging process. This means that the Δc^{ae}_{Gd} in the aerogels is underestimated by a couple of mM.

The capacitive deionisation commenced with the application of 1 V potential difference to the carbon aerogel electrodes immersed in solution. The voltage is accompanied by the movement of electrons from the potentiostat into the porous structure of the aerogel. Ions from the solution form a double layer to compensate the charged surface and a current flows through the solution between the electrodes. The registered movement of Gd^{3+} bears close resemblance to the current distribution shown in Fig. 4.1(b) with the region of highest electric potential gradient between the disks experiencing an instantaneous change in ion concentration (see Fig. 4.11(a)). It was witnessed how Gd^{3+} ions are expelled from the positively charged aerogel disk on the left and migrate into the negatively charged aerogel disk on the right. The double layer is continuously

filled with new ions during the charging process. First, these arrive from the oppositely charged aerogel. Once the co-ion concentrations (ions of the same charge as the aerogel) within the electrodes are depleted, the aerogels begin to leach ions from the surrounding solution (see Fig. 4.11(b) and concentration evolution in Fig. 4.11(g)). This continues until the final capacity has been reached and no further ions can be accommodated at $\Delta c_{\mathrm{Gd}}^{\mathrm{ae}} \approx 30\,\mathrm{mM}$ in the negatively charged aerogel. The arrival at this plateau in neutron transmittance was after approximately 60 min.

Then, the voltage was switched off and the aerogels discharged (Figs. 4.11(c) and (d)). The ions trapped in their respective aerogels were liberated and rushed to compensate their corresponding counterions in the opposing electrode. Furthermore, ions diffused out of the pores into the reservoir solution, in which the $Gd(NO_3)_3$ concentration increases again (Fig. 4.11(d)). This behaviour is best visualised by inspecting the time series showing $\Delta c_{\mathrm{Gd}}^{\mathrm{ae}}$ in the carbon aerogels with respect to the first image of the discharge series, which is shown in Fig. 4.12).

Inspection of the right aerogel showed that the anodic dissolution and cathodic deposition of Ag ($Ag_{(s)} \rightleftharpoons Ag^{+}_{(aq)} + e^{-}$) as side reactions took place. The standard electrode potential for silver is 0.8 V and the slightly acidic environment of the $Gd(NO_3)_3$ solution is beneficial for the dissolution. At a potential difference of 1 V, dissolution is bound to take place[48]. The resulting electroplating was restricted to the high electric field region on the curved surface between the aerogels. Due to the screening of the electric field inside the pores, it is unlikely that monovalent Ag deposited within the mesopores. This situation is even more plausible when considering the head start that the Gd^{3+} ions gained during their migration into the pores while Ag+ was being stripped from the silver connection. During the charging process the development of this layer is difficult to see, but remnants can be seen on the surface of the right aerogel in Figs. 4.11(c–f). It may be that mesopores were closed by this silver deposition, but the effect on the Gd^{3+} dynamics is assumed to have been small.

In addition, the adsorption of NO_3^- in the porous structure of the Gd^{3+} carrying aerogel was evident during the discharge. The blocking of mesopores by co-ion adsorption is an unwanted effect that decreases the efficiency and reversibility of the capacitive deionisation process [529]. Ion exchange membranes between the electrodes can alleviate this inherent issue by only allowing ions of one charge to pass through to the other side [321,529]. There has also been an important recent development in the capacitive deionisation community, which aims to solve the issue by dispensing with purely capacitive carbon electrodes and employing Faradaic electrodes in their stead [324,331–336].

After the 65 min discharge of the electrodes, the aerogels were charged up at the reversed voltage −1.0 V and the Gd ions moved in the opposite direction (Figs. 4.11(e) and 4.11(f)). The migration of Gd^{3+} was mainly confined to the transfer of the previously adsorbed Gd^{3+} from the mesopores of the right to those of the left aerogel. Fewer ions are taken from the solution during the recorded second charging period of around 75 min. An overview of $\Delta c_{\mathrm{Gd}}^{\mathrm{ae}}$ restricted to the change in the carbon aerogel during the second charging process is provided by Fig. 4.13.

[48] The original experimental plan foresaw a connection made of conductive carbon glue. This did not arrive in time for the experiments because it was classified as a hazardous material by customs which delayed its release.

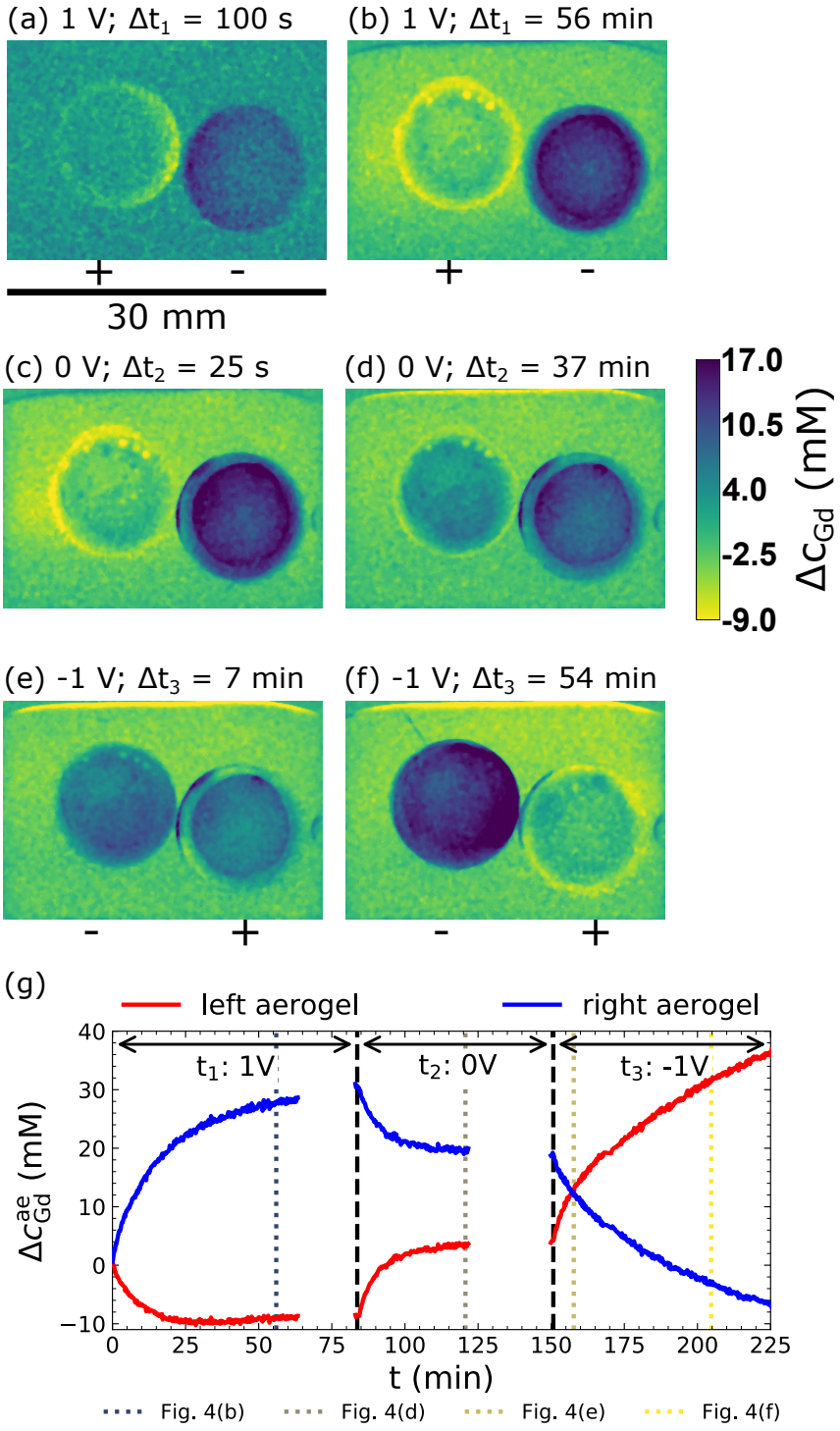

Figure 4.11 – Neutron images converted to Δc_{Gd} along the path length of the cell during capacitive deionisation of 3 mL 70 mM $Gd(NO_3)_3$ solution by two carbon aerogel disks with 0.5 mm minimum separation. (a–b) Charge: 1 V, total time $t_1 = 85$ min. (c–d) Discharge: 0 V, total time $t_2 = 65$ min (e–f) Reverse charge: -1 V, total time $t_3 = 82$ min. Gas bubbles due to oxygen evolution form on the positive electrodes during the charging process. (g) Mean $\Delta c^{\mathrm{ae}}_{\mathrm{Gd}}$ evolution in the aerogels. During the charge process approximately 10 mM Gd^{3+} is transferred from the left to the right aerogel. The remaining 20 mM of Gd^{3+} are adsorbed from the solution. Non-reversibility by the discharge process caused by co-ion adsorption is evident and an inverse voltage is required to unblock the pores.

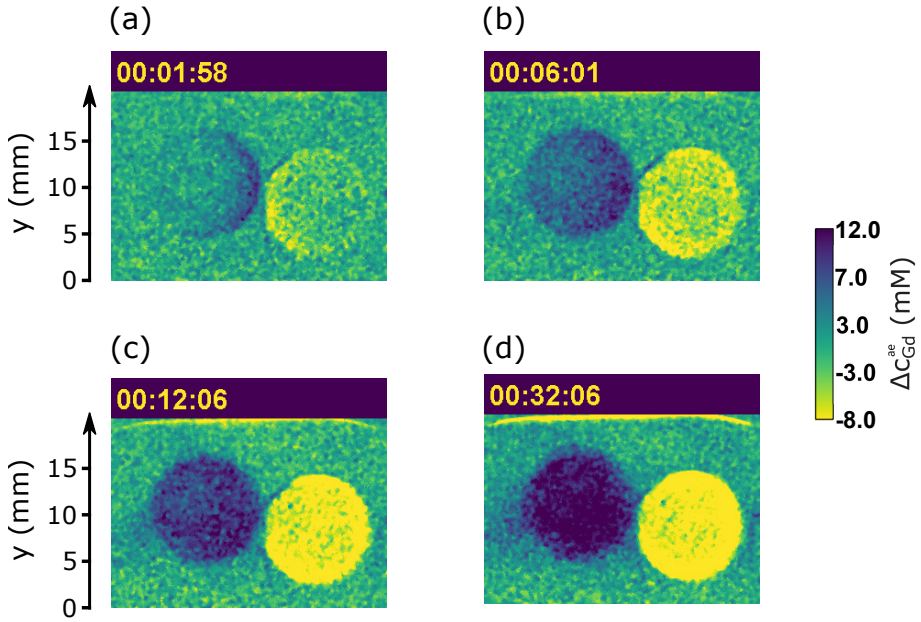

Figure 4.12 – **Carbon aerogel discharge process at 0 V.** Δ^{ae}_{Gd} in the aerogel with respect to the first image of the discharge process is shown. This is in contrast to Figs. 4.11(c–d), which show the mean change in the entire cell with respect to the beginning of the entire capacitive deionisation. The Gd^{3+} from the charging process transfers from the right to the left aerogel. The Gd^{3+} leaks into the solution in the left middle part of the cuvette, which is pronounced in (d).

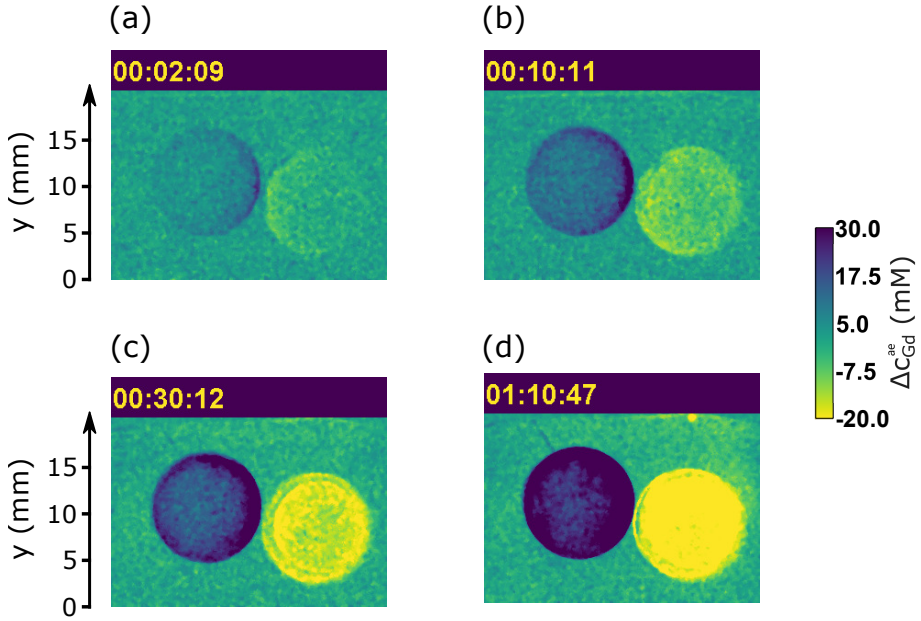

Figure 4.13 – **Carbon aerogel charge process at −1 V.** Δ^{ae}_{Gd} in the aerogels with respect to the first image of this charge process is shown. This is in contrast to Figs. 4.11(e–f), which show the mean change in the entire cell with respect to the beginning of the entire capacitive deionisation. The remaining Gd^{3+} in the positively charged right aerogel (after the discharge in Fig. 4.12) is forced into the negatively charged left aerogel by migration. This consumes most of the cell current and only a faint desalination of the surrounding is liquid visible. The image in (d) is taken approximately 5 min before the right electrode detached from the silver wire.

The dynamics of the electrosorption can be further elucidated by inspecting the readout of the potentiostat and comparing it to the $\Delta c^{\mathrm{ae}}_{\mathrm{Gd}}$ values extracted from the neutron transmission images. The data are summarised in Fig. 4.14. The upper two panels show the applied cell voltage E and the measured current response I. A value for the transferred charge Q in coulombs is obtained by integration of the current (Fig. 4.14(c)). This in turn can be converted to a concentration of trivalent ions by division with Faraday's constant and the aerogel volume ($V \approx 0.3\,\mathrm{mL}$). Then a comparison with the actually measured $\Delta c^{\mathrm{ae}}_{\mathrm{Gd}}$ in the right aerogel, which is displayed in the bottom panel (d) (the blue line from Fig. 4.11), is possible. The ratio between the adsorbed salt and the measured charge is defined as the charge efficiency Λ of the capacitive deionisation cell [326, 567–569]. Thus, the charge efficiency for Gd^{3+} is calculable by $\Lambda_{\mathrm{Gd}} = \frac{3\Delta^{\mathrm{ae}}_{\mathrm{Gd}}}{\Delta Q}$, which is approximately 0.55 for the first charge. The value drops to around 0.3 for the second charging process after the discharge. Charge efficiencies should approach unity in a good capacitive deionisation cell. The calculated values are low and the current is not efficiently used.

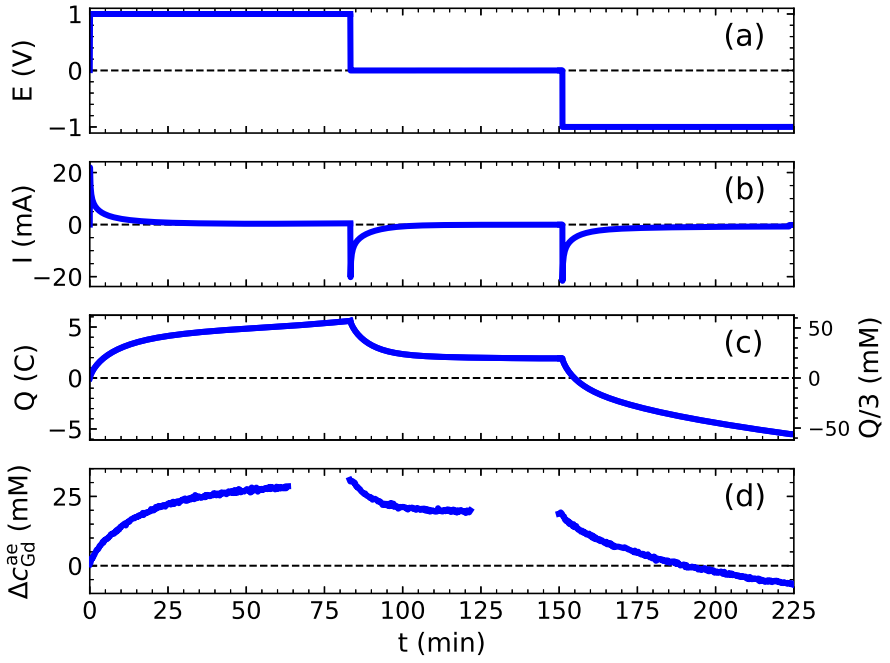

Figure 4.14 – Comparison of the readout from the potentiostat and $\Delta c^{\mathrm{ae}}_{\mathrm{Gd}}$ detected by neutron imaging. (a–b) The cell voltage and the measured current. (c) The integrated current shows the charge Q, which can be converted to a concentration of trivalent ions (see right y-axis). (d) The neutron imaged $\Delta c^{\mathrm{ae}}_{\mathrm{Gd}}$ in the right aerogel (see Fig. 4.11). The charge efficiency Λ_{Gd} based solely on the capture of Gd^{3+} is 0.55 during the first charge, but then drops to around 0.3.

The main reasons for this have already been mentioned. On the one hand, both the initial expulsion and later adsorption of NO_3^- ions contributes only to the transferred charge, not the neutron imaged $\Delta c^{\mathrm{ae}}_{\mathrm{Gd}}$. An easy way to improve the efficiency during the discharge process is to increase the voltage to other values than zero [568]. But this does not solve the issue completely and a barrier is needed that blocks co-ions from travelling into the respective electrodes.

Solutions of higher concentration exacerbate the issue and Λ tends to decrease with salt concentration [569]. This reaffirms the importance of introducing ion exchange membranes between the electrodes in what is called membrane capacitive deionisation and usually increases Λ by at least 20% [321,326]. On the other hand, the anodic dissolution of Ag and subsequent electroplating on the aerogel surface will have taken up significant amounts of the cell current. Thus, the true Λ factoring in the charge transfer due to the deposition of Ag is higher than the unreasonably low Λ_{Gd}. In general, electroplating of ions is not necessarily unwelcome during capacitive deionisation, as it allows the separation of electroactive ion species. However, previous reports indicate that adsorbed ions of higher valency screen the electrodes and prevent monovalent ions from adsorbing [570]. Resistive losses in the thin wire connections will also have played a role in the low charge efficiency value. A solid current collector for the carbon aerogels with greater contact area would serve to minimise these.

Faradaic reactions at the aerogel surface contribute to parasitic currents. These can range from the reduction of dissolved oxygen to the gradual oxidation of the carbon itself [321,340,571]. The reduction of dissolved oxygen can be carried out with four electrons [572]:

$$\mathrm{O_2 + 2H_2O + 4e^- \longrightarrow 4OH^-} \quad E^0 = 0.401\,\mathrm{V}, \tag{4.7}$$

with the reduction potential $E^0 = 0.401\,\mathrm{V}$ against a standard hydrogen electrode [573]. Oxygen can also be reduced via a two electron exchange and hydrogen peroxide ($\mathrm{HO_2^-}$) formation (Eq. 4.8):

$$\mathrm{O_2 + H_2O + 2e^- \longrightarrow HO_2^- + OH^-} \quad E^0 = -0.065\,\mathrm{V}. \tag{4.8}$$

This reaction causes the pH value to rise, but is severely diffusion-limited [573]. An estimate of the quantity of dissolved $\mathrm{O_{2(aq)}}$ is possible with Henry's law. The $\mathrm{O_{2(aq)}}$ concentration equals $5.15 \times 10^{-5}\,\mathrm{M}$ at a pressure of 0.21 atm [572]. In addition, the oxidation reaction of carbon [574,575], which is facilitated under acidic conditions, is given by:

$$\mathrm{C + 2H_2O \longrightarrow CO_2 + 4H^+ + 4e^-} \quad E^0 = 0.21\,\mathrm{V}. \tag{4.9}$$

A thermodynamically unfavourable oxidation to carbon monoxide (CO) can also occur under high voltages [574]:

$$\mathrm{C + H_2O \longrightarrow CO + 2H^+ + 2e^-} \quad E^0 = 0.518\,\mathrm{V}, \tag{4.10}$$

$$\mathrm{CO + H_2O \longrightarrow CO_2 + 2H^+ + 2e^-} \quad E^0 = -0.103\,\mathrm{V}. \tag{4.11}$$

This gives rise to the gradual dissolution of the porous carbon electrode, which loses mass and can in extreme cases even crumble [321]. Such an effect has been reported for positively charged capacitive deionisation electrodes after long charging cycles [576]. Gas bubble formation

within the porous capacitive deionisation electrodes is a frequent occurrence at voltages above 1.2 V and has been previously investigated by neutron imaging [530]. The aforementioned pH fluctuations during capacitive deionisation make the occurrence of these reactions possible at lower voltages [573].

More critical for this experiment was the electrochemical reaction of the silver. The gradual decomposition of the silver paint connection by anodic dissolution eventually severed the connection to the potentiostat. Approximately 75 min into the second charging process, the right aerogel detached from the wire and sunk to the bottom of the cell. In the wake of this, the system was decidedly out of thermodynamic equilibrium, as the desalination caused a vertical $Gd(NO_3)_3$ concentration gradient. The removal of ions lowered the density of the solution, making it rise due to buoyancy. An estimation of the density change $\Delta\rho$ due to the variation in $Gd(NO_3)_3$ concentration is possible with literature values from pycnometric measurements of aqueous rare earth nitrate solutions by Spedding et al. [496]. At concentrations below 1 M, a linear relationship between Δc_{Gd} and $\Delta\rho$ exists. The coefficient is $\alpha \approx 0.29\,M^{-1}$ with respect to the pure solvent density ρ_0. Thus, the density change due to $\Delta c_{Gd} = 5$ mM in D_2O ($\rho_0 = 1107\,kg\,m^{-3}$) is:

$$\Delta\rho = \rho_0 \alpha \Delta c_{Gd} = 1.605\,kg\,m^{-3}. \tag{4.12}$$

The emergence of this concentration profile in the solution is shown in Fig. 4.15. A return to a homogeneous system is imposed by diffusion, which is a lengthy process under normal conditions and even more protracted when considering slow diffusion from the pores of the aerogel. This situation is depicted in the vertical concentration change profiles during the capacitive deionisation procedure in Figs. 4.15(c–e). It should be noted that these plots show the evolution Δc_{Gd} with respect to the initial concentration profile in the cell before the charge process. This was after Gd^{3+} ions had already been transported into the macropores via diffusion and convection. A vertical concentration profile was already present in the solution due to this.

Fig. 4.15(c) shows Δc_{Gd} during the first charge at 1 V. The greatest decline in Gd^{3+} concentration (-6 mM with respect to the beginning of the charging process) occurred to the left of the aerogels at the height of their horizontal axis. This stratification was mechanically stable, as the initial Gd^{3+} concentration had already decreased by approximately 2 mM at the top of the cell. As soon as the electric field was removed, the aerogels released their ions, which flattened the concentration profile. The minimum in Δc_{Gd} disappeared, but the concentration profile did not return to its original state. Instead, a near-linear concentration profile developed. Switching the voltage to -1 V did not greatly shift the concentration profile adjacent to the negatively charged aerogel (Fig. 4.15(e)). This can be seen in Figs. 4.11(b), (c) and (f).

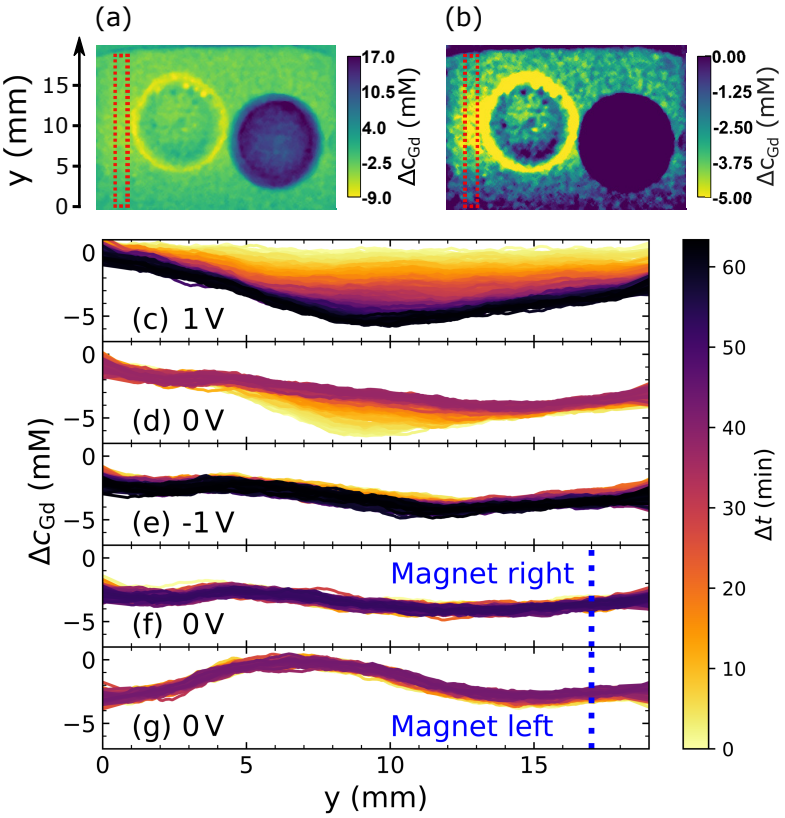

Figure 4.15 – (a) Neutron image converted to Δc_{Gd}: 56 min into charge at 1 V (70 mM $Gd(NO_3)_3$ solution, see Fig. 4.11). (b) Modified contrast for greater visibility of Δc_{Gd} in solution. Vertical profile plots were extracted from the red framed area and are shown in the panels below. (c-g) Vertical Δc_{Gd} concentration evolution in liquid left of aerogels with respect to the initial situation prior to charging. The individual panels are consecutive and the time displayed by the colour bar is set to restart in each of them. (c) Charge at 1 V: The liquid is desalinated and a vertical concentration gradient established by the liberated D_2O. The desalination is particularly pronounced on the axis of the two aerogels. (d) Discharge at 0 V: Gd^{3+} leaves the right aerogel and the concentration profile is flattened. The original concentration profile is not re-established. (e) Charge at -1 V: The concentration profile remains intact, except for a slight decrease in concentration at the bottom of the cell. (f–g) 20 mm Nd-Fe-B magnet at the side of the cell. The height of the magnet is indicated by the vertical blue dotted lines. (f) Magnet right: The left area is unaffected by the magnet 30 mm to the right (see Fig. 4.16(a)). (g) Magnet left: The magnet attracts 4 mM of $Gd(NO_3)_3$ towards the left side of the cell (see Fig. 4.16(b)).

Approximately 20 min after the interruption of the charging process, a 20 mm Nd-Fe-B cube magnet was placed adjacent to the cell to demonstrate a magnetic redistribution of the electrolytic solution (Fig. 4.16). The distinctive contour of the magnetic field gradient force (see Fig. 4.1(a)) is clearly visible as a $\Delta c_{\mathrm{Gd}} \approx 5$ mM of Gd^{3+} region on the inside of the cell facing the magnet. Swapping the position of the magnet after 90 min from the right to the left of the cell created a symmetric situation with magnetically attracted ions transferring from the right to the left (Fig. 4.16(b) and vertical concentration profile in Fig. 4.15(g)). Evidently, the magnet upset hydrostatic stability and caused movement of the bulk fluid with higher $Gd(NO_3)_3$ concentration at the bottom of the cell by convection. This can be understood by comparing the magnetic $E_{\mathrm{mag}} = \frac{\Delta c \chi}{2\mu_0} B^2$ and gravitational $E_{\mathrm{grav}} = \Delta\rho g \Delta y$ ($g = 9.81\,\mathrm{m\,s^{-2}}$) energy densities. In a mag-

netic field of $B = 0.35\,\mathrm{T}$ and a concentration gradient of $\Delta c_{\mathrm{Gd}} = 5\,\mathrm{mM}$, these are approximately equal at a height of $\Delta y = 5\,\mathrm{mm}$ ($E_{\mathrm{mag}} = E_{\mathrm{grav}} \approx 80\,\mathrm{mJ\,m^{-3}}$). This value corresponds well with the observed hovering concentration enriched zone next to the magnet in Fig. 4.16.

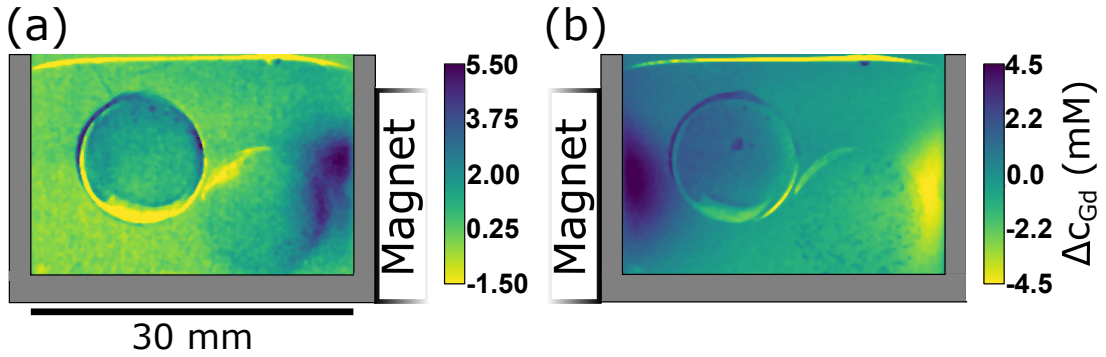

Figure 4.16 – Neutron image converted to Δc_{Gd}: Discharging carbon aerogels with 20 mm magnet cube to sides of the cell. Gd^{3+} ions are drawn into the magnetic field gradient. The right aerogel is disconnected and lies at the bottom of the cell. (a) Magnet to the right: Δc_{Gd} with respect to the end of the capacitive deionisation process in Fig. 4.11. (b) Magnet to left: Δc_{Gd} with respect to (a) is shown. The heightened c_{Gd} has vacated the region on the right and moved to the left with the magnet.

The initial stabilisation of the $Gd(NO_3)_3$ in the field gradient is almost instantaneous, but as time progresses, the magnetised region can be seen to slightly expand as more ions were drawn into it. This reshuffling of the Gd^{3+} concentration is subtle and difficult to perceive in the time-resolved neutron images, even after averaging groups of pixels and median filtering.

In any case, removal of the magnet re-establishes the status quo as was shown in the previous chapter. The concentration gradient will revert to the original state of mechanical stability by purely density-difference driven convection, ensuring $\nabla\rho \times \mathbf{g} \overset{!}{=} 0$. The system returns to a homogeneous equilibrium, whether the magnet is present or not. Hence, the concentration profile can only be magnetically manipulated in the time window set by this diffusional process. As a direct consequence, the magnet is also able to refresh the depleted $Gd(NO_3)_3$ concentration around a desalinating porous electrode by perpetually dragging magnetic fluid into its vicinity. This was not captured in the neutron imaging experiments, due to unforeseen issues with the spallation source on the last day of the allocated measuring time. However, the obtained results in Fig. 4.16 show the snapshot of the final state of magnetically modified mechanical stability, which the magnetic field gradient would have continuously worked to impose.

An experiment carried out with a potential difference of 0.5 V and the carbon aerogels on the bottom of the cell showed that Gd^{3+} ions can still enter the macropores of the positively charged aerogel during the first charge. In contrast to Fig. 4.13, where the expulsion of Gd^{3+} co-ions during the first charge was obvious, the Gd concentration in the positive electrode decreased slightly at 0.5 V.

4.4. Capacitive Deionisation with Activated Carbon Cloths

The second part of the neutron imaging experiments aimed to elucidate the electrosorption in activated carbon cloths. These are made up of microporous fibres, which provide enormous surface areas (up to $3500\,\mathrm{m^2\,g^{-1}}$ [321]) and adsorptive capabilities. Activated carbon cloths are created by carbonisation and activation of a phenol–formaldehyde polymer precursor. The phenol–formaldehyde resin is melt-spun into fibres prior to the pyrolysis. Unlike carbon aerogels, activated carbons have been widely commercialised and are the most commonly encountered porous carbon material. Applications are centred around gas adsorption and water treatment. Examples include face masks, room air cleaners and dechlorination. Naturally, the adsorptive properties eventually attracted the attention of the capacitive deionisation community in the late 2000s, resulting in a number of publications investigating the desalination performance [567, 568, 576–586]. Optimisation of performance by surface functionalisation has been the main direction of the research, although unanswered questions concerning the electrosorption mechanism in the microporous fibres remain. Significant overlapping of electric double layer occurs between micropores ($< 2\,\mathrm{nm}$), which can only accommodate approximately 10 ions [326,337,587]. Similarly to the last section on the carbon aerogels, the present discussion about the activated carbon cloths will begin with the presentation of a material characterisation and then discuss to the neutron imaging experiments.

4.4.1. Characterisation of Activated Carbon Cloths

Four activated carbon fabrics were provided by the company Kynol® Europa GmbH. Three of these were activated carbon cloths with brand names ACC-5092-10 (ACC-10), ACC-5092-15 (ACC-15), ACC-5092-20 (ACC-20) and one activated carbon felt ACNW-160-13 (ACNW-13). These materials comprise pyrolysed and activated novoloid fibres [588, 589], which are arranged in a fabric of approximately 0.6 mm thickness with a ribbed surface. The results of their characterisation will be presented below, beginning with scanning electron microscopy followed by nitrogen gas adsorption measurements. An electrochemical investigation of the chrono-amperometric response will also be reported after the material characterisation.

Scanning Electron Microscopy

An overview of SEM images of the activated carbon cloth ACC-20 at different magnifications is provided in Fig. 4.17. The overall morphologies of ACC-10, ACC-15 and ACC-20 are near to identical and not shown here. They show carbon fibres of approximately 15 µm diameter that form interwoven bundles in a repeating pattern. The rope-like bundles are in the order of 500 µm, which becomes apparent when the cloth is cut and the bundles at the edge unravel.

By contrast, the carbon fibres of activated carbon felt ACNW-13 are not arranged in ordered bundles and are instead randomly distributed across the sample (see Fig. 4.18). The fibres themselves are consistent in terms of diameter and surface smoothness with no obvious signs of porosity.

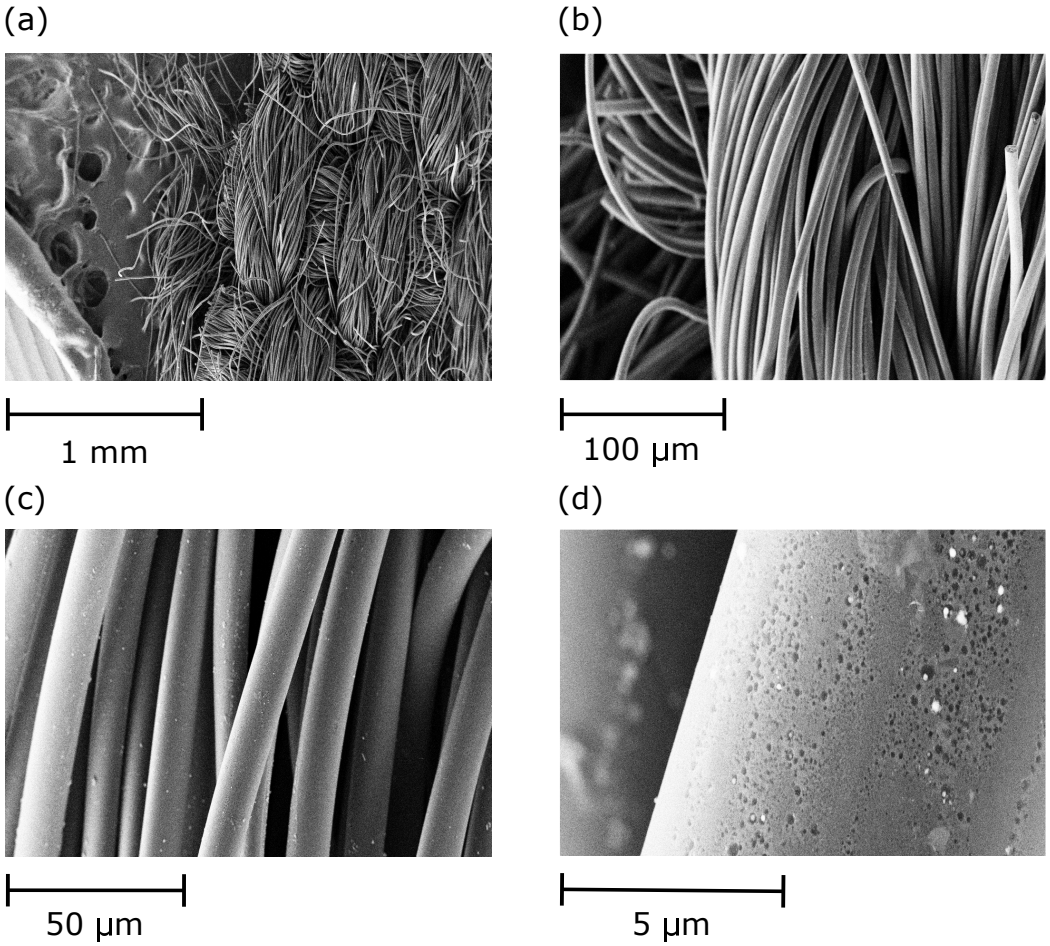

Figure 4.17 – **SEM images of activated carbon cloth ACC-20.** The morphology of ACC-10 and ACC-15 is identical to ACC-20. (a) Carbon fibres of ∼15 nm diameter are arranged in rope-like bundles. The image is taken at the edge of the cloth. (b–c) Bundles of fibres at higher magnifications. (d) Spots in the order of 300 nm appear on the surface of a fibre. Micropores are below the resolution of the SEM.

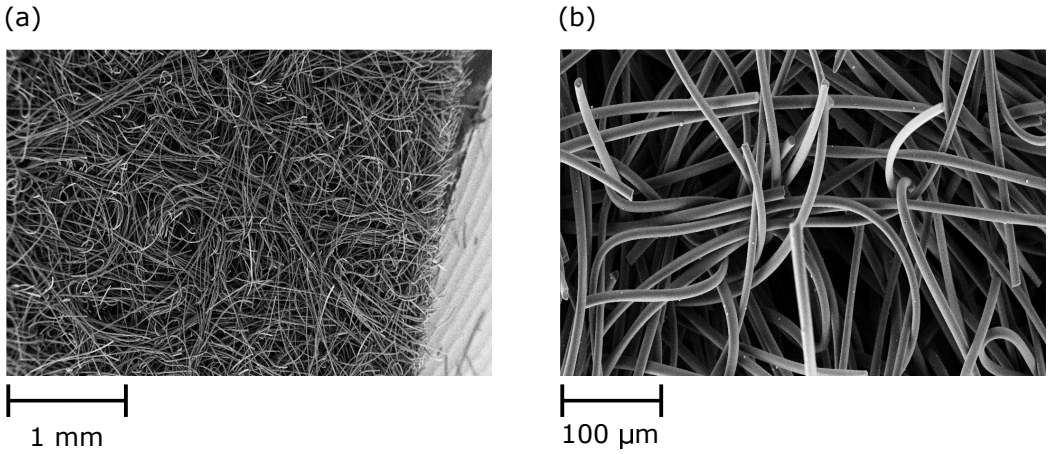

Figure 4.18 – **SEM images of activated carbon felt ACNW-13.** The carbon fibres of the felt are not arranged as bundles like ACC-20 (Fig. 4.17), but are loosely interwoven instead.

Pore Size Determination by Gas Adsorption Method

The activated carbon cloths are microporous (<2 nm diameter) and porosity in this size range is suitable for investigation by gas adsorption. All samples were de-gassed for 1 h at 200 °C under vacuum prior to analysis. Measured nitrogen adsorption isotherms of the cloths were of Type-I, which means an abrupt rise in the pressure due to filling of micropores. No hysteresis occurred as was the case for the Type-IV adsorption isotherm measured for the carbon aerogel in Section 4.3.1 [558, 590]. Type-I isotherms are observed for the adsorption of a monolayer of adsorbate on materials whose pore sizes are not much larger than the cross-sectional area of the adsorbate. For a N_2 molecule this is usually assumed to be 0.162 nm^2. Under such conditions, the BET theory is no longer applicable and other models for the evaluation of the isotherm are required [591]. One theory that describes the N_2 adsorption isotherms in microporous carbon structures is the N_2-Carbon QSDFT (Quenched Solid State Density Functional Theory[49]) model [595–597], for slit-shape pores. This model can describe carbon materials with pore sizes between 0.35–40 nm and was used to interpret the data presented here.

The measured cumulative pore volumes of the four samples are plotted in Fig. 4.19. Although the cloth samples each took on adsorbate within the same tight pore range (<2.5 nm), the quantity of gas adsorbed differed significantly from sample to sample.

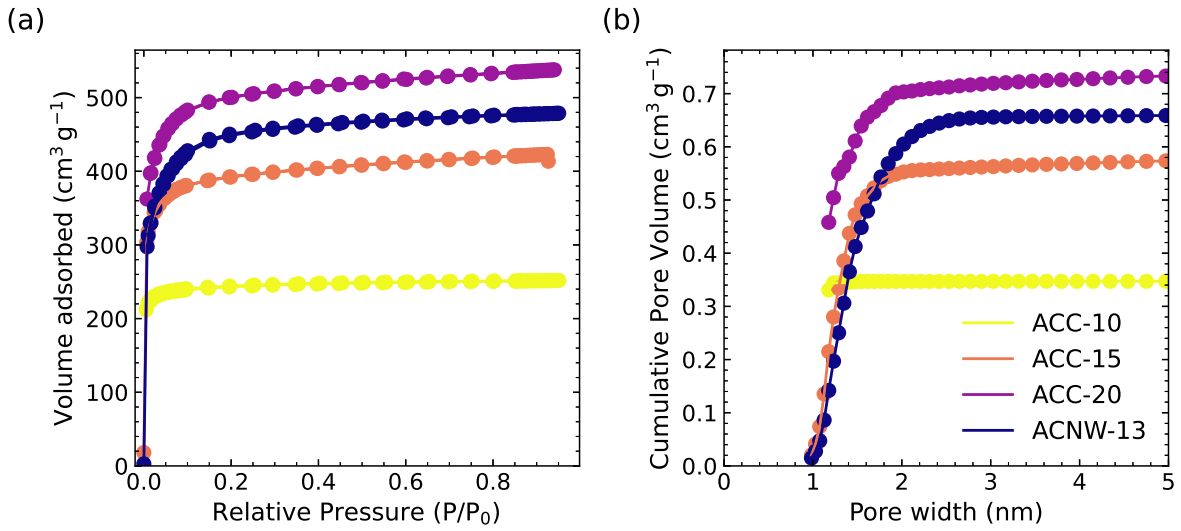

Figure 4.19 – N_2 adsorption isotherms and cumulative pore volumes of the activated carbon cloths. Each exhibit a Type-I isotherm typical of micropores. (a) N_2 adsorption isotherms. (b) Cumulative pore volumes of the activated carbon cloth samples are extracted with the N_2-Carbon QSDFT model.

[49] This method is classified as classical density functional theory (DFT), which describes many-body systems of interacting molecules, mainly in inhomogeneous fluids [592–594]. The mathematical framework of quantum (DFT), which has become the standard method for predicting the electronic structure of materials, is the same as that of classical DFT. The variation principle with respect to density functions is used to minimise the grand potential instead of the quantum mechanical energy functional.

The results of the gas adsorption surface area measurements and the weights of the cloths are summarised in Table 5. Within the series of woven cloths ACC-10, ACC-15 and ACC-20, the pore volume increases from 0.347 to 0.583 and finally to 0.745 $cm^3\,g^{-1}$. These values are due to micropores present within the fibres. These are beyond the resolution of SEM (Fig. 4.17). This is also reflected in the weights ($g\,m^{-2}$) of the cloths: the values being inversely proportional to the pore volumes.

Cloth	Specific surface area ($m^2\,g^{-1}$)	Pore volume ($cm^3\,g^{-1}$)	Weight ($g\,m^{-2}$)
ACC-10	985	0.347	200
ACC-15	1541	0.583	170
ACC-20	1959	0.745	135
ACNW-13	1725	0.661	-

Table 5 – Summary of QSDFT nitrogen gas adsorption data for the activated carbon cloths. The porosity increases across the series ACC-10→ACC-15→ACC-20, which is reflected both in the specific surface area and the weight of the material. The obtained values are in the range of previously reported results of microporous activated carbon cloths [584,586,598]. The approximate values for the weight were supplied by Kynol®.

The pore size distributions of the cloths are shown in Fig. 4.20. In QSDFT, the pore size is calculated as pore width, assuming that the pores behave as slits. For the ACC series it can be seen that the pore width is exclusively below 2 nm. Similarities between ACC-15 and ACC-20 are evident in the form of their peak centred at a pore width of around 1.3 nm. All the pores of ACC-10 lie below a width of 1.3 nm, which is at the resolution limit of the instrumentation. Due to the lower data processing limit, the curves of ACC-10 and ACC-20 are truncated at a value of around 1.2 nm. Average pore sizes could not be reliably deduced, but the surface area and pore volume values are unaffected.

Not only does ACC-10 have the lowest average pore width of all samples, it also has the lowest surface area ($985\,m^2g^{-1}$). A general relationship exists in the literature, whereby smaller pores give rise to larger surface areas, and vice versa. However, for the activated carbon cloths, the dominant factor ruling the surface area is the pore volume, with lower pore volumes resulting in fewer available surfaces for gas adsorption, and a lower surface area (see Table 5). Hence, the porosity within the carbon fibres is directly related to the pore volume. A similar hierarchy of values was reported for Kynol® activated carbon cloths from the same manufacturer, although the absolute values differ significantly from those measured here and estimates by the manufacturer [585,586]. These measurement by Lenz et al. relied on argon gas adsorption with QSDFT theory [586]. The reason for the discrepancy is not clear, but may be due to the de-gassing procedure, affecting the measured sample weight.

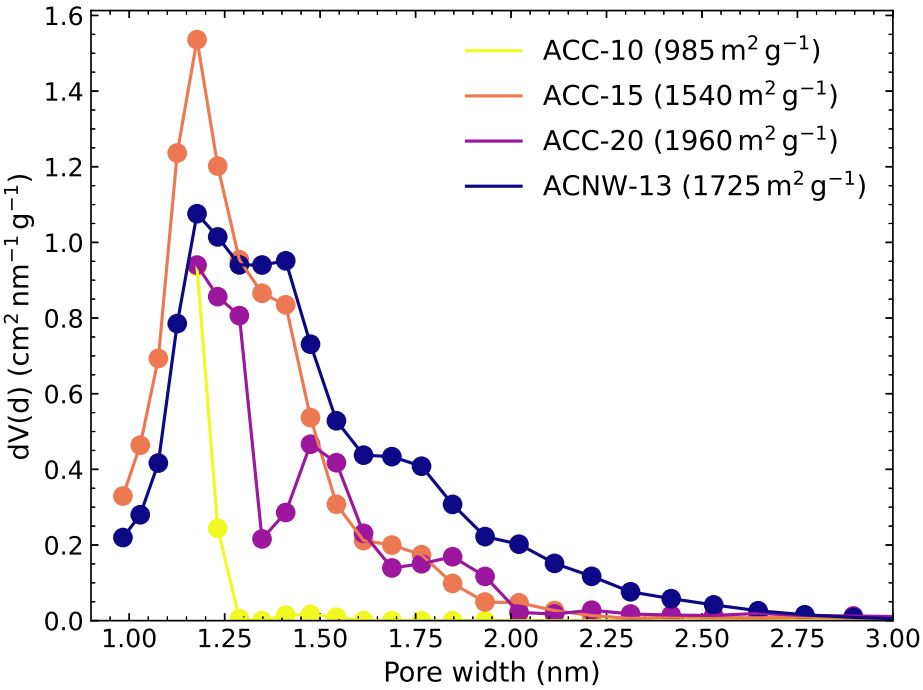

Figure 4.20 – Pore size distribution according to the QSDFT model for the adsorption isotherms. The specific surface area is shown in the legend together with the sample name. ACC-20 has the highest pore volume and surface area. ACNW-13 has a wider distribution of pore sizes than the other cloths.

The activated carbon felt ACNW-13 is somewhat unusual as it has the broadest pore size distribution of the activated carbon cloths studied. It has a high pore volume and is also the only cloth with pores greater than 2 nm. It is suggested that a high pore volume plus high interconnectivity of pores combine to generate large surface area values; 1725 m^2g^{-1} in the case of ACNW-13.

Measured surface area values apply to samples as a whole, meaning that the adsorbate forms a monolayer coverage on all exterior surfaces and also on any pores present beneath the surface. Therefore, macro-morphology does play a role in the surface area, but because surface area increases dramatically with smaller pore sizes, it is the micropores within the fibres that are the over-riding contributor to the surface area. Of the cloths studied here, a hierarchy exists in terms of the surface area and, as previously noted, the pore volume (see Table 5). The SEM images (see Fig. 4.17) revealed that the macro-texture and arrangement of these samples is similar. Therefore, it can be concluded that the change in surface area is primarily a function of the porosity within the fibres, with a minor contribution from the interspacings or pore openings between the fibres.

Differential Scanning Calorimetry and Thermogravimetric Analysis

DSC/TGA was performed on a piece of activated carbon cloth (ACC-20) with a scan rate of 5 K per minute, both with regular air and under nitrogen atmosphere (see Fig. 4.21). The results are similar to those for the carbon aerogel in Section 4.3.1 and indicate a high, near to exclusive

carbon composition. Unsurprisingly, the TGA with an air filled chamber showed the combustion of carbon above a temperature of 500 °C accompanied by a steep decline in the sample weight (Fig. 4.21 (a)). This combustion reaction manifests itself as a peak in the DSC data.

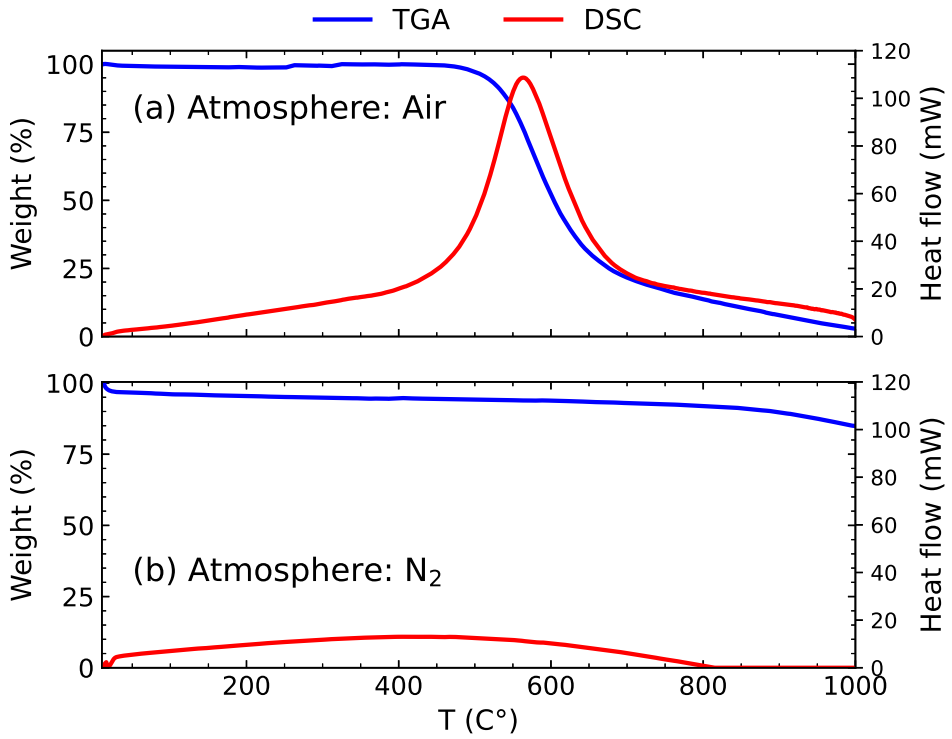

Figure 4.21 – DSC/TGA measurement of activated carbon cloth (ACC-20). (a) In air: TGA (blue) and DSC (red) show the exothermic combustion of carbon at temperatures above 500 °C. (b) Carbon does not react below 2000 °C under nitrogen atmosphere. Early stage weight loss is due to moisture in the sample.

The presence of moisture in the samples is captured as a weight loss < 100°C, which highlights the importance of the outgassing prior to the nitrogen gas adsorption porosity measurements. Under inert nitrogen atmosphere, only water evaporation is visible (Fig. 4.21 (b)). Carbon does not react with nitrogen below a temperature of 2000 °C. Apart from the weight loss due to evaporating water, there may have been reaction with tiny amounts of hydrogen in the sample.

X-Ray Diffraction

The x-ray diffraction pattern of an activated carbon cloth is shown in Fig. 4.22. Broad peaks of graphite (101) and (110) are visible at 44° and 79° respectively [565, 566]. This once again indicates micrographitic structure similar to that of the carbon aerogel in Section 4.3.1 [599], although the microfibres are likely to be composed of many disordered layers of graphene sheets [589]. The (101) peak at 44° overlaps with the (100) peak at 42°. The (002) peak is faintly discernible as a change of slope in the background at 25°. There are no other contributions to the x-ray diffraction pattern as expected.

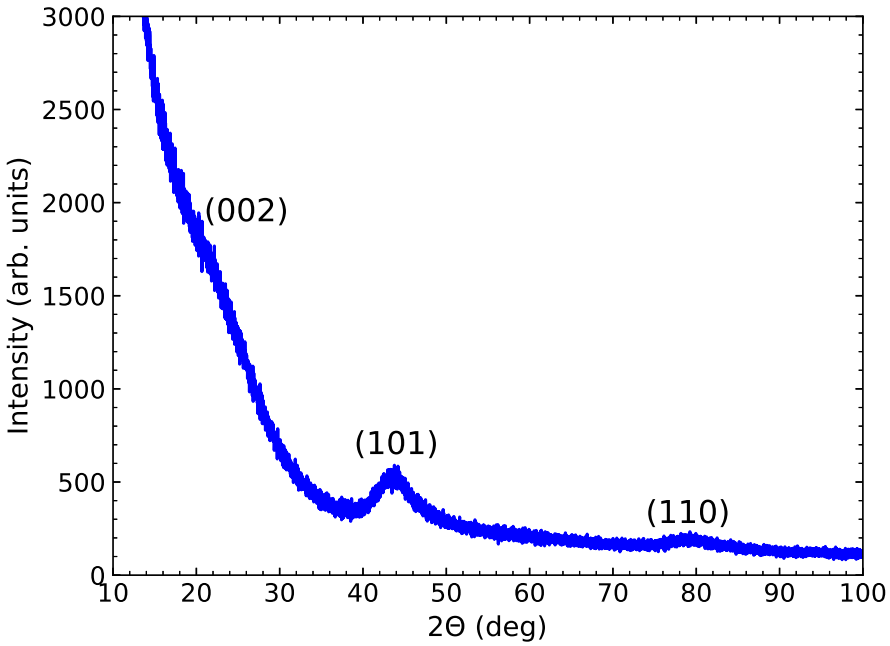

Figure 4.22 – **X-ray diffraction pattern of activated carbon cloth (ACC-20).** The broad peak at around 44° incorporates the (100) and (101) Bragg peaks of graphite. The (110) peak is at 79°. The (002) graphite peak at 25° is buried amid the background.

Chrono-Amperometry

The investigation of the current response to a potential step is known as chrono[50]-amperometry. Activated carbon cloth electrodes were cut to sizes of 9mm × 20mm and placed 3 mm apart from each other in a 3d-printed electrochemical cell. Measurements were only performed with the lowest and highest surface area cloths. These were ACC-10 and ACC-20, respectively. The electrode surfaces were facing each other and the connections to the potentiostat (Metrohm Autolab: PGSTAT 302N) power leads were ensured by 100 µm diameter Pt wires, which pierced the cloths. A 1 M $DyCl_3$ solution was injected into the cell and it was covered by a cap. The setup is essentially that of a supercapacitor with a large gap and no spacer. Measurements were performed in a two electrode configuration, as the employment of a reference electrode is only necessary for the monitoring of Faradaic processes and voltages on the electrodes. In fact, the higher sensitivity of a three electrode setup to these side reactions is a hindrance for the analysis of the ion storage capacity of porous electrodes [600]. Square wave chrono-amperometry was performed by applying 5 min potential steps followed by a discharge phase at 0 V, all the while measuring the current response. After every discharge step the voltage was increased by 0.1 V, from $E = 0.1$ V at the beginning to a final value of $E = 1.2$ V. The results with ACC-20 electrodes are shown in Fig. 4.23.

[50] χρονος: time

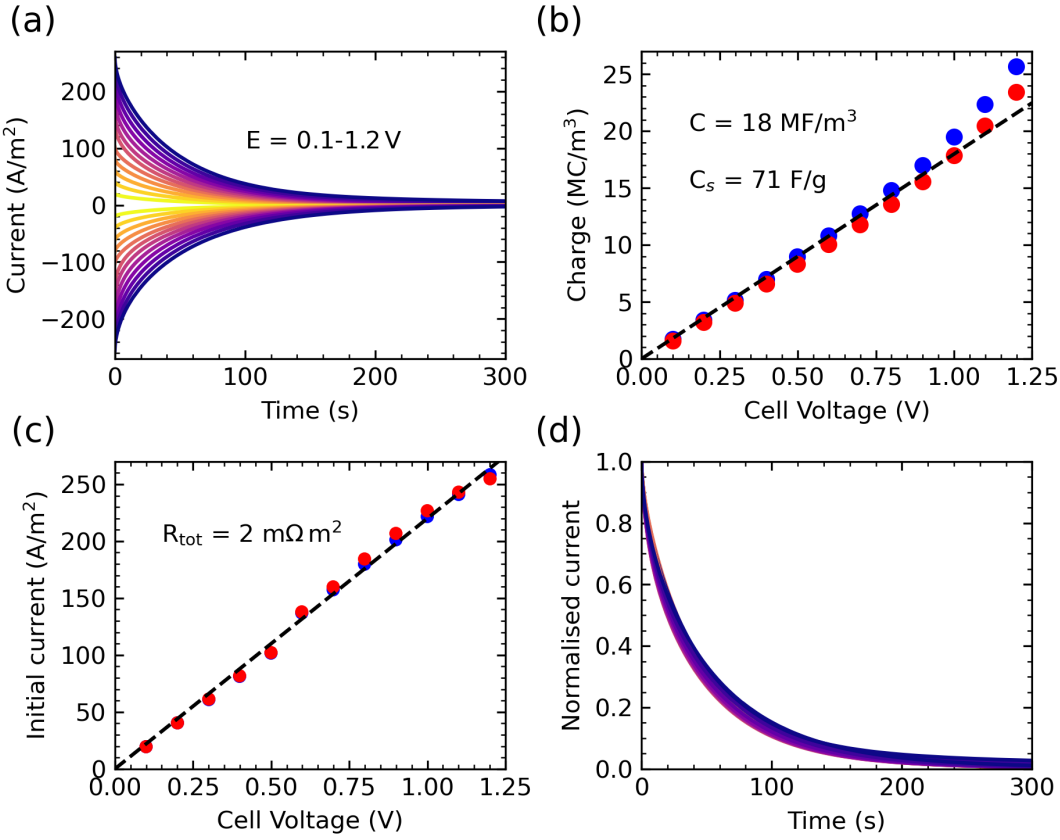

Figure 4.23 – Square wave chrono-amperometry of two microporous ACC-20 cloths ($1960\,\mathrm{m^2 g^{-1}}$). (a) Current response to 300 s potential steps between $E = 0.1$ V and $E = 1.2$ V with a step size of 0.1 V. Every charge is followed by a 300 s discharge at 0 V. (b) Integrated charge density. Blue points indicates charging and red points the discharge. Leakage currents cause the charging values to deviate at higher voltages. Capacitance C and specific capacitance C_s are extracted from the slope. (c) The total resistance R_{tot} can be extracted from the initial current I_0 plotted over applied cell voltage. (d) The current curves in (a) are normalised by I_0 and fall on a single curve.

All the current responses decay exponentially with time as can be seen in Fig. 4.23(a). There is a proportionality between the initial current I_0 to the applied voltage as expected by Ohm's law. By treating the two electrode cell as a resistor-capacitor (RC) circuit, it is possible to extract capacitance and resistance values from the data.

Integration of the current density and division by the electrode thickness leads to the charge density, which is shown in Fig. 4.23(b). These values cannot be directly converted to the adsorbed ions, because a large part of the measured current is caused by co-ion migration. This was made clear in the discussion of the charge efficiency Λ for the carbon aerogels in Section 4.3.2 above. The blue data points indicate the accumulated charge during the charging phase and the red points while discharging. Evidently, Faradaic (non-capacitive) currents contributed to higher charge values during the charging phase. This worsens at higher voltages as can be seen in the departure from the linear behaviour. A reason for the decreased current could be a change in resistance due to oxygen bubbles that form on the electrodes and modify the current distribution [601].

The capacitance C is the proportionality factor between the charge and the cell voltage. It equals $C = 18\,\mathrm{MF\,m^{-3}}$ for ACC-20. A conversion to the specific capacitance can be carried out by dividing C by the mass density $\rho = 0.25\,\mathrm{g\,mL^{-1}}$, which results in $C_s = 71\,\mathrm{F\,g^{-1}}$. This is a reasonable value for a single porous carbon electrode [321, 600, 602]. Members of the porous electrode community usually show the actual system capacity $C_{\mathrm{sys}} = \frac{C_s}{4}$. This is a quarter of the specific capacitance and around $18\,\mathrm{C\,g^{-1}}$ for the ACC-20 system with 1 $DyCl_3$.

As previously mentioned, the initial current I_0 is proportional to the applied voltage E and is shown in Fig. 4.23(c). A value for the total resistance R_{tot} is obtained from the slope and the expression for the initial current $I_0 = \frac{E}{2R_{\mathrm{tot}}}$. In the ACC-20 cell with its Pt wire connection, the value was $R_{\mathrm{tot}} = 2\,\mathrm{m\Omega\,m^2}$. It is assumed that a combination of electrolyte resistance and the piercing Pt wire connection were responsible for this. A division of all charge-discharge curves by the initial current I_0 leads to a normalised curve that captures the current behaviour at all applied voltages fairly well (see Fig. 4.23(d)). Sophisticated models for the double layer charging in porous electrodes, such as the transmission line model, exist and predict the collapsing of all charge/discharge curves onto such a mastercurve [321].

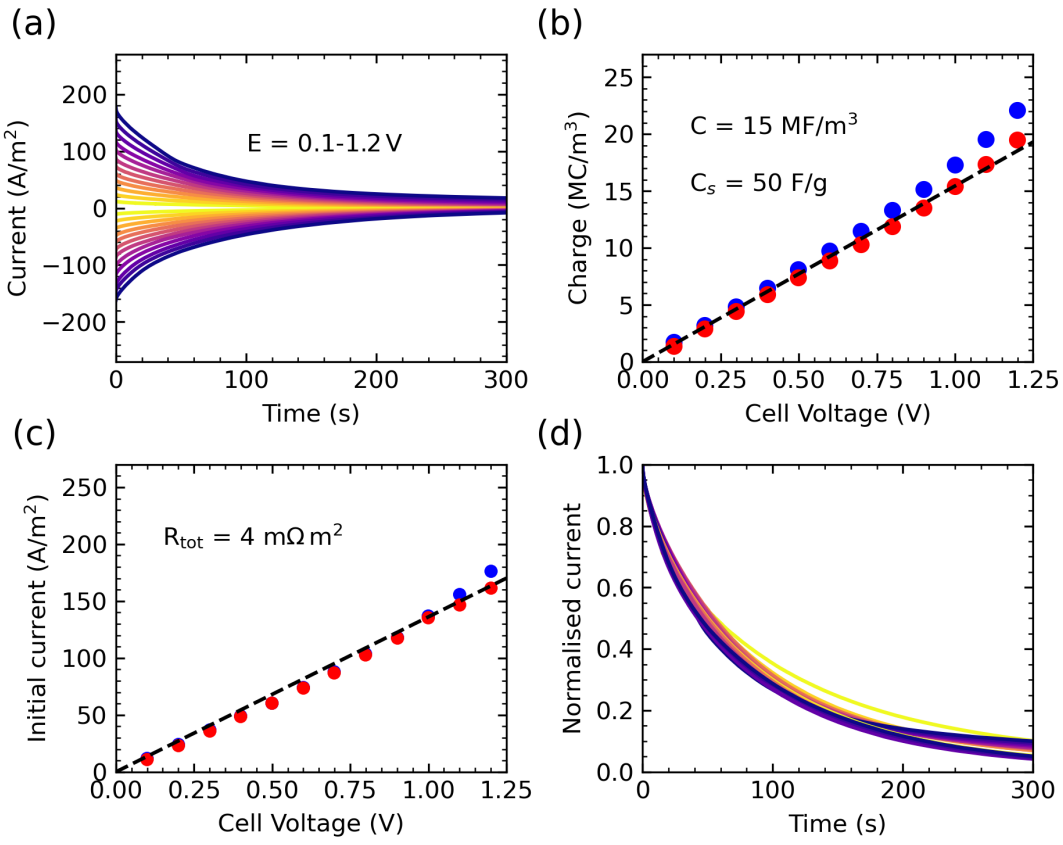

Figure 4.24 – Square wave chrono-amperometry of two microporous ACC-10 cloth ($985\,\mathrm{m^2 g^{-1}}$). See Fig. 4.23 for explanation.

The crucial value of interest here is the specific capacitance $C_s = 71\,\mathrm{F\,g^{-1}}$, which indicates good electrosorptive properties. An identical analysis was carried out for ACC-10 electrodes in the same 1 M $DyCl_3$ solution. The results of this are shown in Fig. 4.24 and indicate a lower

specific capacitance of $C_s = 50\,\mathrm{F\,g^{-1}}$ for the lower density cloth (see Table 5). This indicates that ACC-10 is less beneficial for application in capacitive deionisation cells. Uncertainties mainly stem from different surfaces due to unravelling carbon fibres during the cutting of the electrodes and differing connections with the Pt wires.

There is a general tendency for higher charge affinity during electrosorption with high surface area materials. The specific surface areas from nitrogen gas adsorption measurements indicated $1959\,\mathrm{m^2g^{-1}}$ for ACC-20 and only $985\,\mathrm{m^2g^{-1}}$ for ACC-10 (see Table 5). Previous capacitive deionisation experiments with activated carbon cloths from Kynol® indicate that the effect of the heightened surface area is measurable, but subtle [585,586]. For this reason, neutron imaging experiments were only performed with the highest surface area cloth ACC-20.

Attempts were made to measure an influence of a magnetic field gradient on charge and discharge currents of the porous electrodes. A 20 mm Nd-Fe-B magnet cube behind the electrodes did not change the current in any reproducible way. A Lorentz force effect with the magnetic field orthogonal to the current was also not measurable. Previous chrono-amperometric studies on metal electrodepositions have shown that higher limiting currents are necessary to observe an effect in a cell with wider spaced distance between the electrodes [61, 62]. These limiting current densities reached $j = 50\,\mathrm{A\,m^{-2}}$. The magnitude of the Lorentz force density $\mathbf{F_L} = \mathbf{j} \times \mathbf{B}$ in a magnetic field of $B = 0.5$ is around $25\,\mathrm{N\,m^{-3}}$. The metal depositions were not concerned with capacitive currents and the convection of the paramagnetic fluid is key to any magnetic effect on the current readout.

4.4.2. Neutron Imaging of Capacitive Deionisation with Activated Carbon Cloths

Experimental Setup

The neutron imaging experiments were performed under the same conditions as those described in Sections 4.2.1 and 4.3.2 above. A sketch of the experiment is shown in Fig. 4.25. The sample holder was changed from the PTFE cell in Section 4.3.2 to an optical glass[51] cuvette (Hellma®) with a path length of 5 mm. This was placed 1 cm in front of the detector. The outside dimensions of the cuvettes were 40 mm × 23.6 mm × 7.5 mm (height × width × depth).

Porous activated carbon cloth (ACC) electrodes from ACC-20 were cut to approximately 7 mm wide and 43 mm long stripes. The cut cloths were soaked in D_2O to avoid air bubble formation during the neutron imaging experiments. After soaking in D_2O, the cloths were pierced with 100 µm diameter silver wires and hook clipped to the power leads of a potentiostat (Biologic SP-300). The cloths were then stuck to the inside front window of the cuvette by capillary forces and the cuvette was filled with 3.5 mL 70 mM $Gd(NO_3)_3$ solution in D_2O. A dark-current corrected neutron image during the first charging process, normalised by the open neutron beam, is shown in Fig. 4.25(b).

[51] Although this type of crown glass was free of borosilicate and therefore had a good neutron transmittance value, it turned out to be a poor choice due to neutron activation of the glass. The reason for this was probably a significant sodium oxide (Na_2O) content. ^{23}Na nuclei are prone to neutron capture to form radioactive ^{24}Na with a half-life of 16 h. The short-term radioactivity by decay to ^{24}Mg under emission of an electron and γ-rays is intense.

Parafilm was used to cover the cell and minimise evaporation and D_2O-H_2O exchange [499]. In this experiment, the silver wires were not in direct contact with the $Gd(NO_3)_3$ solution. As a consequence, the top 10 mm of each carbon cloth electrode was protruding from the cell and not immersed in the $Gd(NO_3)_3$ solution. Nonetheless, $Gd(NO_3)_3$ solution climbed up the cloth via capillary action. To minimise the evaporation from these exposed soaked carbon cloths, the top part was wrapped with Kapton tape.

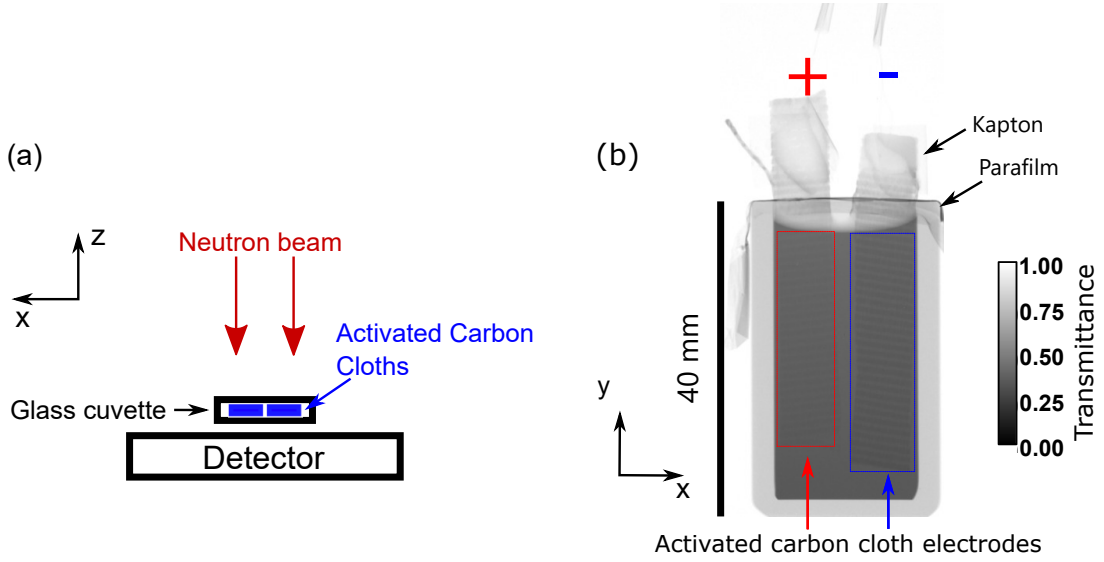

Figure 4.25 – Neutron imaging setup: Capacitive deionisation with activated carbon cloths. (a) Sketch of the experimental setup (top view). The glass cuvette contained the activated carbon cloths electrodes and $Gd(NO_3)_3$ solution. The electrodes were connected to a potentiostat. (b) Dark-current corrected neutron image (normalised by open beam: $T = \frac{I-I_{dc}}{I_0-I_{dc}}$) of the 5 mm path length cuvette with 70 mM $Gd(NO_3)_3$ solution: 40 min into first charge at 0.7 V. Right electrode: negative charge (Gd^{3+}); Left electrode: positive charge (NO_3^-). Heightened c_{Gd} in the right electrode lowers the neutron transmission and vice versa for the left electrode. The ribbed structure of the cloths with 1 mm ribs is clearly visible in the image.

Results and Discussion

Consecutive voltages of 0.7 V, 0 V and -0.7 V were applied to the ACC electrodes and the migration of the Gd^{3+} ions into the micropores was monitored in situ by variations in the neutron attenuation. Small changes in the transmittance were converted to Gd concentration changes Δ_{Gd} in the ACC electrodes with Eq. 4.6 in Section 4.3.2.

The Δ_{Gd} maps resulting from the first charge at 0.7 V are displayed in Fig. 4.26 and the time evolution of the mean Δ_{Gd} within the activated carbon cloth electrodes is shown in Fig. 4.26. The accumulation of Gd^{3+} is measurable and even visually perceivable within a minute of applying the potential difference. A plateau is reached after 40 min. Once again there are gaps in the recorded data due to placing the black-body grid in front of the sample when it is in a stationary state.

A difference to the previously treated carbon aerogel is that the path length Δz in the equation for Δ_{Gd} is lower: $\Delta c_{Gd} = -\ln\left(\frac{I(t_2)/I(t_1)}{\sigma_{Gd} N_A \Delta z}\right)$. At approximately 0.55 mm thickness, the activated

carbon cloths were thinner than the carbon aerogel monolith ($\sim 2.5\,\mathrm{mm}$). The micropores of the cloth had a maximum capacity of $14\,\mathrm{mM}$ Gd^{3+} at $0.7\,\mathrm{V}$. Few ions from the bulk solution were adsorbed, which is appreciable when inspecting Fig. 4.27. The concentration changes within the ACC electrodes are generally symmetric, meaning that the ions are predominately exchanged from one to the other. This meant that changes of Gd^{3+} concentration in the bulk liquid were essentially undetectable by neutron imaging at a path length of $5\,\mathrm{mm}$ in the glass cuvette. As a result the approximation of using the ACC electrode thickness as path length in the calculation of Δ_{Gd} is accurate and incurs no uncertainty.

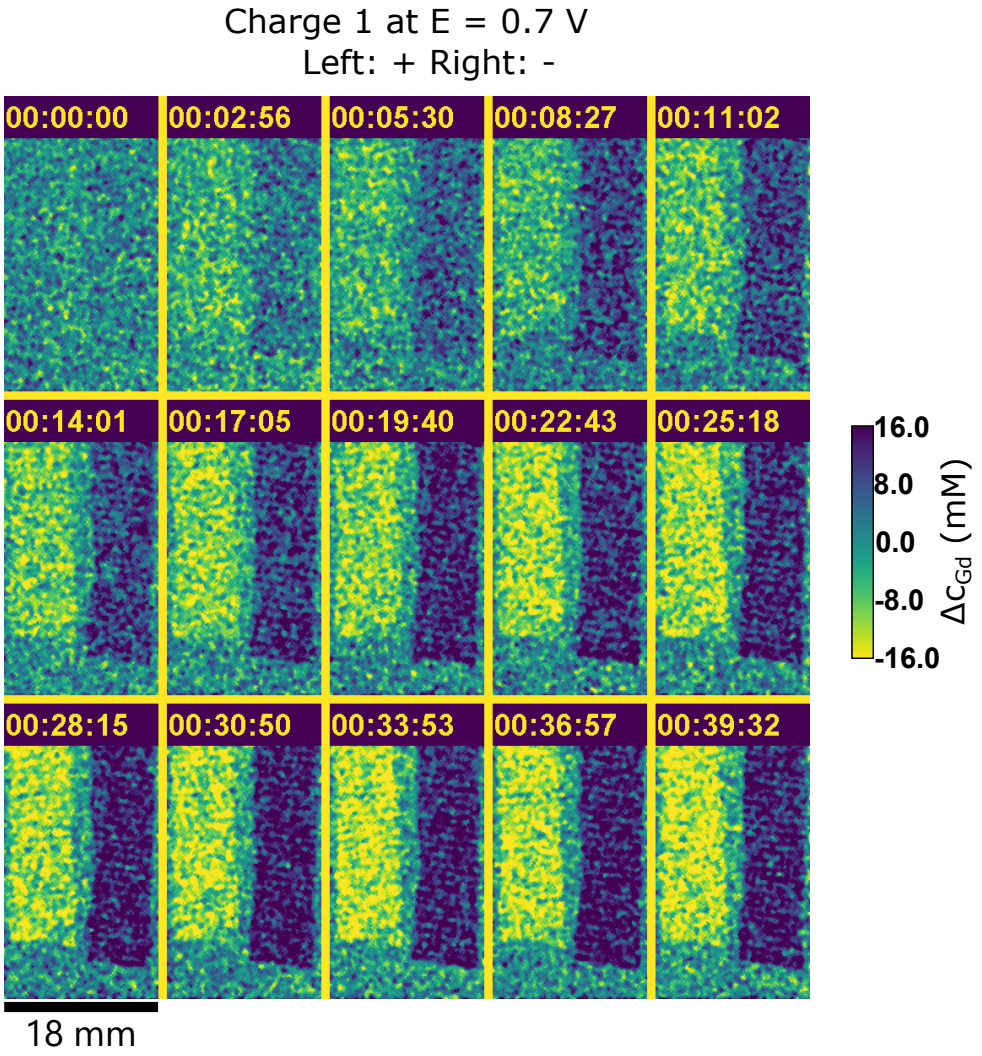

Figure 4.26 – Neutron images converted to Δ_{Gd} within 0.55 mm thick activated carbon cloth electrodes. The electrodes were in 5 mm path length glass cuvette full of 70 mM $Gd(NO_3)_3$ solution. Charge process at 0.7 V. Right electrode: negatively polarised, left electrode: positively polarised. The images are restricted to below the liquid surface. The ribbed structure of the cloth can still be seen amid the grainy noise.

During the discharge of the electrodes at 0 V, most of the Gd^{3+} remained trapped in the 1 nm micropores. This blocking of the micropores after adsorption of NO_3^- is widespread and degrades the cloths. Both cloths kept half their adsorbed ions with $\Delta_{Gd} = 7\,\mathrm{mM}$ after the first discharge.

None of the charge processes following the first one recovered its Gd^{3+} adsorption capability of approximately 14 mM with respect to the initial concentration distribution. However, the ACC electrodes were always able to transfer approximately 14 mM Gd^{3+} to the negatively charged cloth. The left electrode in the first charge at -0.7 V went from $\Delta_{Gd} \approx -6.5$ mM to $\Delta_{Gd} \approx 7$ mM, while the converse was true for the right electrode. The initial three charges are symmetric around the y-axis with $\Delta_{Gd} = 0$. At the second discharge at 0 V, the left electrode lost all its adsorbed Gd^{3+} and returned to the initial state.

A pulse of -0.7 V was applied during the last charge phase, directly after application of an 0.7 V charging current. This rapidly removed all the ions from the micropores, which can be seen in the sharp descent of Δ_{Gd}. Then the ions transferred onto the oppositely charged side. Applying a non-zero voltage during the discharge phase has been known to mitigate co-ion adsorption [568].

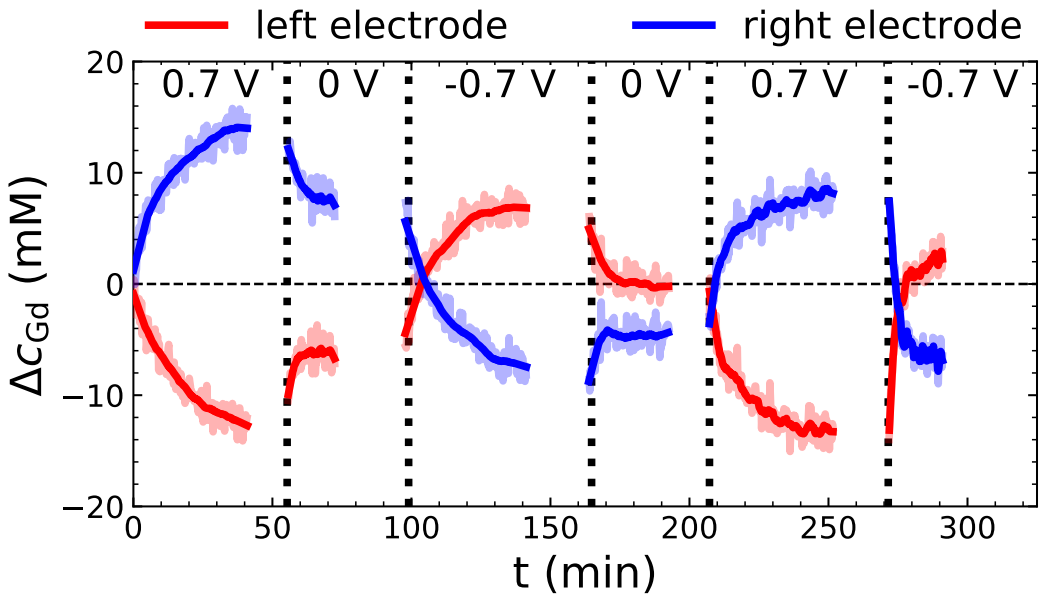

Figure 4.27 – Mean concentration change in the ACC electrodes with respect to the initial situation prior to the first charge. The converted neutron images corresponding to the first charge at -0.7 V are shown in Fig. 4.26. A comparison of the measured Δc_{Gd} with data from the potentiostat is shown in Fig. 4.28. Gaps in the recorded data are caused by a black-body grid blocking the sample.

The Gd^{3+} ion concentration attributed to adsorption in the micropores of the ACC can be compared to the readout from the potentiostat. The comparison is shown in Fig. 4.28. The top two panels show the applied potential and measured current. The noisy voltage reading at the end of the first discharge process indicates that the installation of the black-body grid caused interference with the wire connection to the potentiostat. The connection stabilised upon its removal. The charge resulting from the integrated current signal is shown in Fig. 4.28(c). The left y-axis indicates the value in coulombs and on the right converted to a concentration of trivalent ions. Division by Faraday's constant and the activated carbon cloth volume ($V \approx 0.12$ mL)

leads to this value. Thus, a charge of 2 C is equivalent to 57.6 mM of trivalent ions. The charge efficiency $\Lambda = \frac{3\Delta_{Gd}}{\Delta Q}$ can be calculated from these values and this is summarised in Table 6. The ratios during the discharge processes are also shown for comparison.

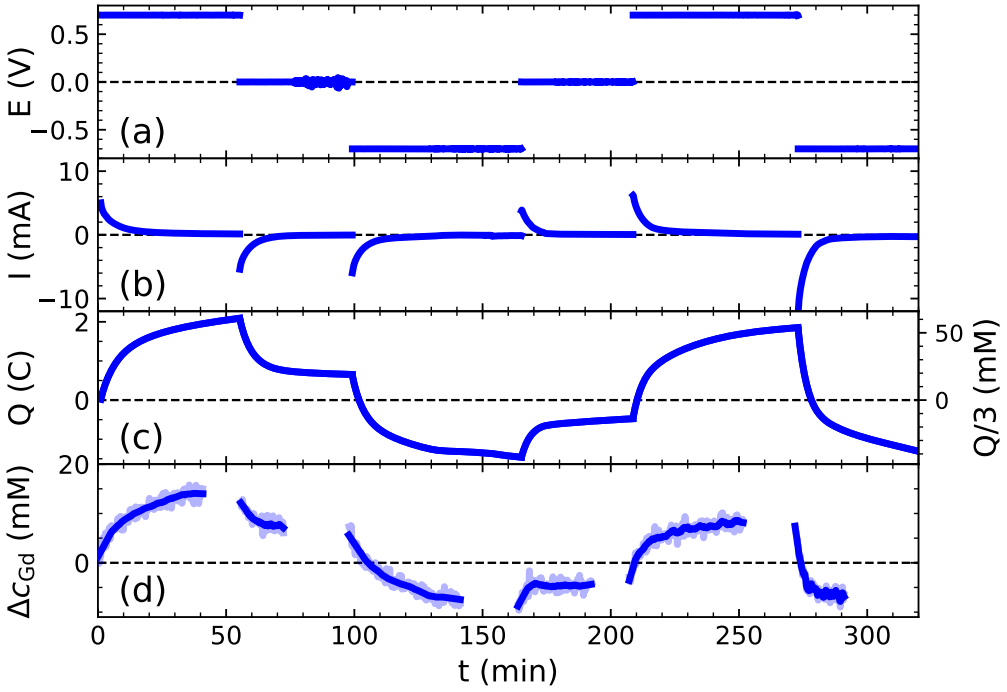

Figure 4.28 – Comparison of the readout from the potentiostat and Δc_{Gd} detected by neutron imaging. (a–b) The cell voltage and the measured current. (c) The integrated current shows the charge Q, which can be converted to a concentration of trivalent ions (see right y-axis). (d) The neutron imaged Δc_{Gd} in the right aerogel (see Fig. 4.11). The charge efficiency Λ_{Gd} based solely on the capture of Gd^{3+} is 0.24 during the first charge, but then drops to around 0.14.

	E (V)	$\frac{\Delta Q}{3}$ (mM)	Δc_{Gd} (mM)	Λ
Charge 1	0.7	60.82	14	0.23
Discharge 1	0	41.8	7	0.17
Charge 2	-0.7	-61.5	15	0.24
Discharge 2	0	28.6	4	0.14
Charge 3	0.7	67.7	12	0.18
Charge 4	-0.7	91.6	15	0.17

Table 6 – Charge efficiency Λ of activated carbon cloth connected to power source with silver wires. Corresponding values shown in Fig. 4.28. The applied voltage E (V) is displayed alongside the accumulated charge converted to a concentration of trivalent ions $\frac{\Delta Q}{3}$. The measured Δc_{Gd} via neutron imaging only accounts for around 20% of the charge indicated by the potentiostat.

The Λ values are around 24% during the first two charging process and drop to 18% for the third and fourth charge. These values are low, but not unusual for capacitive deionisation with ACC electrodes. Avraham et al. reported $\Lambda \approx 36\,\%$ for a cell voltage of 0.6 V [568]. They were able to double the efficiency of the system by never allowing the ACC electrodes to fully discharge. This was accomplished by successive switching between 0.4 V and 0.6 V. This choice of potential window effectively quashes migration of counterions into the electrodes during the desorption phase. Kim et al. also reported charge efficiencies below 40% for ACC capacitive deionisation electrodes operated at 0.6 V [585]. This study also contains Λ values for ACC capacitive deionisation cells without current collectors that usually consist of a titanium backing frame. The absence of a sturdy current collector led to a 26% drop in charge efficiency. Without a current collector there is an energy loss due to high resistance. The electrical resistivity of activated carbon cloths is around $4 \times 10^{-4}\,\Omega\,\mathrm{m}$ [585], one order of magnitude lower than regular graphite. This will undoubtedly dissipate energy during operation at constant voltages. Both salt adsorption capacity and charge efficiency are severely impacted by this. In the present experiment, the current had to traverse around 10 mm of activated carbon cloth before reaching the solution (see Fig. 4.25(b)). In comparison, the carbon aerogels had the electric conductivity of regular graphite and less resistive losses due to direct silver connections to the monoliths in solution.

A magnet was placed next to the ACC electrodes during later charge and discharge cycles to investigate a possible modification of the Gd^{3+} ion transfer. No clear effect of the magnet on the electrosorption process was measurable. Unlike in the capacitive deionisation cycles with the carbon aerogel electrodes, no large scale concentration changes were recorded in the cell during the capacitive deionisation process. Hence, the magnetic field gradient had no means to modify the $Gd(NO_3)_3$ concentration distribution, although a Moses effect [514,603] was observed when the edges of the magnet coincided with the surface interface of the $Gd(NO_3)_3$ solution. Depending on the vertical position of the magnet, the interface was pulled up or down.

There was a large gradient of Gd^{3+} ions (∇c_{Gd}) on the surface of the ACC electrodes and within the micropores themselves, this becomes steep. But any effect of the Kelvin force is trounced by the massive electrostatic forces in the overlapping electric double layer. From an energetic point of view, the interaction of the microscopic magnetic dipoles with the magnetic field is irrelevant here. For all intents and purposes it is inconceivable that a magnetic field would have any effect on the electrosorption of ions in micropores.

4.5. Conclusion

The dynamic neutron imaging experiments provided a clear record of the capacitive deionisation of paramagnetic $Gd(NO_3)_3$ solutions by porous carbon electrodes. For disk shaped carbon aerogel electrodes with a broad pore size distribution comprising meso- and macropores, both the Gd^{3+} ion transport inside the porous carbon electrode and the diffusion limited desalting of the bulk solution were captured. In the case of microporous activated carbon cloths, the neutron radiographs provided information about the adsorption in the micropores. In general, thermal

neutrons are more suitable for the imaging of Gd^{3+} concentrations than cold neutrons due to their lower neutron absorption cross section. Both higher concentrations and path lengths can be probed with the superior penetrative properties.

From a capacitive deionisation point of view, the experiments affirm the consensus that ion exchange membranes or even Faradaic electrodes are necessary to ensure high charge efficiencies and avoid co-ion adsorption [321, 324, 326, 330, 336]. The far from complete desorption of Gd^{3+} ions from the mesopores of the carbon aerogel and the micropores of the activated carbon cloths can be directly visualised by inspection of neutron images. Furthermore, the method is useful to directly determine the change of salt adsorption properties after successive cycles. Although inconclusive, the experiments indicate more favourable properties of the carbon aerogel monoliths for capacitive deionisation in comparison to the activated carbon cloths. The measured charge efficiency was higher, although the activated carbon cloths had more than twice the specific surface area. This indicates that pores of small size do not necessarily contribute to higher capacitive deionisation performance. A study of activated carbon aerogels may provide answers to whether an increase in surface area can improve salt adsorption capability [604, 605].

From a magnetic point of view, the unstirred solutions provide an interesting model system to probe how concentration distributions can be modified by magnetoconvection. A vertical concentration gradient of $Gd(NO_3)_3$ was created by the capacitive deionisation with the carbon aerogel electrodes and a magnetic field gradient was able to disturb the hydrostatic stability. The electric driving force from the porous electrodes represents an addition to the previously studied evaporation controlled magnetic enrichment method [154, 155, 161, 162, 164–166]. Specifically, the customisability of the geometry for the harvesting of ions in a cyclical process is noteworthy.

More generally, a magnetic field gradient affects the bulk solution when the capacitive deionisation electrodes adsorb ions and create a concentration gradient. A paramagnetic salt solution will be pulled towards the porous electrode backed by a permanent magnet with a stray field normal to the electrode surface. Magnetically structured paramagnetic electrodeposits previously showed the effect of bulk magnetoconvection into a field gradient on an electrode. It is unclear, if magnetoconvection is resilient enough to exist in conventional capacitive deionisation cells run with flowing salt solution. A bulk flow of the liquid might wipe out any concentration gradients before the magnetic field gradient has the chance to act. However, a 2019 experimental study of magnetic forces in a microelectrode-microfluidic system showed that magnetic manipulation of the reaction products is possible under flow [53]. This study employed a magnetised Co-Fe microstrip behind the electrode and demonstrated effects of both the Lorentz and the Kelvin force. Such an experiment is worth investigating with a porous microelectrode instead of the conventional one. Previous studies have already demonstrated the accelerated transport of paramagnetic ions from unstirred solutions through a porous membrane in magnetic fields [264, 606]. Miniaturisation of the capacitive deionisation cell will serve to maximise the concentration and potential gradients within.

Porous carbon electrodes offer many hitherto unexplored opportunities in combination with magnetic field gradients in general. Research on different ion selective mechanisms in the electrosorbing pores, such as selectivity by hydration or ionic radii, is ongoing [345–349] and may

complement magnetoconvection towards the desalinating electrodes. Such a cell may integrate small magnets or even incorporate a magnetic material directly in the porous electrode [607,608], thus generating larger magnetic field gradients. A magnetic field normal to a ferromagnetic porous electrode was shown to increase the efficiency of water electrolysis via the Lorentz force (MHD stirring) [607]. A recent study published in 2021 included magnetite nanoparticle in porous activated carbon electrodes via co-precipitation [608]. These magnetic nanoparticles were ripped out of the porous electrodes during capacitive deionisation with a flow. Parts of the capacitive deionisation electrodes invariably become fluidised while running under flow and must be separated from the water. This study showed that magnetic separation of the magnetite particles connected to the carbon electrode was a useful approach to achieve this. Charge efficiencies of over 100% were achieved with these magnetic carbon electrodes. In the field of organic aerogels, magnetic microparticles (10–15 µm) have been shown to create artifical porous networks by alignment in a magnetic field during gelation [564]. Bespoke geometries with magnetic inclusion may be created by this method, although pyrolysis of the magnetically modified aerogel was not reported. A curious thought is that low density carbon aerogels, which have adsorbed a significant concentration of paramagnetic ions, will gain a paramagnetic susceptibility themselves and can be moved around with a magnetic field gradient.

Neutron imaging with higher temporal and spatial resolutions [609–611] will lead to further improvements in dynamic measurements of ion movement in porous materials. A slight drawback to neutron imaging of desalination processes is the reliance on D_2O, but the chemical properties hardly differ with respect to regular water. Previous studies with flow-through cells [528, 529] showed the possibility of analysing more realistic capacitive deionisation cells than the unstirred version reported here.

Two interesting recent developments in neutron imaging are worth mentioning. The first is the unlocking of small-angle neutron scattering information via dark-field imaging [451–454]. This technique involves the detection of small-angle scattering signals from microstructure and their conversion to a real space image. Small-angle neutron scattering can resolve particles in the range of 1–100 nm. The pores of carbon-based capacitive deionisation electrodes fall in this range and have been previously studied with this scattering method [523, 524, 612–616]. Dark-field imaging can draw upon this information from reciprocal space and create a real space image. Dynamic dark-field measurements have only been performed stroboscopically up to now. The second development is the use of polarised neutrons to detect magnetic fields [449,455–458]. Due to their half integer spin, neutrons can interact with magnetic fields and it is possible to measure a magnetic image contrast by acquiring subsequent images with neutrons polarised at 180° to each other. Both these techniques are still in their infancy, but offer unique opportunities for experiments once they become more established.

Back to capacitive deionisation: one point that has not been discussed up to now is the influence of the pH value close to the electrode on the aquatic chemistry of the rare earth ions. In the Pourbaix diagram of the rare earths (Fig. 2.10), it can be seen that the rare earth ions precipitate as insoluble hydroxides under basic conditions. Strong fluctuation in the pH value during electrosorption in capacitive deionisation cells with and without a membrane have been

reported by HASSANVAND et al. [573] in 2018. A basic pH during the adsorption phase presents an issue for rare earth ions as a hydroxide precipitation is triggered. This bares the risk of clogging up the pores of the electrode and degrading the capacitive deionisation cell. However, a controlled rare earth hydroxide precipitation may serve a purpose in a potential magnetically aided rare earth separation. This will be the topic of the next chapter.

5. Rare Earth Electrolysis under Magnetic Field Gradients

When they were up, they were up,
And when they were down,
they were down,
And when they were only halfway up,
They were neither up nor down.

The Grand Old Duke of York
English Nursery Rhyme

This chapter reports experiments on the electrochemical separation of rare earths from nitrate solutions with the aid of a magnetic field gradient. These experiments were carried out as part of the REMEDY project. *All data are proprietary and the method must remain confidential.*

5.1. Introduction

The previous chapter focused on the electrosorption of Gd^{3+} in the electrical double layers of porous carbon electrodes. No chemical conversion of the Gd^{3+} ions takes place in an electrosorption process. This is convenient, since the rare earths are very electropositive, meaning that their standard reduction potentials at around $-2.3\,V$ are strongly negative (see Fig. 2.10 and Table 2 in Section 2.4). Thus, the electrochemical stability window of water prohibits the electrodeposition of rare earth metals from aqueous solutions. Direct electrodeposition is restricted to deposition from molten salts [617] or organic electrolytes [618,619]. The former must be carried out at temperatures of around 900°C.

Electrochemical reactions from aqueous solutions containing trivalent rare earth ions (RE^{3+}) are relegated to the formation of gelatinous rare earth hydroxides at the cathode. This is due to the electrochemical generation of a basic environment with high concentration of hydroxide ions OH^- that locally shifts the pH. Nitrate (NO_3^-) is reduced to nitrite (NO_2^-) at the working electrode electrode:

$$NO_3^- + H_2O + 2e^- \longrightarrow NO_2^- + 2OH^-_{(aq)}. \tag{5.1}$$

This releases OH^- ions into the solution around the cathode. In addition, the electrolysis of water can lead to the formation of OH^-. This is accompanied by the release of hydrogen:

$$2H_2O + 2e^- \longrightarrow H_{2(g)} + 2OH^-_{(aq)}. \tag{5.2}$$

A glance at the Pourbaix diagrams (Fig. 5.1) for Gd and Y shows the pH-boundary between ions and hydroxides as the vertical lines. The precipitation of the water-insoluble rare earth (RE) hydroxides ($RE(OH)_3$) at the working electrode is given by the hydrolysis reaction with the hydroxide ions:

$$RE^{3+}_{(aq)} + 3OH^-_{(aq)} \rightleftharpoons RE(OH)_{3(s)}. \tag{5.3}$$

The electrochemically precipitated rare earth hydroxide can then be dehydrated and rare earth sesquioxides (RE_2O_3) are formed at high temperatures.

As was mentioned in Section 2.4, the basicity of the rare earths differs along the series due to changes in their ionic radii [380–382]. The pH at which the hydroxides precipitate varies with the basicity and exploiting this in a separation process is a real possibility.

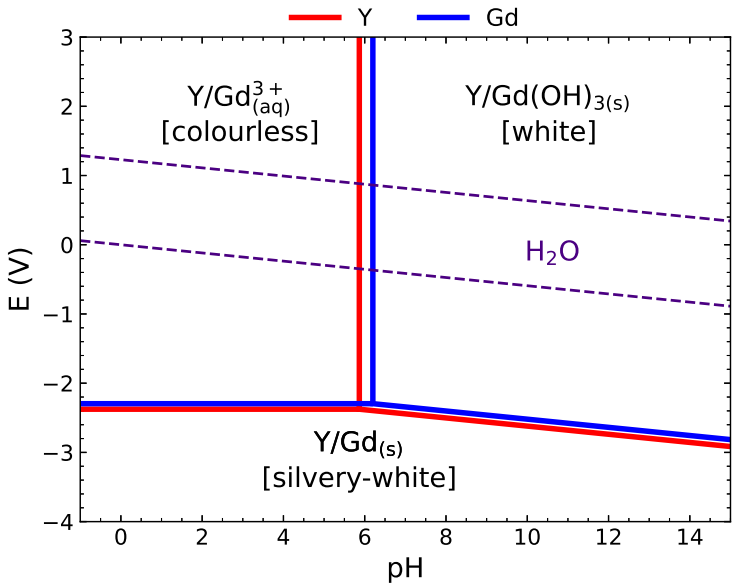

Figure 5.1 – Pourbaix diagram of Y (red) and Gd (blue) at c = 0.5 M [350]. Rare earth nitrate solutions are slightly acidic and the RE^{3+} form dominates. The vertical lines show the pH value boundary between the solvated RE^{3+} and their respective hydroxides. For Gd and Y, the pH boundaries of hydroxide precipitation are within 0.5 of each other.

The first separation of rare earths via electrolysis of chloride solution was reported by Gerhart Krüss as early as 1893 [378]. The fractionation of electrochemically precipitated rare earth hydroxides was seriously explored in the United States during the First World War [395–397] and later at the University of Illinois in the 1920s [398,399]. All these experimental findings show a proclivity for the heavy rare earths with lower basicity to form hydroxides on the electrode before the light rare earths, which are more resistant to reduction. However, the separation of the individual heavy rare earths in the hydroxides was nowhere near as efficient as that between light and heavy rare earths.

This research was carried out before the discovery of rare earth separation by ion exchange, when fractional crystallisation or precipitation methods were the norm. Despite the fact that these fractionation methods were prohibitively time consuming, they failed to deliver pure rare earth elements [350]. It is important to realise that an electrochemical rare earth hydroxide precipitation does not offer any distinction from any other form of precipitation [383–394]. The sole difference is the customisability of the electrode geometry in which the precipitation takes place and greater control of the local environment by tuning the electrode potential. This also comes with drawbacks, such as gradual blocking of the electrode by hydroxides which slows the reaction down.

5.2. Experimental Aim and Rationale

The aim of the experiments presented in this chapter was to analyse the effect of a magnetic field gradient on the mass transport of the paramagnetic rare earth ions during their hydrolysis to hydroxides and subsequent dehydration to oxides. This was done with a view to a magnetically directed separation of paramagnetic from non-magnetic rare earths on the electrode.

A sketch of the motivation behind the experiment is depicted in Fig. 5.2. Magnetic field gradients are generated by permanent Nd-Fe-B magnets behind the working electrode as in previously reported magnetoelectrochemical experiments [76–79]. Despite the similarity of the experimental setups, the key difference lies in the fact that no electroplating of the rare earth metals is possible. In contrast, copper is reduced to a metallic state via deposition from Cu^{2+} in solution and a concentration gradient forms right above the cathode surface. The insoluble rare earth hydroxides are gelatine-like and stick to the cathode surface in a much less uniform layer. Hence, the magnetic field gradient can act both on the forming paramagnetic ion concentration gradient and the precipitated paramagnetic hydroxide. In essence, the experiment is more similar to the magnetic field gradient that was successful in aiding separation of rare earths via crystallisation reported by Higgins et al. [438].

The reaction in question was the reduction of water-insoluble rare earth hydroxides from a binary mixture of concentrated rare earth nitrates. Due to lanthanide contraction of the ionic radii along the series, Y^{3+} is classified as a heavy rare earth (see Fig. 2.8). Thus, it has proven to be particular elusive to separation due to similarity in basicity. Its hydroxide precipitates in a near identical way to that of other heavy rare earths. In contrast to the paramagnetic heavy rare earths (except Lu, with its full 4f orbital), Y^{3+} is diamagnetic. For this reason, a mixture of paramagnetic $Gd(NO_3)_3$ and non-magnetic $Y(NO_3)_3$ solutions was chosen as a model system for the magnetically aided separation process. In this way, an observed separation could be ascribed to the magnetic field gradient with greater certainty.

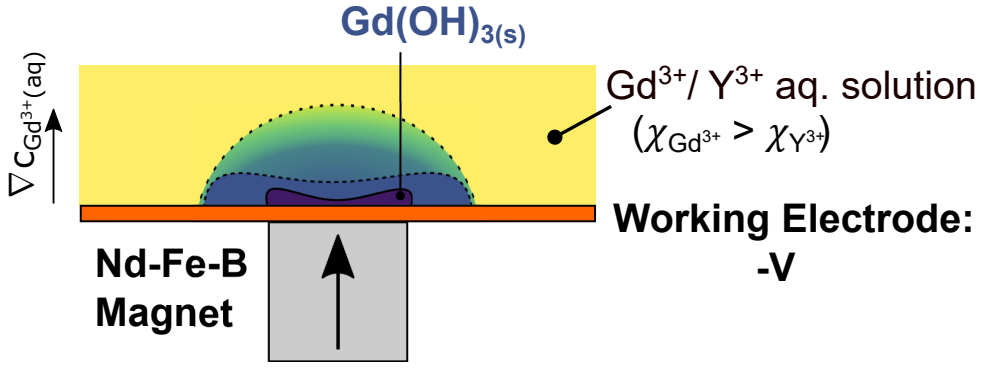

Figure 5.2 – Sketch of the anticipated rare earth hydroxide precipitation. The working electrode creates a concentration gradient of rare earth ions. Paramagnetic Gd^{3+} precipitates in form of $Gd(OH)_3$. The magnet can capture the solid $Gd(OH)_3$ and cause the bulk liquid to flow towards the magnet via magnetoconvection. The $Gd(OH)_3$ is expected to accumulate at the magnet edges where the gradients are most intense. Lower quantities of $Y(OH)_3$ should form elsewhere on the electrode.

The expected situation at the cathode after precipitation under a magnetic field gradient can be seen in Fig. 5.2. The aim of the experiments was to show that the Gd^{3+} ions accumulate on the electrode in vicinity of the magnets, where they precipitate as hydroxides. Thus, a separation of $Gd(OH)_3$ from the non-magnetic Y^{3+} should be achievable.

5.3. Materials and Methods

A glass electrochemical cell was fitted with a 3d-printed polymer lid and holder for the electrodes. A sketch of the electrode setup is shown in Fig. 5.3. A Ag/AgCl reference electrode and a wound Pt wire counter electrode were used throughout (see Fig. 5.3(a)). The reference electrode was placed in a saturated KCl salt bridge to avoid contamination from the rare earth nitrate solution.

An aqueous solution of paramagnetic 0.5 M $Gd(NO_3)_3$ and non-magnetic 0.5 M $Y(NO_3)_3$ was prepared from the respective hexahydrated nitrate salts. The electrochemical cell was filled with 40 mL of this solution and placed in a glass jacketed cell with temperature controlled by circulating water. A thermocouple in the electrochemical cell provided temperature readings and was used to ensure isothermal experimental conditions. All of the electrodes were connected to a Metrohm Autolab potentiostat (Metrohm Autolab: PGSTAT 302N) by cables with BNC connectors.

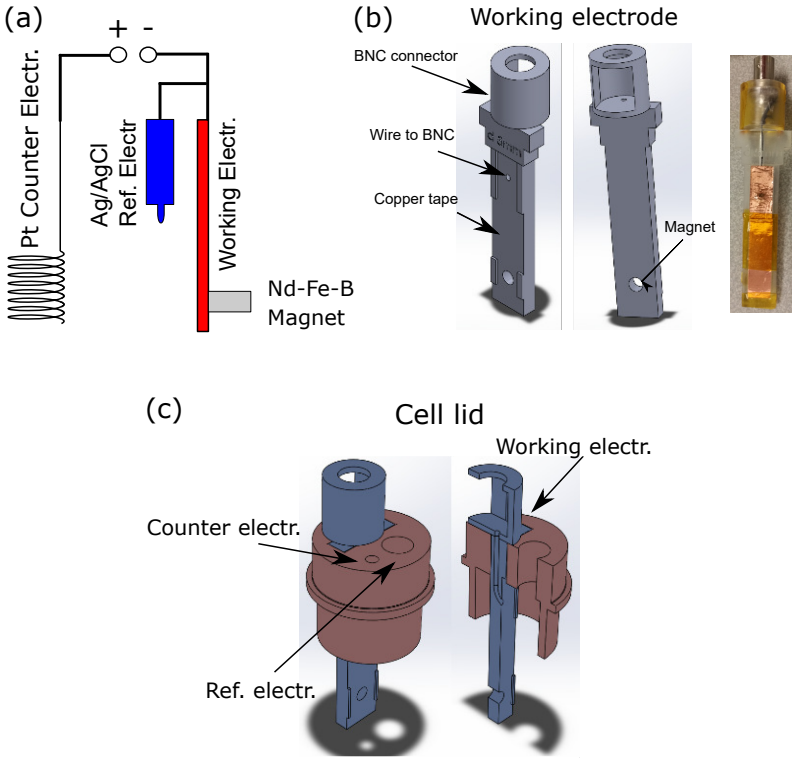

Figure 5.3 – Set up of the electrochemical cell: (a) Sketch of three electrodes with magnet. (b) Design for the 3d printed working electrode holder. The final assembly is shown to the right of the sketches. (c) Design of the 3d printed lid for the electrochemical cell. Openings for the working electrode, the counter electrode and salt bridge of the reference electrode are indicated.

Two different working electrode materials were used for the experiment. Copper tape with a thickness of 30 µm was chosen for the identification of the ideal voltage and temperature for the reaction. This changed to sputter deposited gold on an oxidised silicon wafer for the study of the electrodeposits, as the rare earth hydroxides detach from the copper easily. The deposition area was limited to 1 cm^2 by ensuring isolation of the rest of the copper with Kapton tape. The precipitation from nitrate solutions in form of rare earth hydroxide is strongly temperature dependent and no appreciable effect was observed below a temperature of $T = 40\,°C$.

A 5 mm diameter Nd-Fe-B magnet cylinder, with 5 mm length and field strength of 0.4 T at the surface, was slotted into the hole in the holder. The magnet was pushed against the working electrode for maximum magnetic field. Calculated field profiles are shown in Fig. 5.4. The distance between electrode surface and magnet was around 0.1 mm for the Cu and 0.5 mm for the Au electrode. Contamination by the Ni coating of the Nd-Fe-B magnets was avoided by covering the magnet surface with nail varnish.

The only other configuration of magnets used were two 10 mm cubes that were placed next to each other head to tail (↑↓). This causes a magnetic field of 0 T on a line between the magnets, because the fields cancel each other out. The calculated magnetic field profile above the working electrode is shown in Fig. 5.5.

Solutions of Gd^{3+} and Y^{3+} are colourless. Both Gd and Y oxide powders have a white colour and are visually indistinguishable. This necessitates quantitative elemental analysis of the products on the working electrode by energy dispersive x-ray analysis (EDX) in combination with scanning electron microscopy (see Section 5.4.3).

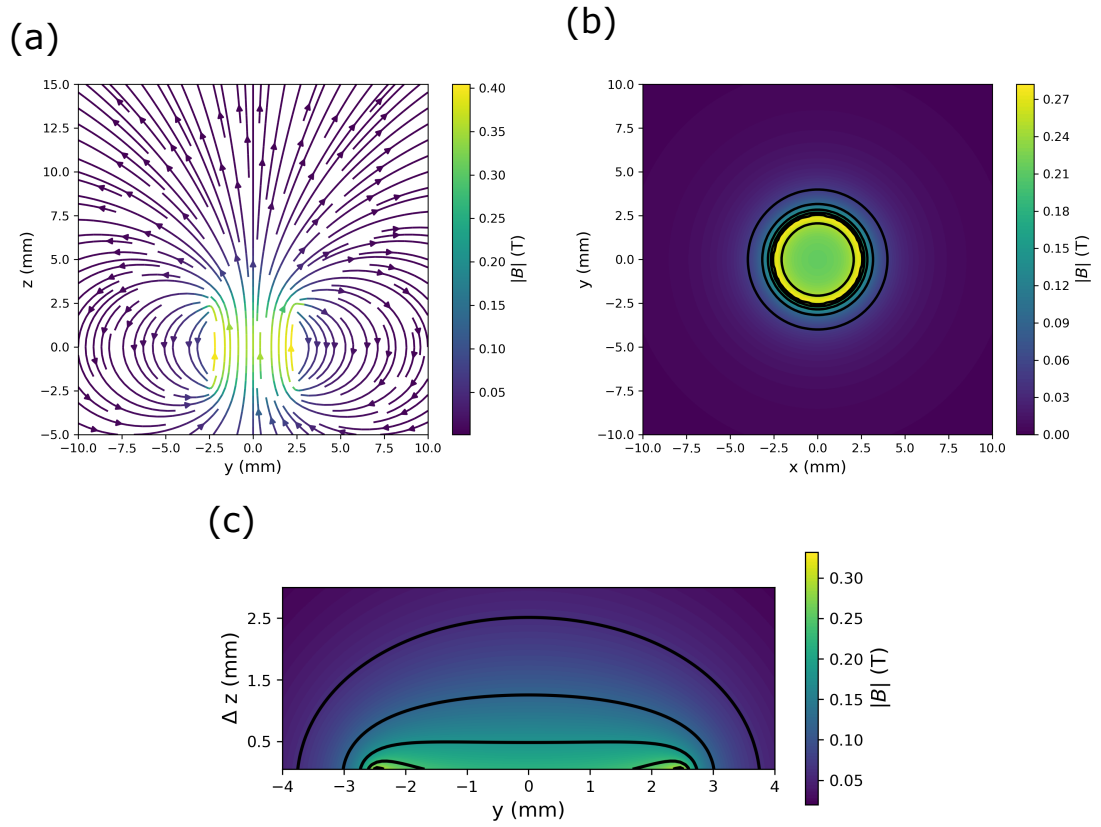

Figure 5.4 – Calculated magnetic field profile of cylindrical Nd-Fe-B magnet: 5 mm diameter and 5 mm length. Calculations were performed with the Magpylib Python package [620]. (a) Streamline plot of magnetic flux density of magnet. The cylinder is located at -2.5 mm to 2.5 mm and magnetised in z-direction. (b) Stray field in the xy-plane 0.1 mm above the magnet surface. (c) Stray field in the yz-plane above the magnet.

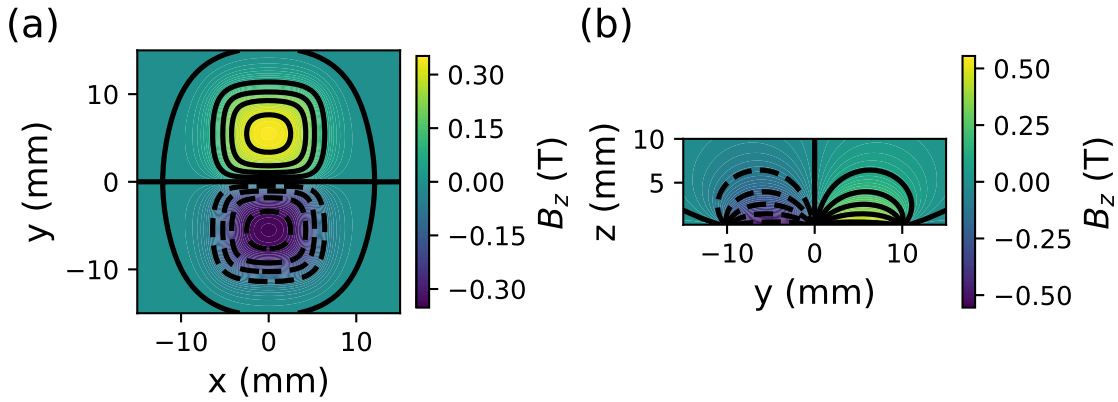

Figure 5.5 – Calculated vertical magnetic field profiles of two 10 mm magnet cubes placed (↑↓).
(a) Stray field in the xy-plane 2 mm above the magnet surface. The magnetic field is 0 T on the separation line. (b) Vertical magnetic field profile above the magnet surface.

5.4. Results

5.4.1. Cyclic Voltammetry

The technique of cyclic voltammetry was used to characterise the conversion of the solvated rare earth cations to hydroxides prior to the electrodeposition experiments. This involves scanning the voltage slowly to a target potential and then sweeping back to the origin, all the while recording the current. A chemical reaction changes the slope of the current. A tell-tale sign of a specific reaction is a peak that appears when the reactant becomes depleted in the vicinity of the electrode. This is due to the limiting of the reaction current by mass transport. In non-stirred solutions, the reacting species must be replenished at the electrode by diffusion from the surrounding bulk solution.

Only the reduction of rare earths was of interest. Therefore, the voltage was limited to the range of 0 V to −1.5 V versus the Ag/AgCl reference electrode, beginning and ending at 0 V with a scan rate of $5\,\mathrm{mV\,s^{-1}}$. The measurements shown in Figs. 5.6 and 5.7 were obtained with Cu tape working electrodes of $1\,\mathrm{cm^2}$ backed by 5 mm diameter cylindrical magnets.

The resulting cyclic voltammograms at $T = 40°\mathrm{C}$, 50°C and 60°C are plotted in Fig. 5.6. The temperature dependence of the reaction is clearly evident from the higher currents at $T = 60°\mathrm{C}$ and the noticeable dip in current around −0.55 V when the rare earth precipitation sets in. The two main reactions in the electrochemical cell can be readily identified in the cyclic voltammograms at $T = 40°\mathrm{C}$ and 50°C. In addition to the precipitation at the heart of the experiment, there is also a large current contribution of the electrolysis of water, which becomes dominant below −1.2 V. Small gas bubbles form on the electrode at such negative voltages. An oxidation reaction takes place on the anode. Conversely, a reduction of nitrate to nitrite occurs on the cathode. The respective reaction are:

$$\text{Anode:} \quad 2\mathrm{H_2O} \longrightarrow \mathrm{O_{2(g)}} + 4\mathrm{H^+_{(aq)}} + 4\mathrm{e^-} \quad E^0 = 1.23\,\mathrm{V}, \tag{5.4}$$

$$\text{Cathode:} \quad \mathrm{NO^-_{3(aq)}} + \mathrm{H_2O} + 2\mathrm{e^-} \longrightarrow \mathrm{NO^-_{2(aq)}} + 2\mathrm{OH^-_{(aq)}} \quad E^0 = 0.01\,\mathrm{V}. \tag{5.5}$$

For increased visibility of the different regimes, the current was also plotted against time in Fig 5.7. Voltages below −1.2 V, in which the current nosedives due to the electrolysis of water are visible. The evolution of hydrogen bubbles at the cathode is an unwelcome side effect which hinders the formation of smooth deposits.

Another unwanted effect at the electrode is the blocking of the copper tape by insoluble rare earth hydroxides. This in turn limits the providable current and sets a natural limit to the obtainable hydroxide. A way to avoid this would be to rotate the working electrode in order to keep its surface free. However, this would obviously hamper the magnetic capturing of the hydroxide. The formation of the hydroxides should be decoupled from their precipitation and capturing. This would be beneficial for the magnetohydrostatic separation.

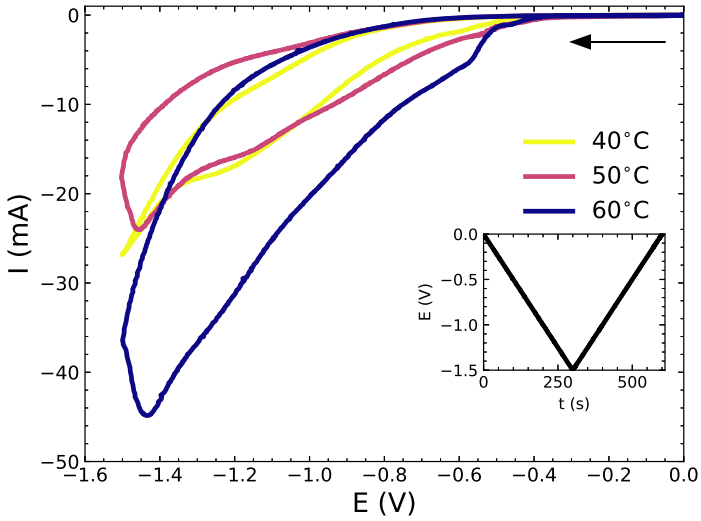

Figure 5.6 – Cyclic voltammograms (scan rate: 5 mV/s; E vs. Ag/AgCl) of $Gd/Y(OH)_3$ precipitation from a binary 0.5 M $Gd/Y(NO_3)_3$ solution. The working electrode was 1 cm^2 Cu tape backed by a 5 mm cylindrical magnet. Voltage values and time are shown in the inset. The reaction is strongly temperature dependent. The main precipitation reaction begins at −0.55 V. However, the bulk reaction only occurs below −1.0 V which manifests itself in the pronounced change in slope. The reaction is overshadowed by the electrolysis of water at voltages lower than −1.2 V.

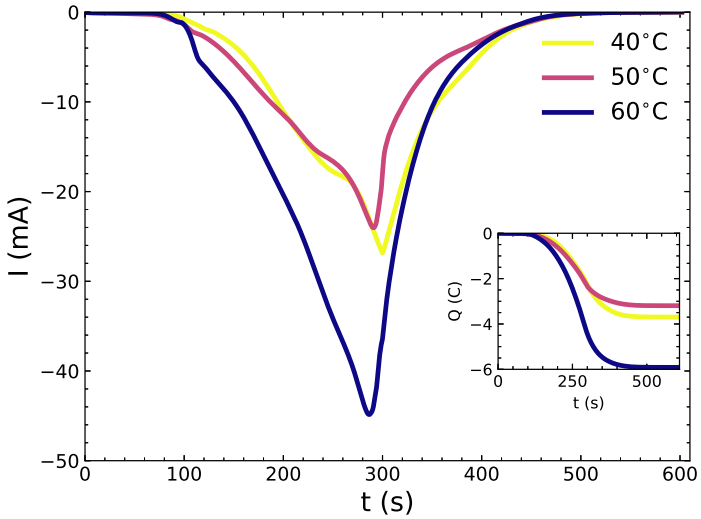

Figure 5.7 – Current versus time during cyclic voltammograms (scan rate: 5 mV s^{-1}; see Fig. 5.6) of the rare earth hydroxide precipitation on a 1 cm^2 Cu working electrode backed by a 5 mm cylindrical magnet. The inset shows the accumulation of charge Q on the electrodes.

The cyclic voltammetry obtained with a Au electrode is shown in Fig. 5.8. Its shape is different from that of the cyclic voltammograms obtained with the Cu tape electrode. The absence of the oxide layer and differing adsorption properties may be the reason for this. It is unclear what causes the diffusion limited reduction peak at −1.05 V. The aqueous rare earth cations

and nitrate anions must be replenished by mass transport, which is mainly diffusion based. But these are not mass-transport limited at concentrations of 1 M and 3 M, respectively. One explanation could be a reduction reaction of another metal cation species that may have entered the solution due to inadequate isolation of the connections or the magnet. Be that as it may, the region in which water electrolysis dominates begins at voltages below −1.2 V.

The main conclusion from the cyclic voltammetry measurements is the narrowing down of the area of interest to potentials between −1.0 V and −1.2 V. This choice maximises the obtainable ionic current while keeping parasitic gas bubbles due to water electrolysis to a minimum.

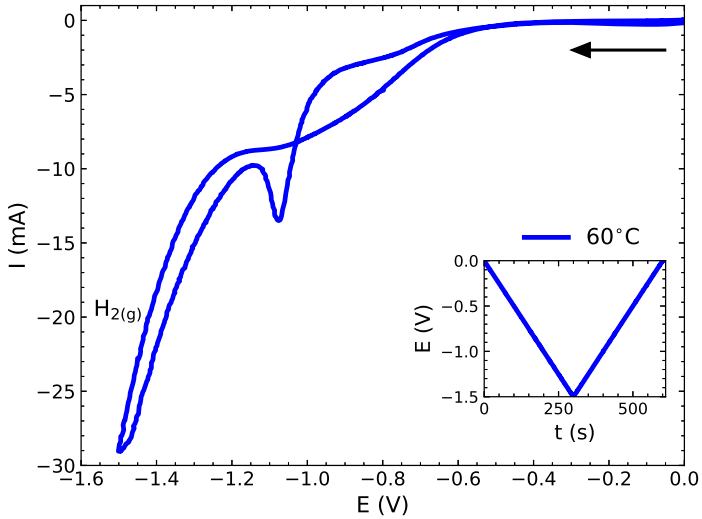

Figure 5.8 – Cyclic voltammograms (scan rate: 5 mV s^{-1}; E vs. Ag/AgCl) of Gd/Y(OH)$_3$ precipitation from 0.5 M Gd/Y(NO$_3$)$_3$ solution on a 1 cm^2 Au working electrode backed by a 5 mm cylindrical magnet (T = 60°C). The main hydroxide precipitation occurs at the sharp peak at −1.05 V. Water electrolysis takes over the measured current above −1.2 V.

5.4.2. Potentiostatic Electrodeposition

At first, potentiostatic electrodepositions were performed on 1 cm×1 cm Cu working electrodes at $T = 40$°C, 50°C and 60°C. The voltages were set to −0.8 V, −1.0 V, −1.2 V and finally −1.5 V. The cutoff for the deposition was set to a charge of $Q_{\text{cut}} = -0.5$ C on the Cu working electrodes. The resulting current over time is shown in Fig. 5.9 and the measured charge in Fig 5.10. All the deposits reach −0.5 C within 20 s, except at −0.8 V and 40°C. None of the charges reached a plateau at this deposition duration (see Fig 5.10). The short deposition times were chosen to avoid the immediate loss of the precipitated hydroxide layers that crack at high thicknesses.

The cathodically precipitated rare earth hydroxides are colourless and gelatinous. When removed from the cell, they lose their water and dehydrate. At elevated temperatures, the dehydration can also take place at the electrode. At $T = 60$ °C, this became noticeable and smoother deposits formed. Photographs of the dried working electrodes post-electrodeposition at $T = 60$ °C can bee seen in Fig. 5.11. From visual inspection of the obtained electrodeposits, the smoothest hydroxides were those at $T = 60$ °C and $E = -1.1$ V.

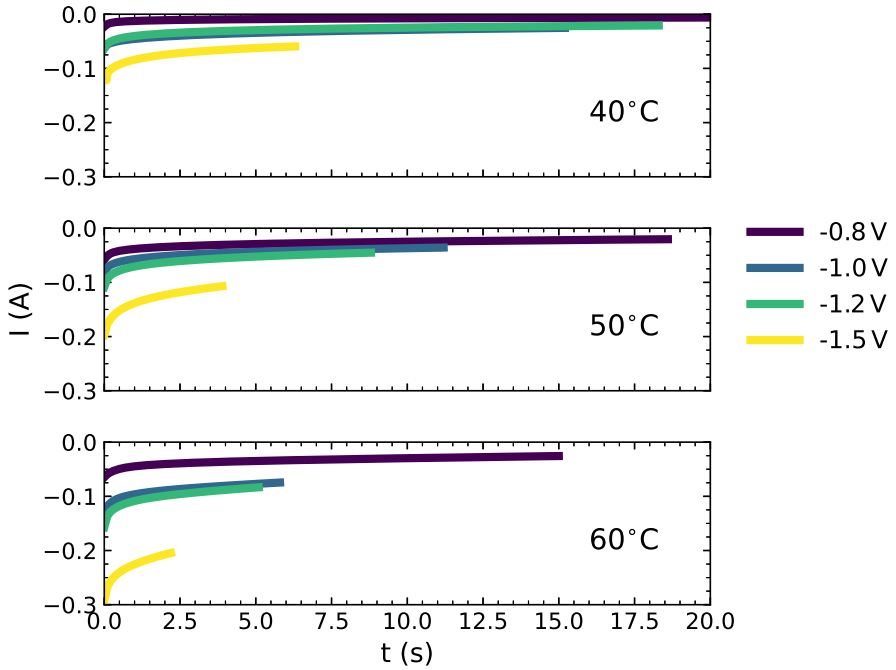

Figure 5.9 – Current versus time for the potentiostatic $Gd/Y(NO_3)_3$ deposition on 1 cm^2 Cu (charge cutoff: −0.5 C). The absolute value of the current increases with temperature.

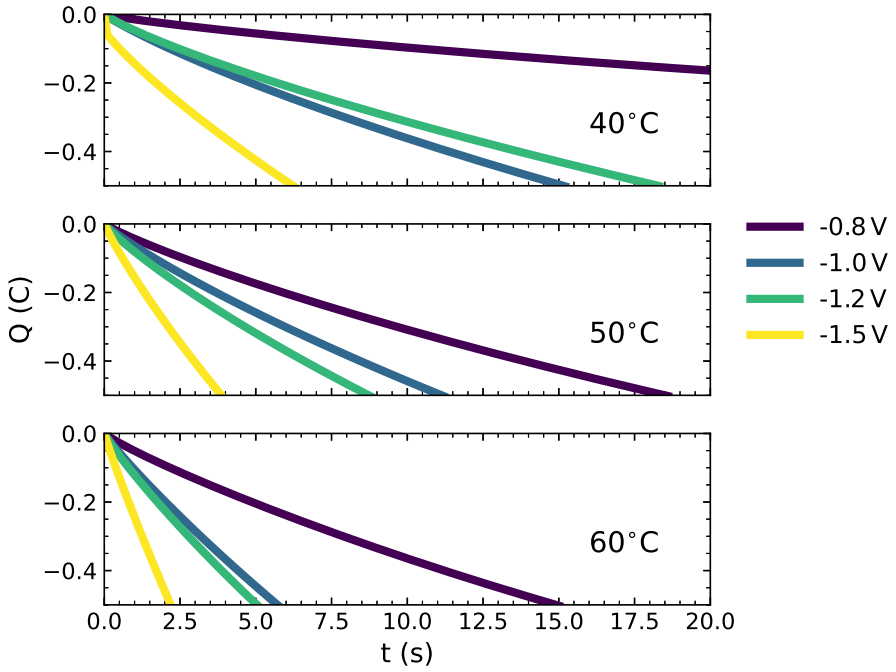

Figure 5.10 – Charge versus time for the potentiostatic $Gd/Y(NO_3)_3$ deposition on 1 cm^2 Cu (see Fig. 5.9). The deposition time decreases with the voltage and higher temperatures.

The brittle nature of the drying hydroxide is clearly evident in Figs. 5.11(e–g). Widespread cracking and peeling off from the electrode was observed for all the precipitated hydroxides. Most of the product in Figs. 5.11(a–d) was lost during the transfer out of the cell and removal of the Cu tape from the electrode.

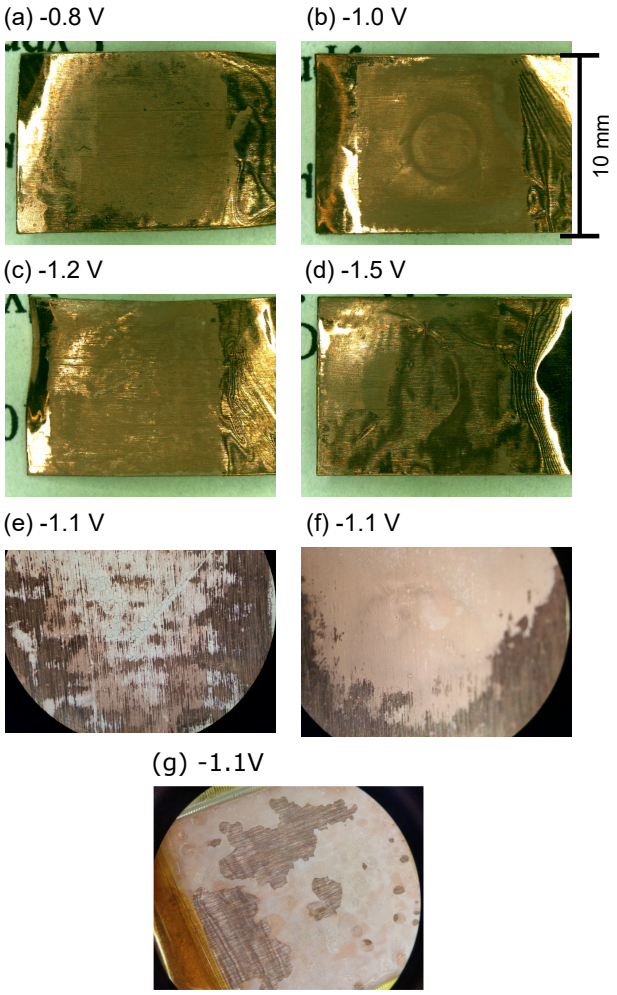

Figure 5.11 – Cathodic electrodeposits on Cu electrodes at 60 °C backed by 5 mm diameter cylindrical Nd-Fe-B magnet. The contour of the magnet is visible on the Cu tape in (b). The deposited white hydroxide layer was brittle and the majority peeled of the Cu surface upon removal from the cell. The cracked hydroxide layer can be seen in (e–g). The hydroxide has not completely dried yet in (f) and (g). An effect of the magnetic field gradient on the hydroxide layer is not clear from these pictures.

The contour of the magnet was not overtly recognisable in the depositions on Cu electrodes. Most of the hydroxide detached from the oxidised surface of the Cu tape. For this reason, the working electrode material was switched to Au. The Au was sputter deposited on silicon oxide and cut to 1 cm^2 squares with a dicer. The rare earth hydroxides can cling to this metallic surface and the hydroxide is held in place after removal from the liquid. This allows the electrolysis to be carried out at longer times and thicker layer of hydroxide to form. The cut off for the charge could thus be set to a substantially higher value than with the Cu tape electrode.

A slither of silver paint was used to contact the Au to the copper tape that led to the BNC connector of the working electrode holder. Isolation of the silver paint and the copper tape was ensured with Kapton tape and nail varnish (see Fig. 5.12).

The resulting electrodeposits for $Q_{\mathrm{cut}} = -4\,\mathrm{C}$ and $T = 60°\mathrm{C}$ can be seen in Fig. 5.12. For Figs. 5.12(a–c), a 5 mm diameter cylindrical magnet of equal length was used again. The circular contour of the magnet is clearly visible in the deposits. At $-1.0\,\mathrm{V}$ nearly half the hydroxide layer peeled off the Au surface while withdrawing the working electrode from the cell (Fig. 5.12(a)). The parasitic effect of gas bubble formation from water electrolysis is evident from the coarse surface at $-1.2\,\mathrm{V}$ (Fig. 5.12(c)).

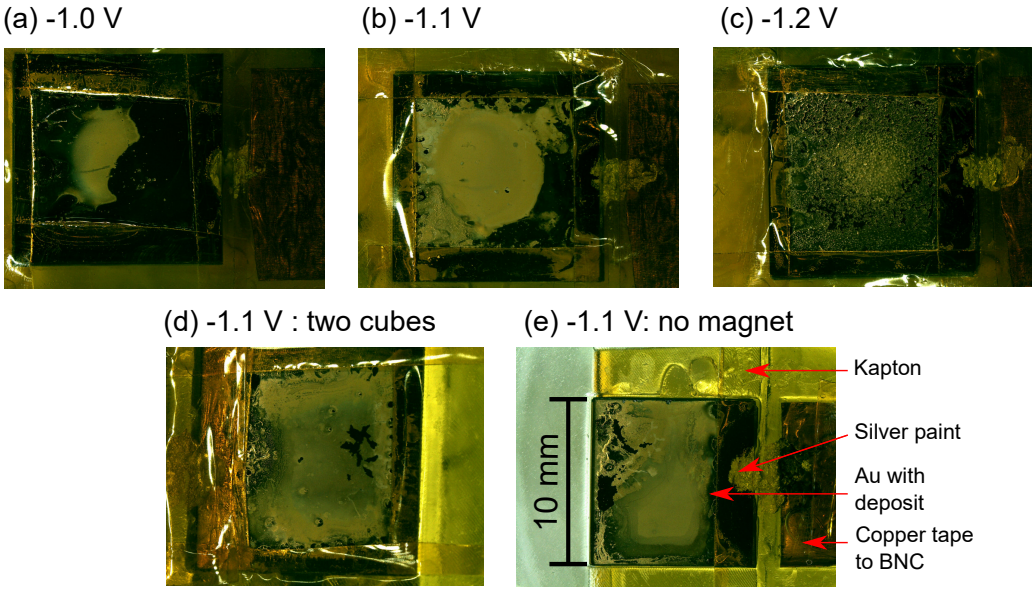

Figure 5.12 – Electrodeposits on Au working electrodes at 60 °C: The deposits follow the magnetic field profile shown in Figs. 5.4–5.5. (a–c) Deposits above 5 mm diameter cylindrical Nd-Fe-B magnets. (a) Half the deposit at $-1.0\,\mathrm{V}$ detached from the Au before the photograph was taken. (c) H_2 bubbles impacted the deposition at $-1.2\,\mathrm{V}$. (d) Two 10 mm magnet cubes (↑↓) have a 0 T horizontal line between them. The deposition rate here was lower. (e) The deposition with no magnetic field is slightly inhomogeneous due to natural convection and cracking of the hydroxide layer.

Two 10 mm magnet cubes placed head to tail (↑↓) behind the Au electrode cause a line with 0 T. The deposition at $-1.1\,\mathrm{V}$ with this configuration (see Fig. 5.12(d)) is clearly less pronounced in this low field segment and the deposition rate is higher at the sides.

The deposition without a permanent magnet is inhomogeneous (see Fig. 5.12(e)). An alteration of the deposition by natural convection exists, although it is not clear from the photograph. Concentration gradients at the vertical electrodes build up due to the conversion of the ions into the reaction products. Gravity acts on the concentration profile and causes a convective flow. A minimisation of this contribution is possible by placing the working electrode horizontally at the bottom of the electrochemical cell. Thus, the deposition takes place in the direction of gravity. Magnetoconvection will still play a roll in this configuration, pulling the inhomogeneous solution towards areas of high field gradient.

5.4.3. Analysis of Precipitated Rare Earth Hydroxides

Both the liberated rare earth hydroxides were white and the investigation of a possible enrichment of Gd^{3+} called for the use of an EDX scan. The rare earths differs in their characteristic x-rays. This is related to their electronic structure, which are completely unalike for Gd^{3+} ($6s^0 5d^0 4f^7$) and Y^{3+} ($5s^0 4d^0$).

The smoothest sample obtained with −1.1 V (see Fig. 5.12(b)) was analysed with SEM (see Fig. 5.13). Three regions of the deposit were scanned with approximately the same magnification: the edge of the deposit (a), 2 mm towards the centre (b) and at the centre (c). EDX scans were taken at two points within 5 µm wide areas of the respective micrographs. Areas with least cracking of the hydroxide layer were chosen.

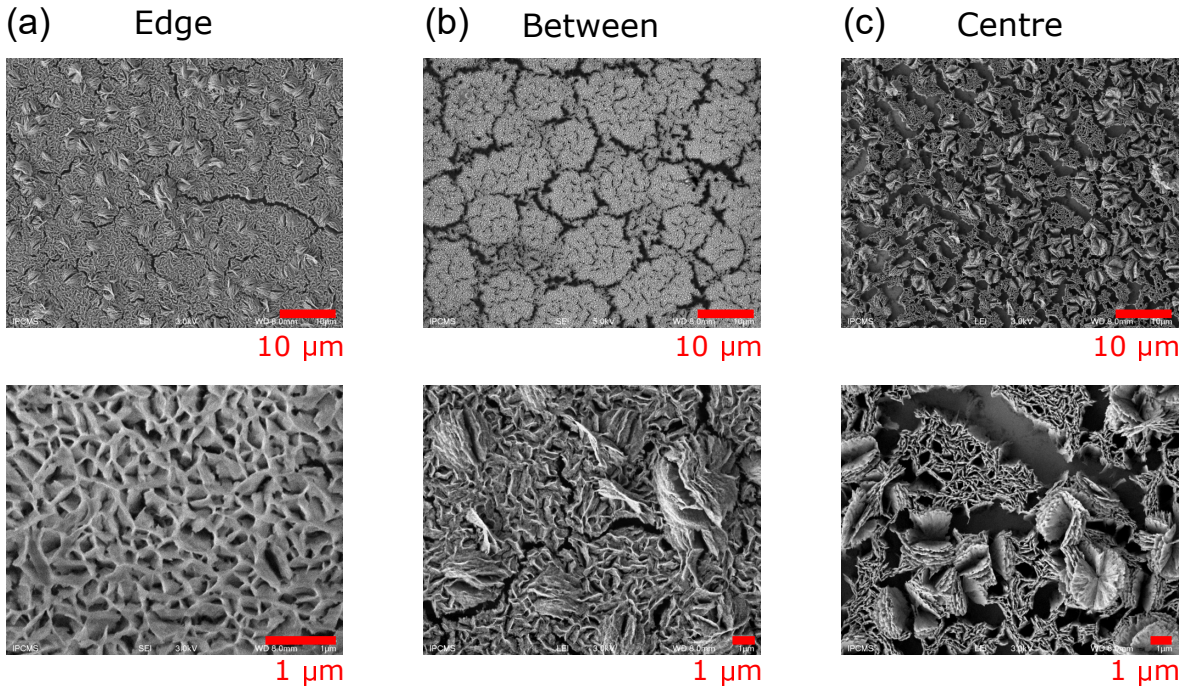

Figure 5.13 – SEM images of the precipitated Gd/Y hydroxides on Au (−1.1 V with cylindrical magnet; see Fig. 5.12(b)). The images are from the edge to the centre of the deposit. The intermediate region is 2 mm towards the centre from the edge. The general structure of the dried hydroxide is granular. Cracks (∼ 2 µm) form on the rare earth hydroxides upon drying, creating island-like structures of 10–20 µm. Accordion-like petals (∼ 2 µm) of rare earth hydroxides are discernible towards the centre.

Cracks in the oxide, through which the Au surface can be seen, are clearly visible in the SEM images. These form during the drying of the hydroxide powder and are unavoidable. Towards the centre, the deposit itself is structured in a network of petals (∼ 1 µm thickness) that have an accordion-like appearance. Their density decreases at the edge of the deposit, which has larger continuous areas.

The resulting EDX spectra for the different areas of the sample are plotted in Fig. 5.14. There are characteristic x-rays of seven elements present in the spectra. All of the spectra are dominated by the peaks belonging to O (Kα: 0.525 keV), Gd (M: 1.185 keV) and Y (L_α:

1.923 keV) as expected. Less pronounced peaks of C (K_α: 0.277 keV), N (K_α: 0.392 keV), Cu (L_α: 0.930 keV) and Au (M: 2.123 keV) are also present. The Au contribution to the spectrum is due to cracks in the deposit that uncover the Au electrode surface. A side reaction involving Cu from the connection to the potentiostat is a possible explanation for the Cu peak.

Close-ups of the O, Gd and Y peaks are presented in Fig. 5.15. There are differences in the rare earth intensities across the sample, with a trend towards higher detector counts away from the centre of the deposit. However, the contribution of Au is largest in the middle of the deposit, which indicates more widespread cracking (see Fig. 5.13(c)). The relative intensities of the Gd to the Y peaks are similar in different places on the sample. Oxygen is also related to the presence of rare earth hydroxides and the intensity of its peak varies in the same fashion. The trend of decreasing intensity towards the middle is most clear for O and Gd.

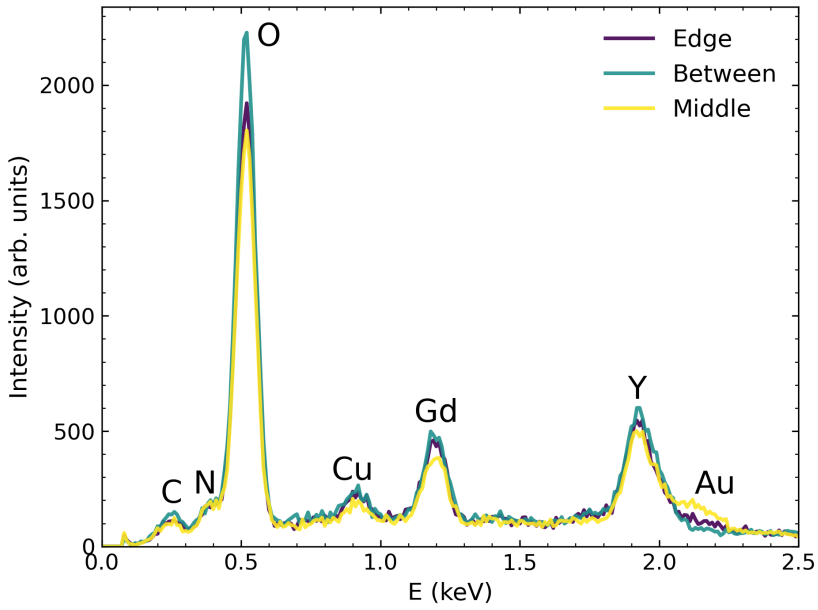

Figure 5.14 – EDX spectra of the deposited hydroxide layer in Fig. 5.12(b) with SEM images in Fig. 5.13. EDX scans were performed on a 5 µm wide window in three regions of Fig. 5.13. The peaks are assigned their corresponding element. The intensities towards the centre of the deposit decrease. See close-up plots of the main peaks of O, Gd and Y are in Fig. 5.15.

It is possible to extract the percentage values of elemental contributions to the EDX spectra and relate these to percentage concentrations. The results of the EDX scans are summarised in Table 7. Calculations of the elemental concentration (in at%) show that the Y ($\sim$14 %), the Gd ($\sim$20 %) and the O ($\sim$66 %) concentrations do not vary to a high degree across the deposit. The slight spatial variation in the order of 1 % are due to changes in the relief of the deposits, which are difficult to analyse. Despite the elevated Gd concentration that the EDX suggests, the Y component is still much higher than suggested from the expected magnetically altered situation in Fig. 5.2. Due to the high uncertainty of the EDX analysis of the cracked hydroxide, it is doubtful that the concentration of Gd is really 6% than the Y concentration. Besides

concentrating the hydroxides in the magnetic field gradient, no effect of the magnet upon the composition of the deposit was measurable.

Location	Oxygen	Gadolinium	Yttrium
Edge	66%	20%	13%
Between	66%	19%	14%
Centre	66%	18%	14%

Table 7 – Calculated concentration (at%) from EDX: These values were obtained from the spectra in Figs. 5.14–5.15. The slight decrease in Gd and increase of Y towards the middle is inconclusive. There is an uncertainty introduced by the differing surfaces of the cracked hydroxide structure (see Fig. 5.13).

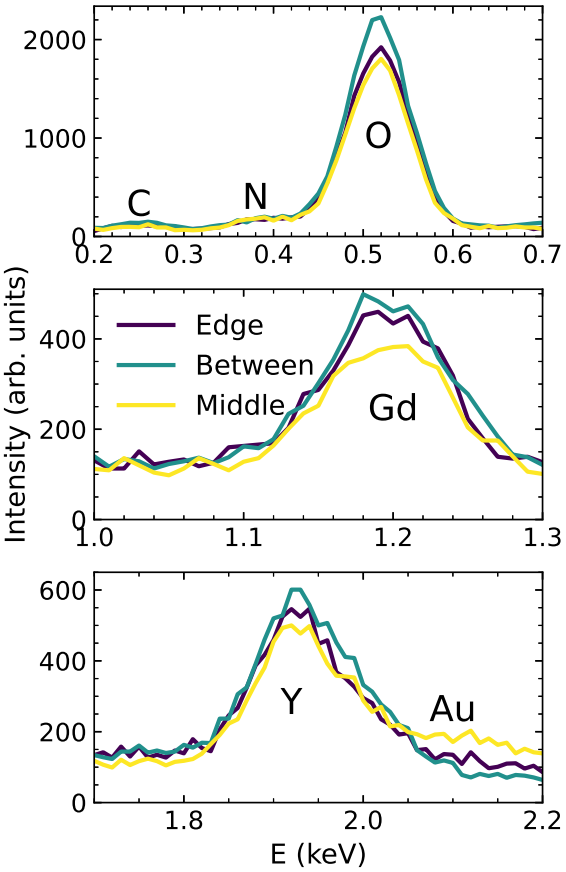

Figure 5.15 – Close-ups of the main peaks due to O, Gd and Y from the EDX spectra in Fig. 5.14. The intensity of these peaks is lower at the centre than the outside of the deposit. But the Au contribution here is highest, indicating cracks that uncover the electrode.

5.5. Conclusion

Rare earth hydroxides were precipitated by electrolysis of a mixed solution of $Gd(NO_3)_3$ and $Y(NO_3)_3$. Ideal conditions for the hydroxide precipitation were determined to be 60 °C and −1.1 V. The dried hydroxides form brittle oxide powders. These crack and detach easily from rough and oxidised Cu working electrodes. For a magnetic separation close to the electrode surface, this is counterproductive. Smooth Au electrodes avoid this problem by retaining the hydroxide on the surface. Furthermore, the cracking of the hydroxide layer could be reduced by employing multi-stage deposition and an intercalation with a cationic polymer [621, 622].

Although the precipitated rare earth hydroxides were structured by the magnetic field gradients of permanent magnets, the desired magnetic separation of $Gd(OH)_3$ from $Y(OH)_3$ failed to materialise. Both paramagnetic Gd^{3+} as well as non-magnetic Y^{3+} were present in the deposits and their relative concentration was unaffected by the position in the magnetic field gradient. Considering the nearly identical electrochemical properties of Gd^{3+} and Y^{3+}, this is understandable. The pH values at which Gd/Y hydrolyse are close (see Fig. 5.1) and the precipitation ranges overlap. Their fractional precipitation requires fine tuning of the pH [623]. Evidently, this was not ensured during the electrolysis carried out here.

A purely magnetic separation of ions is thermodynamically impossible (see Section 2.1). Magnetoconvection can only modify the flow of the bulk solution towards the electrode, which causes the structuring in the magnetic field profile. This is well understood for electroplating from paramagnetic solutions (see Section 2.3.2) [66, 69–71, 74, 76–82]. Any real separation of electrochemically generated reaction products from multicomponent solutions originates in differing behaviours in aqueous solutions.

A more reliable separation by fractional hydrolysis is achievable for rare earths with significantly varying ionic radii and basicities. Precipitation from a bath containing La^{3+} and a paramagnetic heavy rare earth ion would be the ideal case. Magnetic field gradients may lead to increased separation from the precipitated non-magnetic $La(OH)_3$. Recent reports of crystallisation from such a binary organic solution in a magnetic field gradient has yielded increased separation under certain conditions [438].

From a fundamental point of view, the fractional hydrolysis of rare earth by electrolysis is plagued by the same issues now as it was one century ago. Controlling the pH locally close to the electrode is insufficiently accurate to ensure satisfactory fractionate hydrolysis of all the rare earths. Moreover, the fractionated rare earths will never achieve high purity. The removal of the rare earths from the liquid state and precipitation as a solid is problematic for large scale application. These inadequacies were the reason why research into the approach was halted in the first half of the 20th century.

There is a growing interest in the fractional precipitation by varying the pH of the rare earth solution non-electrochemically [400]. A magneto-hydrostatic separation of the hydroxides from each other may be achievable, but it is critical that the hydroxides precipitate separately.

Despite what has been said, a magnetic structuring of electrochemically generated reaction products is still an area worth investigating. Magnetic field effects on the precipitation of

paramagnetic hydroxides from solutions of ions remain largely unexplored. A systematic study is needed to determine the extent to which the capturing of the magnetic hydroxide species is achievable. An adjustment of the pH value and new configurations of magnets should be explored.

6. Conclusion

Wer nichts als Chemie versteht,
versteht auch die nicht recht.

Georg Christoph Lichtenberg
(1742–1799)
Sudelbuch J [J 860] (1789)

Three experimental works centred on paramagnetic $Gd(NO_3)_3$ solutions were presented in this thesis. Stray fields of permanent magnets were able to pull concentrations of these towards them when there was a concentration gradient present in the system. Chapter 3 dealt with cold neutron imaging of diffusing $Gd(NO_3)_3$ solutions. Diffusion will eventually homogenise any concentration of paramagnetic ions if no driving force is introduced. In multicomponent systems such as tertiary $Gd(NO_3)_3 - Y(NO_3)_3 - D_2O - H_2O$, the differing diffusivities of the individual components destabilise the system mechanically and cause a hydrodynamic instability. It was demonstrated that such a salt fingering instability with a paramagnetic component can be prevented by the presence of a magnetic field gradient. The magnet levitates the paramagnetic fluid and bestows greater stability on the system.

The driving force for diffusion is a gradient of the chemical potential. This must be overcome when paramagnetic ions are to be enriched from homogeneous solutions. Chapter 4 demonstrated that electrosorption in porous carbon electrodes with high surface areas are a viable method with which this can be accomplished. Dynamic thermal neutron imaging experiments tracked the capacitive deionisation of 70 mM $Gd(NO_3)_3$ solutions with carbon aerogels and activated carbon cloths. The carbon aerogel monoliths contained both meso- and macropores. Neutron imaging was able to map the uptake of Gd^{3+} ions by the cylindrical aerogel electrodes and the depletion in the surrounding solution. Such a desalination process can trigger density differences in an electrochemical cell of paramagnetic $Gd(NO_3)_3$ solution. A magnetic field gradient can deform the paramagnetic fluid and redistribute the concentration.

The electrolysis of rare earth nitrate solutions under magnetic field gradients was analysed in Chapter 5. Rare earth ions from mixtures of $Gd(NO_3)_3$ and $Y(NO_3)_3$ precipitated as hydroxides in basic environments that were electrochemically created close to electrodes backed by Nd-Fe-B permanent magnets. The precipitated hydroxides formed cracked layers that followed the contour of the magnetic field profile. However, there was no proclivity for the paramagnetic Gd hydroxide to concentrate in regions of higher magnetic field. The hydroxides remained mixed, indicating that the chemical similarity of the heavy rare earths Gd^{3+} and Y^{3+} was still the overriding factor. A magnetic field gradient can only modify bulk flow towards the electrode via magnetoconvection or capture insoluble paramagnetic species from the solution.

The bottom line is that any convective phenomenon based on concentration differences of a paramagnetic fluid will be modified by a magnetic field gradient. This goes to show that the microscopic magnetic forces on the individual non-interacting magnetic moments are transmitted to the bulk fluid, which is thus deformed.

7. Outlook

Recht hat er, aber heute gilt ebenso:
Wer nichts von Chemie versteht,
versteht alles andere auch nicht recht.

Hans-Jürgen Quadbeck-Seeger
(*1939)
Der Wechsel allein ist das Beständige

This thesis concludes with an outlook on possible directions that research in the field of paramagnetic ionic solutions could take in the future. Several propositions pertaining to the findings of the neutron imaging experiments have already been put forward in Sections 3.4 and 4.5. The key results of the carried out research are the observation of double-diffusive convection with a component of paramagnetic ions and the capacitive deionisation with focus on a paramagnetic solution.

The phenomenon of the paramagnetic salt fingering instability merits further investigation. The interplay of multicomponent diffusion, gravity and magnetic fields in hydrodynamic instabilities has hitherto only been explored for ferrofluids. Paramagnetic salt fingering instabilities differ due to higher diffusion coefficients and lower magnetic susceptibilities. An open question is whether these instabilities can also be accelerated by a magnetic field and what role thermomagnetic convection could play when temperature gradients are included. In combination with thermodiffusive studies [624] of rare earth ions, the results may relate back to a magnetically aided separation and provide understanding on the individual factors involved. An interesting experiment may be a repeat of the original magnetically modified Clusius-Dickel thermal diffusion column. Ideally, the concentration evolution of a paramagnetic rare earth ion such as Gd^{3+} would be monitored in situ. Neutron imaging may provide the ideal method with which this could be accomplished due to its penetrative properties. A setup based on spectroscopy that can differentiate between rare earth ions is also thinkable with a transparent window.

The electrosorption of paramagnetic ions from their solution in porous carbon electrodes is an approach that has hitherto been overlooked by the research community. Further studies are necessary to investigate the flow of the paramagnetic bulk fluid towards and into the porous structure. The flow towards the electrode should be understandable with the previous research on structured paramagnetic electrodeposits on regular metallic electrodes [74]. However, the electrosorption of the paramagnetic ions in the porous structure is a departure from the step-like concentration gradient encountered when electroplating paramagnetic salt solutions. Whether the flow of a paramagnetic fluid can be magnetically modified within the porous network is an interesting question. It is certainly thinkable that a magnetically modified flow of the bulk fluid into at least the macropores should occur. Recently, investigations of thermodiffusive mass transport and separation of liquid mixtures in porous systems have been reported [625–629], which may be of interest for paramagnetic salt solutions. This calls for fundamental research on paramagnetic fluid flow in porous structures.

Ion selectivity in capacitive deionisation cells is under active research. Although it is dubious that magnetic forces play a role in the electrosorption process in the electric double layer, the magnetically modified flow in the cell and possibly in the porous structure is worth investigating for paramagnetic solutions. This is potentially relevant in the new research area of rare earth ion separation via adsorption in functionalised mesoporous materials [521,522]. This has proved to be successful with mesoporous silica and mesoporous carbon, both with bimodal pore size distributions as the carbon aerogels investigated here. The technique is based on solid phase extraction in the functionalised porous network with interaction between organic ligand and the rare earths. Neither electric field nor magnetic fields have been applied in such materials yet and it is unclear what their effect would be.

However, the question whether magnetic fields will provide the panacea for current arduous rare earth separation methods can be answered with a resounding no. Magnetic effects are too weak to significantly influence the current separation processes. What is more, the magnetic susceptibility differences decrease significantly after each step of refinement, rendering the mixture inconducive to magnetic separation and relegating any envisaged application of magnetic field gradients to the first step in the separation process. Potential solutions to the problems facing rare earth separation should be sought in chemical methods, while not abandoning research on paramagnetic salt solutions entirely. Because one thing is for certain, the manipulation of fluids containing tenuous magnetic dipoles with a magnet at a distance will continue to intrigue humanity for generations to come.

8. References

[1] U. T. Andres, G. M. Bunin and B. B. Gil, Magnetohydrostatic separation, J. Appl. Mech. Tech. Phys. **7**, 109 (1966).

[2] S. Khalafalla, Magnetic separation of the second kind: Magnetogravimetric, magnetohydrostatic, and magnetohydrodynamic separations, IEEE Trans. Magn. **12**, 455 (1976).

[3] U. T. Andres, Magnetic liquids, Mater. Sci. Eng. **26**, 269 (1976).

[4] N. Hirota, M. Kurashige, M. Iwasaka, M. Ikehata, H. Uetake, T. Takayama, H. Nakamura, Y. Ikezoe, S. Ueno and K. Kitazawa, Magneto-Archimedes separation and its application to the separation of biological materials, Physica B **346-347**, 267 (2004), Proceedings of the 7th International Symposium on Research in High Magnetic Fields.

[5] N. Ramachandran and F. Leslie, Using magnetic fields to control convection during protein crystallization—analysis and validation studies, J. Cryst. Growth, **274**, 297 (2005).

[6] P. A. Dunne, J. Hilton and J. M. D. Coey, Levitation in paramagnetic liquids, J. Magn. Magn. Mater. **316**, 273 (2007).

[7] S. Liu, M. Leaper and N. Miles, Vertical flotation of particles in a paramagnetic fluid, Powder Technol. **261**, 71 (2014).

[8] M. Iranmanesh and J. Hulliger, Magnetic separation: its application in mining, waste purification, medicine, biochemistry and chemistry, Chem. Soc. Rev. **46**, 5925 (2017).

[9] E. Turker and A. Arslan-Yildiz, Recent Advances in Magnetic Levitation: A Biological Approach from Diagnostics to Tissue Engineering, ACS Biomater. Sci. Eng. **4**, 787 (2018).

[10] S. Ge and G. M. Whitesides, "Axial" Magnetic Levitation Using Ring Magnets Enables Simple Density-Based Analysis, Separation, and Manipulation, Anal. Chem. **90**, 12239 (2018).

[11] S. Ge, Y. Wang, N. J. Deshler, D. J. Preston and G. M. Whitesides, High-Throughput Density Measurement Using Magnetic Levitation, J. Am. Chem. Soc. **140**, 7510 (2018).

[12] S. Ge, A. Nemiroski, K. A. Mirica, C. R. Mace, J. W. Hennek, A. A. Kumar and G. M. Whitesides, Magnetic Levitation in Chemistry, Materials Science, and Biochemistry, Angew. Chem. Int. Ed. **59**, 17810 (2020).

[13] M. Schieber, The effects of high magnetic fields on the isothermal dissolution and growth rates of $Fe(NH_4)_2(SO_4)_2 \cdot 6\,H_2O$ and $KAl(SO_4)_2 \cdot 12\,H_2O$ seed crystals, J. Cryst. Growth **1**, 131 (1967).

[14] J. Qi and N. I. Wakayama, The combined effects of magnetic field and magnetic field gradients on convection in crystal growth, Phys. Fluids **16**, 3450 (2004).

[15] P. W. G. Poodt, M. C. R. Heijna, K. Tsukamoto, W. J. de Grip, P. C. M. Christianen, J. C. Maan, W. J. P. van Enckevort and E. Vlieg, Suppression of convection using gradient magnetic fields during crystal growth of $NiSO_4 \cdot 6\,H_2O$, Appl. Phys. Lett. **87**, 214105 (2005).

[16] P. W. G. Poodt, M. C. R. Heijna, P. C. M. Christianen, W. J. P. van Enckevort, W. J. de Grip, K. Tsukamoto, J. C. Maan and E. Vlieg, Using Gradient Magnetic Fields to Suppress Convection during Crystal Growth, Cryst. Growth Des. **6**, 2275 (2006).

[17] J. R. Carruthers and R. Wolfe, Magnetothermal Convection in Insulating Paramagnetic Fluids, J. Appl. Phys. **39**, 5718 (1968).

[18] E. Blums, A. Cēbers and M. M. Maiorov, *Magnetic fluids* (Walter de Gruyter, 1996), Chapter 6, p. 295.

[19] D. Braithwaite, E. Beaugnon and R. Tournier, Magnetically controlled convection in a paramagnetic fluid, Nature **354**, 134 (1991).

[20] S. Maki, M. Ataka, T. Tagawa, H. Ozoe and W. Mori, Natural convection of a paramagnetic liquid controlled by magnetization force, AIChE J. **51**, 1096 (2005).

[21] T. Bednarz, E. Fornalik, T. Tagawa, H. Ozoe and J. S. Szmyd, Experimental and numerical analyses of magnetic convection of paramagnetic fluid in a cube heated and cooled from opposing verticals walls, Int. J. Therm. Sci. **44**, 933 (2005).

[22] T. P. Bednarz, C. Lei, J. C. Patterson and H. Ozoe, Effects of a transverse, horizontal magnetic field on natural convection of a paramagnetic fluid in a cube, Int. J. Therm. Sci. **48**, 26 (2009).

[23] T. Bednarz, J. C. Patterson, C. Lei and H. Ozoe, Enhancing natural convection in a cube using a strong magnetic field — Experimental heat transfer rate measurements and flow visualization, Int. J. Heat Mass Transf. **36**, 781 (2009).

[24] J. Huang, D. D. Gray and B. F. Edwards, Magnetic control of convection in nonconducting diamagnetic fluids, Phys. Rev. E **58**, 5164 (1998).

[25] I. Mogi, C. Umeki, K. Takahashi, S. Awaji, K. Watanabe and M. Motokawa, Control of Thermal Convection in Water by Strong Gradient Magnetic Fields, Jpn. J. Appl. Phys. **42**, L715 (2003).

[26] F. Klauer, E. Turowski and T. v. Wolff, Sauerstoffanalyse von Gasgemischen auf physikalischer Grundlage, Angew. Chem. **54**, 494 (1941).

[27] A. P. Wills and L. G. Hector, The Magnetic Susceptibility of Oxygen, Hydrogen and Helium, Phys. Rev. **23**, 209 (1924).

[28] H. Senftleben, Magnetische Beeinflussung des Wärmeleitvermögens paramagnetischer Gase, Phys. Z. **31**, 822 (1930).

[29] H. Senftleben, Über den Einfluß von magnetischen und elektrischen Feldern auf den Wärmestrom in Gasen, Z. Phys. **74**, 757–769 (1932).

[30] H. Senftleben and J. Pietzner, Die Einwirkung magnetischer Felder auf das Wärmeleitvermögen von Gasen. I, Ann. Phys. **408**, 907 (1933).

[31] M. v. Laue, Der Einfluß eines Magnetfeldes auf Wärmeleitung und Reibung in paramagnetischen Gasen, Ann. Phys. **415**, 1 (1935).

[32] H. Senftleben and J. Pietzner, Die Einwirkung magnetischer Felder auf das Wärmeleitvermögen von Gasen. II. Abhängigkeit von der Richtung zwischen Magnetfeld und Wärmestrom, Ann. Phys. **419**, 108 (1936).

[33] H. Senftleben and J. Pietzner, Die Einwirkung magnetischer Felder auf das Wärmeleitvermögen von Gasen. III. Druckabhängigkeit bei kleinen Gasdrucken, Ann. Phys. **419**, 117 (1936).

[34] H. Senftleben and J. Pietzner, Die Einwirkung magnetischer Felder auf das Wärmeleitvermögen von Gasen. IV Untersuchungen an Mischungen von Sauerstoff mit diamagnetischen Gasen, Ann. Phys. **422**, 541 (1937).

[35] H. Senftleben and H. Gladisch, Der Einfluß magnetischer Felder auf die innere Reibung von Gasen (Untersuchungen an Stickoxyd), Ann. Phys. **425**, 471 (1938).

[36] C. Gorter, Zur Interpretierung des Senftleben-Effektes, Naturwissenschaften **26**, 140 (1938).

[37] F. Zernike and C. van Lier, Theory of the Senftleben effect, Physica **6**, 961 (1939).

[38] J. Beenakker, G. Scoles, H. Knaap and R. Jonkman, The influence of a magnetic field on the transport properties of diatomic molecules in the gaseous state, Phys. Lett. **2**, 5 (1962).

[39] J. J. M. Beenakker and F. R. McCourt, Magnetic and Electric Effects on Transport Properties, Annu. Rev. Phys. Chem. **21**, 47 (1970).

[40] W. Honeywell, D. Elliot and J. Vevai, Large magnetic field effect on oxygen gas thermal conductivity at 77°K, Phys. Lett. A **38**, 265 (1972).

[41] H. Moraal and F. R. McCourt, Formal Kinetic Theory of the Senftleben Effects, J. Chem. Phys. **56**, 1588 (1972).

[42] W.-H. Park and W. I. Honeywell, Magnetothermal Convection of Polyatomic Gases in Homogeneous Magnetic Fields Part I: Theory, Chem. Eng. Commun. **1**, 167 (1974).

[43] D. C. Clark and W. I. Honeywell, Magnetothermal convection of oxygen gas in nonuniform magnetic fields, AIChE J. **23**, 553 (1977).

[44] W. I. Honeywell and J. E. Vevai, Magnetically enhanced thermal convection in oxygen gas, AIChE J. **24**, 1035 (1978).

[45] T. Bednarz, T. Tagawa, M. Kaneda, H. Ozoe and J. S. Szmyd, Magnetic and Gravitational Convection of Air with a coil inclined around the X Axis, Numer. Heat Transf.; A: Appl. **46**, 99 (2004).

[46] K. Song, S. Wu, T. Tagawa, W. Shi and S. Zhao, Thermomagnetic Convection of Paramagnetic Gas in an Enclosure under No Gravity Condition, Fluids **4** (2019).

[47] J. M. D. Coey, R. Aogaki, F. Byrne and P. Stamenov, Magnetic stabilization and vorticity in submillimeter paramagnetic liquid tubes, Proc. Natl. Acad. Sci. U.S.A. **106**, 8811 (2009).

[48] P. Dunne *et al.*, Liquid flow and control without solid walls, Nature **581**, 58 (2020).

[49] P. U. Arumugam, E. A. Clark and I. Fritsch, Use of Paired, Bonded NdFeB Magnets in Redox Magnetohydrodynamics, Anal. Chem. **77**, 1167 (2005).

[50] N. Pamme, Magnetism and microfluidics, Lab Chip **6**, 24 (2006).

[51] M. C. Weston, M. D. Gerner and I. Fritsch, Magnetic Fields for Fluid Motion, Anal. Chem. **82**, 3411 (2010).

[52] N.-T. Nguyen, Micro-magnetofluidics: interactions between magnetism and fluid flow on the microscale, Microfluid. Nanofluidics **12**, 1 (2012).

[53] V. Haehnel, F. Z. Khan, G. Mutschke, C. Cierpka, M. Uhlemann and I. Fritsch, Combining magnetic forces for contactless manipulation of fluids in microelectrode-microfluidic systems, Sci. Rep. **9**, 5103 (2019).

[54] J. A. Shercliff, The dynamics of conducting fluids under rotational magnetic forces, Sci. Prog. **66**, 151 (1979).

[55] G. Mutschke and A. Bund, On the 3D character of the magnetohydrodynamic effect during metal electrodeposition in cuboid cells, Electrochem. Commun. **10**, 597 (2008).

[56] L. M. A. Monzon and J. M. D. Coey, Magnetic fields in electrochemistry: The Lorentz force. A mini-review, Electrochem. Commun. **42**, 38 (2014).

[57] O. Devos, A. Olivier, J. P. Chopart, O. Aaboubi and G. Maurin, Magnetic Field Effects on Nickel Electrodeposition, J. Electrochem. Soc. **145**, 401 (1998).

[58] O. Devos, O. Aaboubi, J.-P. Chopart, E. Merienne, A. Olivier and J. Amblard, Magnetic Field Effects on Nickel Electrodeposition: II. A Steady-State and Dynamic Electrochemical Study, J. Electrochem. Soc. **145**, 4135 (1998).

[59] J. M. D. Coey, G. Hinds and M. E. G. Lyons, Magnetic-field effects on fractal electrodeposits, EPL **47**, 267 (1999).

[60] G. Hinds, F. E. Spada, J. M. D. Coey, T. R. Ní Mhíocháin and M. E. G. Lyons, Magnetic Field Effects on Copper Electrolysis, J. Phys. Chem. B **105**, 9487 (2001).

[61] C. O'Reilly, G. Hinds and J. M. D. Coey, Effect of a Magnetic Field on Electrodeposition: Chronoamperometry of Ag, Cu, Zn, and Bi, J. Electrochem. Soc. **148**, C674 (2001).

[62] T. Weier, J. Hüller, G. Gerbeth and F.-P. Weiss, Lorentz force influence on momentum and mass transfer in natural convection copper electrolysis, Chem. Eng. Sci. **60**, 293 (2005).

[63] S. Mühlenhoff, G. Mutschke, D. Koschichow, X. Yang, A. Bund, J. Fröhlich, S. Odenbach and K. Eckert, Lorentz-force-driven convection during copper magnetoelectrolysis in the presence of a supporting buoyancy force, Electrochim. Acta **69**, 209 (2012).

[64] J. König, M. Neumann, S. Mühlenhoff, K. Tschulik, T. Albrecht, K. Eckert, M. Uhlemann, T. Weier, L. Büttner and J. Czarske, Optical velocity measurements of electrolytic boundary layer flows influenced by magnetic fields, Eur. Phys. J. Special Topics **220**, 79 (2013).

[65] M. Huang, G. Marinaro, X. Yang, B. Fritzsche, Z. Lei, M. Uhlemann, K. Eckert and G. Mutschke, Mass transfer and electrolyte flow during electrodeposition on a conically shaped electrode under the influence of a magnetic field, J. Electroanal. Chem. **842**, 203 (2019).

[66] M. I. Ismail and T. Z. Fahidy, A novel magnetoelectrolytic reactor, Can. J. Chem. Eng. **57**, 734 (1979).

[67] S. Koehler and A. Bund, Investigations on the Kinetics of Electron Transfer Reactions in Magnetic Fields, J. Phys. Chem. B **110**, 1485 (2006).

[68] O. Y. Gorobets, V. Y. Gorobets, D. O. Derecha and O. M. Brukva, Nickel Electrodeposition under Influence of Constant Homogeneous and High-Gradient Magnetic Field, J. Phys. Chem. C **112**, 3373 (2008).

[69] K. Tschulik, J. A. Koza, M. Uhlemann, A. Gebert and L. Schultz, Effects of well-defined magnetic field gradients on the electrodeposition of copper and bismuth, Electrochem. Commun. **11**, 2241 (2009).

[70] K. Tschulik, J. A. Koza, M. Uhlemann, A. Gebert and L. Schultz, Magnetoelectrochemical Surface Structuring: Electrodeposition of Structured Metallic Layers in Magnetic Gradient Fields, ECS Trans. **25**, 149 (2010).

[71] K. Tschulik, R. Sueptitz, J. Koza, M. Uhlemann, G. Mutschke, T. Weier, A. Gebert and L. Schultz, Studies on the patterning effect of copper deposits in magnetic gradient fields, Electrochim. Acta **56**, 297 (2010).

[72] K. Tschulik, X. Yang, G. Mutschke, M. Uhlemann, K. Eckert, R. Sueptitz, L. Schultz and A. Gebert, How to obtain structured metal deposits from diamagnetic ions in magnetic gradient fields?, Electrochem. Commun. **13**, 946 (2011).

[73] K. Tschulik, C. Cierpka, G. Mutschke, A. Gebert, L. Schultz and M. Uhlemann, Clarifying the Mechanism of Reverse Structuring during Electrodeposition in Magnetic Gradient Fields, Anal. Chem. **84**, 2328 (2012).

[74] G. Mutschke, K. Tschulik, T. Weier, M. Uhlemann, A. Bund and J. Fröhlich, On the action of magnetic gradient forces in micro-structured copper deposition, Electrochim. Acta **55**, 9060 (2010).

[75] G. Mutschke, K. Tschulik, M. Uhlemann, A. Bund and J. Fröhlich, Comment on "Magnetic Structuring of Electrodeposits", Phys. Rev. Lett. **109**, 229401 (2012).

[76] P. Dunne, L. Mazza and J. M. D. Coey, Magnetic Structuring of Electrodeposits, Phys. Rev. Lett. **107**, 024501 (2011).

[77] P. Dunne, R. Soucaille, K. Ackland and J. M. D. Coey, Structuring of electrodeposits with permanent magnet arrays, Magnetohydrodynamics **48**, 331 (2012).

[78] P. Dunne, R. Soucaille, K. Ackland and J. M. D. Coey, Magnetic structuring of linear copper electrodeposits, J. Appl. Phys. **111**, 07B915 (2012).

[79] P. Dunne and J. M. D. Coey, Patterning metallic electrodeposits with magnet arrays, Phys. Rev. B **85**, 224411 (2012).

[80] H. A. Murdoch, D. Yin, E. Hernández-Rivera and A. K. Giri, Effect of applied magnetic field on microstructure of electrodeposited copper, Electrochem. Commun. **97**, 11 (2018).

[81] M. Huang, K. Eckert and G. Mutschke, Magnetic-field-assisted electrodeposition of metal to obtain conically structured ferromagnetic layers, Electrochim. Acta **365**, 137374 (2021).

[82] G. Marinaro, M. Huang, G. Mutschke, X. Yang and K. Eckert, Oscillatory Copper Deposition on Conical Iron Electrodes in a Nonuniform Magnetic Field, Magnetochemistry **7**, 46 (2021).

[83] J. Navarro and F. Zhao, Life-Cycle Assessment of the Production of Rare-Earth Elements for Energy Applications: A Review, Front. Energy Res. **2**, 45 (2014).

[84] F. Xie, T. A. Zhang, D. Dreisinger and F. Doyle, A critical review on solvent extraction of rare earths from aqueous solutions, Miner. Eng. **56**, 10 (2014).

[85] N. Leventis and X. Gao, Magnetohydrodynamic Electrochemistry in the Field of Nd-Fe-B Magnets. Theory, Experiment, and Application in Self-Powered Flow Delivery Systems, Anal. Chem. **73**, 3981 (2001).

[86] K. Binnemans, P. T. Jones, B. Blanpain, T. Van Gerven, Y. Yang, A. Walton and M. Buchert, Recycling of rare earths: a critical review, J. Clean. Prod. **51**, 1 (2013).

[87] Y. Yang, A. Walton, R. Sheridan, K. Güth, R. Gauß, O. Gutfleisch, M. Buchert, B.-M. Steenari, T. Van Gerven, P. T. Jones and K. Binnemans, REE Recovery from End-of-Life NdFeB Permanent Magnet Scrap: A Critical Review, J. Sustain. Metall. **3**, 122 (2017).

[88] K. Binnemans, P. McGuiness and P. T. Jones, Rare-earth recycling needs market intervention, Nat. Rev. Mater. **6**, 459 (2021).

[89] P. W. Selwood and B. S. Hopkins, Ionic Migration and Magnetism in the Separation of the Rare Earths, Trans. Amer: Electrochem. Soc. **55**, 59 (1929).

[90] P. Selwood, *Magnetochemistry* (Interscience Publishers Inc., New York, 1943).

[91] W. Prandtl and A. Grimm, Über die Aufsuchung des Elementes Nr. 61, Z. Anorg. Allg. Chem. **136**, 283 (1924).

[92] L. F. Yntema, Observations on the Rare Earths. XV. A Search for Element Sixty-One, J. Am. Chem. Soc. **46**, 37 (1924).

[93] J. A. Harris, L. F. Yntema and B. S. Hopkins, The Element of Atomic Number 61; Illinium, Nature **117**, 792 (1926).

[94] J. A. Harris and B. S. Hopkins, Observations on the Rare Earths XXIII. Element No. 61 Part One. Concentration and Isolation in Impure State, J. Am. Chem. Soc. **48**, 1585 (1926).

[95] J. A. Harris, L. F. Yntema and B. S. Hopkins, Observations on the Rare Earths XXIII. Element No. 61 Part Two. X-Ray Analysis, J. Am. Chem. Soc. **48**, 1594 (1926).

[96] B. S. Hopkins, Illinium—The new rare earth, J. Franklin Inst. **204**, 1 (1927).

[97] W. Prandtl, Auf der Suche nach dem Element Nr. 61, Angew. Chem. **39**, 897 (1926).

[98] W. Prandtl and A. Grimm, Auf der Suche nach dem Element Nr. 61 (II), Angew. Chem. **39**, 1333 (1926).

[99] I. Noddack, Das Periodische System der Elemente und seine Lücken, Angew. Chem. **47**, 301 (1934).

[100] Die Suche nach dem Element 61, Nachr. Chem. Tech. **13**, 287 (1965).

[101] R. Guillaumont, Completion and extension of the periodic table of elements beyond uranium, C. R. Phys. **20**, 617 (2019), La science en mouvement 2 : de 1940 aux premières années 1980 – Avancées en physique.

[102] M. Fontani, M. V. Orna and M. Costa, Chemists and physicists behaving badly: The shadow side of two elemental discoveries, C. R. Chim. **23**, 231 (2020).

[103] J. B. Taylor., Magnetic Moments of the Alkali Metal Atoms, Phys. Rev. **28**, 576 (1926).

[104] O. Stern, Ein Weg zur experimentellen Prüfung der Richtungsquantelung im Magnetfeld, Z. Physik **7**, 249–253 (1921).

[105] W. Gerlach and O. Stern, Der experimentelle Nachweis der Richtungsquantelung im Magnetfeld, Z. Physik **9**, 349 (1922).

[106] I. Estermann, History of molecular beam research: Personal reminiscences of the important evolutionary period 1919–1933, Am. J. Phys. **43**, 661 (1975).

[107] R. J. Meyer and U. Müller, Über das Gadolinium. Trennungsmethoden in der Reihe der Terbin- und Yttererden, Z. Anorg. Allg. Chem. **109**, 1 (1919).

[108] P. W. Selwood, The Separation of Certain Rare Earths, J. Am. Chem. Soc. **57**, 1145 (1935).

[109] J. Kendall and B. L. Clarke, The Separation of Rare Earths by the Ionic Migration Method, Proc. Natl. Acad. Sci. **11**, 393 (1925).

[110] J. Kendall and W. West, An Attempred Separation of Hafnium and Zirconium by the Ionic Migration Method, J. Am. Chem. Soc. **48**, 2619 (1926).

[111] J. Kendall, Separations by the Ionic Migration Method, Science **67**, 163 (1928).

[112] D. Haas and W. H. Rodebush, Observations on the Rare Earths. XXXIX. The Transference Numbers of the Chlorides of Neodymium, Samarium and Gadolinium. Part II. Measurement of the Transference Numbers, J. Am. Chem. Soc. **55**, 3238 (1933).

[113] L. G. Longsworth and D. A. MacInnes, Transference Numbers of Lanthanum Chloride at 25° by the Moving Boundary Method, J. Am. Chem. Soc. **60**, 3070 (1938).

[114] F. H. Spedding, P. E. Porter and J. M. Wright, Transference Numbers of Rare Earth Chlorides in Aqueous Solution at 25°, J. Am. Chem. Soc. **74**, 2778 (1952).

[115] F. H. Spedding and J. L. Dye, Conductances, Transference Numbers and Activity Coefficients of Aqueous Solutions of Some Rare Earth Chlorides at 25°, J. Am. Chem. Soc. **76**, 879 (1954).

[116] F. H. Spedding and S. Jaffe, Conductances, Transference Numbers and Activity Coefficients of Some Rare Earth Perchlorates and Nitrates at 25°, J. Am. Chem. Soc. **76**, 884 (1954).

[117] R. E. Rosensweig, *Ferrohydrodynamics* (Dover Publications, Incorporated, 1998).

[118] G. M. Santos, A tale of oblivion: Ida Noddack and the 'universal abundance' of matter, Notes Rec. **68**, 373 (2014).

[119] J. Noddack and W. Noddack, Die Herstellung von einem Gram Rhenium, Z. Anorg. Allg. Chem. **183**, 353 (1929).

[120] W. Noddack and I. Tacke, Die Ekamangane, Naturwissenschaften **13**, 567–574 (1930).

[121] I. Noddack and W. Noddack, Die Häufigkeit der chemischen Elemente, Naturwissenschaften **18**, 757 (1930).

[122] I. Noddack, Über die Allgegenwart der chemischen Elemente, Angew. Chem. **49**, 835 (1936).

[123] I. Noddack, über das Element 93, Angew. Chem. **47**, 653 (1934).

[124] I. Noddack, Über das Element 93, Angew. Chem. **47**, 653 (1934).

[125] E. Fermi, Possible Production of Elements of Atomic Number Higher than 92, Nature **133**, 898 (1934).

[126] M. Quack, Error and Discovery: Why Repeating Can Be New, Angew. Chem. Int. Ed. **52**, 9362 (2013).

[127] I. Noddack, Bemerkung zu den Untersuchungen von O. Hahn, L. Meitner und F. Straßmann über die Produkte, die bei der Bestrahlung von Uran mit Neutronen entstehen, Naturwissenschaften **27**, 212 (1939).

[128] Anmerkung der Redaktion, Naturwissenschaften **27**, 213 (1939).

[129] F. Krafft, *Im Schatten der Sensation : Leben und Wirken von Fritz Strassmann / dargestellt von Fritz Krafft nach Dokumenten und Aufzeichnungen* (Verlag Chemie, 1981).

[130] H. Werner, *1933–1945: Eine bedrückende Zeit* (John Wiley & Sons, Ltd, 2017), Chapter 5, pp. 52–65.

[131] B. Van Tiggelen and A. Lykknes, Ida and Walter Noddack through better and worse: an Arbeitsgemeinschaft in chemistry, in *For better or for worse? Collaborative couples in the sciences*, pp. 103–147, Springer, 2012.

[132] J. D. Cockcroft, George de Hevesy. 1885-1966, Biogr. Mem. Fellows R. Soc. **13**, 125 (1967).

[133] U. Deichmann, *Forschung und Karrieren einzelner Chemiker und Biochemiker im nationalsozialistischen Deutschland* (John Wiley & Sons, Ltd, 2001), Chapter 7, pp. 357–427.

[134] Glückwunsch für Herrn Professor Noddack, Z. Phys. Chem. **209O**, 133 (1958).

[135] W. Noddack and E. Wicht, Eine neue Methode zur Trennung der seltenen Erden, Ber. Bunsenges. Phys. Chem. **56**, 893 (1952).

[136] I. Noddack and E. Wicht, Zur Trennung der Seltenen Erden im inhomogenen Magnetfeld, Chem. Techn. **7**, 3 (1955).

[137] W. Noddack, I. Noddack and E. Wicht, Zur Trennung der seltenen Erden im inhomogenen Magnetfeld, Ber. Bunsenges. Phys. Chem. **62**, 77 (1958).

[138] K. Clusius and G. Dickel, Neues Verfahren zur Gasentmischung und Isotopentrennung, Naturwissenschaften **26**, 546 (1938).

[139] K. Clusius and G. Dickel, Zur Trennung der Chlorisotope, Naturwissenschaften **27**, 148 (1939).

[140] K. Clusius and G. Dickel, Das Trennrohrverfahren bei Flüssigkeiten, Naturwissenschaften **27**, 148 (1939).

[141] K. Clusius and G. Dickel, Das Trennrohr: I. Grundlagen eines neuen Verfahrens zur Gasentmischung und Isotopentrennung durch Thermodiffusion, Z. Phys. Chem. **44B**, 397 (1939).

[142] E. W. Becker, Das Trennrohr mit hohem Druck und radialem elektrischen Feld 1 II. Erscheinungen der Turbulenz:, Z. Naturforsch. A **2**, 447 (1947).

[143] G. Guthrie, J. N. Wilson and V. Schomaker, Theory of the Thermal Diffusion of Electrolytes in a Clusius Column, J. Chem. Phys. **17**, 310 (1949).

[144] W. M. Rutherford, F. W. Weyler and C. F. Eck, Apparatus for the Thermal Diffusion Separation of Stable Gaseous Isotopes, Rev. Sci. Instrum. **39**, 94 (1968).

[145] P. G. Grodzka and B. Facemire, Clusius-Dickel Separation: A New Look at an Old Technique, Sep. Sci. **12**, 103 (1977).

[146] G. Müller and G. Vasaru, The Clusius-Dickel Thermal Diffusion Column – 50 Years after its Invention, Isotopenpraxis **24**, 455 (1988).

[147] B. S. Light, M. Zepeda-Rosales, Y. Li and C. R. Safinya, Forced Crowding of Colloids by Thermophoresis and Convection in a Custom Liquid Clusius–Dickel Microdevice, Langmuir **37**, 675 (2021).

[148] D. I. Ryabchikov and E. A. Terent'eva, Progress in Methods for the Separation of Rare-Earth Elements, Russ. Chem. Rev. **29**, 589 (1960).

[149] H. Poltmann, *Zur Röntgenspektroskopie der Seltenen Erden* (Dissertation, Universität Erlangen, 1960).

[150] W. Noddack and G. Oertel, Über die Trennung der Seltenen Erden mit Ionenaustauschern, Z. Anorg. Allg. Chem. **318**, 122 (1962).

[151] W. Noddack and W. Korneli, Über den Einfluß der Acidität des Elutionsmittels auf den Trenneffekt bei der Trennung von Yttererden an Ionenaustauschern, Z. Anorg. Allg. Chem. **323**, 220 (1963).

[152] W. Noddack and J. Woidt, Die Trennung und Reindarstellung der Yttererden an Ionenaustauschern mit Hilfe einer „Zwei-Stufen-Trennmethode“, Z. Anorg. Allg. Chem. **323**, 209 (1963).

[153] Y. Chen and B. Zheng, What Happens after the Rare Earth Crisis: A Systematic Literature Review, Sustainability **11** (2019).

[154] X. Yang, K. Tschulik, M. Uhlemann, S. Odenbach and K. Eckert, Enrichment of Paramagnetic Ions from Homogeneous Solutions in Inhomogeneous Magnetic Fields, J. Phys. Chem. Lett. **3**, 3559 (2012).

[155] B. Pulko, X. Yang, Z. Lei, S. Odenbach and K. Eckert, Magnetic separation of Dy(III) ions from homogeneous aqueous solutions, Appl. Phys. Lett. **105**, 232407 (2014).

[156] X. Yang, K. Tschulik, M. Uhlemann, S. Odenbach and K. Eckert, Magnetic Separation of Paramagnetic Ions From Initially Homogeneous Solutions, IEEE Trans. Magn. **50**, 1 (2014).

[157] A. F. Demirörs, P. P. Pillai, B. Kowalczyk and B. A. Grzybowski, Colloidal assembly directed by virtual magnetic moulds, Nature **503**, 99–103 (2013).

[158] K. Kołczyk, M. Wojnicki, D. Kutyła, R. Kowalik, P. Żabiński and A. Cristofolini, Separation of Ho^{3+} in static magnetic field, Arch. Metall. Mater. **61**, 1919 (2016).

[159] B. Ji, P. Wu, H. Ren, S. Zhang, A. Rehman and L. Wang, Segregation behavior of magnetic ions in continuous flowing solution under gradient magnetic field, Chinese Phys. B **25**, 074704 (2016).

[160] E. L. Cussler, *Diffusion: Mass Transfer in Fluid Systems* (Cambridge University Press, Third Edition, 2009).

[161] Z. Lei, B. Fritzsche and K. Eckert, Evaporation-Assisted Magnetic Separation of Rare-Earth Ions in Aqueous Solutions, J. Phys. Chem. C **121**, 24576 (2017).

[162] I. R. Rodrigues, L. Lukina, S. Dehaeck, P. Colinet, K. Binnemans and J. Fransaer, Magnetomigration of Rare-Earth Ions Triggered by Concentration Gradients, J. Phys. Chem. Lett. **8**, 5301 (2017).

[163] I. R. Rodrigues, L. Lukina, S. Dehaeck, P. Colinet, K. Binnemans and J. Fransaer, Magnetophoretic Sprinting: A Study on the Magnetic Properties of Aqueous Lanthanide Solutions, J. Phys. Chem. C **122**, 23675 (2018).

[164] I. R. Rodrigues, L. Lukina, S. Dehaeck, P. Colinet, K. Binnemans and J. Fransaer, Effect of Magnetic Susceptibility Gradient on the Magnetomigration of Rare-Earth Ions, J. Phys. Chem. C **123**, 23131 (2019).

[165] Z. Lei, B. Fritzsche and K. Eckert, Stability criterion for the magnetic separation of rare-earth ions, Phys. Rev. E **101**, 013109 (2020).

[166] Z. Lei, B. Fritzsche and K. Eckert, Magnetic separation of rare-earth ions: Transport processes and pattern formation, Phys. Rev. Fluids **6**, L021901 (2021).

[167] H. S. Harned and B. B. Owen, *The Physical Chemistry of Electrolytic Solutions* (Reinhold Pub. Corp., New York City, Third Edition, 1958).

[168] E. A. Guggenheim, *Thermodynamics: An Advanced Treatment for Chemists and Physicists* (North-Holland, Seventh Edition, 1985).

[169] F. M. M. Morel and J. G. Hering, *Principles and applications of aquatic chemistry* (John Wiley & Sons, 1993).

[170] J. Newman and K. E. Thomas-Alyea, *Electrochemical systems* (John Wiley & Sons, Third Edition, 2004).

[171] C. Kittel and H. Kroemer, *Thermal physics* (Wiley New York, 1970), Chapter 5, pp. 119–125.

[172] C. J. King, *Separation processes* (McGraw-Hill Book Company; 2nd Edition, 1980).

[173] J. A. Wesselingh and R. Krishna, *Mass transfer in multicomponent mixtures* (VSSD, Delft University Press; 1st edition, 2000).

[174] W. Greiner, L. Neise and H. Stöcker, *Thermodynamics and statistical mechanics* (Springer, 2012), Chapter 4, p. 95.

[175] F. M. M. Morel and J. G. Hering, *Principles and applications of aquatic chemistry* (John Wiley & Sons, 1993), Chapter 5, pp. 70–82.

[176] G. N. Lewis, Outlines of a new system of thermodynamic chemistry, Proc. Am. Acad. Arts Sci. **43**, 259 (1907).

[177] J. A. Rard, L. E. Shiers, D. J. Heiser and F. H. Spedding, Isopiestic determination of the activity coefficients of some aqueous rare earth electrolyte solutions at 25°C. 3. The rare earth nitrates, J. Chem. Eng. Data **22**, 337 (1977).

[178] B. Fourest, J. Duplessis and F. David, Comparison of Diffusion Coefficients and Hydrated Radii for some Trivalent Lanthanide and Actinide Ions in Aqueous Solution, Radiochim. Acta **36**, 191 (1984).

[179] E. A. Guggenheim, The Conceptions of Electrical Potential Difference between Two Phases and the Individual Activities of Ions, J. Phys. Chem. **33**, 842 (1929).

[180] E. A. Guggenheim, *Thermodynamics: An Advanced Treatment for Chemists and Physicists* (North-Holland, Seventh Edition, 1985), Chapter 8, pp. 299–302.

[181] S. W. Boettcher, S. Z. Oener, M. C. Lonergan, Y. Surendranath, S. Ardo, C. Brozek and P. A. Kempler, Potentially Confusing: Potentials in Electrochemistry, ACS Energy Lett. **6**, 261 (2021).

[182] J. Newman and K. E. Thomas-Alyea, *Electrochemical systems* (John Wiley & Sons, Third Edition, 2004), Appendix A, pp. 603–604.

[183] F. J. Millero, Molal volumes of electrolytes, Chem. Rev. **71**, 147 (1971).

[184] F. H. Spedding, M. J. Pikal and B. O. Ayers, Apparent Molal Volumes of Some Aqueous Rare Earth Chloride and Nitrate Solutions at 25°, J. Phys. Chem. **70**, 2440 (1966).

[185] F. M. M. Morel and J. G. Hering, *Principles and applications of aquatic chemistry* (John Wiley & Sons, 1993), Chapter 5, pp. 82–85.

[186] J. Newman and K. E. Thomas-Alyea, *Electrochemical systems* (John Wiley & Sons, Third Edition, 2004), Chapter 2, pp. 69–70.

[187] E. A. Guggenheim, The thermodynamics of magnetization., Proc. R. Soc. A **155**, 70 (1936).

[188] E. A. Guggenheim, *Thermodynamics: An Advanced Treatment for Chemists and Physicists* (North-Holland, Seventh Edition, 1985), Chapter 11.

[189] Y. Zimmels, Thermodynamics in the presence of electromagnetic fields, Phys. Rev. E **52**, 1452 (1995).

[190] J. Koenigsberger, Magnetische Susceptibilität von Flüssigkeiten und festen Körpern, Ann. Phys. **302**, 698 (1898).

[191] J. C. McLennan and C. S. Wright, On the Susceptibility of Mixtures of Salt Solutions, Phys. Rev. (Series I) **24**, 276 (1907).

[192] A. Heydweiller, Ist die Magnetisierungszahl der Eisen- und Mangansalzlösungen abhängig von der Feldstärke?, Ann. Phys. **317**, 608 (1903).

[193] P. Alstrøm, P. Hjorth and R. Mattuck, Paradox in the classical treatment of the Stern–Gerlach experiment, Am. J. Phys. **50**, 697 (1982).

[194] S. Singh and N. K. Sharma, Comment on "Paradox in the classical treatment of the Stern–Gerlach experiment", Am. J. Phys. **52**, 274 (1984).

[195] P. Alstrøm, Concerning S. Singh and N. Sharma: "Comment on 'Paradox in the classical treatment of the Stern–Gerlach experiment'", Am. J. Phys. **52**, 275 (1984).

[196] H. Schmidt-Böcking, L. Schmidt, H. J. Lüdde, W. Trageser, A. Templeton and T. Sauer, The Stern-Gerlach experiment revisited, Eur. Phys. J. H **41**, 327–364 (2016).

[197] H. Kallmann and F. Reiche, Über den Durchgang bewegter Moleküle durch inhomogene Kraftfelder, Z. Phys. **6**, 352 (1921).

[198] S. Y. T. van de Meerakker, H. L. Bethlem, N. Vanhaecke and G. Meijer, Manipulation and Control of Molecular Beams, Chem. Rev. **112**, 4828 (2012).

[199] N. F. Mott and N. H. D. Bohr, The scattering of fast electrons by atomic nuclei, Proc. R. Soc. A **124**, 425 (1929).

[200] B. M. Garraway and S. Stenholm, Does a flying electron spin?, Contemp. Phys. **43**, 147 (2002).

[201] L. Brillouin, Is It Possible to Test by a Direct Experiment the Hypothesis of the Spinning Electron?, Proc. Natl. Acad. Sci. U.S.A. **14**, 755 (1928).

[202] H. Batelaan, T. J. Gay and J. J. Schwendiman, Stern-Gerlach Effect for Electron Beams, Phys. Rev. Lett. **79**, 4517 (1997).

[203] B. M. Garraway and S. Stenholm, Observing the spin of a free electron, Phys. Rev. A **60**, 63 (1999).

[204] G. A. Gallup, H. Batelaan and T. J. Gay, Quantum-Mechanical Analysis of a Longitudinal Stern-Gerlach Effect, Phys. Rev. Lett. **86**, 4508 (2001).

[205] H. Batelaan, Electrons, Stern–Gerlach magnets, and quantum mechanical propagation, Am. J. Phys. **70**, 325 (2002).

[206] S. McGregor, R. Bach and H. Batelaan, Transverse quantum Stern–Gerlach magnets for electrons, New J. Phys. **13**, 065018 (2011).

[207] C. Henkel, G. Jacob, F. Stopp, F. Schmidt-Kaler, M. Keil, Y. Japha and R. Folman, Stern–Gerlach splitting of low-energy ion beams, New J. Phys. **21**, 083022 (2019).

[208] V. G. Levich, Concerning a sensational effect, Phys.-Uspekhi **9**, 316 (1966).

[209] L. Onsager and R. M. Fuoss, Irreversible Processes in Electrolytes. Diffusion, Conductance and Viscous Flow in Arbitrary Mixtures of Strong Electrolytes, J. Phys. Chem. **36**, 2689 (1932).

[210] S. De Groot and P. Mazur, *Non-Equilibrium Thermodynamics* (Dover Publications, 2013).

[211] R. E. Oesper and M. Speter, The Faraday-Whewell Correspondence Concerning Electro-Chemical Terms, Sci. Mon. **45**, 535 (1937).

[212] R. Sydney, Scientist: The story of a word, Ann. Sci. **18**, 65 (1962).

[213] J. Maxwell, On physical lines of force, Philos. Mag. **23**, 11 (1861).

[214] J. C. Maxwell, A Dynamical Theory of the Electromagnetic Field, Philos. Trans. R. Soc. **155**, 459 (1865).

[215] R. Colley, Experimentelle Untersuchung eines Falles der Arbeitsleistung des galvanischen Stromes, Ann. Phys. **233**, 370 (1876).

[216] R. Colley, Nachtrag zur Abhandlung: Experimentelle Untersuchung eines Falles von Arbeitsleistung des galvanischen Stroms, Ann. Phys. **233**, 624 (1876).

[217] R. Colley, Ueber die Existenz einer dielectrischen Polarisation in Electrolyten, Ann. Phys. **251**, 94 (1882).

[218] R. Colley, Ueber die in einem geschlossenen Stromkreise geleistete Arbeit äusserer Kräfte, Ann. Phys. **252**, 39 (1882).

[219] R. Colley, Nachweis der Existenz der Maxwell'schen electromotorischen Kraft Y_{me}, Ann. Phys. **253**, 55 (1882).

[220] W. Hittorf, Ueber die Wanderungen der Ionen während der Elektrolyse, Ann. Phys. **182**, 513 (1859).

[221] R. C. Tolman, E. W. Osgerby and T. D. Stewart, The Acceleration of Electrical Conductors., J. Am. Chem. Soc. **36**, 466 (1914).

[222] T. Des Coudres, Unpolarisirbare electrolytische Zellen unter dem Einflusse der Centrifugalkraft, Ann. Phys. **285**, 284 (1893).

[223] T. Des Coudres, Formel für Diffusionsvorgänge in einem Cylinder von endlicher Länge bei Einwirkung der Schwere, Ann. Phys. **291**, 213 (1895).

[224] T. Des Coudres, Messungen der electromotorischen Kraft Colley'scher Gravitationselemente, Ann. Phys. **293**, 232 (1896).

[225] R. C. Tolman, The Electromotive Force Produced in Solutions by Centrifugal Action, Proc. Am. Acad. Arts Sci. **46**, 109 (1910).

[226] R. C. Tolman, The Electromotive Force Produced in Solutions by Centrifugal Action., J. Am. Chem. Soc. **33**, 121 (1911).

[227] R. C. Tolman, *The electromotive force produced in solutions by centrifugal action* (PhD Thesis - Massachusetts Institute of Technology, Dept. of Chemistry, 1910).

[228] R. C. Tolman and T. D. Stewart, The Electromotive Force Produced by the Acceleration of Metals, Phys. Rev. **8**, 97 (1916).

[229] R. C. Tolman, S. Karrer and E. W. Guernsey, Further Experiments on the Mass of the Electric Carrier in Metals, Phys. Rev. **21**, 525 (1923).

[230] R. C. Tolman and L. M. Mott-Smith, A Further Study of the Inertia of the Electric Carrier in Copper, Phys. Rev. **28**, 794 (1926).

[231] D. A. MacInnes, The Electromotive Force Centrifuge, the Development of a Tool for Research, Proc. Am. Philos. Soc. **97**, 51 (1953).

[232] F. Blaha, Use of a magnetic field in detecting corrosion currents, Nature **166**, 607 (1950).

[233] I. Riess, What does a voltmeter measure?, Solid State Ion. **95**, 327 (1997).

[234] A. Fick, Ueber Diffusion, Ann. Phys. **170**, 59 (1855).

[235] A. Fick, V. On liquid diffusion, Philos. Mag. **10**, 30 (1855).

[236] E. L. Cussler, *Diffusion: Mass Transfer in Fluid Systems* (Cambridge University Press, Third Edition, 2009), Chapter 6, pp. 161–171.

[237] R. Krishna, Problems and pitfalls in the use of the Fick formulation for intraparticle diffusion, Chem. Eng. Sci. **48**, 845 (1993).

[238] R. Krishna and J. Wesselingh, The Maxwell-Stefan approach to mass transfer, Chem. Eng. Sci. **52**, 861 (1997).

[239] S. Umino and J. Newman, Temperature Dependence of the Diffusion Coefficient of Sulfuric Acid in Water, J. Electrochem. Soc. **144**, 1302 (1997).

[240] E. L. Cussler, *Diffusion: Mass Transfer in Fluid Systems* (Cambridge University Press, Third Edition, 2009), Chapter 7, pp. 211–214.

[241] T. J. Mcdougall, Double-diffusive convection caused by coupled molecular diffusion, J. Fluid Mech. **126**, 379–397 (1983).

[242] J. S. Turner, Multicomponent Convection, Ann. Rev. Fluid Mech. **17**, 11 (1985).

[243] J. Newman and K. E. Thomas-Alyea, *Electrochemical systems* (John Wiley & Sons, Third Edition, 2004), Chapter 1, pp. 10–13.

[244] D. J. Tritton, *Physical fluid dynamics* (Oxford University Press, 2nd Edition, 1988).

[245] M. Rieutord, *Fluid Dynamics: An Introduction* (Springer, 2015).

[246] V. G. Levich, *Physicochemical Hydrodynamics* (Prentice-Hall, 1962).

[247] C. Wagner, The Role of Natural Convection in Electrolytic Processes, J. Electrochem. Soc. **95**, 161 (1949).

[248] J. Slepian, Electromagnetic Ponderomotive Forces within Material Bodies, Proc. Natl. Acad. Sci. U.S.A. **36**, 485 (1950).

[249] W. F. Brown, Electric and Magnetic Forces: A Direct Calculation. I, Am. J. Phys. **19**, 290 (1951).

[250] W. F. Brown, Electric and Magnetic Forces: A Direct Calculation. II, Am. J. Phys. **19**, 333 (1951).

[251] J. Byrne, Ferrofluid hydrostatics according to classical and recent theories of the stresses, Proc. Inst. Electr. Eng. **124**, 1089 (1977).

[252] J. R. Melcher, *Continuum electromechanics* (MIT Press Cambridge, 1981).

[253] E. Blums, A. Cēbers and M. M. Maiorov, *Magnetic fluids* (Walter de Gruyter, 1996).

[254] M. Zahn, Derivation of the Korteweg-Helmholtz Electric and Magnetic Force Densities Including Electrostriction and Magnetostriction from the Quasistatic Poynting's Theorems, in *2006 IEEE Conference on Electrical Insulation and Dielectric Phenomena*, pp. 186–189, 2006.

[255] H. M. Lai, W. M. Suen and K. Young, Microscopic Derivation of the Helmholtz Force Density, Phys. Rev. Lett. **47**, 177 (1981).

[256] W. Smith-White, XLIII. On the mechanical forces in dielectrics, Philos. Mag. **40**, 466 (1949).

[257] M. Rieutord, *Fluid Dynamics: An Introduction* (Springer, 2015), Chapter 10, pp. 387–388.

[258] D. J. Korteweg, Ueber die Veränderung der Form und des Volumens dielectrischer Körper unter Einwirkung electrischer Kräfte, Ann. Phys. **245**, 48 (1880).

[259] H. Helmholtz, Ueber die auf das Innere magnetisch oder dielectrisch polarisirter Körper wirkenden Kräfte, Ann. Phys. **249**, 385 (1881).

[260] J. R. Melcher, *Continuum electromechanics* (MIT Press Cambridge, 1981), Chapter 3.

[261] G. Kirchhoff, Ueber die Formänderung, die ein fester elastischer Körper erfährt, wenn er magnetisch oder diëlectrisch polarisirt wird, Ann. der Phys. **260**, 52 (1885).

[262] G. Kirchhoff, Ueber einige Anwendungen der Theorie der Formänderung, welche ein Körper erfährt, wenn er magnetisch oder dielectrisch polarisirt wird, Ann. der Phys. **261**, 601 (1885).

[263] N. Leventis and A. Dass, Demonstration of the Elusive Concentration-Gradient Paramagnetic Force, J. Am. Chem. Soc. **127**, 4988 (2005).

[264] J. A. Svendsen and M. Waskaas, Mathematical modelling of mass transfer of paramagnetic ions through an inert membrane by the transient magnetic concentration gradient force, Phys. Fluids **32**, 013606 (2020).

[265] G. Quincke, Electrische Untersuchungen, Ann. Phys. **260**, 347 (1885).

[266] D. G. Lahoz and G. Walker, An experimental analysis of electromagnetic forces in liquids, J. Phys. D: Appl. Phys. **8**, 1994 (1975).

[267] G. Quincke, Electrische Untersuchungen, Ann. Phys. **264**, 529 (1886).

[268] Y. Gingras, Mechanical forces acting within non-polar fluid dielectrics, Phys. Lett. A **76**, 117 (1980).

[269] J. M. D. Coey, F. M. F. Rhen, P. Dunne and S. McMurry, The magnetic concentration gradient force—Is it real?, J. Solid State Electrochem. **11**, 711 (2007).

[270] M. Grinfeld and P. Grinfeld, An unexpected paradox in the Kelvin ponderomotive force theory, Results Phys. **5**, 101 (2015).

[271] J. Larmor, IX. A dynamical theory of the electric and luminiferous medium.– Part III. relations with material media, Philos. Trans. R. Soc. A **190** (1897).

[272] G. Livens, XIII. On the mechanical relations of dielectric and magnetic polarization, Philos. Mag. **32**, 162 (1916).

[273] P. Mazur and S. de Groot, On pressure and ponderomotive force in a dielectric Statistical mechanics of matter in an electromagnetic field II, Physica **22**, 657 (1956).

[274] S. S. Hakim and J. B. Higham, An Experimental Determination of the Excess Pressure produced in a Liquid Dielectric by an Electric Field, Proc. Phys. Soc. **80**, 190 (1962).

[275] D. Lahoz, Force density in fluid dielectrics, Phys. Lett. A **79**, 181 (1980).

[276] I. Brevik, Fluids in electric and magnetic fields: Pressure variation and stability, Can. J. Phys. **60**, 449 (1982).

[277] S. De Groot and P. Mazur, *Non-Equilibrium Thermodynamics* (Dover Publications, 2013), Chapter 14, pp. 388–396.

[278] B. S. Park, H. S. Choi, J. O. Park, J. H. Wang and I. H. Park, Equality of the Kelvin and Korteweg–Helmholtz Force Densities Inside Dielectric Materials, IEEE Trans. Magn. **56**, 1 (2020).

[279] J. H. Irving and J. G. Kirkwood, The Statistical Mechanical Theory of Transport Processes. IV. The Equations of Hydrodynamics, J. Chem. Phys. **18**, 817 (1950).

[280] B.-T. Chu, Thermodynamics of Electrically Conducting Fluids, Phys. Fluids **2**, 473 (1959).

[281] D. J. Tritton, *Physical fluid dynamics* (Oxford University Press, 2nd Edition, 1988), Chapter 6, pp. 81–88.

[282] J. A. Shercliff, *Magnetohydrodynamics* (Film produced by Educational Services Inc., Watertown, Mass., U.S.A., 1965).

[283] E. Blūms, Free convection in an isothermic magnetic fluid caused by magnetophoretic transport of particles in the presence of a non-uniform magnetic field, J. Magn. Magn. Mater. **65**, 343 (1987).

[284] D. J. Tritton, *Physical fluid dynamics* (Oxford University Press, 2nd Edition, 1988), Chapter 12, pp. 139–147.

[285] A. J. Bard, L. R. Faulkner, J. Leddy and C. G. Zoski, *Electrochemical methods: fundamentals and applications* (Wiley New York, 1980).

[286] C. Brett and A. M. Oliveira Brett, *Electrochemistry: principles, methods, and applications* (Oxford University Press, 1993).

[287] E. J. Dickinson and A. J. Wain, The Butler-Volmer equation in electrochemical theory: Origins, value, and practical application, J. Electroanal. Chem. **872**, 114145 (2020), Dr. Richard Compton 65th birthday Special issue.

[288] N. Elgrishi, K. J. Rountree, B. D. McCarthy, E. S. Rountree, T. T. Eisenhart and J. L. Dempsey, A Practical Beginner's Guide to Cyclic Voltammetry, J. Chem. Educ. **95**, 197 (2018).

[289] F. G. Cottrell, Der Reststrom bei galvanischer Polarisation, betrachtet als ein Diffusionsproblem, Z. Phys. Chem. **42U**, 385 (1903).

[290] J. Newman and K. E. Thomas-Alyea, *Electrochemical systems* (John Wiley & Sons, Third Edition, 2004), Chapter 1, pp. 15–18.

[291] H. Bagard, Phénomène de Hall dans les liquides, J. Phys. Theor. Appl. **5**, 499–508 (1896).

[292] R. Heilbrun, Über den sogenannten Halleffekt in Elektrolyten, Ann. Phys. **320**, 988 (1904).

[293] R. Aogaki, K. Fueki and T. Mukaibo, Application of Magnetohydrodynamic Effect to the Analysis of Electrochemical Reactions 1. MHD Flow of an Electrolyte Solution in an Electrode-Cell with a short Rectangular Channel, Denki Kagaku **43**, 504 (1975).

[294] R. Aogaki, K. Fueki and T. Mukaibo, Application of Magnetohydrodynamic Effect to the Analysis of Electrochemical Reactions 2. Diffusion Process in MHD Forced Flow of Electrolyte Solutions, Denki Kagaku **43**, 509 (1975).

[295] R. Aogaki, K. Fueki and T. Mukaibo, Diffusion Process in Viscous Flow of Electrolyte Solution in Magnetohydrodynamic Pump Electrodes, Denki Kagaku **44**, 89 (1976).

[296] S. Mohanta and T. Z. Fahidy, The effect of a uniform magnetic field on mass transfer in electrolysis, Can. J. Chem. Eng. **50**, 248 (1972).

[297] S. Mohanta and T. Fahidy, Mass transfer in a magnetoelectrolytic flow cell, Electrochim. Acta **19**, 835 (1974).

[298] M. I. Ismail and T. Z. Fahidy, Morphological characteristics of copper deposition on stainless steel cathodes, J. Appl. Electrochem. **11**, 543 (1981).

[299] A. Olivier and T. Z. Fahidy, Morphological characteristics of copper deposition on stainless steel cathodes, J. Appl. Electrochem. **12**, 417–423 (1982).

[300] T. Z. Fahidy, Magnetoelectrolysis, J. Appl. Electrochem. **13**, 553 (1983).

[301] T. Z. Fahidy, Characteristics of surfaces produced via magnetoelectrolytic deposition, Prog. Surf. Sci. **68**, 155 (2001).

[302] P. Fricoteaux, B. Jonvel and J.-P. Chopart, Magnetic Effect during Copper Electrodeposition: Diffusion Process Considerations, J. Phys. Chem. B **107**, 9459 (2003).

[303] O. Aaboubi, J. P. Chopart, J. Douglade, A. Olivier, C. Gabrielli and B. Tribollet, Magnetic Field Effects on Mass Transport, J. Electrochem. Soc. **137**, 1796 (1990).

[304] O. Devos, O. Aaboubi, J.-P. Chopart, A. Olivier, C. Gabrielli and B. Tribollet, Is There a Magnetic Field Effect on Electrochemical Kinetics?, J. Phys. Chem. A **104**, 1544 (2000).

[305] A. Olivier, J.-P. Chopart, J. Amblard, E. Merienne and O. Aaboubi, Direct and indirect electrokinetic effect inducing a forced convection. EKHD and MHD transfer functions, ACH Models Chem. **137**, 213 (2000).

[306] J.-P. Chopart, O. Aaboubi, E. Merienne, A. Olivier and J. Amblard, MHD-control on limiting Faradaic currents, Energy Convers. Manag. **43**, 365 (2002).

[307] S. Legeai, M. Chatelut, O. Vittori, J.-P. Chopart and O. Aaboubi, Magnetic field influence on mass transport phenomena, Electrochim. Acta **50**, 51 (2004).

[308] K. Rabah, J.-P. Chopart, H. Schloerb, S. Saulnier, O. Aaboubi, M. Uhlemann, D. Elmi and J. Amblard, Analysis of the magnetic force effect on paramagnetic species, J. Electroanal. Chem. **571**, 85 (2004).

[309] A. Alemany and J.-P. Chopart, *An Outline of Magnetoelectrochemistry* (Springer Netherlands, Dordrecht, 2007), pp. 391–407.

[310] A. Bund, S. Koehler, H. Kuehnlein and W. Plieth, Magnetic field effects in electrochemical reactions, Electrochim. Acta **49**, 147 (2003).

[311] S. R. Ragsdale, K. M. Grant and H. S. White, Electrochemically Generated Magnetic Forces. Enhanced Transport of a Paramagnetic Redox Species in Large, Nonuniform Magnetic Fields, J. Am. Chem. Soc. **120**, 13461 (1998).

[312] K. M. Grant, J. W. Hemmert and H. S. White, Magnetic focusing of redox molecules at ferromagnetic microelectrodes, Electrochem. Commun. **1**, 319 (1999).

[313] M. D. Pullins, K. M. Grant and H. S. White, Microscale Confinement of Paramagnetic Molecules in Magnetic Field Gradients Surrounding Ferromagnetic Microelectrodes, J. Phys. Chem. B **105**, 8989 (2001).

[314] K. M. Grant, J. W. Hemmert and H. S. White, Magnetic Field-Controlled Microfluidic Transport, J. Am. Chem. Soc. **124**, 462 (2002).

[315] J. Theodoor and G. Overbeek, The role of energy and entropy in the electrical double layer, Colloids Surf. **51**, 61 (1990).

[316] M. Janssen and R. van Roij, Reversible Heating in Electric Double Layer Capacitors, Phys. Rev. Lett. **118**, 096001 (2017).

[317] M. Janssen, E. Griffioen, P. M. Biesheuvel, R. van Roij and B. Erné, Coulometry and Calorimetry of Electric Double Layer Formation in Porous Electrodes, Phys. Rev. Lett. **119**, 166002 (2017).

[318] H. Helmholtz, Ueber einige Gesetze der Vertheilung elektrischer Ströme in körperlichen Leitern mit Anwendung auf die thierisch-elektrischen Versuche, Ann. Phys. **165**, 211 (1853).

[319] M. Gouy, Sur la constitution de la charge électrique à la surface d'un électrolyte, J. Phys. Theor. Appl. **9**, 457 (1910).

[320] D. L. Chapman, LI. A contribution to the theory of electrocapillarity, Philos. Mag. **25**, 475 (1913).

[321] S. Porada, R. Zhao, A. van der Wal, V. Presser and P. Biesheuvel, Review on the science and technology of water desalination by capacitive deionization, Prog. Mater. Sci. **58**, 1388 (2013).

[322] O. Stern, Zur Theorie der elektrolytischen Doppelschicht, Z. Elektrochem. Angew. Phys. Chem. **30**, 508 (1924).

[323] M. Qasim, M. Badrelzaman, N. N. Darwish, N. A. Darwish and N. Hilal, Reverse osmosis desalination: A state-of-the-art review, Desalination **459**, 59 (2019).

[324] M. E. Suss and V. Presser, Water Desalination with Energy Storage Electrode Materials, Joule **2**, 10 (2018).

[325] A. Mahmoud, J. Olivier, J. Vaxelaire and A. F. Hoadley, Electrical field: A historical review of its application and contributions in wastewater sludge dewatering, Water Res. **44**, 2381 (2010).

[326] M. E. Suss, S. Porada, X. Sun, P. M. Biesheuvel, J. Yoon and V. Presser, Water desalination via capacitive deionization: what is it and what can we expect from it?, Energy Environ. Sci. **8**, 2296 (2015).

[327] B. Zdravkov, J. Čermák, M. Šefara and J. Janků, Pore classification in the characterization of porous materials: A perspective:, Cent. Eur. J. Chem. **5**, 385 (2007).

[328] S. Porada, B. B. Sales, H. V. M. Hamelers and P. M. Biesheuvel, Water Desalination with Wires, J. Phys. Chem. Lett. **3**, 1613 (2012).

[329] Y. Liu, C. Nie, X. Liu, X. Xu, Z. Sun and L. Pan, Review on carbon-based composite materials for capacitive deionization, RSC Adv. **5**, 15205 (2015).

[330] Y.-J. Kim and J.-H. Choi, Enhanced desalination efficiency in capacitive deionization with an ion-selective membrane, Sep. Purif. Technol. **71**, 70 (2010).

[331] M. Pasta, C. D. Wessells, Y. Cui and F. La Mantia, A Desalination Battery, Nano Lett. **12**, 839 (2012).

[332] J. Lee, S. Kim, C. Kim and J. Yoon, Hybrid capacitive deionization to enhance the desalination performance of capacitive techniques, Energy Environ. Sci. **7**, 3683 (2014).

[333] P. Srimuk, F. Kaasik, B. Krüner, A. Tolosa, S. Fleischmann, N. Jäckel, M. C. Tekeli, M. Aslan, M. E. Suss and V. Presser, MXene as a novel intercalation-type pseudocapacitive cathode and anode for capacitive deionization, J. Mater. Chem. A **4**, 18265 (2016).

[334] M. Torkamanzadeh, L. Wang, Y. Zhang, z. Budak, P. Srimuk and V. Presser, MXene/Activated-Carbon Hybrid Capacitive Deionization for Permselective Ion Removal at Low and High Salinity, ACS Appl. Mater. Interfaces **12**, 26013 (2020).

[335] P. Srimuk, X. Su, J. Yoon, D. Aurbach and V. Presser, Charge-transfer materials for electrochemical water desalination, ion separation and the recovery of elements., Nat. Rev. Mater. **5**, 517–538 (2020).

[336] Q. Li, Y. Zheng, D. Xiao, T. Or, R. Gao, Z. Li, M. Feng, L. Shui, G. Zhou, X. Wang and Z. Chen, Faradaic Electrodes Open a New Era for Capacitive Deionization, Adv. Sci. **7**, 2002213 (2020).

[337] P. Biesheuvel, S. Porada, M. Levi and M. Z. Bazant, Attractive forces in microporous carbon electrodes for capacitive deionization, J. Solid State Electrochem. **18**, 1365 (2014).

[338] J. Nordstrand and J. Dutta, Basis and Prospects of Combining Electroadsorption Modeling Approaches for Capacitive Deionization, Physics **2**, 309 (2020).

[339] P. M. Biesheuvel, Y. Fu and M. Z. Bazant, Diffuse charge and Faradaic reactions in porous electrodes, Phys. Rev. E **83**, 061507 (2011).

[340] C. Zhang, D. He, J. Ma, W. Tang and T. D. Waite, Faradaic reactions in capacitive deionization (CDI) - problems and possibilities: A review, Water Res. **128**, 314 (2018).

[341] A. Mani, T. A. Zangle and J. G. Santiago, On the Propagation of Concentration Polarization from Microchannel-Nanochannel Interfaces Part I: Analytical Model and Characteristic Analysis, Langmuir **25**, 3898 (2009).

[342] T. A. Zangle, A. Mani and J. G. Santiago, On the Propagation of Concentration Polarization from Microchannel-Nanochannel Interfaces Part II: Numerical and Experimental Study, Langmuir **25**, 3909 (2009).

[343] A. Mani and M. Z. Bazant, Deionization shocks in microstructures, Phys. Rev. E **84**, 061504 (2011).

[344] S. Schlumpberger, N. B. Lu, M. E. Suss and M. Z. Bazant, Scalable and Continuous Water Deionization by Shock Electrodialysis, Environ. Sci. Technol. Lett. **2**, 367 (2015).

[345] C. J. Gabelich, T. D. Tran and I. H. M. Suffet, Electrosorption of Inorganic Salts from Aqueous Solution Using Carbon Aerogels, Environ. Sci. Technol. **36**, 3010 (2002).

[346] Y. Li, C. Zhang, Y. Jiang, T.-J. Wang and H. Wang, Effects of the hydration ratio on the electrosorption selectivity of ions during capacitive deionization, Desalination **399**, 171 (2016).

[347] M. R. Cerón, F. Aydin, S. A. Hawks, D. I. Oyarzun, C. K. Loeb, A. Deinhart, C. Zhan, T. A. Pham, M. Stadermann and P. G. Campbell, Cation Selectivity in Capacitive Deionization: Elucidating the Role of Pore Size, Electrode Potential, and Ion Dehydration, ACS Appl. Mater. Interfaces **12**, 42644 (2020).

[348] X. Zhang, K. Zuo, X. Zhang, C. Zhang and P. Liang, Selective ion separation by capacitive deionization (CDI) based technologies: a state-of-the-art review, Environ. Sci.: Water Res. Technol. **6**, 243 (2020).

[349] J. G. Gamaethiralalage, K. Singh, S. Sahin, J. Yoon, M. Elimelech, M. E. Suss, P. Liang, P. M. Biesheuvel, R. L. Zornitta and L. C. P. M. de Smet, Recent advances in ion selectivity with capacitive deionization, Energy Environ. Sci. **14**, 1095 (2021).

[350] G. K. Schweitzer and L. L. Pesterfield, *The Aqueous Chemistry of the Elements* (Oxford University Press, 2010), Chapter 12, pp. 261–287.

[351] Z. Zhang, Q. Jia and W. Liao, Chapter 277 - Progress in the Separation Processes for Rare Earth Resources, in *Handbook on the Physics and Chemistry of Rare Earths*, edited by J.-C. Bünzli and V. K. Pecharsky Vol. 48, pp. 287 – 376, Elsevier, 2015.

[352] G. M. Mudd and S. M. Jowitt, Rare earth elements from heavy mineral sands: assessing the potential of a forgotten resource, Appl. Earth Sci. **125**, 107 (2016).

[353] S. Freed, S. I. Weissman, F. E. Fortess and H. F. Jacobson, Ions of Europium Distributed Between Different Configurations in Homogeneous Solutions, J. Chem. Phys. **7**, 824 (1939).

[354] M. Van de Voorde, B. Geboes, T. Vander Hoogerstraete, K. Van Hecke, T. Cardinaels and K. Binnemans, Stability of europium(ii) in aqueous nitrate solutions, Dalton Trans. **48**, 14758 (2019).

[355] P. Falconnet, The economics of rare earths, Journal of the Less Common Metals **111**, 9 (1985).

[356] D. Atwood, *The Rare Earth Elements: Fundamentals and Applications* (Wiley, 2012).

[357] D. W. Pearce and P. W. Selwood, Anomalous valences of the rare earths, J. Chem. Educ. **13**, 224 (1936).

[358] P. Thyssen and K. Binnemans, Chapter 248 - Accommodation of the Rare Earths in the Periodic Table: A Historical Analysis, in *Handbook on the Physics and Chemistry of Rare Earths*, edited by K. A. Gschneidner, J.-C. G. Bünzli and V. K. Pecharsky Vol. 41, pp. 1–93, Elsevier, 2011.

[359] G. Charalampides, K. I. Vatalis, B. Apostoplos and B. Ploutarch-Nikolas, Rare Earth Elements: Industrial Applications and Economic Dependency of Europe, Procedia Econ. Finance **24**, 126 (2015), International Conference on Applied Economics (ICOAE) 2015, 2-4 July 2015, Kazan, Russia.

[360] F. H. Spedding and K. C. Jones, Heat Capacities of Aqueous Rare Earth Chloride Solutions at 25°, J. Phys. Chem. **70**, 2450 (1966).

[361] F. H. Spedding and M. J. Pikal, Relative Viscosities of Some Aqueous Rare Earth Chloride Solutions at 25°, J. Phys. Chem. **70**, 2430 (1966).

[362] Y. Marcus, Ionic radii in aqueous solutions, Chem. Rev. **88**, 1475 (1988).

[363] H. Ohtaki and T. Radnai, Structure and dynamics of hydrated ions, Chem. Rev. **93**, 1157 (1993).

[364] A. Habenschuss and F. H. Spedding, The coordination (hydration) of rare earth ions in aqueous chloride solutions from x-ray diffraction. I.$TbCl_3$,$DyCl_3$, $ErCl_3$,$TmCl_3$,and $LuCl_3$, J. Chem. Phys. **70**, 2797 (1979).

[365] A. Habenschuss and F. H. Spedding, The coordination (hydration) of rare earth ions in aqueous chloride solutions from x-ray diffraction. II. $LaCl_3$, $PrCl_3$, and $NdCl_3$, J. Chem. Phys. **70**, 3758 (1979).

[366] A. Habenschuss and F. H. Spedding, The coordination (hydration) of rare earth ions in aqueous chloride solutions from x-ray diffraction. III. $SmCl_3$, $EuCl_3$, and series behavior, J. Chem. Phys. **73**, 442 (1980).

[367] J. Näslund, P. Lindqvist-Reis, I. Persson and M. Sandström, Steric Effects Control the Structure of the Solvated Lanthanum(III) Ion in Aqueous, Dimethyl Sulfoxide, and N,N'-Dimethylpropyleneurea Solution. An EXAFS and Large-Angle X-ray Scattering Study, Inorg. Chem. **39**, 4006 (2000).

[368] L. Helm and A. E. Merbach, Inorganic and Bioinorganic Solvent Exchange Mechanisms, Chem. Rev. **105**, 1923 (2005).

[369] I. Persson, P. D'Angelo, S. De Panfilis, M. Sandström and L. Eriksson, Hydration of Lanthanoid(III) Ions in Aqueous Solution and Crystalline Hydrates Studied by EXAFS Spectroscopy and Crystallography: The Myth of the "Gadolinium Break", Chem. Eur. J. **14**, 3056 (2008).

[370] P. D'Angelo, S. De Panfilis, A. Filipponi and I. Persson, High-Energy X-ray Absorption Spectroscopy: A New Tool for Structural Investigations of Lanthanoids and Third-Row Transition Elements, Chem. Eur. J. **14**, 3045 (2008).

[371] P. D'Angelo, A. Zitolo, V. Migliorati and I. Persson, Analysis of the Detailed Configuration of Hydrated Lanthanoid(III) Ions in Aqueous Solution and Crystalline Salts by Using K- and L3-Edge XANES Spectroscopy, Chem. Eur. J. **16**, 684 (2010).

[372] M. Laing, Gadolinium: Central Metal of the Lanthanoids, J. Chem. Educ. **86**, 188 (2009).

[373] R. V. Parish, *The Metallic Elements* (Longman: London, 1977), Chapter 6.

[374] D. A. Johnson, Third ionization potentials and sublimation energies of the lanthanides, J. Chem. Soc. A , 1525 (1969).

[375] S. P. Sinha, A Systematic Correlation of the Properties of the f-Transition Metal Ions, in *Rare Earths*, pp. 1–64, Berlin, Heidelberg, 1976, Springer Berlin Heidelberg.

[376] J. A. Peters, K. Djanashvili, C. F. Geraldes and C. Platas-Iglesias, The chemical consequences of the gradual decrease of the ionic radius along the Ln-series, Coord. Chem. Rev. **406**, 213146 (2020).

[377] M. Pourbaix, *Atlas of Electrochemical Equilibria in Aqueous Solutions* (National Association of Corrosion Engineers, 2nd Edition, 1974).

[378] G. Krüss, Elektrolyse von Lösungen seltener Erden, Z. Anorg. Chem. **3**, 60 (1893).

[379] W. Noddack and A. Brukl, Die Reduktionspotentiale der Dreiwertigen Erden, Angew. Chem. **50**, 362 (1937).

[380] G. v. Hevesy, *Überblick über das chemische Verhalten der seltenen Erden* (Springer Berlin Heidelberg, Berlin, Heidelberg, 1927), pp. 16–31.

[381] G. Endres, Über die Basizität der seltenen Erden, Z. Anorg. Allg. Chem. **205**, 321 (1932).

[382] G. R. Sherwood and B. S. Hopkins, Observations on the Rare Earths. XXXIII. Studies in Basicity1, J. Am. Chem. Soc. **55**, 3117 (1933).

[383] S. H. Katz and C. James, Hydrolysis of Rare Earth Sulfates., J. Am. Chem. Soc. **36**, 779 (1914).

[384] P. H. M.-P. Brinton and C. James, The Rates of Hydrolysis of the Rare Earth Carbonates and the Serial Order of the Rare Earth Elements., J. Am. Chem. Soc. **43**, 1446 (1921).

[385] W. Prandtl and J. Rauchenberger, Über die Trennung der seltenen Erden durch basische Fällung. (I), Ber. Dtsch. Chem. Ges. **53**, 843 (1920).

[386] W. Prandtl and J. Rauchenberger, Über die Trennung der seltenen Erden durch basische Fällung. II, Z. Anorg. Allg. Chem. **120**, 120 (1921).

[387] W. Prandtl and J. Lösch, Über die Trennung der seltenen Erden durch basische Fällung. III. Die quantitative Trennung des Cers von den übrigen Erden, Z. Anorg. Allg. Chem. **122**, 159 (1922).

[388] W. Prandtl and J. Rauchenberger, Über die Trennung der seltenen Erden durch basische Fällung. IV, Z. Anorg. Allg. Chem. **122**, 311 (1922).

[389] W. Prandtl and J. Lösch, Über die Trennung der seltenen Erden durch basische Fällung. V. Die Darstellung von Cer-, Lanthan- und bunten Erden aus thoriumfreien Monaziterden, Z. Anorg. Allg. Chem. **127**, 209 (1923).

[390] W. Prandtl and J. Rauchenberger, Über die Trennung der seltenen Erden durch basische Fällung. VI, Z. Anorg. Allg. Chem. **129**, 176 (1923).

[391] W. Prandtl and K. Huttner, Über die Trennung der seltenen Erden durch basische Fällung. VII. Die Darstellung von reinem Praseodymoxyd, Z. Anorg. Allg. Chem. **136**, 289 (1924).

[392] W. Prandtl, Über die Trennung der seltenen Erden durch basische Fällung. VIII. Die Darstellung von reinem Yttriumoxyd, Z. Anorg. Allg. Chem. **143**, 277 (1925).

[393] W. Prandtl, Über die Trennung der seltenen Erden durch basische Fällung. IX. Die Darstellung von reinem Erbiumoxyd, Z. Anorg. Allg. Chem. **198**, 157 (1931).

[394] W. Prandtl, Über die Trennung der seltenen Erden durch basische Fällung. X. Die Darstellung von reinem Ytterbiumoxyd, Z. Anorg. Allg. Chem. **209**, 13 (1932).

[395] L. M. Dennis and B. J. Lemon, The Electrolysis of Solutions of the Rare Earths., J. Am. Chem. Soc. **37**, 131 (1915).

[396] L. M. Dennis and P. A. v. d. Meulen, The Electrolysis of Solutions of the Rare Earths. II., J. Am. Chem. Soc. **37**, 1963 (1915).

[397] L. M. Eennies and A. B. Ray, The Electrolysis of Solutions of the Rare Earths III., J. Am. Chem. Soc. **40**, 174 (1918).

[398] J. W. Neckers and H. C. Kremers, Observations on the Rare Earths. XXVII. I. Fractional Precipitation of the Cerium Group Earth by Electrolysis. II. Solubility of Rare Earth Oxalates in Nitric Acid, J. Am. Chem. Soc. **50**, 950 (1928).

[399] H. C. Kremers and B. S. Hopkins, Fractional Hydrolysis Of Rare Earths By Electrolysis, Trans. Amer: Electrochem. Soc. **55**, 199 (1929).

[400] A. B. Patil, R. P. W. J. Struis, A. Testino and C. Ludwig, Extraction of Rare Earth Metals: The New Thermodynamic Considerations Toward Process Hydrometallurgy, in *Rare Metal Technology 2021*, edited by G. Azimi, T. Ouchi, K. Forsberg, H. Kim, S. Alam, A. A. Baba and N. R. Neelameggham, pp. 187–194, Cham, 2021, Springer International Publishing.

[401] F. H. Spedding, A. F. Voigt, E. M. Gladrow and N. R. Sleight, The Separation of Rare Earths by Ion Exchange. I. Cerium and Yttrium, J. Am. Chem. Soc. **69**, 2777 (1947).

[402] F. H. Spedding, A. F. Voigt, E. M. Gladrow, N. R. Sleight, J. E. Powell, J. M. Wright, T. A. Butler and P. Figard, The Separation of Rare Earths by Ion Exchange. II. Neodymium and Praseodymium, J. Am. Chem. Soc. **69**, 2786 (1947).

[403] F. H. Spedding, E. I. Fulmer, T. A. Butler, E. M. Gladrow, M. Gobush, P. E. Porter, J. E. Powell and J. M. Wright, The Separation of Rare Earths by Ion Exchange. III. Pilot Plant Scale Separations, J. Am. Chem. Soc. **69**, 2812 (1947).

[404] F. H. Spedding, E. I. Fulmer, T. A. Butler and J. E. Powell, The Separation of Rare Earths by Ion Exchange. IV. Further Investigations Concerning Variables Involved in the Separation of Samarium, Neodymium and Praseodymium, J. Am. Chem. Soc. **72**, 2349 (1950).

[405] F. H. Spedding, E. I. Fulmer, J. E. Powell and T. A. Butler, The Separation of Rare Earths by Ion Exchange. V. Investigations with One-tenth Per Cent. Citric Acid-Ammonium Citrate Solutions1, J. Am. Chem. Soc. **72**, 2354 (1950).

[406] F. H. Spedding, E. I. Fulmer, J. E. Powell, T. A. Butler and I. S. Yaffe, The Separation of Rare Earths by Ion Exchange. VI. Conditions for Effecting Separations with Nalcite HCR and One-tenth Per Cent. Citric Acid-Ammonium Citrate Solutions, J. Am. Chem. Soc. **73**, 4840 (1951).

[407] F. H. Spedding and J. E. Powell, The Separation of Rare Earths by Ion Exchange. VII. Quantitative Data for the Elution of Neodymium, J. Am. Chem. Soc. **76**, 2545 (1954).

[408] F. H. Spedding and J. E. Powell, The Separation of Rare Earths by Ion Exchange. VIII. Quantitative Theory of the Mechanism Involved in Elution by Dilute Citrate Solutions, J. Am. Chem. Soc. **76**, 2550 (1954).

[409] J. Bochinski, M. Smutz and F. H. Spedding, Separation of monazite rare earths by solvent extraction, Ind. Eng. Chem. Res. **50**, 157 (1958).

[410] J. M. D. Coey, *Magnetism and Magnetic Materials* (Cambridge University Press, First Edition, 2010), Chapter 4.

[411] N. W. Ashcroft and N. D. Mermin, *Solid State Physics* (Brooks/Cole, 1976), Chapter 31.

[412] F. Hund, Zur Deutung verwickelter Spektren, insbesondere der Elemente Scandium bis Nickel, Z. Phys. **33**, 345–371 (1925).

[413] J. H. Van Vleck, On Dielectric Constants and Magnetic Susceptibilities in the New Quantum Mechanics Part III—Application to Dia- and Paramagnetism, Phys. Rev. **31**, 587 (1928).

[414] H. Kurzen, L. Bovigny, C. Bulloni and C. Daul, Electronic structure and magnetic properties of lanthanide 3+ cations, Chem. Phys. Lett. **574**, 129 (2013).

[415] A. Landé, Über den anomalen Zeemaneffekt (Teil I), Z. Phys. **1**, 231 (1921).

[416] S. Meyer, Über den Zusammenhang einiger physikalischer Eigenschaften mit der Elektronenordnung in den Elementen, Naturwissenschaften **8**, 284 (1920).

[417] R. Ladenburg, Atombau und Periodisches System der Elemente, Z. Elektrochem. Angew. Phys. Chem. **26**, 262 (1920).

[418] P. Dunne, *Magnetochemistry and Magnetic Separation* (Springer International Publishing, 2020), pp. 1–39.

[419] P. Pascal, Magnetochemical researches, Ann. Chim. Phys **19**, 5 (1910).

[420] R. F. W. Bader and T. A. Keith, Properties of atoms in molecules: Magnetic susceptibilities, J. Chem. Phys. **99**, 3683 (1993).

[421] H. D. Stearns., The Magnetic Susceptibility of Water, Phys. Rev. (Series I) **16**, 1 (1903).

[422] W. J. de Haas and P. Drapier, Magnetochemische Untersuchungen. Messung der absoluten Suszeptibilität des Wassers, Ann. Phys. **347**, 673 (1913).

[423] H. Decker, Die magnetische Suszeptibilität von wäßrigen Lösugen der Salze seltener Erden, Ann. Phys. **384**, 324 (1926).

[424] P. W. Selwood, Deformation of Electron Shells. III. The Magnetic Susceptibility of Neodymium Nitrate, J. Am. Chem. Soc. **53**, 1799 (1931).

[425] P. W. Selwood, Paramagnetism and the Molecular Field of Neodymium, J. Am. Chem. Soc. **55**, 3161 (1933).

[426] P. W. Selwood, Magnetic Susceptibilities of Some Europium and Gadolinium Compounds, J. Am. Chem. Soc. **55**, 4869 (1933).

[427] P. W. Selwood, Magnetochemical Properties of Samarium, J. Am. Chem. Soc. **56**, 2392 (1934).

[428] D. W. Pearce, Anomalous Valence and Periodicity Within the Rare Earth Group., Chem. Rev. **16**, 121 (1935).

[429] E. Bauer and A. Piccard, Les coefficients d'aimantation des gaz paramagnétiques et la théorie du magnéton, J. Phys. Radium **1**, 97 (1920).

[430] L. L. Quill, P. W. Selwood and B. Hopkins, Observations on the Rare Earths. XXX. Studies in the Absorption Spectra, J. Am. Chem. Soc. **50**, 2929 (1928).

[431] P. W. Selwood, Deformation of Electron Shells. II. Absorption Spectrum, Molecular Volume and Refraction of Certain Rare Earth Salts, J. Am. Chem. Soc. **52**, 4308 (1930).

[432] P. W. Selwood, A New Line in the Absorption Spectrum of Samarium., J. Am. Chem. Soc. **52**, 1937 (1930).

[433] K. Kolczyk-Siedlecka, M. Wojnicki, X. Yang, G. Mutschke and P. Zabinski, Experiments on the magnetic enrichment of rare-earth metal ions in aqueous solutions in a microflow device, J. Flow Chem. **9**, 175 (2019).

[434] C.-D. Ho and S.-H. Chen, Improvement in Performance of Thermal Diffusion Columns on Heavy Water Enrichment under Sidestream Operations and Flow-Rate Fraction Variations, Sep. Sci. Technol. **39**, 3373 (2004).

[435] M. Rahman and M. Saghir, Thermodiffusion or Soret effect: Historical review, Int. J. Heat Mass Transf. **73**, 693 (2014).

[436] W. Köhler and K. I. Morozov, The Soret Effect in Liquid Mixtures – A Review, J. Non-Equilib. Thermodyn. **41**, 151 (2016).

[437] D. Caldwell and S. Eide, Separation of seawater by Soret diffusion, Deep Sea Res. Part I Oceanogr. Res. Pap. **32**, 965 (1985).

[438] R. F. Higgins, T. Cheisson, B. E. Cole, B. C. Manor, P. J. Carroll and E. J. Schelter, Magnetic Field Directed Rare-Earth Separations, Angew. Chem. Int. Ed. **59**, 1851 (2020).

[439] H.-G. Stosch, Neutron Activation Analysis of the Rare Earth Elements (REE) – With Emphasis on Geological Materials, Phys. Sci. Rev. **1**, 20160062 (2016).

[440] V. F. Sears, Neutron scattering lengths and cross sections, Neutron News **3**, 26 (1992).

[441] E. Lehmann, P. Trtik and D. Ridikas, Status and Perspectives of Neutron Imaging Facilities, Phys. Procedia **88**, 140 (2017), Neutron Imaging for Applications in Industry and Science Proceedings of the 8th International Topical Meeting on Neutron Radiography (ITMNR-8) Beijing, China, September 4-8, 2016.

[442] J. Brenizer, A Review of Significant Advances in Neutron Imaging from Conception to the Present, Phys. Procedia **43**, 10 (2013).

[443] H. Kallmann and E. Kuhn, Photographic Detection of Slowly Moving Neutrons, United States Patent 2 186 757, January 9, 1940.

[444] O. Peter, Neutronen-Durchleuchtung, Z. Naturforsch. **1**, 557 (1946).

[445] S. Niese, The discovery of organic solid and liquid scintillators by H. Kallmann and L. Herforth 50 years ago, J. Radioanal. Nucl. Chem. **241**, 499–501 (1999).

[446] S. Niese, Scintillation of Organic Compounds Discovered by H. Kallmann, L. Herforth and I. Broser, J. Radioanal. Nucl. Chem. **250**, 581 (2001).

[447] J. Chadwick, Possible Existence of a Neutron, Nature **129**, 312 (1932).

[448] S. Kawasaki, A thermal neutron television system using a high yield neutron generator, Nucl. Instrum. Methods Phys. Res. **62**, 311 (1968).

[449] N. Kardjilov, I. Manke, R. Woracek, A. Hilger and J. Banhart, Advances in neutron imaging, Mater. Today **21**, 652 (2018).

[450] P. Trtik, J. Hovind, C. Grünzweig, A. Bollhalder, V. Thominet, C. David, A. Kaestner and E. H. Lehmann, Improving the Spatial Resolution of Neutron Imaging at Paul Scherrer Institut – The Neutron Microscope Project, Phys. Procedia **69**, 169 (2015).

[451] B. Betz, R. P. Harti, M. Strobl, J. Hovind, A. Kaestner, E. Lehmann, H. Van Swygenhoven and C. Grünzweig, Quantification of the sensitivity range in neutron dark-field imaging, Rev. Sci. Instrum. **86**, 123704 (2015).

[452] M. Siegwart, R. P. Harti, V. Manzi-Orezzoli, J. Valsecchi, M. Strobl, C. Grünzweig, T. J. Schmidt and P. Boillat, Selective Visualization of Water in Fuel Cell Gas Diffusion Layers with Neutron Dark-Field Imaging, J. Electrochem. Soc. **166**, F149 (2019).

[453] M. Bacak, J. Valsecchi, J. Čapek, E. Polatidis, A. Kaestner, A. Arabi-Hashemi, I. Kruk, C. Leinenbach, A. Long, A. Tremsin, S. Vogel, E. Watkins and M. Strobl, Neutron dark-field imaging applied to porosity and deformation-induced phase transitions in additively manufactured steels, Mater. Des. **195**, 109009 (2020).

[454] J. Valsecchi, M. Strobl, R. P. Harti, C. Carminati, P. Trtik, A. Kaestner, C. Grünzweig, Z. Wang, K. Jefimovs and M. Kagias, Characterization of oriented microstructures through anisotropic small-angle scattering by 2D neutron dark-field imaging, Commun. Phys. **3**, 1 (2020).

[455] N. Kardjilov, I. Manke, M. Strobl, A. Hilger, W. Treimer, M. Meissner, T. Krist and J. Banhart, Three-dimensional imaging of magnetic fields with polarized neutrons, Nature Phys. **4**, 399 (2009).

[456] M. Strobl, N. Kardjilov, A. Hilger, E. Jericha, G. Badurek and I. Manke, Imaging with polarized neutrons, Physica B **404**, 2611 (2009).

[457] N. Kardjilov, I. Manke, A. Hilger, M. Strobl and J. Banhart, Neutron imaging in materials science, Mater. Today **14**, 248 (2011).

[458] M. Strobl, H. Heimonen, S. Schmidt, M. Sales, N. Kardjilov, A. Hilger, I. Manke, T. Shinohara and J. Valsecchi, Polarization measurements in neutron imaging, J. Phys. D: Appl. Phys. **52**, 123001 (2019).

[459] N. Kardjilov, F. de Beer, R. Hassanein, E. Lehmann and P. Vontobel, Scattering corrections in neutron radiography using point scattered functions, Nucl. Instrum. Methods Phys. Res **542**, 336 (2005).

[460] P. Boillat, C. Carminati, F. Schmid, C. Grünzweig, J. Hovind, A. Kaestner, D. Mannes, M. Morgano, M. Siegwart, P. Trtik, P. Vontobel and E. Lehmann, Chasing quantitative biases in neutron imaging with scintillator-camera detectors: a practical method with black body grids, Opt. Express **26**, 15769 (2018).

[461] C. Carminati, P. Boillat, F. Schmid, P. Vontobel, J. Hovind, M. Morgano, M. Raventos, M. Siegwart, D. Mannes, C. Grünzweig, P. Trtik, E. Lehmann, M. Strobl and A. Kaestner, Implementation and assessment of the black body bias correction in quantitative neutron imaging, PLOS ONE **14**, 1 (2019).

[462] H. Rauch and S. A. Werner, *Neutron Interferometry: Lessons in Experimental Quantum Mechanics, Wave-Particle Duality, and Entanglement* (Oxford University Press, Second Edition, 2015), Chapter 1, pp. 1–12.

[463] A. Franczak, K. Binnemans and J. Fransaer, Magnetomigration of rare-earth ions in inhomogeneous magnetic fields, Phys. Chem. Chem. Phys. **18**, 27342 (2016).

[464] P. Trtik, M. Morgano, R. Bentz and E. Lehmann, 100Hz neutron radiography at the BOA beamline using a parabolic focussing guide, MethodsX **3**, 535 (2016).

[465] R. Zboray and P. Trtik, In-depth analysis of high-speed, cold neutron imaging of air-water two-phase flows, Flow. Meas. Instrum. **66**, 182 (2019).

[466] n_TOF Collaboration *et al.*, Cross section measurements of ^{155,157}Gd(n,γ) induced by thermal and epithermal neutrons, Eur. Phys. J. A **55**, 9 (2019).

[467] T. A. Butcher, G. J. M. Formon, P. Dunne, T. M. Hermans, F. Ott, L. Noirez and J. M. D. Coey, Neutron imaging of liquid-liquid systems containing paramagnetic salt solutions, Appl. Phys. Lett. **116**, 022405 (2020).

[468] F. Ott, C. Loupiac, S. Désert, A. Hélary and P. Lavie, IMAGINE: A Cold Neutron Imaging Station at the Laboratoire Léon Brillouin, Phys. Procedia **69**, 67 (2015).

[469] F. E. Hoare, Diamagnetic susceptibility of heavy water, Nature **137**, 497 (1936).

[470] E. P. Furlani, *Permanent magnet and electromechanical devices: materials, analysis, and applications* (Academic Press, San Diego, 2001).

[471] J. Schindelin, I. Arganda-Carreras, V. K. Erwin Frise, M. Longair, T. Pietzsch, C. R. Stephan Preibisch, S. Saalfeld, B. Schmid, D. J. W. Jean-Yves Tinevez, V. Hartenstein, K. Eliceiri, P. Tomancak and A. Cardona, Fiji: an open-source platform for biological-image analysis, Nat. Methods **9**, 676–682 (2012).

[472] M. D. Abràmoff, P. J. Magalhães and S. J. Ram, Image processing with ImageJ, J. Biophotonics Int. **11**, 36 (2004).

[473] C. Schneider, W. Rasband and K. Eliceiri, NIH Image to ImageJ: 25 years of image analysis, Nat. Methods **9**, 671–675 (2012).

[474] E. L. Cussler, *Diffusion: Mass Transfer in Fluid Systems* (Cambridge University Press, Third Edition, 2009), Chapter 6, p. 162.

[475] Z. Huang, A. De Luca, T. J. Atherton, M. Bird, C. Rosenblatt and P. Carlès, Rayleigh-Taylor Instability Experiments with Precise and Arbitrary Control of the Initial Interface Shape, Phys. Rev. Lett. **99**, 204502 (2007).

[476] V. Tsiklashvili, P. E. R. Colio, O. A. Likhachev and J. W. Jacobs, An experimental study of small Atwood number Rayleigh-Taylor instability using the magnetic levitation of paramagnetic fluids, Phys. Fluids **24**, 052106 (2012).

[477] J. S. Turner and H. Stommel, A new case of convection in the presence of combined vertical salinity and temperature gradients, Proc. Natl. Acad. Sci. U.S.A. **52**, 49 (1964).

[478] M. E. Stern, Lateral mixing of water masses, Deep-Sea Res. Oceanogr. Abstr. **14**, 747 (1967).

[479] M. E. Stern and J. S. Turner, Salt fingers and convecting layers, Deep-Sea Res. Oceanogr. Abstr. **16**, 497 (1969).

[480] V. Vitagliano, A. Zagari, R. Sartorio and M. Corcione, Dissipative structures and diffusion in ternary systems, J. Phys. Chem. **76**, 2050 (1972).

[481] H. E. Huppert and P. C. Manins, Limiting conditions for salt-fingering at an interface, Deep-Sea Res. Oceanogr. Abstr. **20**, 315 (1973).

[482] V. Vitagliano, R. Sartorio and L. Costantino, Cation exchange diffusion experiments, J. Phys. Chem. **78**, 2292 (1974).

[483] H. E. Huppert and P. F. Linden, On heating a stable salinity gradient from below, J. Fluid Mech. **95**, 431–464 (1979).

[484] A. B. Tsinober, Y. Yahalom and D. J. Shlien, A point source of heat in a stable salinity gradient, J. Fluid Mech. **135**, 199 (1983).

[485] R. Mills, A. Perera, J. P. Simonin, L. Orcil and P. Turq, Coupling of diffusion processes in multicomponent electrolyte solutions, J. Phys. Chem. **89**, 2722 (1985).

[486] V. Vitagliano, G. Borriello, C. D. Volpe and O. Ortona, Instabilities in free diffusion boundaries of NaCl-sucrose-H_2O solution at 25°C, J. Solution Chem. **15**, 811–826 (1986).

[487] J. D. Wells, Solvent fluxes, coupled diffusion, and convection in concentrated ternary solutions, J. Phys. Chem. **90**, 2433 (1986).

[488] J.-H. Xie, K. Julien and E. Knobloch, Fixed-flux salt-finger convection in the small diffusivity ratio limit, Phys. Fluids **32**, 126601 (2020).

[489] R. W. Schmitt, Double Diffusion in Oceanography, Ann. Rev. Fluid Mech. **26**, 255 (1994).

[490] R. W. Schmitt, J. R. Ledwell, E. T. Montgomery, K. L. Polzin and J. M. Toole, Enhanced Diapycnal Mixing by Salt Fingers in the Thermocline of the Tropical Atlantic, Science **308**, 685 (2005).

[491] H. Stommel, A. B. Arons and D. Blanchard, An oceanographical curiosity: the perpetual salt fountain, Deep Sea Res. **3**, 152 (1956).

[492] M. E. Stern, The "Salt-Fountain" and Thermohaline Convection, Tellus **12**, 172 (1960).

[493] H. E. Huppert and M. A. Hallworth, Static and dynamic stability criteria during free diffusion in a ternary system, J. Phys. Chem. **88**, 2902 (1984).

[494] E. Mauerhofer, K. P. Zhernosekov and F. Rösch, Limiting transport properties of lanthanide and actinide ions in pure water:, Radiochim. Acta **91**, 473 (2003).

[495] F. Martelli, S. Abadie, J.-P. Simonin, R. Vuilleumier and R. Spezia, Lanthanoids(III) and actinoids(III) in water: Diffusion coefficients and hydration enthalpies from polarizable molecular dynamics simulations:, Pure Appl. Chem. **85**, 237 (2012).

[496] F. H. Spedding, L. E. Shiers, M. A. Brown, J. L. Baker, L. Guitierrez, L. S. McDowell and A. Habenschuss, Densities and apparent molal volumes of some aqueous rare earth solutions at 25°C. III. Rare earth nitrates, J. Phys. Chem. **79**, 1087 (1975).

[497] J. A. Rard and F. H. Spedding, Isopiestic determination of the activity coefficients of some aqueous rare-earth electrolyte solutions at 25°C. 6. Europium trinitrate, yttrium nitrate, yttrium chloride, J. Chem. Eng. Data **27**, 454 (1982).

[498] A. W. Hakin, J. L. Liu, K. Erickson, J.-V. Munoz and J. A. Rard, Apparent molar volumes and apparent molar heat capacities of $Pr(NO_3)_3$(aq), $Gd(NO_3)_3$(aq), $Ho(NO_3)_3$(aq), and $Y(NO_3)_3$(aq) at T=(288.15, 298.15, 313.15, and 328.15) K and p=0.1 MPa, J. Chem. Thermodyn. **37**, 153 (2005).

[499] J. K. Im, L. Jeong, J. Crha, P. Trtik and J. Jeong, High-resolution neutron imaging reveals kinetics of water vapor uptake into a sessile water droplet, Matter **4**, 2083 (2021).

[500] J. Taylor and G. Veronis, Experiments on Salt Fingers in a Hele Shaw Cell, Science **231**, 39 (1986).

[501] G. Oster and M. Yamamoto, Density Gradient Techniques., Chem. Rev. **63**, 257 (1963).

[502] G. Oster, Density Gradients, Sci. Am. **213**, 70 (1965).

[503] Y. H. Zurigat, K. Bang and A. J. Ghajar, Methods for producing linear density gradients in laboratory tanks, Energy **15**, 23 (1990).

[504] L. Middleton and J. R. Taylor, A general criterion for the release of background potential energy through double diffusion, J. Fluid Mech. **893**, R3 (2020).

[505] A. Cebers and M. M. Maiorov, Magnetostatic instabilities in plane layers of magnetizable fluids, Magnetohydrodynamics **16**, 21–27 (1980).

[506] M. M. Maiorov and A. Cebers, Magnetic microconvection on the diffusion front of ferroparticles, Magnetohydrodynamics **19**, 376 (1983).

[507] K. Ērglis, A. Tatulcenkov, G. Kitenbergs, O. Petrichenko, F. G. Ergin, B. B. Watz and A. Cēbers, Magnetic field driven micro-convection in the Hele-Shaw cell, J. Fluid Mech. **714**, 612 (2013).

[508] G. Kitenbergs, A. Tatulcenkovs, K. Ērglis, O. Petrichenko, R. Perzynski and A. Cēbers, Magnetic field driven micro-convection in the Hele-Shaw cell: the Brinkman model and its comparison with experiment, J. Fluid Mech. **774**, 170–191 (2015).

[509] G. Kitenbergs, K. Ērglis, R. Perzynski and A. Cēbers, Magnetic particle mixing with magnetic micro-convection for microfluidics, J. Magn. Magn. Mater. **380**, 227 (2015).

[510] M. S. Krakov, A. R. Zakinyan and A. A. Zakinyan, Instability of the miscible magnetic/non-magnetic fluid interface, J. Fluid Mech. **913**, A30 (2021).

[511] G. Kitenbergs and A. Cēbers, Rivalry of diffusion, external field and gravity in microconvection of magnetic colloids, J. Magn. Magn. Mater. **498**, 166247 (2020).

[512] J. Dodoo and A. A. Stokes, Shaping and transporting diamagnetic sessile drops, Biomicrofluidics **13**, 064110 (2019).

[513] J. Dodoo and A. A. Stokes, Field-induced shaping of sessile paramagnetic drops, Phys. Fluids **32**, 061703 (2020).

[514] B. Fritzsche, G. Mutschke, T. J. Meinel, X. Yang, Z. Lei and K. Eckert, Oscillatory surface deformation of paramagnetic rare-earth solutions driven by an inhomogeneous magnetic field, Phys. Rev. E **101**, 062601 (2020).

[515] J. C. Farmer, J. H. Richardson, D. V. Fix, S. L. Thomson and S. C. May, *Desalination with carbon aerogel electrodes* (Technical Report, 1996).

[516] A. Hemmatifar, A. Ramachandran, K. Liu, D. I. Oyarzun, M. Z. Bazant and J. G. Santiago, Thermodynamics of Ion Separation by Electrosorption, Environ. Sci. Technol. **52**, 10196 (2018).

[517] L. Wang, J. E. Dykstra and S. Lin, Energy Efficiency of Capacitive Deionization, Environ. Sci. Technol. **53**, 3366 (2019).

[518] L. Wang, C. Violet, R. M. DuChanois and M. Elimelech, Derivation of the Theoretical Minimum Energy of Separation of Desalination Processes, J. Chem. Educ. **97**, 4361 (2020).

[519] A. E. Kennelly, The Linear Resistance between Parallel Conducting Cylinders in a Medium of Uniform Conductivity, Proc. Am. Philos. Soc. **48**, 142 (1909).

[520] K. Roy, P. Devi and P. Kumar, Magnetic-field induced sustainable electrochemical energy harvesting and storage devices: Recent progress, opportunities, and future perspectives, Nano Energy **87**, 106119 (2021).

[521] L. L. Perreault, S. Giret, M. Gagnon, J. Florek, D. Larivière and F. Kleitz, Functionalization of Mesoporous Carbon Materials for Selective Separation of Lanthanides under Acidic Conditions, ACS Appl. Mater. Interfaces **9**, 12003 (2017).

[522] Y. Hu, J. Florek, D. Larivière, F.-G. Fontaine and F. Kleitz, Recent Advances in the Separation of Rare Earth Elements Using Mesoporous Hybrid Materials, Chem. Rec. **18**, 1261 (2018).

[523] S. Boukhalfa, L. He, Y. B. Melnichenko and G. Yushin, Small-Angle Neutron Scattering for In Situ Probing of Ion Adsorption Inside Micropores, Angew. Chem. Int. Ed. **52**, 4618 (2013).

[524] S. Boukhalfa, D. Gordon, L. He, Y. B. Melnichenko, N. Nitta, A. Magasinski and G. Yushin, In Situ Small Angle Neutron Scattering Revealing Ion Sorption in Microporous Carbon Electrical Double Layer Capacitors, ACS Nano **8**, 2495 (2014).

[525] D. Schwahn, V. Pipich, R. Kasher and Y. Oren, Accumulation of GdCl3in the feed of a reverse osmosis system during desalination as determined by neutron absorption, J. Phys. Conf. Ser. **746**, 012039 (2016).

[526] J. P. Owejan, J. J. Gagliardo, S. J. Harris, H. Wang, D. S. Hussey and D. L. Jacobson, Direct measurement of lithium transport in graphite electrodes using neutrons, Electrochim. Acta **66**, 94 (2012).

[527] B. Song, I. Dhiman, J. C. Carothers, G. M. Veith, J. Liu, H. Z. Bilheux and A. Huq, Dynamic Lithium Distribution upon Dendrite Growth and Shorting Revealed by Operando Neutron Imaging, ACS Energy Lett. **4**, 2402 (2019).

[528] K. Sharma, H. Z. Bilheux, L. M. H. Walker, S. Voisin, R. T. Mayes, J. O. Kiggans Jr., S. Yiacoumi, D. W. DePaoli, S. Dai and C. Tsouris, Neutron imaging of ion transport in mesoporous carbon materials, Phys. Chem. Chem. Phys. **15**, 11740 (2013).

[529] K. Sharma, Y.-H. Kim, J. Gabitto, R. T. Mayes, S. Yiacoumi, H. Z. Bilheux, L. M. H. Walker, S. Dai and C. Tsouris, Transport of Ions in Mesoporous Carbon Electrodes during Capacitive Deionization of High-Salinity Solutions, Langmuir **31**, 1038 (2015).

[530] Y.-H. Kim, K. Tang, J. Chang, K. Sharma, S. Yiacoumi, R. Mayes, H. Bilheux, L. Santodonato and C. Tsouris, Potential limits of capacitive deionization and membrane capacitive deionization for water electrolysis, Sep. Sci. Technol. **54**, 2112 (2019).

[531] K. Meyer and P. Klobes, Comparison between different presentations of pore size distribution in porous materials, Fresenius J. Anal. Chem. **363**, 174–178 (1999).

[532] K. S. Sing, Adsorption methods for the characterization of porous materials, Adv. Colloid Interface Sci. **76-77**, 3 (1998).

[533] K. Sing, The use of nitrogen adsorption for the characterisation of porous materials, Colloids Surf. **187-188**, 3 (2001).

[534] E. H. Lehmann, P. Vontobel and L. Wiezel, Properties of the radiography facility NEUTRA at SINQ and its potential for use as European reference facility, Nondestr. Test. Eval. **16**, 191 (2001).

[535] J. F. Beacom and M. R. Vagins, Antineutrino Spectroscopy with Large Water Čerenkov Detectors, Phys. Rev. Lett. **93**, 171101 (2004).

[536] Just add salt, Phys. World **17**, 7 (2004).

[537] N. Kardjilov, A. Hilger, I. Manke, M. Strobl, M. Dawson and J. Banhart, New trends in neutron imaging, Nucl. Instrum. Methods. Phys. Res. A **605**, 13 (2009).

[538] N. Kardjilov, M. Dawson, A. Hilger, I. Manke, M. Strobl, D. Penumadu, F. Kim, F. Garcia-Moreno and J. Banhart, A highly adaptive detector system for high resolution neutron imaging, Nucl. Instrum. Methods. Phys. Res. A **651**, 95 (2011).

[539] C. Tötzke, I. Manke, A. Hilger, G. Choinka, N. Kardjilov, T. Arlt, H. Markötter, A. Schröder, K. Wippermann, D. Stolten, C. Hartnig, P. Krüger, R. Kuhn and J. Banhart, Large area high resolution neutron imaging detector for fuel cell research, J. Power Sources **196**, 4631 (2011).

[540] J. Crha, J. Vila-Comamala, E. Lehmann, C. David and P. Trtik, Light Yield Enhancement of 157-Gadolinium Oxysulfide Scintillator Screens for the High-Resolution Neutron Imaging, MethodsX **6**, 107 (2019).

[541] C. Grünzweig, G. Frei, E. Lehmann, G. Kühne and C. David, Highly absorbing gadolinium test device to characterize the performance of neutron imaging detector systems, Rev. Sci. Instrum. **78**, 053708 (2007).

[542] S. S. Kistler, Coherent Expanded Aerogels and Jellies, Nature **127**, 741 (1936).

[543] R. Pekala, Organic aerogels from the polycondensation of resorcinol with formaldehyde, J. Mater. Sci. **24**, 3221 (1989).

[544] R. Pekala, C. Alviso, F. Kong and S. Hulsey, Aerogels derived from multifunctional organic monomers, J. Non-Cryst. Solids **145**, 90 (1992).

[545] G. C. Ruben, R. W. Pekala, T. M. Tillotson and L. W. Hrubesh, Imaging aerogels at the molecular level, J. Mater. Sci. **27**, 4341–4349 (1992).

[546] S. T. Mayer, R. W. Pekala and J. L. Kaschmitter, The Aerocapacitor: An Electrochemical Double-Layer Energy-Storage Device, J. Electrochem. Soc. **140**, 446 (1993).

[547] J. C. Farmer, D. V. Fix, G. V. Mack, R. W. Pekala and J. F. Poco, Capacitive Deionization of NaCl and NaNO3 Solutions with Carbon Aerogel Electrodes, J. Electrochem. Soc. **143**, 159 (1996).

[548] J. C. Farmer, S. M. Bahowick, J. E. Harrar, D. V. Fix, R. E. Martinelli, A. K. Vu and K. L. Carroll, Electrosorption of Chromium Ions on Carbon Aerogel Electrodes as a Means of Remediating Ground Water, Energy Fuels **11**, 337 (1997).

[549] T.-Y. Ying, K.-L. Yang, S. Yiacoumi and C. Tsouris, Electrosorption of Ions from Aqueous Solutions by Nanostructured Carbon Aerogel, J. Colloid Interface Sci. **250**, 18 (2002).

[550] K.-L. Yang, T.-Y. Ying, S. Yiacoumi, C. Tsouris and E. S. Vittoratos, Electrosorption of Ions from Aqueous Solutions by Carbon Aerogel: An Electrical Double-Layer Model, Langmuir **17**, 1961 (2001).

[551] P. Xu, J. E. Drewes, D. Heil and G. Wang, Treatment of brackish produced water using carbon aerogel-based capacitive deionization technology, Water Res. **42**, 2605 (2008).

[552] M. E. Suss, T. F. Baumann, W. L. Bourcier, C. M. Spadaccini, K. A. Rose, J. G. Santiago and M. Stadermann, Capacitive desalination with flow-through electrodes, Energy Environ. Sci. **5**, 9511 (2012).

[553] M. E. Suss, P. Biesheuvel, T. F. Baumann, M. Stadermann and J. G. Santiago, In Situ Spatially and Temporally Resolved Measurements of Salt Concentration between Charging Porous Electrodes for Desalination by Capacitive Deionization, Environ. Sci. Technol. **48**, 2008 (2014).

[554] J.-H. Lee and S.-J. Park, Recent advances in preparations and applications of carbon aerogels: A review, Carbon **163**, 1 (2020).

[555] T. A. Butcher, L. Prendeville, A. Rafferty, P. Trtik, P. Boillat and J. M. D. Coey, Neutron Imaging of Paramagnetic Ions: Electrosorption by Carbon Aerogels and Macroscopic Magnetic Forces, J. Phys. Chem. C **125**, 21831 (2021).

[556] E. W. Washburn, The Dynamics of Capillary Flow, Phys. Rev. **17**, 273 (1921).

[557] S. Brunauer, P. H. Emmett and E. Teller, Adsorption of Gases in Multimolecular Layers, J. Am. Chem. Soc. **60**, 309 (1938).

[558] S. Brunauer, L. S. Deming, W. E. Deming and E. Teller, On a Theory of the van der Waals Adsorption of Gases, J. Am. Chem. Soc. **62**, 1723 (1940).

[559] E. P. Barrett, L. G. Joyner and P. P. Halenda, The Determination of Pore Volume and Area Distributions in Porous Substances. I. Computations from Nitrogen Isotherms, J. Am. Chem. Soc. **73**, 373 (1951).

[560] J. C. Groen, L. A. Peffer and J. Pérez-Ramírez, Pore size determination in modified micro- and mesoporous materials. Pitfalls and limitations in gas adsorption data analysis, Microporous Mesoporous Mater. **60**, 1 (2003).

[561] M. F. De Lange, T. J. Vlugt, J. Gascon and F. Kapteijn, Adsorptive characterization of porous solids: Error analysis guides the way, Microporous Mesoporous Mater. **200**, 199 (2014).

[562] J. Wang, L. Angnes, H. Tobias, R. A. Roesner, K. C. Hong, R. S. Glass, F. M. Kong and R. W. Pekala, Carbon aerogel composite electrodes, Anal. Chem. **65**, 2300 (1993).

[563] R. W. Pekala, J. C. Farmer, C. T. Alviso, T. D. Tran, S. T. Mayer, J. M. Miller and B. Dunn, Carbon aerogels for electrochemical applications, J. Non-Cryst. Solids **225**, 74 (1998).

[564] N. Leventis, I. A. Elder, G. J. Long and D. R. Rolison, Using Nanoscopic Hosts, Magnetic Guests, and Field Alignment to Create Anisotropic Composite Gels and Aerogels, Nano Lett. **2**, 63 (2002).

[565] Y. Wang, J. E. Panzik, B. Kiefer and K. K. M. Lee, Crystal structure of graphite under room-temperature compression and decompression, Sci. Rep. **2**, 520 (2012).

[566] T. Qiu, J.-G. Yang, X.-J. Bai and Y.-L. Wang, The preparation of synthetic graphite materials with hierarchical pores from lignite by one-step impregnation and their characterization as dye absorbents, RSC Adv. **9**, 12737 (2019).

[567] E. Avraham, Y. Bouhadana, A. Soffer and D. Aurbach, Limitation of Charge Efficiency in Capacitive Deionization, J. Electrochem. Soc. **156**, P95 (2009).

[568] E. Avraham, M. Noked, Y. Bouhadana, A. Soffer and D. Aurbach, Limitations of Charge Efficiency in Capacitive Deionization, J. Electrochem. Soc. **156**, P157 (2009).

[569] R. Zhao, P. Biesheuvel, H. Miedema, H. Bruning and A. van der Wal, Charge Efficiency: A Functional Tool to Probe the Double-Layer Structure Inside of Porous Electrodes and Application in the Modeling of Capacitive Deionization, J. Phys. Chem. Lett. **1**, 205 (2010).

[570] C.-H. Hou and C.-Y. Huang, A comparative study of electrosorption selectivity of ions by activated carbon electrodes in capacitive deionization, Desalination **314**, 124 (2013).

[571] K. G. Gallagher and T. F. Fuller, Kinetic model of the electrochemical oxidation of graphitic carbon in acidic environments, Phys. Chem. Chem. Phys. **11**, 11557 (2009).

[572] B. Shapira, E. Avraham and D. Aurbach, Side Reactions in Capacitive Deionization (CDI) Processes: The Role of Oxygen Reduction, Electrochim. Acta **220**, 285 (2016).

[573] A. Hassanvand, G. Q. Chen, P. A. Webley and S. E. Kentish, A comparison of multicomponent electrosorption in capacitive deionization and membrane capacitive deionization, Water Res. **131**, 100 (2018).

[574] S. Maass, F. Finsterwalder, G. Frank, R. Hartmann and C. Merten, Carbon support oxidation in PEM fuel cell cathodes, J. Power Sources **176**, 444 (2008).

[575] H.-S. Oh, J.-G. Oh, S. Haam, K. Arunabha, B. Roh, I. Hwang and H. Kim, On-line mass spectrometry study of carbon corrosion in polymer electrolyte membrane fuel cells, Electrochem. Comm. **10**, 1048 (2008).

[576] I. Cohen, E. Avraham, Y. Bouhadana, A. Soffer and D. Aurbach, The effect of the flow-regime, reversal of polarization, and oxygen on the long term stability in capacitive de-ionization processes, Electrochim. Acta **153**, 106 (2015).

[577] Y. Bouhadana, E. Avraham, A. Soffer and D. Aurbach, Several basic and practical aspects related to electrochemical deionization of water, AIChE J. **56**, 779 (2010).

[578] E. Avraham, M. Noked, A. Soffer and D. Aurbach, The feasibility of boron removal from water by capacitive deionization, Electrochim. Acta **56**, 6312 (2011).

[579] Y. Bouhadana, E. Avraham, M. Noked, M. Ben-Tzion, A. Soffer and D. Aurbach, Capacitive Deionization of NaCl Solutions at Non-Steady-State Conditions: Inversion Functionality of the Carbon Electrodes, J. Phys. Chem C **115**, 16567 (2011).

[580] M. T. Z. Myint and J. Dutta, Fabrication of zinc oxide nanorods modified activated carbon cloth electrode for desalination of brackish water using capacitive deionization approach, Desalination **305**, 24 (2012).

[581] G. Wang, Q. Dong, Z. Ling, C. Pan, C. Yu and J. Qiu, Hierarchical activated carbon nanofiber webs with tuned structure fabricated by electrospinning for capacitive deionization, J. Mater. Chem. **22**, 21819 (2012).

[582] K. Laxman, M. T. Z. Myint, M. Al Abri, P. Sathe, S. Dobretsov and J. Dutta, Desalination and disinfection of inland brackish ground water in a capacitive deionization cell using nanoporous activated carbon cloth electrodes, Desalination **362**, 126 (2015).

[583] X. Gao, S. Porada, A. Omosebi, K.-L. Liu, P. Biesheuvel and J. Landon, Complementary surface charge for enhanced capacitive deionization, Water Res. **92**, 275 (2016).

[584] M. Gineys, R. Benoit, N. Cohaut, F. Béguin and S. Delpeux-Ouldriane, Behavior of activated carbon cloths used as electrode in electrochemical processes, Chem. Eng. J. **310**, 1 (2017).

[585] C. Kim, P. Srimuk, J. Lee, S. Fleischmann, M. Aslan and V. Presser, Influence of pore structure and cell voltage of activated carbon cloth as a versatile electrode material for capacitive deionization, Carbon **122**, 329 (2017).

[586] M. Lenz, J. Zabel and M. Franzreb, New Approach for Investigating Diffusion Kinetics Within Capacitive Deionization Electrodes Using Electrochemical Impedance Spectroscopy, Front. Mater. **7**, 229 (2020).

[587] C. Pean, B. Daffos, B. Rotenberg, P. Levitz, M. Haefele, P.-L. Taberna, P. Simon and M. Salanne, Confinement, Desolvation, And Electrosorption Effects on the Diffusion of Ions in Nanoporous Carbon Electrodes, J. Am. Chem. Soc. **137**, 12627 (2015).

[588] M. Shimada, S. Takigami, Y. Nakamura, Y. Abe, T. Iizuka and N. Makiyama, Efficiently activated carbon fiber derived from grafted novoloid fiber, J. Appl. Polym. Sci. **48**, 1121 (1993).

[589] J. S. Hayes Jr, Nanostructure of activated carbon fibers and kinetics of adsorption/desorption, in *Proceedings of the Air & Waste Management Association's Annual Conference & Exhibition, 95th*, pp. 23–27, 2002.

[590] I. Langmuir, Chemical Reactions at Low Pressure., J. Am. Chem. Soc. **37**, 1139 (1915).

[591] J. Rouquerol, P. Llewellyn and F. Rouquerol, Is the BET equation applicable to microporous adsorbents?, Stud. Surf. Sci. Catal. **160**, 49 (2007).

[592] A. V. Neimark, P. I. Ravikovitch and A. Vishnyakov, Bridging scales from molecular simulations to classical thermodynamics: density functional theory of capillary condensation in nanopores, J. Phys.: Condens. Matter **15**, 347 (2003).

[593] J. Wu, Density functional theory for chemical engineering: From capillarity to soft materials, AIChE J. **52**, 1169 (2006).

[594] A. P. Hughes, U. Thiele and A. J. Archer, An introduction to inhomogeneous liquids, density functional theory, and the wetting transition, Am. J. Phys. **82**, 1119 (2014).

[595] A. V. Neimark, Y. Lin, P. I. Ravikovitch and M. Thommes, Quenched solid density functional theory and pore size analysis of micro-mesoporous carbons, Carbon **47**, 1617 (2009).

[596] G. Y. Gor, M. Thommes, K. A. Cychosz and A. V. Neimark, Quenched solid density functional theory method for characterization of mesoporous carbons by nitrogen adsorption, Carbon **50**, 1583 (2012).

[597] M. Kwiatkowski, V. Fierro and A. Celzard, Crystal structure of graphite under room-temperature compression and decompression, Adsorption **25**, 1673–1682 (2019).

[598] H. A. Maddah and M. A. Shihon, *Activated carbon cloth for desalination of brackish water using capacitive deionization* (Desalination and Water Treatment, BoD–Books on Demand, 2018), pp. 17–36.

[599] K. Kaneko, C. Ishii, M. Ruike and H. Kuwabara, Origin of superhigh surface area and microcrystalline graphitic structures of activated carbons, Carbon **30**, 1075 (1992).

[600] M. D. Stoller and R. S. Ruoff, Best practice methods for determining an electrode material's performance for ultracapacitors, Energy Environ. Sci. **3**, 1294 (2010).

[601] F. Hine and K. Murakami, Bubble Effects on the Solution IR Drop in a Vertical Electrolyzer Under Free and Forced Convection, J. Electrochem. Soc. **127**, 292 (1980).

[602] S. Zhang and N. Pan, Supercapacitors Performance Evaluation, Adv. Energy Mater. **5**, 1401401 (2015).

[603] S. Ueno and M. Iwasaka, Properties of diamagnetic fluid in high gradient magnetic fields, J. Appl. Phys. **75**, 7177 (1994).

[604] Y. Hanzawa, K. Kaneko, R. W. Pekala and M. S. Dresselhaus, Activated Carbon Aerogels, Langmuir **12**, 6167 (1996).

[605] I. Yang, D. Kwon, M.-S. Kim and J. C. Jung, A comparative study of activated carbon aerogel and commercial activated carbons as electrode materials for organic electric double-layer capacitors, Carbon **132**, 503 (2018).

[606] M. Waskaas, Short-term effects of magnetic fields on diffusion in stirred and unstirred paramagnetic solutions, J. Phys. Chem. **97**, 6470 (1993).

[607] H. Liu, H. Xu, L. Pan, D. Zhong and Y. Liu, Porous electrode improving energy efficiency under electrode-normal magnetic field in water electrolysis, Int. J. Hydrog. Energy **44**, 22780 (2019).

[608] J. Ma, T. Gao, Y. He, K. Zuo, Q. Li and P. Liang, Enhanced Charge Efficiency and Electrode Separation Utilizing Magnetic Carbon in Flow Electrode Capacitive Deionization, ACS EST Engg. **1**, 340 (2021).

[609] M. Morgano, E. Lehmann and M. Strobl, Detectors Requirements for the ODIN Beamline at ESS, Phys. Procedia **69**, 152 (2015).

[610] P. Trtik and E. H. Lehmann, Progress in High-resolution Neutron Imaging at the Paul Scherrer Institut - The Neutron Microscope Project, J. Phys. Conf. Ser. **746**, 012004 (2016).

[611] R. Zboray and P. Trtik, 800 fps neutron radiography of air-water two-phase flow, MethodsX **5**, 96 (2018).

[612] E. Hoinkis and M. Ziehl, A small-angle neutron scattering study of activated carbon fibers, Carbon **41**, 2047 (2003).

[613] P. Pendleton and L. Chen, Small-angle neutron scattering study of activated carbon cloth and ammonium persulfate-modified activated carbon cloth: Effect of oxygen content, Physica B Condens. Matter **385-386**, 644 (2006).

[614] T. X. Nguyen and S. K. Bhatia, Characterization of accessible and inaccessible pores in microporous carbons by a combination of adsorption and small angle neutron scattering, Carbon **50**, 3045 (2012).

[615] S. Mascotto, D. Kuzmicz, D. Wallacher, M. Siebenbürger, D. Clemens, S. Risse, J. Yuan, M. Antonietti and M. Ballauff, Poly(ionic liquid)-derived nanoporous carbon analyzed by combination of gas physisorption and small-angle neutron scattering, Carbon **82**, 425 (2015).

[616] C. J. Jafta, A. Petzold, S. Risse, D. Clemens, D. Wallacher, G. Goerigk and M. Ballauff, Correlating pore size and shape to local disorder in microporous carbon: A combined small angle neutron and X-ray scattering study, Carbon **123**, 440 (2017).

[617] W. Han, M. Li, M.-L. Zhang and Y.-D. Yan, Progress in preparation of rare earth metals and alloys by electrodeposition in molten salts., Rare Met. **35**, 811–825 (2016).

[618] E. Bourbos, I. Giannopoulou, A. Karantonis, I. Paspaliaris and D. Panias, Chapter 13 - Electrodeposition of Rare Earth Metals from Ionic Liquids, in *Rare Earths Industry*, edited by I. Borges De Lima and W. Leal Filho, pp. 199–207, Elsevier, Boston, 2016.

[619] P. Geysens, P.-C. Lin, J. Fransaer and K. Binnemans, Electrodeposition of neodymium and dysprosium from organic electrolytes, Phys. Chem. Chem. Phys. **23**, 9070 (2021).

[620] M. Ortner and L. G. Coliado Bandeira, Magpylib: A free Python package for magnetic field computation, SoftwareX **11**, 100466 (2020).

[621] I. Zhitomirsky and A. Petric, Electrolytic deposition of Gd_2O_3 and organoceramic composite, Mater. Lett. **42**, 273 (2000).

[622] I. Zhitomirsky and A. Petric, Electrochemical deposition of yttrium oxide, J. Mater. Chem. **10**, 1215 (2000).

[623] S. G. Eggermont, R. Prato, X. Dominguez-Benetton and J. Fransaer, Metal removal from aqueous solutions: insights from modeling precipitation titration curves, J. Environ. Chem. **8**, 103596 (2020).

[624] B. Šeta, J. Gavalda, M. M. Bou-Ali, X. Ruiz and C. Santamaria, Determining diffusion, thermodiffusion and Soret coefficients by the thermogravitational technique in binary mixtures with optical digital interferometry analysis, Int. J. Heat Mass Transf. **147**, 118935 (2020).

[625] R. Bennacer, A. Mohamad and M. E. Ganaoui, Thermodiffusion in porous media: Multidomain constitutant separation, Int. J. Heat Mass Transf. **52**, 1725 (2009).

[626] D. Melnikov and V. Shevtsova, Separation of a binary liquid mixture in compound system: Fluid–porous–fluid, Acta Astronaut. **69**, 381 (2011).

[627] A. Rtibi, M. Hasnaoui and A. Amahmid, Analytico-numerical study of optimal separation of species in an inclined Darcy–Brinkman porous cavity saturated with a binary mixture, Acta Astronaut. **98**, 71 (2014).

[628] V. Sints, E. Blums, G. Kronkalns, K. Erglis and M. Maiorov, Experimental research of surfaced nanoparticle thermal transport in a porous medium, Int. J. Heat Mass Transf. **125**, 580 (2018).

[629] V. Yasnou, A. Mialdun, D. Melnikov and V. Shevtsova, Role of a layer of porous medium in the thermodiffusion dynamics of a liquid mixture, Int. J. Heat Mass Transf. **143**, 118480 (2019).

[630] A. Caciagli, R. J. Baars, A. P. Philipse and B. W. Kuipers, Exact expression for the magnetic field of a finite cylinder with arbitrary uniform magnetization, J. Magn. Magn. Mater. **456**, 423 (2018).

[631] E. Ley-Koo, T. A. Góngora and H. Torres-Bustamante, Comment on "Exact expression for the magnetic field of a finite cylinder with arbitrary uniform magnetization" A. Caciagli, R.J. Baars, A.P. Philipse, B.W.M. Kuipers, JMMM 456 (2018) 423–432, J. Magn. Magn. Mater. **508**, 166753 (2020).

[632] A. Vilfan, S. Subramani, E. Bodenschatz, R. Golestanian and I. Guido, Flagella-like Beating of a Single Microtubule, Nano Lett. **19**, 3359 (2019).

[633] A. Zaben, G. Kitenbergs and A. Cēbers, Deformation of flexible ferromagnetic filaments under a rotating magnetic field, J. Magn. Magn. Mater. **499**, 166233 (2020).

[634] A. Zaben, G. Kitenbergs and A. Cēbers, 3D motion of flexible ferromagnetic filaments under a rotating magnetic field, Soft Matter **16**, 4477 (2020).

[635] A. H. McMillan, E. K. Thomée, A. Dellaquila, H. Nassman, T. Segura and S. C. Lesher-Pérez, Rapid Fabrication of Membrane-Integrated Thermoplastic Elastomer Microfluidic Devices, Micromachines **11** (2020).

[636] A. Dellaquila, E. K. Thomée, A. H. McMillan and S. C. Lesher-Pérez, Chapter 4 - Lung-on-a-chip platforms for modeling disease pathogenesis, in *Organ-on-a-chip*, edited by J. Hoeng, D. Bovard and M. C. Peitsch, pp. 133–180, Academic Press, 2020.

[637] E. Kume, P. Baroni and L. Noirez, Strain-induced violation of temperature uniformity in mesoscale liquids, Sci. Rep. **10**, 13340 (2020).

[638] P. Dunne, C. Fowley, G. Hlawacek, J. Kurian, G. Atcheson, S. Colis, N. Teichert, B. Kundys, M. Venkatesan, J. Lindner, A. M. Deac, T. M. Hermans, J. M. D. Coey and B. Doudin, Helium Ion Microscopy for Reduced Spin Orbit Torque Switching Currents, Nano Lett. **20**, 7036 (2020).

[639] E. Kume, A. Zaccone and L. Noirez, Unexpected thermo-elastic effects in liquid glycerol by mechanical deformation, Phys. Fluids **33**, 072007 (2021).

[640] E. Kume and L. Noirez, Identification of Thermal Response of Mesoscopic Liquids under Mechanical Excitation: From Harmonic to Nonharmonic Thermal Wave, J. Phys. Chem. B **125**, 8652 (2021).

[641] E. Kume, P. Baroni and L. Noirez, Highlighting Thermo-Elastic Effects in Confined Fluids, Polymers **13** (2021).

[642] V. Nasirimarekani, F. Benito-Lopez and L. Basabe-Desmonts, Tunable Superparamagnetic Ring (tSPRing) for Droplet Manipulation, Adv. Funct. Mater. **31**, 2100178 (2021).

[643] R. Ahmad, C. Kleineberg, V. Nasirimarekani, Y.-J. Su, S. Goli Pozveh, A. Bae, K. Sundmacher, E. Bodenschatz, I. Guido, T. Vidaković-koch and A. Gholami, Light-Powered Reactivation of Flagella and Contraction of Microtubule Networks: Toward Building an Artificial Cell, ACS Synth. Biol. **10**, 1490 (2021).

[644] A. Vilfan, S. Subramani, E. Bodenschatz, R. Golestanian and I. Guido, Flagella-like Beating of a Single Microtubule, Nano Lett. **19**, 3359 (2019).

[645] V. Nasirimarekani, T. Strübing, A. Vilfan and I. Guido, Tuning the Properties of Active Microtubule Networks by Depletion Forces, Langmuir **37**, 7919 (2021).

[646] U. Bimendra Gunatilake, S. Garcia-Rey, E. Ojeda, L. Basabe-Desmonts and F. Benito-Lopez, TiO_2 Nanotubes Alginate Hydrogel Scaffold for Rapid Sensing of Sweat Biomarkers: Lactate and Glucose, ACS Appl. Mater. Interfaces **13**, 37734 (2021).

A. Appendix

A.1. Magnetic Charge Method for Magnetostatic Field Calculations

This section sketches a standard approach of calculating the magnetic field of permanent magnets [470]. The magnetic field in magnetostatics is conservative: $\nabla \times \mathbf{H} = 0$. Thus, a magnetic scalar potential Φ_m can be introduced:

$$\mathbf{H} = -\nabla \Phi_m. \tag{A.1}$$

With $\mathbf{B} = \mu_0(\mathbf{H} + \mathbf{M})$ and $\nabla \cdot \mathbf{B} = 0$, one obtains Poisson's equation in magnetostatics:

$$\nabla^2 \Phi_m = \nabla \cdot \mathbf{M}. \tag{A.2}$$

A volume and surface integral over the magnetisation $\mathbf{M}(\mathbf{r})$ is the solution to this equation:

$$\Phi_m(\mathbf{r}) = -\frac{1}{4\pi} \int_{V'} \frac{\nabla' \cdot \mathbf{M}(\mathbf{r}')}{|\mathbf{r} - \mathbf{r}'|} d\mathrm{V}' + \frac{1}{4\pi} \oint_{S'} \frac{\hat{\mathbf{n}} \cdot \mathbf{M}(\mathbf{r}')}{|\mathbf{r} - \mathbf{r}'|} d\mathrm{S}', \tag{A.3}$$

the surface S encloses the volume V with the unit normal vector $\hat{\mathbf{n}}$. The integrands define the volume and surface charge density. The volume charge density is defined as:

$$\rho_m = -\nabla \cdot \mathbf{M}, \tag{A.4}$$

and the surface charge density as:

$$\sigma_m = \mathbf{M} \cdot \hat{\mathbf{n}}. \tag{A.5}$$

For a permanent magnet cube with saturation magnetisation M_s that is magnetised along the z-axis, the magnetisation can be assumed to be constant $\mathbf{M} = M_s \hat{\mathbf{z}}$ and the volume charge density is zero ($\rho_m = \nabla \cdot \mathbf{M} = 0$). The surface charge density remains and is defined as $\sigma_s = M_s$ on the top surface and $\sigma_s = -M_s$ on the bottom surface. Insertion into Eq. A.3 and carrying out the integration leads to the magnetic field distribution. The stray field in x-direction is:

$$\begin{aligned} B_x(x,y,z) &= \frac{\mu_0 M_s}{4\pi} \sum_{k=1}^{2} \sum_{m=1}^{2} (-1)^{k+m} \ln[F(x,y,z,x_m,y_1,y_2,z_k)] \\ F(x,y,z,x_m,y_1,y_2,z_k) &= \frac{(y-y_1) + \sqrt{(x-x_m)^2 + (y-y_1)^2 + (z-z_k)^2}}{(y-y_2) + \sqrt{(x-x_m)^2 + (y-y_2)^2 + (z-z_k)^2}}. \end{aligned} \tag{A.6}$$

The stray field in y-direction is:

$$\begin{aligned} B_y(x,y,z) &= \frac{\mu_0 M_s}{4\pi} \sum_{k=1}^{2} \sum_{m=1}^{2} (-1)^{k+m} \ln[H(x,y,z,x_1,x_2,y_m,z_k)] \\ H(x,y,z,x_1,x_2,y_m,z_k) &= \frac{(x-x_1) + \sqrt{(x-x_1)^2 + (y-y_m)^2 + (z-z_k)^2}}{(x-x_2) + \sqrt{(x-x_2)^2 + (y-y_m)^2 + (z-z_k)^2}}. \end{aligned} \tag{A.7}$$

Finally, the stray field in z-direction is:

$$B_z(x,y,z) = \frac{\mu_0 M_s}{4\pi} \sum_{k=1}^{2} \sum_{n=1}^{2} \sum_{m=1}^{2} (-1)^{k+n+m} \arctan\left[\frac{(x-x_m)(y-y_m)}{(z-z_k)} g(x,y,z;x_n,y_m,z_k)\right]$$
$$g(x,y,z;x_n,y_m,z_k) = \frac{1}{\sqrt{(x-x_n)^2+(y-y_m)^2+(z-z_k)^2}}. \tag{A.8}$$

In the case of cylindrical permanent magnets elliptic integrals must be solved, which is significantly more involved [470, 630, 631]. Dedicated programmes exist for the modelling of such systems [620].

B. List of Publications and Presentations

- **T. A. Butcher**, L. Prendeville, A. Rafferty, P. Trtik, P. Boillat and J. M. D. Coey
  Neutron Imaging of Paramagnetic Ions: Electrosorption by Carbon Aerogels and Macroscopic Magnetic Forces
  The Journal of Physical Chemistry C **125**, 21831 (2021)

- D. Zahn, F. Jakobs, Y. W. Windsor, H. Seiler, T. Vasileiadis, **T. A. Butcher**, Y. Qi, D. Engel, U. Atxitia, J. Vorberger, and R. Ernstorfer
  Lattice dynamics and ultrafast energy flow between electrons, spins, and phonons in a 3d ferromagnet
  Physical Review Research **3**, 023032 (2021)

- J. Klotz, **T. A. Butcher**, T. Förster, J. Hornung, I. Sheikin, P. Wisniewski, A. Jesche, J. Wosnitza and D. Kaczorowski
  Fermi surface investigation of the noncentrosymmetric superconductor α-PdBi
  Physical Review B **101**, 235139 (2020)

- **T. A. Butcher**, G. J. M. Formon, P. Dunne, T. M. Hermans, F. Ott, L. Noirez and J. M. D. Coey
  Neutron imaging of liquid-liquid systems containing paramagnetic salt solutions
  Applied Physics Letters **116**, 022405 (2020)

- Poster at the "7th International Symposium on Integrated Functionalities"
  T. A. Butcher and J. M. D. Coey,
  Liquid-in-liquid manipulation and properties of paramagnetic ionic solutions
  University College Dublin, Ireland (11.8.–14.8.2019)

- Poster at the "International Conference on Magnetic Fluids – ICMF 2019"
  T. A. Butcher, G. Formon, L. Noirez and J. M. D. Coey
  Neutron imaging of paramagnetic ionic solutions
  Paris, France (8.7.–12.7.2019)

- **T. A. Butcher**, J. Hornung, T. Förster, M. Uhlarz, J. Klotz, I. Sheikin, J. Wosnitza and D. Kaczorowski
  Fermi surface investigation of the semimetal $TaAs_2$
  Physical Review B **99**, 245112 (2019)

Acknowledgements

I extend my gratitude to Prof. Dr. Michael Coey for supervising this PhD. I am also thankful to Prof. Dr. Igor Shvets and Prof. Dr. Jan Fransaer for their willingness to act as the examiners of my thesis.

My particular thanks goes to Dr. Peter Dunne and Dr. Aran Rafferty for their advice on magnetoelectrochemistry and porous material characterisation, respectively. I greatly appreciated the help they gave me and especially thank Dr. Aran Rafferty for characterising the porous properties of the carbon materials in his laboratory.

Furthermore, I am grateful to Lucy Prendeville for her assistance during the neutron imaging experiments at the NEUTRA station in the Paul Scherrer Institute. I thank Dr. Niclas Teichert for scanning electron microscopy characterisation.

Finally, I acknowledge the funding of my PhD by the European Commission under grant agreement No. 766007. This work formed part of the MAMI Innovative Training Network which aimed to combine magnetism and microfluidics [48, 467, 555, 632–646].